Spring 2016

Subterranean photobioreactors for commercial-industrial scale algal culture

Daniel James Vidt

Department: Mining Engineering

SUBTERRANEAN PHOTOBIOREACTORS FOR COMMERCIAL-INDUSTRIAL SCALE ALGAL CULTURE

by

DANIEL JAMES VIDT

A DISSERTATION

Presented to the Faculty of the Graduate School of the

MISSOURI UNIVERSITY OF SCIENCE AND TECHNOLOGY

In Partial Fulfillment of the Requirements for the Degree of

DOCTOR OF PHILOSOPHY

in

MINING ENGINEERING

2016

Approved by:

Lana Alagha, Adviser
Melanie Mormile
Samuel Frimpong
Kwame Awuah-Offei
Dev Niyogi

ABSTRACT

There are many potential benefits to the mining industry accruing from the application of algal biotechnology. The main benefits are in the production of biodiesel and in the remediation of mining brownfields. The research in this study was centered in the original idea that these brownfields represent a tremendous opportunity for use as a hybrid model for redevelopment into sustainable "mines" of biomass. The ability of these underground spaces serving as bioreactors to control all aspects of the growing environment, from lighting, to temperature, to biosecurity, are key advantages that have been identified in the literature. The many benefits inherent in sequestering the growth of phototrophic, halotolerant, eukaryotic, green microalgae within underground mining spaces mitigates many of the recognized shortcomings of current commercial-industrial models for algae culture. The singular challenge to the entire model was the effective production of light energy and fostering maximum photosynthetic efficiency within the microalgae. As a result, the focus on the experimental laboratory work concentrated on the development of tools and techniques for evaluation of different lighting regimes with an algae species chosen from a family with an industrial-commercial pedigree. The fundamental experimental work with the microalgae *Dunaliella viridis* revealed a novel and unforeseen aspect of experiments with monochromatic light sources. The results demonstrated surprising and potentially beneficial morphology changes as a result of the lighting treatments. Capitalization on these benefits in the proposed hybrid model were then examined in a collection of proposed future experiments, sustainability analysis, and fundamental economic analysis.

ACKNOWLEDGMENTS

I would first like to thank Dr. Mariesa Crow and Dr. David Summers for launching my Ph.D. work with generous laboratory start-up support from the Missouri University of Science and Technologies' Energy Research and Development Center. I am also extremely grateful for the stalwart support of my exceptional academic adviser Dr. Lana Alagha in helping me bring my degree to a successful conclusion. I know it was not an easy task to get me through, but you succeeded where many have failed and I thank you for giving me a chance. My co-adviser, Dr. Melanie Mormile, was another essential part of my success and who I cannot thank her enough for all of her help and support during my protracted stay in graduate school at MS&T. I was honored to have Dr. Kwame Awuah-Offei be a part of my committee. I hope I can one day be as knowledgeable and respected. Dr. Samuel Frimpong was a tremendous supporter on my committee and within the mining department. I heartily thank him for all of his help sustaining my dream of obtaining my Ph.D. and keeping the faith. I want to thank Dr. Dev Niyogi for his wonderful assistance and excellent contributions toward finishing my degree. Thanks to John Tyler for his engineering acumen as it was "instrumental" to the success of the project. A very special thanks to Bill Eads for going far above and beyond the call of duty in support of my work. I would also like to thank a few very special individuals from the Bigelow Labs and the CCMP in Booth Bay, ME: Dr. Bob Anderson, Dr. Nicole Poulton, and Julie Sexton. I would like to thank my wonderful wife for her support all of these years. Lastly, I would like to thank my Mom and Dad for their essential role in this momentous accomplishment.

TABLE OF CONTENTS

Page

LIST OF ILLUSTRATIONS

LIST OF TABLES

NOMENCLATURE

Abbreviation/Symbol	Description
AC	Alternating current
AMD	Acid mine drainage
ANFO	Ammonium nitrate-fuel oil mixture
ANOVA	Analysis of variance
BTEX	Benzene, toluene, ethyl benzene, and xylene
CA	Carbonic anhydrase
CFM	cubic feet per minute
Chl	Chlorophyll
Chl-a	Chlorophyll a
Chl-b	Chlorophyll b
CMM	Coal mine methane
DCM	Droplet containment peristaltic pump
DMM	Digital mulitmeter
DOC	Diesel oxidation catalyst
DOE	U.S. Department of Energy
DPF	Diesel particulate filters
DPM	Diesel particulate matter
EIA	U.S. Energy Information Administration
EL-wire	Electroluminescent wire

EPA	U.S. Environmental Protection Agency
EPA-RFS2	U.S. Environmental Protection Agency Renewable Fuel Standard as amended by 2007 Energy Independence and Security Act
FAME	Fatty acid methyl ester
FC	Flow cytometery
FL(#)	Fluorescent channel #
FSC	Forward scatter channel
GARD Guide	Global Acid Rock Drainage Guide
GEO	Genetically engineered organism
GHG	Greenhouse gas
GMO	Genetically modified organism
HRAP	High rate algal ponds
ITS	Internal transcribed spacer
LC50	Median lethal concentration
LDPE	Low-Density Polyethylene
LED	Light emitting diodes
LED	Light-emitting diode
LHD	Load, Haul, and Dump machines
LPM	Liter per minute
m	Rate of mortality
M/NM	Metal and Non-Metal
MIW	Mine Influenced Water
MS&T	Missouri University of Science & Technology

MSHA	Mining Safety and Health Administration
N	Represents the population as a count of individuals
$\overline{n}$	Mean cell population density (cells·mL-1)
NA	Carrying capacity of the environment or the maximum sustainable population
NBB	National Biodiesel Board
NEI	United States National Emissions Inventory
NIST	U.S. Department of Commerce National Institute of Standards and Technology
OPS	Open-pond system
PAR	Photosynthetically active radiation
PBR	Photobioreactor
PCB	Printed circuit board
PEI	Polyetherimide
PES	Polyethersulfone
PM 2.5	Particulate emissions of 2.5 micrometers in diameter and smaller
PPFD	photosynthetic photon flux density
PSII	Photosystem II
PVC	Polyvinylchloride
QA&AC	Quality assurance and quality control
r	Mathusian parameter or intrinsic rate of increase or instantaneous rate of increase
R^2	Coefficient of determination
rDNA	Ribosomal deoxyribonucleic acid
RGB	Red-green-blue additive color model

RIN	Renewable identification number
RO	Reverse osmosis
S	Salinity
SD	Standard deviation of the mean
SE	Standard error of the mean
SIP	Sample injection port
SSC	Side scatter channel
T_2	Doubling time
TDS	Total dissolved solids
trans	Transferrin membrane-bound proteins
UTEX	The Culture Collection of Algae at the University of Texas at Austin
WTI	West Texas Intermediate
λ	Wavelength
μ	Specific growth rate
ρ_T	Water density as a function of temperature only (in °C)
ρ_{water}	The density of water based on temperature (in °C) and the salinity (g·kg-1)
MK	Russian abbreviation for the SI unit “micrometer”

1. INTRODUCTION

1.1 BACKGROUND OF RESEARCH PROBLEM

There are many unique potential benefits in the multidisciplinary synergy of developing algal biotechnologies from a mining engineering perspective. Mining engineers are extensively trained to routinely deal with the monumental logistical challenges of moving tremendous amounts of material for the cost-effective production of wholesale commodities. Mining engineers are also keenly aware of the omnipresent focus on cost-effectiveness of every aspect of operations. This unique skill-set of the mining engineer is the needed perspective for the nascent commercial-industrial algae industry to foster the development of a viable production model. Important mining engineering concepts like limiting the re-handle of materials and proper ventilation of vast tunnel complexes for removal of gasses are foreign concepts to biotechnologists. Likewise, the sensitivities to the ambient environment and the specific culture conditions for microorganisms are equally foreign to most practicing mining engineers. However, the success of the project investigated in this manuscript, relies on a deep understanding of such multidisciplinary knowledge. Not only will mining engineering be obviously important for supplying the necessary raw materials to support a large-scale algae industry, relevant engineering and operational philosophies and principles for bringing bulk commodities to market will also be required to move microalgae out of novel laboratory experiments into being a potent disruptive technology that can transform how organic, carbon-based commodities are created.

1.1.1. Mining Engineering Interest in Algae Biodiesel The greatest benefit that algal biomass can deliver to the mining industry is the development of a stable,

sustainable source of liquid fuel. From the 1970's to the 1980's algae was going to "save" the developed world from shortages of liquid fossil fuels [1]. Should suitable amounts of algae derived biodiesel come to market via the proposed project model, it may "save" some mining operations also. With diesel fuel costs consuming hundreds of millions of dollars in coal mining operations [2, 3] and having similar impacts in metal/nonmetal mining [3], the prospect that biodiesel derived from algae could provide lower production costs; could improve capital equipment availability; and could improve working conditions while being environmentally sustainable makes the concept proposed extremely attractive to the mining industry as a whole.

1.1.2. Mining Engineering Interest in Algae for Remediation. Apart from the direct impact of a cost effective and stable fuel supply, another considerable benefit to the mining industry is the development of commercial-industrial microalgae production in facilities on abandoned/vacant/unused mining properties. In addition to ameliorating energy costs and volatility, placing major culture facilities on mining properties would help to solve a major mine management issue: environmental remediation and reclamation. Considerable economic and environmental challenges face mining companies in the remediation of mine influenced waters. The perpetual and pervasive nature of contamination from metals, acid, and residual chemicals from various operations, combined with the colossal scale of the contamination makes for a tremendous challenge for mining stakeholders to formulate effective and efficient models. This project will put forth the idea that the large scale cultivation of algae on mine sites could provide a significant remedy.

1.1.3. Obstacles to Industrial Algae Development. The last nationally sponsored assessment of resources related to algal culture as an "energy crop" was from 1978 to 1996 and summarized under the *Aquatic Species Program* [4] by the U.S. Department of Energy. This landmark study illustrated many issues with the production of fuels, specifically biodiesel, from photoautotrophic algae. Issues outlined in the closeout report, and in a myriad of subsequent research efforts around the world, enumerated several major impediments for the creation of an effective model for commercial-industrial cultivation of microalgae. In brief, the impediments enumerated in the literature include:

- Negative impacts due to variation in ambient light
- Negative impacts due to variation in ambient temperature
- Negative impacts due to a lack of biosecurity
- Competition for water resources with agriculture and municipalities
- Exorbitant infrastructure and manpower costs

As a direct result of these major obstacles, industrial culture of algae has been limited to niche markets employing culture models of minimal infrastructure producing high value commodities.

1.1.4. Description of Standard Algae Culture Models. Approaches to mitigating some of these issues have resulted in the development of two entrenched and diametrically opposed models for algae culture: the open-pond system (OPS) and the closed-photobioreactor (PBR) system. Table 1.1 lists the different systems and qualitatively classifies key features or design aspects. The information for Table 1.1 was provided from a review of selected publications [5-7]. The table is a general outline of

characteristics for comparison between the two general model types as defined in the research literature and industry.

Notable specific variations of OPS include raceway systems or high rate algal ponds (HRAPs). In engineering terms, these systems consist of mixed batch reactors as well as plug-flow designs. The specific variations have been engineered in an attempt to address some issues related to algae production and the operational costs inherent in OPS. However, they all share similar general physical and operational characteristics in that they are open to the ambient environment and rely on solar illumination of the microalgae.

Closed-photobioreactor systems include many plug-flow designs and batch reactors that are completely enclosed by transparent or translucent materials designed to encapsulate the algae for greater control of the culture environment. Again, specific variations and modified reactor designs have been engineered to attempt to increase production and reduce costs. These reactor types include flat-plate, tubular airlift reactor types that are common in bench-scale experimentation [8-15].

From a review of Table 1.1, it can be seen that many significant obstacles remain regardless of the conventional approach, OPS or PBR, to the development of commercial-industrial scale production of algae biomass as a viable replacement for fossil-carbon based commodities. While OPS systems are less costly to build and operate, they allow very little control over growth conditions resulting in low population densities and limited growing seasons when compared to PBR systems. Additionally, OPS are not very efficient in utilizing volumetric space as the typically shallow ponds take up much more area relative to the volume of the culture system.

Table 1.1. Comparing and Contrasting Open-Pond Systems and Closed-Photobioreactor Systems.

Feature or Design Aspect	Open-Pond System	Closed-Photobioreactor System
Area to Volume Ratio	Large	Small
Algae Species	Restricted	Flexible
Algae Species Selection, Main Criteria	Growth competition	Shear-resistance
Harvesting Efficiency	Low	High
Population Density	Low	High
Cultivation Period	Limited growth season	Extended growth season (natural light) to unlimited for artificial illumination.
Contamination	Possible	Unlikely and easily controlled
Light Utilization Efficiency	Poor to Fair (w/mixing)	Fair to excellent
Gas Transfer	Poor	Fair/high
Temperature Control	None to Poor (limited)	Excellent (precise)
Most Costly Parameter	Mixing	Oxygen Control, Temperature control (Lighting if artificial)
Initial Capital Investment	Small	High

Photobioreactor systems, regardless of artificial or natural illumination, are very expensive to construct compared to OPS which so far precludes their industrial use for lower value commodities like biodiesel. Furthermore, the PBR systems expend considerable operational costs on pumping and mixing of the culture when compared to

open pond systems, as the smaller surface to volume ratio requires that oxygen gas be removed and carbon dioxide gas be provided via mechanical means. As is demonstrated, neither traditional design is appropriate for the development of commercial-industrial scale of microalgal biomass production.

An ideal model growth system would consist of a hybrid of the two algae growth systems presented in Table 1.1. Such a hybrid system would have the same complete control of growth conditions as the PBR systems, but have a very low capital investment. Additionally, sustainability considerations would also be addressed whereby the development of greenfields would be mitigated, and brownfields would be redeveloped. Water resources would be highly conserved and not compete with agriculture or municipalities. Operations would be located near enough to existing population centers to minimize ancillary development of roads and infrastructure to support the workforce needed to support the commercial-industrial scale envisioned.

The novel idea of utilizing vacant/abandoned/unused underground mining brownfields was investigated as the ideal amalgam of the open-pond and closed photobioreactor systems. Vast underground complexes remain as industrial brownfields when deposits are exhausted and represent a tremendous opportunity for use as bioreactors. Underground mining operations extracting high-volume, low-value commodities such as limestone create voluminous room-and-pillar mines that are either already equipped, or require very little retrofitting and improvement for conversion into culture systems for algae. The inherent control of all aspects of the culture environment in the underground conveys all of the recognized benefits of PBR systems, but at a commercial-industrial scale. Furthermore, the properties are typically within short

distance of population centers and would provide substantial economic benefits with little, if any, necessary additional infrastructure in terms of roads and utilities.

The lynch pin in the success of the hybrid model envisioned in the project is the efficient production, distribution, and absorbance of photosynthetically active radiation (PAR). Without cost-effective energy balance in the system, whereby the light energy is readily converted into microalgal biomass, the proposed system will fail. As a result, the experimental investigations were focused on the interactions of light and biomass to determine if the cultivation of industrial quantities of algae could be accomplished in the underground spaces of vacant/abandoned/unused mine complexes.

1.2. STATEMENT OF RESEARCH PROBLEM

The most critical experimental aspects of the project were focused strictly on elucidating, quantitatively and qualitatively, the effects of artificial illumination regimes on a model halotolerant, strictly photoautotrophic, eukaryotic, green microalgae for the express purpose of growing such biomass in underground mining brownfields. The complete light security in underground mines means that absolutely all electromagnetic energy for algae growth must be provided via artificial illumination. Optimization of the lighting system is the linchpin for the model growth system proposed in this work. The confluence of the economics and environmental sustainability lay with being able to provide light energy efficiently and effectively to the photosynthetic apparatus of the algae in an effort to maximize energy capture. Since the very first description of a photosynthetic, eukaryotic, unicellular green alga's (*Cladophora* sp.) preferential uptake of red and blue wavelengths by Theodor Engelman in 1881, the intervening 130 years of research have further refined his initial findings to the point that any basic textbook

touches on the subject as illustrated in Figure 1.1 [16]. The photosynthetic pigments in Figure 1.1 are chlorophyll *a* (Chl-a) and chlorophyll *b* (Chl-b) that were both extracted in dimethyl ether [17]. However, the exact nature of the incident light needed to optimize algae energy accumulation and storage remains a subject of vast amounts of research effort. The sheer number of interdependent experimental variables, the existence of several "black boxes" of unknown biochemical function, and even the discovery of the influence of quantum entanglement [18-21] preclude a complete description of a universal model of photosynthesis. As a result, the literature review provided a very detailed background for formulating an experimental strategy. However, existing research studies could not provide the veracity necessary for determining if the proposed model of underground algae cultivation could be economically and environmentally viable. To this end, many experiments were designed and conducted to elucidate the relationships between growth rates and light treatments. The data from the experiments could then be utilized in formulas for engineering, economic, and environmental evaluations of the proposed model for industrial scale algae production in underground mines. In such a way the model would be evaluated to determine the extent to which it would be amenable to scale-up for the development of commercial and industrial production of bulk commodity algal biomass within the existing infrastructure of abandoned/vacant/unused underground mines.

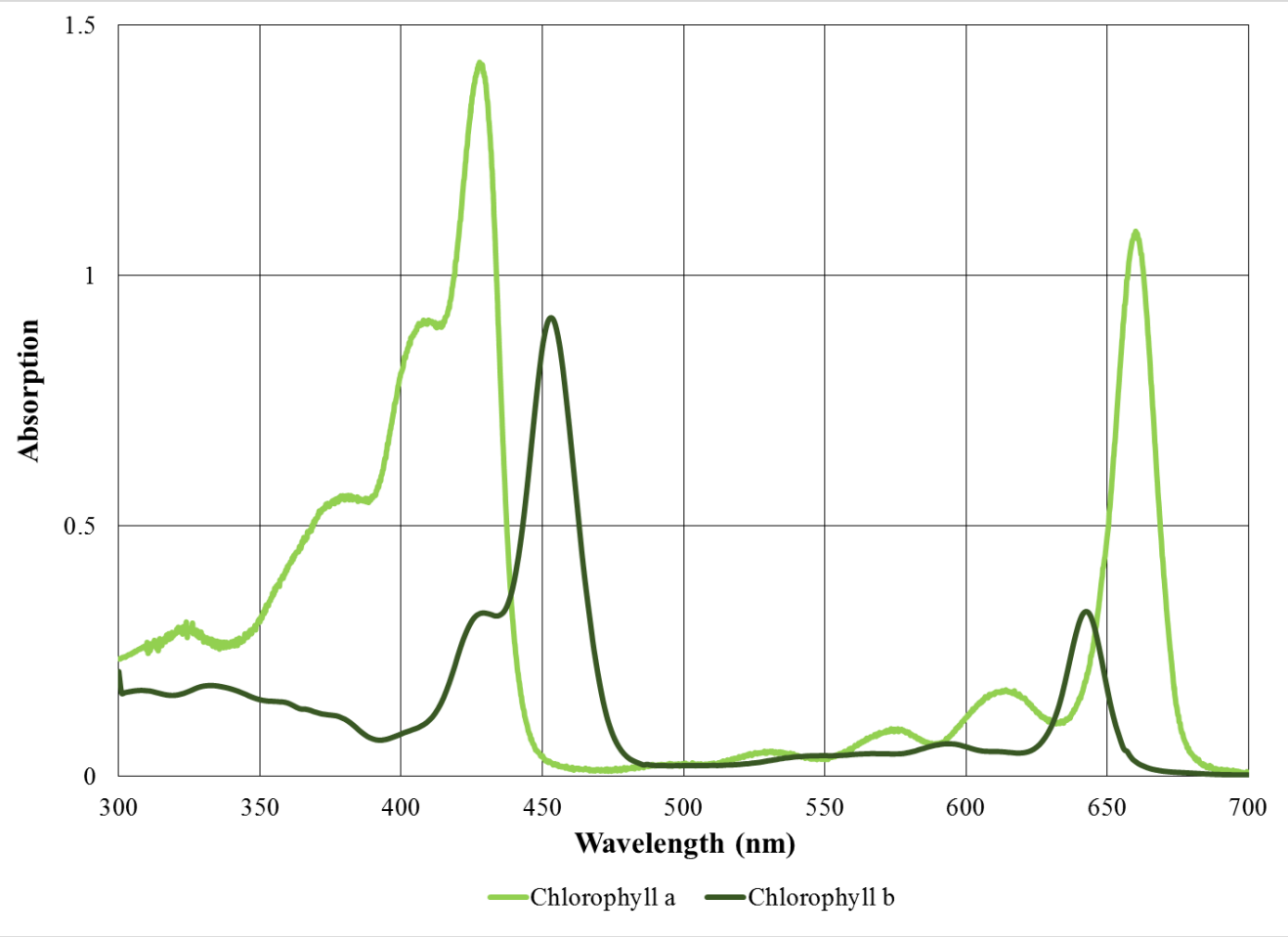

Figure 1.1. Absorbance spectrum of chlorophyll *a* (Chl-*a*) and chlorophyll *b* (Chl-*b*). Pigments were extracted in dimethyl ether and plot data was provided by [17]. Peak absorptions for Chl-*a* are at 428 nm and 661 nm. Peak absorptions for Chl-*b* are 453 nm and 643 nm.

Given the size and the scope of the implications of this project for not only the mining industry, but also for the much wider potential impacts on national, global, social, environmental, and economic issues, the research study described in this manuscript is only a beginning of what could become a powerful “disruptive technology” in the production of carbon-based commodities.

1.3. OBJECTIVES AND SCOPE OF RESEARCH

The project reported in this manuscript for the partial fulfillment of the PhD requirements of mining engineering was undertaken to provide an initial assessment of the possibilities for engineering a hybrid model of large-scale cultivation of algal biomass and the development of relevant engineering considerations arising from the deployment of biotechnologies within the brownfields of underground mining operations. Initially, research was done to assess current trends in biodiesel manufacture to further discern direct and indirect applications of algae biotechnology in the mining industry. The goal of this research project was to demonstrate that the use of abandoned/vacant/unused underground mining infrastructure to culture strictly photoautotrophic, eukaryotic, halotolerant, green algae for biomass production on a commercial-industrial scale will provide meaningful advantages to OPC and PBR systems. Pursuant to testing this goal, the following objective was required:

(i) To identify and isolate the factors of artificial illumination leading to the highest growth rate in algae, including constant versus pulsed light and blue versus red wavelength.

1.4. RESEARCH METHODOLOGY

A 2x2, fully-crossed factorial experiment was designed to test the interaction of the wavelength of light (λ) to a lighting regime of either pulsed or constant illumination. Table 1.2 illustrates the experimental organization under the factorial design. The experiments evolved into a 2x3 factorial experiment as substantial morphological difference manifested themselves in the experimental treatments.

Table 1.2. Table of Factorial Experiments

	Illumination Type	
Wavelength of Illumination	Constant Illumination	Flashing Illumination (45.6 Hz)
Red peak emission wavelength (λ) ≈ 450 nm	Constant Illumination, Blue	Flashing Illumination, Blue
Blue peak emission wavelength (λ) ≈ 660 nm	Constant Illumination, Red	Flashing Illumination, Red

The original two-way ANOVA (analysis of variance) was replaced by a three-way ANOVA when the cell morphology difference became evident. The ANOVA was preceded by separate tests for normality and equal variance of the data. The test for normality was accomplished using the Shapiro-Wilk Test for Normality and the Brown-Forsythe Test was used to evaluate the homeoedasticidy. The three-way ANOVA was followed up with the Holm-Šídák method for pairwise multiple comparison of the data in lieu of multiple t-tests to compute the significance of the results (but not the confidence

interval). Additionally, Mann-Whitney Rank Sum Tests were applied to the growth rate data to determine the statistical significance of the data from the experiments.

Experimental treatments were conducted with triple replication for each treatment cross in the experiment and descriptive statistics were developed to represent each individual cross in the experiment. The mean values and associated descriptive statistics were recorded and employed in downstream data analysis. Standard Deviation (SD), Standard Error of the Mean (SE), and Kurtosis were all calculated as part of the descriptive statistics.

1.5. SCIENTIFIC MERIT

The multidisciplinary nature of this research project lends itself to contributing to the expansion of the knowledge frontier in multiple fields. The fundamental experimental research revealed novel information about how *Dunaliella viridis* responds to the experimental treatments where different light wavelengths and illumination regimes were applied. The unique morphological response to the different lighting experiments provides new design considerations for commercial-industrial algal facilities. The absolute light security found in underground mines lends credibility to the hybrid model presented for redevelopment and remediation of mines.

1.5.1. Novelty of Fundamental Phycology Research. The fundamental research that led to the discovery of light-mediated morphology changes was a significant finding of the research project. The novelty of the discovery in the laboratory work was an original contribution to the body of knowledge in the field of phycology. Changes in salinity have been previously described as a key factor in morphological changes within

the genus of *Dunaliella*. However, the physical adaptation of *D. viridis* to different lighting regimes has not been previously encountered in the literature. The experimental results have likely illuminated one of the most perplexing aspects of *D. viridis*. Research published more than four decades ago and in Russian, demonstrated that a variant of *D. viridis* was described as preferring what continues to be thought of as a "stress" morphology [22]. Figure 1.2 is a plate reproduced from Masiuk illustrating the development of the palmella morphology in *D. viridis* variant *palmelloides* [22].

Figure 1.2 shows an illustration reproduced from the work by Masiuk to demonstrate the physically much larger, more deeply pigmented, and non-flagellated coccoid cells of the palmella morphology Masiuk documented in *D. viridis*. The results of the experimental research in this project lend support to the idea that the preference for the palmella stage may have been a seasonal adaptation to shorter wavelengths of light (blue spectrum) that are encountered during summer months when the sun is more directly overhead. Coincidentally, the warmer summer months were also when field sampling is traditionally undertaken in the Ukraine. As a result, the specific behavioral response to wavelength of light may also provide more of an understanding as to why *D. viridis* has been so difficult to classify accurately based on physiology since first being described by Emanuel Téodorescu in 1906 [23].

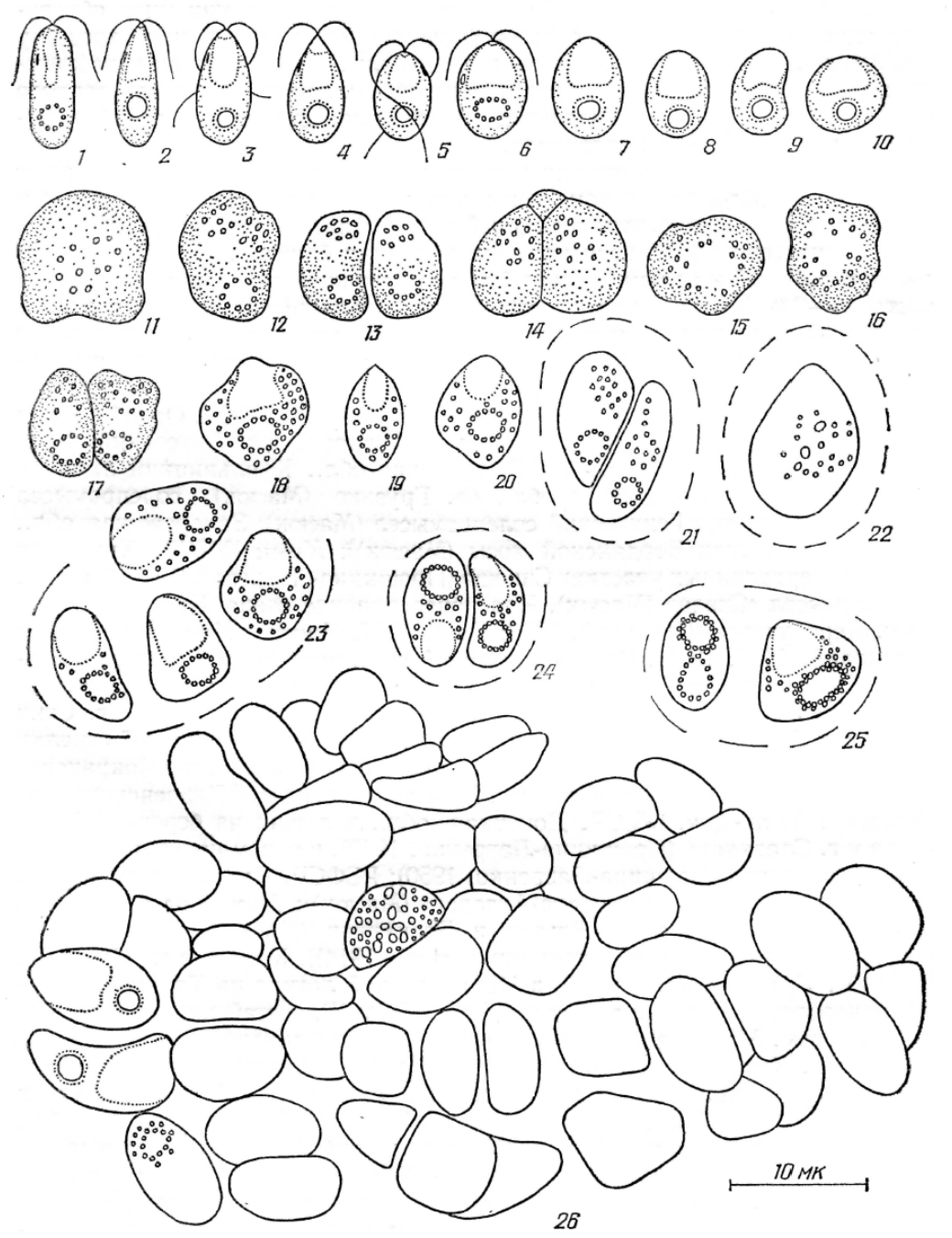

Figure 1.2. Plate reproduced from Masiuk illustrating the development of the palmella morphology in D. *viridis* variant *palmelloides.* Units of measure in the plate are in "мк" which is the Russian abbreviation for metric length "micron" or micrometer [24].

1.5.2. Implications for Development of Algae Industry. The experimental work revealed important insight into previously undervalued design considerations of commercial-industrial culture systems. While the intensity and the duration of light have long been vital design considerations, the specific wavelength of light was not of great concern. Amounts of photosynthetically active radiation (PAR) were only reported, and any specific peak or peaks in the light spectrum were ignored in most of the relevant research in the literature. However, the advent of inexpensive high-output LEDs in discrete wavelengths used in modern grow lights may now require more careful consideration of the composition of wavelengths. Such concerns have already been a major design consideration in commercial horticultural operations. Greenhouse propagation of plants routinely employ different ratios of red and blue light within operations as the light can affect hormone production in the plants resulting in either flowering or vegetative growth [25]. With commercial-industrial algal culture, the light may be used in a similar manner to manipulate the algal morphology to enhance or depress critical aspects in production. For example, *D. virdis* has shown in this project that blue light could be used to "turn" the algae into the easier to harvest, larger morphology thus providing additional cost savings in operations that offset the capital expense of the grow light systems. While not originally part of the scope of the study, the new hypothesis that morphology change has an effect on the biochemical make-up of the algae is important. While the exact nature of the biochemical adaptation in algae to different wavelengths of light is proposed for future work, for now, the idea of simply changing the wavelength of light to induce radical changes in the fractions of proteins,

fats, and carbohydrates within the algae, represents a new factor to consider in the design of commercial-industrial microalgal culture systems.

1.5.3 Contributions to the Field of Mining Engineering. This project was originally conceived to investigate the potential role the mining industry could play in the further development of a viable model of commercial-industrial algal biomass production. The motivating force behind the interest was that the mining industry has already recognized the many benefits of biodiesel. Major mining companies are already investing heavily in biodiesel derived from vegetable sources for use in equipment as well as drilling and blasting operations [26-31]. Many more companies are being incentivized by governments in the countries in which they operate to pursue alternatives to fossil-diesel [32, 33]. Algae-based biodiesel represents a much greater potential for producing the vast amount of fuels needed for wholesale conversion from fossil-diesel than other terrestrial energy crop. Furthermore, the utilization of biodiesel in ancillary operations such as blasting and mineral processing only serve to reinforce the benefit of fostering the production of increased amounts of suitable biomass for biodiesel. Additionally, the improvement in working conditions by the reduction in carcinogenic exhaust in biodiesel fueled equipment is another major benefit to the mining industry. Finally, the prospect of culturing industrial quantities of biomass within existing abandoned/vacant/unused underground mining properties yields even more benefits to mining operations. The ability of algae to be developed into a biotechnology to both produce biomass for biodiesel while simultaneously remediating mine influenced waters is a tremendous benefit to the field of mining engineering. In the research literature,

algae have demonstrated that they can adsorb a wide array of soluble metal ions and can increase the pH of their aqueous environment [34-37].

The final proof of the scientific merit of this project for the mining engineering profession has occurred only recently. In December of 2014, an announcement of a formal research collaboration between a U.K. national laboratory, four research-intensive universities in England, the U.K. Coal Authority and the waste and recycling firm Veolia was made public. Specifically, the group working under the GW4 research project, has just now begun investigations for employing microalgae in the clean-up of mine influenced waters from the Wheal Jane tin mine in Cornwall. The researchers also expect to be able to reclaim the valuable metals from the algae and process the biomass into biofuels. The University of Exeter's Camborne School of Mines has played a major role in the project development and has provided substantial expertise[38].

1.6. STRUCTURE OF DISSERTATION

The dissertation presented in this manuscript in partial fulfillment of the requirements for the Doctor of Philosophy degree in Mining Engineering continues in Section 2 with a full review of the scientific literature commensurate with the scope and scale of the multidisciplinary research that was undertaken. Section 2 demonstrates the applications of algal biotechnologies to the mining engineering field. Additionally, the enterprise of the mass culturing of aquatic microalgae within the industrial brownfields of abandoned/vacant/unused underground mining complexes is also reviewed as a remediation/reclamation technology for mining. Collateral benefits are further examined as part of the background leading to the formulation of a hybrid model of culturing algae underground. The final outcome of Section 2 will provide the reader with a clear

understanding of the many benefits and limitations inherent in sequestering the growth of photoautotrophic, halotolerant, eukaryotic, green microalgae within existing underground mining spaces.

Section 3 describes the extensive materials and methods developed for the fundamental quantitative experimental research expected in a newly founded facility. Included in Section 3 is a discussion of the rationale for the choice of a model microalgal species. The Section also describes the extensive modifications to both the flow cytometer machine and the flow cytometer sampling methods for enumerating algae. Since the singular weakness to the entire proposed algae culture model is the effective production of light energy and the fostering of maximum photosynthetic efficiency within the microalgae, a substantial amount of method development was also devoted to evaluations of light emitting diodes and electronic drivers for the purpose of powering and modulating the light. As a result, Section 3 will provide the background and rationale behind the development of specific tools and techniques for the evaluation of different lighting regimes with a model algae species chosen from a family with an commercial-industrial pedigree.

Section 4 will delineate the results of the fundamental experimental work with the microalgae *D. viridis* within the factorial experiments. Also described in Section 4 are the results that revealed a novel and unforeseen aspect of experiments with monochromatic light sources on *D. viridis*.

Statistical analysis of the results and subsequent discussions about the significance of the results are discussed and summarized in Section 5. Specifically,

Section 5 contains an outline of the specific rationale behind the statistical treatments and their implications on the experimental results.

Section 6 will discuss conclusions that can be drawn from the experimental work and applied to the proposed model of underground cultivation of commercial-industrial quantities of microalgae. Section 6 also describes recommendations for future work in relation to further development and refinement of the utility of cultivation of microalgae in abandoned/vacant/unused underground mine spaces.

2. LITERATURE REVIEW

2.1. INTRODUCTION

The challenge issued in undertaking this research project as part of the fulfillment of the requirements for a PhD in mining engineering was to integrate two seemingly, diametrically opposed fields of research, mining engineering and biotechnology. The production of mined raw materials for profit, and the need for sustainable environmental remediation and reclamation seem to be irreconcilable. However, the integration of mining industry needs for profitable production and mineral processing, with biotechnology for the remediation and reclamation of mining properties, is important and timely. In fact, these disparate fields can be combined to create a synergy of sustainability, both environmentally and economically, to usher in an age of carbon-derived commodities that can replace fossil sources.

The review of the literature provides the context for a better understanding of the needs of the mining industry, and the direct and indirect benefits that algae-derived products and processes can have in addressing those needs. The issues inherent in the full development of the algal biomass industry, and the impact and relevance of this proposed, unique model for commercial-industrial scale algal culture will be discussed. Further, the key aspect to the success of the proposed, hybrid model: efficient and economical lighting, which formed the focus of the fundamental, experimental bench work of this research project will be reviewed. Finally, the literature review will present the challenges facing the accomplishment of this project.

2.2. MINING AND ENERGY

One of the most important considerations in managing modern mining operations is the cost of energy. Everything from the extraction of gravels and sands, to the extraction of rare earths and radioactive elements, carries a substantial overhead in terms of the energy required. At the present time the mining industry uses 3% of the total industrial energy consumed in the United States [33]. Energy costs are projected to be more than 15% of the total cost of production in the mining industry in the US [33]. Further, globally, mining is estimated to consume 5-10% of the total primary energy produced in the world [39].

The mining industry is slowly responding to the new reality, that energy is no longer a dependable operational resource. The industry has slowly and steadily come to grips with energy supply problems affecting the total cost and price stability for mining operations from construction, extraction, and mineral processing. In terms of the perplexing variations in energy costs for mine management, only the time span of the research project needs to be examined. Figure 2.1 is a plot of the spot price of West Texas Intermediate (WTI) benchmark spot prices from June of 2008 to August of 2015 from data provided from the U.S. Energy Information Administration (EIA) [40]. The frenetic activity in the petroleum markets has played havoc with mining operations even when all aspects of energy usage within the mining operations have come under scrutiny by mining managers looking for cost savings. Very tight profit margins mean that an even subtle increase in the price can strain the bottom line of operations to the point of them being shuttered due to high production costs [41-43]. Further, trying to forecast the markets has led to as many discarded theories, as there have been dramatic changes in the price of oil. A case in point would be the theory of “Peak Oil” that was in

vogue among those discussing the oil supply around the 2008 price spike and, coincidentally, at the beginning of this research project [44].

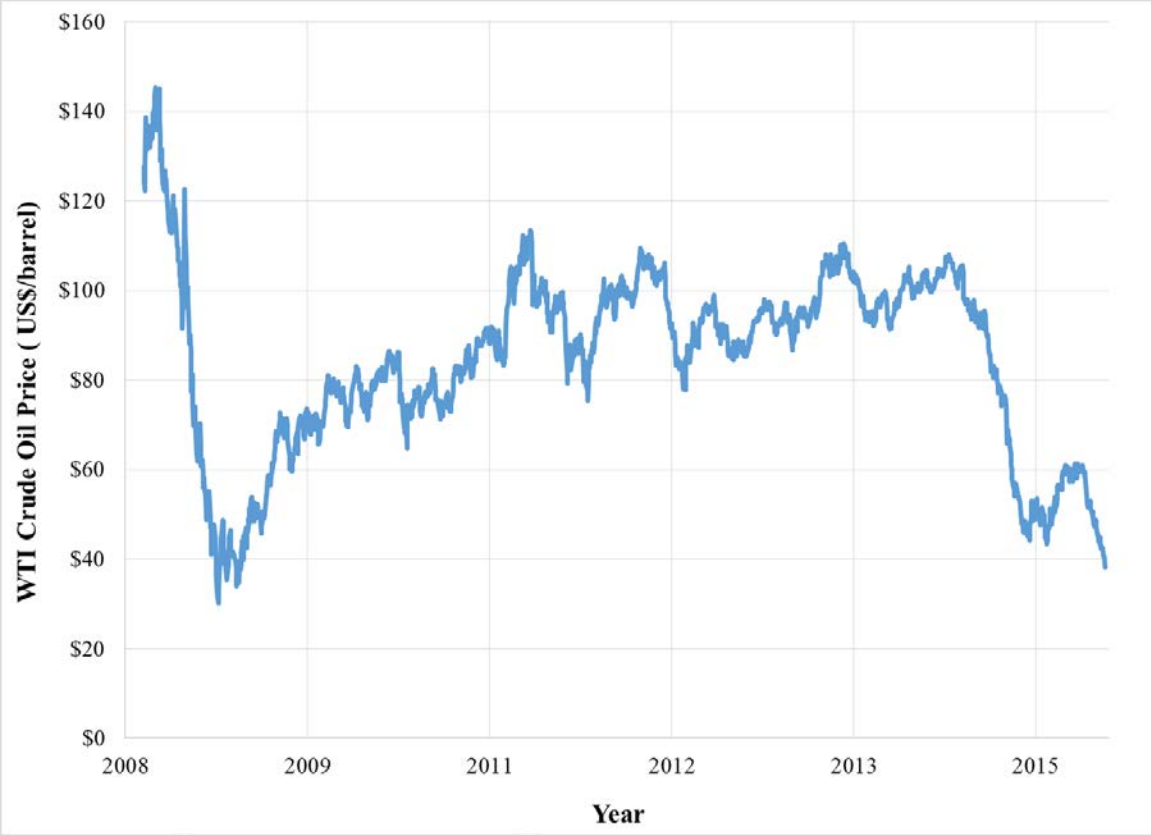

Figure 2.1. Plot of daily WTI spot price, Cushing, OK. Plot data provided from [40].

However, the closing of the world's leading website devoted to Peak Oil, *The Oil Drum*, in 2013, demonstrates the fickle nature of theories in forecasting global trends in the oil supply, even those theories proposed by recognized experts.

Extensive efforts to reduce energy usage have been successfully undertaken in the industry. Other countries have also recognized the significance of mine power usage and

the critical importance of improving energy efficiency. The magnitude of the energy supply problems for the continued prosperity of the mining industry can also be seen in the number of countries involved in creating new initiatives for alternative energy development. Major mining countries such as South Africa and Australia, have implemented strict new energy standards for mining operations [33, 45-47]. However, the rising costs of energy are outstripping these gains in efficiency. Even with maximizing worker efficiency and the employment of highly effective automated systems, energy is still the main currency of production and the driver of profit margins within any given mining operation. Despite the projected savings from research and development, improvements, and the implementation of best practices, the mining industry in the U.S. alone will still require 578.8TBtu·yr $^{-1}$ [3]. In light of the wild fluctuations in the petroleum markets, looking to efficiency solutions to the energy supply issues of the mining industry, can only be part of the answer. With oil markets subject to the whims of geopolitics and production issues, a stable energy supply with the associated price stability, would greatly help mine mangers in project planning and execution. This project proposes a new initiative in that the commercial-industrial scale culture of algae could be an important solution to the energy supply problems in the mining industry, as it could represent a stable, sustainable supply of energy.

2.3. POTENTIAL IMPACTS OF BIODIESEL ON MINING OPERATIONS

In a seminal study published jointly by the U.S. Environmental Protection Agency (EPA), and the U.S. Department of Energy (DOE), energy inputs into different aspects of the extraction and processing of commodities in mining operations were examined. Figure 2.2 represents the energy sources used in the mining industry as reported in 2007

by the DOE [3]. From the graphic in Figure 2.2, diesel fuel is a major portion of the energy used in the mining industry and represents one of the largest opportunities for improvement.

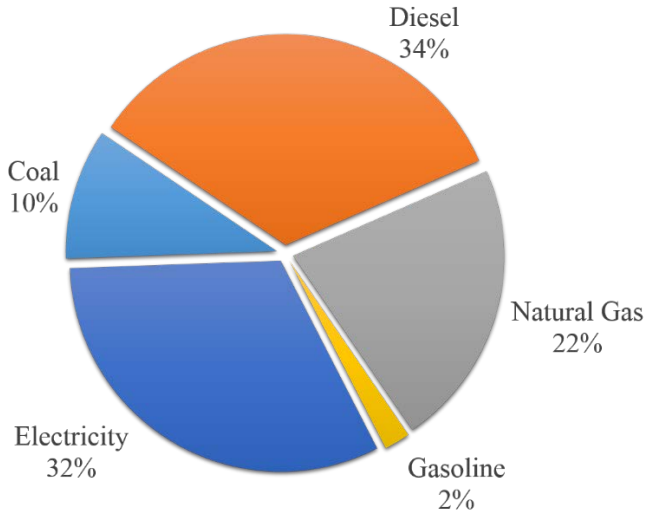

Figure 2.2. Onsite energy sources utilized in U.S. mining industry.

The confluence of the increase in energy pricing and volatility, more dispersed and small ore bodies, and increasing environmental pressure, has made biodiesel a very attractive option for the mining industry. Mining periodicals have recorded a steady stream of mining operations that are looking at biodiesel for cost-savings, improved working conditions, and stability in operational costs. A few mining companies are beginning to invest in biodiesel as their energy and environmental needs continue to grow. Energem Resources, Inc. acquired a 70% stake, costing $5.5 million (US), in a jatropha based biodiesel venture in Mozambique [28]. Mining giant, Rio Tinto, has

entered into agreements in its Pilbara drilling and blasting operations to purchase waste cooking oil for biodiesel [26]. There has even been a case where an energy company divested itself of all mining operations to focus on the development of biodiesel for the mining industry [48]. Major oil and gas developers in Angola have also partnered to develop biodiesel projects for local mining operations [49].

That biodiesel is gaining in importance can be seen as some countries are mandating its use. Australia's E3 Program and the Department of Minerals and Energy (DME) in South Africa have strict mandates for the utilization of alternatives to fossil diesel. The government of Indonesia also introduced legislation that mandates the use of biodiesel in mining [32].

2.3.1. Base Power Production. The deployment of alternative energy infrastructures like windmills and solar panels, also underscores the new reality in mining, that energy costs are significant and any and all options are on the table to mitigate both cost and volatility in the energy supply [50, 51]. Alternative energy programs featuring solar and wind generation, the capture of coal mine methane (CMM), pumped water storage, anaerobic production of methane, and the growth of biomass crops to be burned as fuel are all being evaluated, developed, and deployed across mining operations of many different sizes across the globe. As a specific example, Anglo Platinum Limited demonstrated the use of large scale stationary fuel cell systems, fueled by coal-bed methane located in Lephalale, South Africa [52]. Table 2.1 illustrates the seismic shift in the mining industry to alternative energy generation for base power production. The projects highlighted in the table have been developed within the last ten years and show wide variability in terms of locations and size of operations.

Research into supplanting fossil-diesel by bio-based fuels has been undertaken for the purpose of reducing the cost and volatility in energy in base power production. Many mining companies have already made arrangements to secure biodiesel. The proposed use of algal biodiesel in this project is especially promising as a bio-based fuel for base power production because of its potential to not displace food crops while retaining its renewable and sustainable promise [53, 54].

2.3.2. Power for Mobile Equipment. Energy costs for the transport and handling of materials represents a significant portion of operational capital [3, 55]. Further, oil market volatility presents a challenge to mine management to anticipate the cost of fueling equipment over the duration of contracts, while ensuring profitability. Another factor impacting the energy requirements of mining operations has been touched on in “Lasky’s Law”, whereby there exists an inverse relationship between ore grade and the size of deposits [56]. A similar relationship exists between ore grade and the necessary energy for extracting similar volumes of the mineral. That relationship has been confirmed in case studies [39]. As a result, the use of more mobile fleets of equipment are being deployed at mining properties to bring these more dispersed and lower grade deposits to market. This deployment of more mobile equipment is creating pressure on mining companies to find cost-competitive solutions for the fueling of equipment. Since major deposits of sufficient quantity and quality have been exhausted, and most current deposits are more difficult to access, there has been a retreat from the significant permanent and semi-permanent infrastructure that has traditionally supported

Table 2.1. Listing of Wind and Solar Energy Projects on Mining Properties Worldwide.

Country	Company	Mine	Commodity	Installed Power	Power Type
Chile	Antafagasta Minerals	Los Pembales	Copper	69.5 MW	Solar
Chile	Antafagasta Minerals	Los Pembales	Copper	115 MW	Wind
Chile	Antafagasta Minerals	Sierra Gorda	Copper	24.8MW	Solar
Chile	Minera El Tesoro	Sierra Gorda	Gold, copper, molybdenum	64kW	Solar
Chile	Nyrstar	El Toqui	Zinc and gold	1.5MW	Wind
Suriname	IAMGOLD	Rosebel	Gold	5 MW	Solar
Burkina Faso	IAMGOLD	Esskane	Gold	(in design stage)	Solar
South Africa	Harmony Gold Mining Co. Ltd.	Kalgold	Gold	18MW-40MW (in design stage)	Solar
South Africa	Sibayne Gold	Beatrix, Cooke, Driefontein, & Kloof	Gold	10-MW	Solar
South Africa	Anglo American	Kriel colliery	Coal	240kW	Solar
Tanzania	Shanta Gold	New Luika	Gold	63kW	Solar
Brazil	Vale SA	Carajás	Iron	140 MW	Wind
Australia	Galaxy resources	Mount Cattlin	Lithium	110kW solar 6.4kW wind	Solar & Wind
Australia	BHP	West Kalgoorlie	Nickle	300kW	Solar
Australia	Rio Tinto	Weipa	Bauxite	6.7MW	Solar
Australia	Sandfire Resources	DeGrussa	Copper	10.6 MW	Solar
Canada	Glencore	Raglan	Copper-Nickle	3MW	Wind
Canada	Rio Tinto	Lac de Gras	Diamonds	9.2MW	Wind
United States	Freeport McMoRan	Bagdad	Copper-molybdenum	15MW	Solar
United States	Barrick Gold	McCarran	Gold	1.51Mw	Solar

resource extraction. Centralized energy generation and distribution, primarily the use of corded electricity, has all but disappeared in most mining operations in regards to extraction and hauling equipment. As mining operations have needed to become leaner and more nimble, mobile diesel powered equipment has proven more flexible for deployment in most operations. In the United States alone, 400 mines operate 8300 diesel powered vehicles, and are expected to continue to expand [57]. Well over 85% of underground metal/nonmetal (M/NM) mines utilize diesel powered mine equipment in the United States, with 100% of large mines (more than 500 miners) utilizing diesel powered equipment in the M/NM sector [57]. However, moving to the use of mobile diesel powered equipment has exacerbated problems associated with fossil-based liquid fuel, rising costs and volatility. That these problems are acute is evidenced by the large investments of heavy equipment manufacturers pursuing the development of a large number and diversity of alternative fueled, hybrid-electric, and battery-powered machines [51, 58-60]. In one instance, Vale has also committed hundreds of millions of dollars (US) to converting locomotives and heavy equipment in its Carajas operations to biodiesel blended fuels [61].

That biodiesel can represent a cost effective, stable, economically and environmentally sustainable replacement to fossil-diesel, for use in heavy equipment, has been demonstrated in the literature. The use of biodiesel over fossil-diesel in mining equipment contains other certain advantages. The major advantages of biodiesel over fossil-diesel are a greater cetane (CN) number, absence of aromatics, and a high oxygen content [62]. The greater CN number ascribed to biodiesel fuel is an indicator of the higher combustion speed of biodiesel fuel. The greater CN number means that engines

fueled by biodiesel will run smoother and quieter with less “knocking.” The absence of aromatics, consisting of benzene, toluene, ethyl benzene, and xylene (BTEX) reduces the carcinogenicity of both the fuel and exhaust. The higher oxygen content ensures that the fuel burns more completely, minimizing carbon monoxide.

2.3.3. Benefits to the Working Environment. There are many areas in which the development of algal based biotechnologies can benefit the mining industry. The use of algal derived biodiesel fuel in addition to reducing energy costs and market volatility may have another added advantage, which is as a major contributor to a healthier working environment. A review of the literature shows that the use of biodiesel has dramatically reduced harmful emissions that include toxins, carcinogens, and particulates in mining [63].

Soy-derived biodiesel is the only alternative fuel to be fully vetted under the criterion set forth in the Clean Air Act (1990) Tier 1,and 2 [64-67]. However, it should be noted that no organization other than the National Biodiesel Board (NBB, Jefferson City, MO USA) has successfully submitted data for review by the EPA. The California Environmental Protection Agency concluded a very detailed a Tier 1 concluding that biodiesel use should be encouraged to reduce California’s carbon footprint [68]. Therefore, the advantages reported in the literature concerning biodiesel are primarily from soy-derived fatty acid methyl esters (FAME), as viable amounts of feedstock for fuel and chemicals have yet to be generated at the commercial-industrial scale from photoautotrophic, eukaryotic, green microalgae. A major study conducted by the National Cancer Institute identified fossil-diesel exhaust as a major contributor to lung cancer in miners [69, 70]. The International Agency for Research on Cancer revised their

assessment with an upgrade of fossil-diesel fuel exhaust from Group 2B (possible carcinogen) to a Group 1 (known carcinogen) for humans [71]. Drastically reduced total amounts of emissions and the wholesale elimination of highly toxic and carcinogenic components of fossil-diesel from the cleaner burning biodiesel have been shown in the literature to dramatically improve the working environment in and around extraction and hauling equipment [63, 72-77]. Even in the most modern and efficient diesel engines, the use of off-road diesel fuel has actually increased the number of diesel particulates while making them smaller and more dangerous [78]. Environmental and public health advocates have long tracked the impact of diesel particulates (DPM). As illustrated in Figure 2.3, the total national particulate emissions of 2.5 micrometers in diameter and smaller (PM 2.5) from off-highway engines (including mining equipment) exceeds on-highway emissions according to data retrieved from the National Emissions Inventory (NEI) [79]. In the U.S., heavy duty diesel engines fueled by fossil-diesel found in mining operations can emit between 100 to 200 times the mass of fine particulates, than similar sized engines using more refined fuels like gasoline [80]. Specifically, the DPM exposure of miners in the underground has been a major issue in the United States with landmark legislation passed in the last decade to decrease the allowable DPM in working environments [81, 82]. Biodiesel, being a highly refined fuel, has been shown to reduce diesel particulate in government and industry research studies.

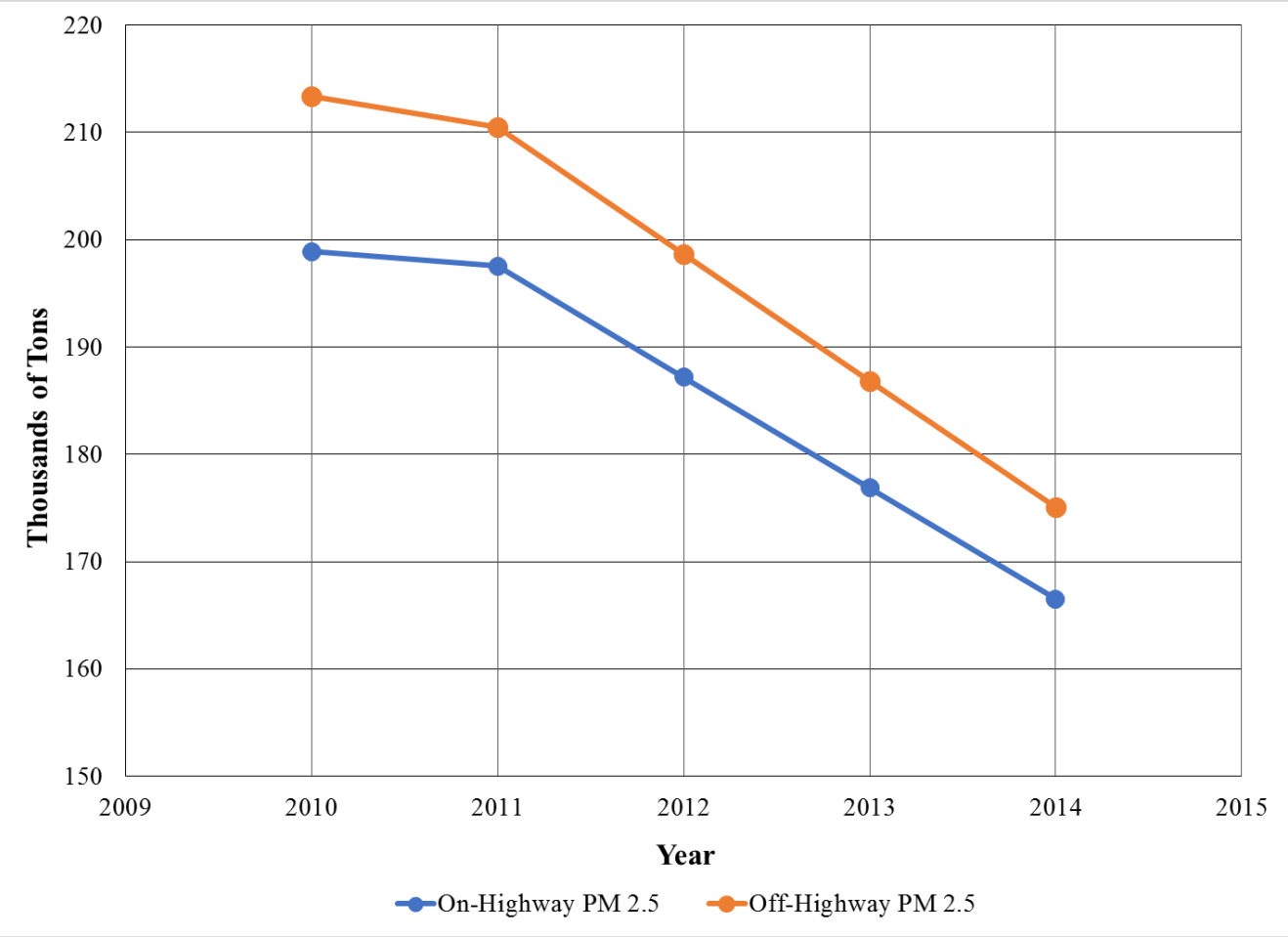

Figure 2.3. Plot of On-Highway and Off-Highway PM 2.5 as reported annually in thousands of tons in the NEI air pollutant emissions trends data maintained by the EPA.

The most dramatic reduction in DPM was found when soy biodiesel demonstrated an 80% reduction in worker exposure to DPM [77]. Biodiesel has also demonstrated improved performance of passively regenerated diesel particulate filters (DPF), such that they could potentially be utilized in underground mines [83, 84]. An excellent review on the use of biodiesel for controlling worker exposure to diesel emissions in underground mines is presented in [85].

With biodiesel a "drop-in" fuel for use in conventional diesel powered equipment, many of the more costly environmental controls and exhaust mitigation equipment can be eliminated. Biodiesel can simply replace fossil-diesel so that mining operations will not have to purchase costly, more efficient engines, install engine control systems, improve or expand ventilation systems, retrofit engine exhaust filtration systems, or use major respiratory protective equipment for workers. With the most immediately tangible aspect of employing algal biomass in mining as a feedstock for biodiesel, harmful emissions affecting workers can be mitigated. Furthermore, the microalgal fatty acid composition

2.3.4. Biodiesel in Explosives for Resource Extraction. Since biodiesel is chemically analogous, but more highly refined then fossil-diesel, it has utility outside of the fuel tanks of power generation and mobile equipment. The second most prevalent use of diesel fuel in mining operations is for mixing with ammonium nitrate to create a bulk explosive. The ammonium nitrate-fuel oil mix (ANFO) is a ubiquitous explosive for the removal of overburden and resource extraction. By utilizing a bio-based diesel in the ANFO, the whole-sale elimination of harmful and toxic chemicals improves the environmental impact. In research conducted at the University of Missouri Science & Technology (MS&T), the use of this biodiesel as a direct replacement for fossil-diesel in

the ANFO (ANSoy) mix was thoroughly explored, and has shown tremendous promise [86]. Again, only soy-based biodiesel has been investigated for this purpose as no research with algae-based diesel has been published.

2.3.5. Biodiesel in Mineral Processing. Research into the use of biodiesel in mineral processing has only recently been investigated. In that research, biodiesel has demonstrated an enhanced ability to float oxidized coal, and was a significantly better collector than fossil-diesel or kerosene [87]. The use of vegetable oil in coal mining has been researched previously for recovering coal from waste fines [88]. Exotic vegetable oils from the polanga (*Calophyllum inophyllum* L.) and mahua (*Madhuca longifolia*) seeds, have demonstrated great potential as flotation collectors in non-coking coals [89]. The use of biodiesel in mineral processing demonstrates yet another potential way that the commercial-industrial scale culture of algae could benefit the mining industry.

2.3.6. Disadvantages of Biodiesel in Mining Operations. To be able to present a complete evaluation of the potential of commercial-industrial scale algae culture, it is necessary to review the potential disadvantages of the use of biodiesel fuel in mining operations. Case studies from research presented in the literature have reported drawbacks to the employment of vegetable based biodiesel under specifically defined circumstances and situations.

2.3.6.1. Problems with biodiesel in supply. With the push by government regulators and environmental groups to reduce greenhouse gas (GHG), and toxic and carcinogenic emissions from the off-road diesel engines used in the mining industry, biodiesel demand could easily outstrip supply. A recent report by the U.S. Energy Information Administration (EIA) in July of 2015, forecasts the necessary growth in

biodiesel as a result of the increased requirements of the U.S. Environmental Protection Agency Renewable Fuel Standard as amended by 2007 Energy Independence and Security Act (EPA-RFS2) [90]. A vigorous commercial-industrial scale algae culture has the potential of significantly adding to the available biodiesel supply.

The law of supply and demand also affects the availability of biodiesel. Two factors affect the supply of biodiesel, the price of oil and the price of the vegetable commodities used in the production of biodiesel. The cost competitiveness of biodiesel is an issue when the price of oil trends down. In 2008, rack prices (wholesale) for biodiesel blended to B99.9 were $4.50 per gallon, which was cost competitive with fossil diesel at the time [77]. However, over the course of this research project, the price of diesel has decreased significantly with retail prices for fossil-diesel falling to nearly half of the wholesale price of biodiesel in 2008. Biodiesel made from algae would still be subject to the competition introduced by the fluctuation in oil prices. Further, biodiesel is subject to spikes in commodity prices as FAMEs are vegetable derived, putting the industry at a further disadvantage to fossil-diesel fuel [77]. However, because algae is currently not traded as a vegetable commodity, this disadvantage would not affect the cost and therefore, the supply of algal-derived biodiesel.

2.3.6.2. Disadvantages with biodiesel in operation. The wholesale change over to biodiesel in mining operations has not occurred even though biodiesel use in mining is eligible for renewable identification numbers (RINs) as specified under §80.1401 EPA-RSF2 [91]. Furthermore, the Mining Safety and Health Administration (MSHA) has not reported receiving negative feedback from mining operations using biodiesel blends up to B99 [75]. One major hurdle is that many of the major heavy equipment manufactures do

not recommend or warrantee the use of the higher diesel blends in their engines. Most major mining equipment and engine manufacturers give guidance on the amount of biodiesel that can be blended with fossil-diesel without voiding warranties on their equipment. As long as biodiesel blends meet or exceed ASTM International's D975 specifications for 6-20% biodiesel blends, mining equipment manufactures will allow up to B20 without voiding engine warranties [92-94]. However, few give any indication that pure biodiesel, B100, is allowed [95]. Many operational issues occur when mining fleets are switched over to running higher blends of biodiesel. These include the following issues outlined in the literature:

- The hygroscopic nature of biodiesel that increases the solubility of water and can promote corrosion and microbial growth [96-98].
- Poor cold temperature performance that includes the crystallization or waxing of fuel which form at the cloud point [99, 100].
- Oxidation stability, whereby the oils breakdown over time in the presence of oxygen [101-103].
- Solvency, where the higher biodiesel blends work as solvents in the fuel systems and can lead to blockages in filters and systems [104, 105].

These issues appear to arise mainly from the basic feedstock used to create the biodiesel and the subsequent quality of the final fuel product. While these issues are significant, they are not insurmountable with proper quality control in fuel procurement, and additional maintenance of equipment. Further, higher quality feedstocks with a better mix of chemical properties could provide solutions to most of the issues. Utilizing oils

that are more saturated would mitigate almost all of the aforementioned issues and have already been characterized in several species of algae [106].

2.3.6.3. Potential negative impact of biodiesel on the working environment. Testing on the biological effects and on the toxicity of biodiesel exhaust has found negative impacts on the working environment in three areas:

(a) The production of harmful organic aerosols. A significant issue was examined in relation to the increase in the soluble organic fraction found on DPM that was emitted by equipment using biodiesel. Testing showed higher organic carbon aerosols in engines that were operated under light-loads and fueled with B50 [62]. Organic aerosols are known to be detrimental for human health on a number of levels. However, the addition of a diesel oxidation catalyst (DOC) effectively reduced the aerosol emissions as did the utilization of B100 in the same testing [107].

(b) An increase in nitrogen oxide emissions. The burning of biodiesel also results in nitrogen oxide emissions and the potential to increase aldehydes, depending on fuel quality [108]. These emissions are likely to create stress in living organisms [109].

(c) A higher mutagenic response. Testing on the general biological effects and on the toxicity of biodiesel exhaust, found another potential problem with the use of biodiesel. In one study, a mutagenicity analysis was conducted using an Ames Salmonella Assay with the bacteria *Salmonella typhimurium*. A higher mutagenic response was

> noted when biodiesel B100 was used under light-engine loading conditions. However, the introduction of a DOC dramatically reduced, between 59% and 69%, of the mutagenic activity [110].

These disadvantages, while reported as part of this complete investigation into the use of biodiesel, are either correctable or small, compared to the significant reductions in the DPM and BTEX associated with fossil-diesel exhaust.

2.4. POTENTIAL FOR PHYCOREMEDIATION OF MINE INFLUENCED WATER.

The large scale cultivation of algae on mine sites can provide other major benefits to mining operations. In addition to ameliorating energy costs and volatility, algae can provide both remediation and reclamation on mining properties. The development of a sustainable mining industry has traditionally been challenged because of the industry's history of the wholesale degradation of the environment, and the highly publicized instances of catastrophic mismanagement of natural resources. Some critics have even gone so far as to characterize mining operations involved in the recovery of metals from pyritic ores as "geochemical trauma" [111]. Mining wastes represent a perpetual and pervasive environmental impact that lingers long after mineral deposits and reclamation funding have been exhausted. Discharge of effluent and water run-off from mining properties represents one of the largest environmental issues facing mining and environmental engineers [112]. Mine influenced waters (MIW) can be delineated into three major categories: acid mine drainage (AMD), metals contamination, and nitrate removal.

Because of the mining industry's acute focus on capital and operational costs, enhancing natural systems has long been at the center for treating MIW [113-116]. As a result, the best documented systems in the literature are systems like engineered wetlands and buried anaerobic microbial cells, as they are very low-cost, low tech solutions [114, 117-120]. Both engineered wetland systems and buried anaerobic microbial cell systems have three significant disadvantages which severely limit their capacity for treating mine waste. First, both systems are affected by changes in ambient temperatures so that they cannot be deployed effectively year round in most climates. Second, both systems are prone to hydrodynamic loading so that eventually the systems need to be stirred or replaced. Third, the systems do not provide a cost benefit. Building and maintaining these systems adds additional cost to the mining industry.

The commercial-industrial cultivation of algae in underground mine sites, as proposed in this project can provide both remediation and reclamation on mining properties without the disadvantages of both the engineered wetland systems, and the buried anaerobic microbial cell systems. Temperature is controlled because the algae are cultured underground. There is no problem with hydrodynamic loading. There is an expectation of a cash crop. Integrated algal culture systems for biofuel and bioremediation have been discussed extensively in the literature, as a means to utilize the full potential of microalgae for both creating a valuable resource in biomass, while simultaneously cleaning up the environment [7, 121-126]. Continuous development of green engineering technologies is paramount to the mining industry as ore body quality continues to decline, and environmental sensitivities become more acute [127, 128]. The limited niche development of applied biotechnological processes like bio-leaching and

bio-hydrometallurgy within mining and mineral recovery, has created a beachhead for a more economically and environmentally sustainable industry built on biotechnology. The research presented in this dissertation was undertaken to demonstrate the confluence of opportunities for the sustainable deployment of algal biotechnologies for environmental remediation and reclamation of mining properties.

2.4.1. Metals Remediation of MIW. Industrial cultures of photoautotrophic, eukaryotic, unicellular, green algae would be uniquely suited to effectively deal with one of the most pervasive environmental problems facing mining companies, dissolved metals in MIW. Dissolved metals exposure has demonstrated negative impacts on fish and invertebrate communities in bodies of water downstream of mines [129]. Human health concerns in regards to acute and long-term exposures to heavy metals related to mining and energy producing operations are well documented around the globe [130-134]. The non-biodegradable nature and bio-magnification potential of these contaminants makes them particularly vexing to remove and recover from mining effluents [135, 136]. Even with the most advanced engineered systems, the sheer volume of waste water to be remediated can result in tremendous costs [137]. In the past, both biological and non-biological systems and strategies have been deployed to address this problem with limited success.

2.4.1.1. Contrast ion exchange with algae bio-sorbents. Many different non-biological strategies utilizing activated carbon, natural zeolite, and synthetic ion exchange resins have been researched, developed, and deployed to address this ubiquitous problem.Bio-sorbents for heavy metal removal are not a novel biotechnology for mining operations as they have been key to surface flow (or aerobic wetland) remediation

systems for decades [114, 115, 138]. The general advantage of biologically mediated adsorption of metals as compared to the most common form of non-biological treatment (ion exchange) can be seen in Table 2.2 that was adapted from the literature [115]. While Table 2.2 does not distinguish between bacterial and algal bio-sorbents, it is clear that bio-sorbents, in general, have some attractive advantages, from an operational standpoint, as they can be very flexible and forgiving.

Table 2.2. General comparisons between bio-sorbent and ion-exchange in terms of key operational characteristics. Reproduced from [115].

Characteristic	Bio-sorbents	Ion-Exchange Resins
Organic Tolerance	Organic contaminants have little or no effect	Organics can foul resins
Osmotic Shock	Not sensitive	Sensitivity to rapid changes in ionic concentration
Metal Selectivity	Metal preference ratio of 2:1; minimizing chromatographic effect	Non-selective resins have metal preference ratio of 150:1
Dissolved Solids Tolerance	High tolerance	Less tolerance to high TDS; Ca, and Mg affect metal loading

As a renewable and inexpensive bio-sorbent, algae have demonstrated much higher uptake capacity of metals then non-biological materials like activated carbon, zeolite, and ion exchange resins [37, 139, 140]. For that reason, studies of bio-sorbents involving algae, have greatly expanded. One review alone examined thirty-seven different algae species for uptake of cadmium, copper, nickel, zinc, and lead [141]. In addition to base metals, precious metals [142] and even radioactive metals absorption by algae has been explored in the literature [143, 144].

2.4.1.2. Bacteria versus algae. Bio-sorbents utilizing bacteria cultures have had a long history of interest from gas, oil, and coal industries for cleaning up soluble metals that are produced directly from the mining and refining of ores, to indirect sources such as the combustion of fossil fuels used by power generation equipment [145]. Many significant studies have reviewed the capacity of not only bacteria, but also algae, yeasts, and fungi for heavy metal removal and recovery [34, 35, 146, 147]. A review of the methods for removal of soluble metals from aqueous solutions by microorganisms include the following.

(a) Volatilization- the methylation of metals.

(b) Extracellular precipitation- immobilization of metals in the environment through complexing with secretions from microorganisms.

(c) Extracellular complexing and accumulation- chelation of metals with cell's siderophore systems or extra cellular polymers in mucilage.

(d) Binding of metals to cell walls or membranes.

(e) Intracellular accumulation via active transport [145].

As a result, one of the most accepted methods for metals remediation on mining properties is the engineered wetland systems [118-120]. While the uptake of metals by other fauna in a wetland are significant, the biomineralization mediated by the anaerobic bacterial assemblages within the wetland systems are key to sequestering the metals from the natural environment. As the engineering has evolved, more focus has been placed on enhancing the biological productivity and activity of bacteria in these systems. The

development of compost reactors and submerged flow constructed wetland systems (CW) have been developed as a result.

2.4.1.3. Algae metal sorption mechanisms. The term “ion-exchange”, as noted in the literature, is actually an umbrella term for experimental observations and not indicative of the precise binding mechanisms that range from physical to chemical in nature [148]. Algae biomass is most often described as operating in a manner similar to ion-exchange resins and many physical and chemical processes have been identified [149, 150]. Metals can be sequestered by algal cells by several different mechanisms, as presented in Figure 2.4 that was adapted from [148]. Beginning on the extreme outer boundary of the cell, extracellular mucilage and exopolysaccharides contribute to a very large portion of the metal binding affinity of algae. Some of the earliest studies on metal affinity of alginates examined the polyuronides, which are polymers of uronic acids like glucuronic and galacturonic acids within the mucilage and cell exterior [151]. Most bio-sorption of metals takes place at or in the cell boundary, where the greatest amounts of negatively charged amino groups reside. Metals may also be actively taken into the cell to become sequestered by a number of detoxification mechanisms. Metals may enter the cytoplasm of the cell due to ion exchange, complexation, electrostatic attraction, or through micro-precipitation within the cells. Once inside the cell, metals may be sequestered by the accumulation on polyphosphate bodies, metallothioneins, and/or phytochelatins, which are specific intercellular metal-binding proteins [152]. Heavy metal ions may also be sequestered within vacuoles. Further, sulfated polysaccharides are responsible for uptake of trivalent species of metals, and can reside in the cytoplasm of the cell along with alginates. However, it is the algal cell wall that is recognized as the

main metals binding site, and contributes greater than 80% of the total metal accumulation [153].

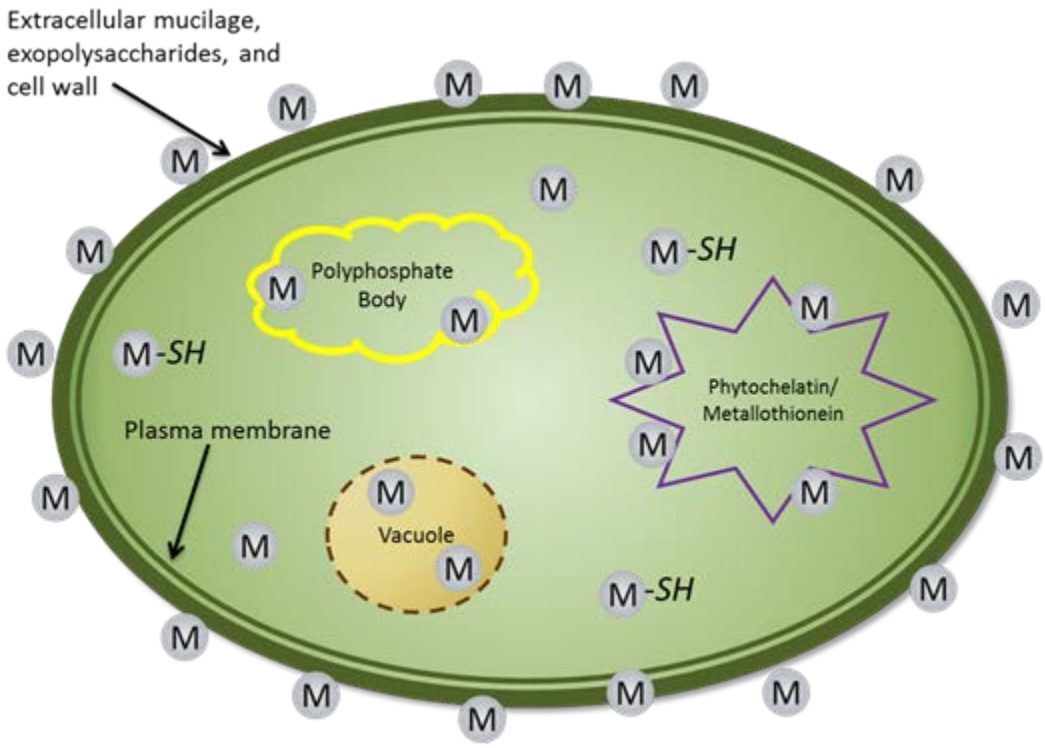

Figure 2.4. Diagram of the relative location and affinity of algal cell to metals in solution.

Analysis of recent literature also points to specific molecular components, and highly developed specificity for metallic ions among algal species. In particular, extracellular polysaccharides function as highly selective, organic ligands [154-157]. These polymers have high concentrations of negative surface charges, and have been shown to be very effective at chelating a number of heavy metal ions [158].

However, these co-production facilities deal primarily with the reduction of nutrients and not necessarily metals [7, 159-162]. In fact, reviews of the literature demonstrate that metal sopriton by algae is novel in comparison to work with fungi and bacteria [163]. Since the late 1940's alginates have been examined for their tremendous capacity to absorb metals in aqueous solutions [151]. However, the identification of microalgae as a biosorbent has only recently been investigated as a way to reclaim toxic and sometimes precious metals for reuse from metal laden mining effluents before they can enter the natural environment [164]. Algae have even been investigated for creating cryptogamic soil crusts to stabilize and cover spoil from oil shale mining [165]. Research in the literature has found that, alive or dead, algae make excellent biosorbents of heavy metals found in aqueous solutions. The use of algae offers some potential upsides that cannot be realized using other conventional methods. These include a low cost of raw materials, no secondary pollution, and the production of a marketable commodity.

Deployment of algae in large scale remediation has been limited due to reported slow and erratic growth rates in open-pond cultures resulting in long retention times that increase capital costs due to the requirement of larger retention tanks and ponds. Harvesting of microalgae presents another large hurdle for their implementation in commercial-industrial applications because of high costs [166]. A possible solution presented in the literature would be to employ macroalgae, seaweeds, or filamentous algae because they offer similar performance to microalgae, but have the benefit of being easier to harvest [167]. However, these same studies conceded that the lower surface-area-to-volume ratio and difficulty in "farming" these organisms may nullify the cost benefit. Another potential problem may arise with the deployment of algae in mixed

metal ion systems found in actual mining effluents. The research literature related to the uptake of metal ions by microalgal species has been commonly limited to an examination of only monometallic aqueous systems [35, 139, 148, 167]. The presence of two or more dissolved metal ions in solution can have dramatic results on the uptake of algae, ranging from synergism to antagonism in the uptake rates of metals by microalgae [168]. Additionally, the health of some microalgae have been negatively impacted by the chemicals used in mineral processing, as well as, diesel fuel [169-171]. Finally, the research in the literature has shown that a number of environmental factors (temperature, alkalinity, salinity, pH, & etc.) also impact the ability of microalgae to treat MIW depending, as well as, the proportions and valance states of the metals in solution [37, 145, 153, 172-175].

However, the aforementioned issues with metals remediation by microalgae can be addressed in the microalgae culture system proposed within the project described in this manuscript. The growth of algae in underground workings of abandoned/vacant/unused mines is highly controlled by virtue of its location. Consistently favorable temperatures and illumination can be maintained for algae species that are best suited for a given contaminant and environmental profile. This control is in contrast to the reality of open-pond systems where algae biotechnologies have been severely limited.

2.4.2. Nitrate Removal from MIW. A major water quality issue for mine sites is nitrate [176]. Modern commercial explosives contain between 70% to 94% of an oxidizer consisting of ammonium, calcium, or sodium nitrate compounds which are highly soluble in water [177]. The massive amounts of large quantity/low frequency

explosives used create significant water quality issues from spillage during handling or from explosives that are left in blast holes that fail to detonate [178]. Residue and spillage of the ANFO mixture represents a large portion of the total environmental contamination on mining properties. Figure 2.5 shows the loading of blastholes with a considerable amount of spillage of excess explosive around each of the holes.

Figure 2.5. Grid of blastholes filled with ANFO. Note gray mounds denote excess nitrogenous chemical around each blasthole.

High rate algal ponds (HRAP) systems, or algal turf scrubbers, have been utilized in wastewater treatment for removal of nitrogen, phosphorous, and potassium nutrients

[179-183]. One finding provides a basis for a combined nutrient removal-metal sequestration system utilizing additional industrial or municipal waste streams to provide a synergistic affect in metals removal. Studies on *Heterosigma akashiwo* show that metal sequestration and storage capacity of the algae increased when phosphate was replete to excessive in the culture media [184]. A major research effort has been undertaken by the United States military to investigate algae's ability to remediate explosive residue. The United States Army has been actively researching the use of algae as a way to recycle M6 artillery round propellant to create biofuel at the Picatinny Arsenal [185]

2.4.3. AMD Remediation. As can be seen from the earliest regulations of MIW, the 1937 exclusion of AMD from the *Clean Streams Law* was a matter of necessity as technologies for the effective treatment of the problem were unavailable [186]. Of primary concern, then and now, is the development of methods to adequately deal with the acidic waters produced, as well as the increased solubility of toxic metals in AMD. AMD, or acid rock drainage (ARD) is the name for waters draining off of mining properties that have come into contact with rocks containing iron sulfide minerals in the form of pyrite (FeS_2) and/or marcasite ($Fe_{11}S_{12}$) that have been exposed to oxygen and water to create sulfuric acid [112, 187, 188]. The primary issue with AMD mitigation is trying to control chemical reactions that are autocatalytic in nature. The reactivity of pyrite is such that it can occur even in dry environments as illustrated in Equation (1) [187].

$$FeS_{2(s)} + 3O_2 \rightarrow FeSO_4 + SO_2 \qquad (1)$$

As outlined within the GARD Guide, mitigation of pyritic reactions is an important goal towards meeting the mining industry's objective of being truly [environmentally] "sustainable" [112].

Pyrite can also react in the absence of oxygen in acidic waters as seen in Equation (2) using only the iron(III) ions (Fe^{3+}) to propagate the formation of acid [189].

$$FeS_{2(s)} + 14Fe^{3+} + 8H_2O \rightarrow 15Fe^{2+} + 2SO_4^{2-} + 16H^+ \quad (2)$$

However, in most mine waste piles and workings, there is sufficient moisture and oxygen present to favor the following set of Equations ((3)-(5) taken from Strumm and Morgan (1996) [190]. When exposed to air and water, the following reaction equations characterize the oxidation of pyrite and the formation of protons to develop acidic water conditions that are commonly described as AMD. The oxidation of pyrite to sulfate releases dissolved iron (II) and acidity into the water as seen in Equation (3).

$$FeS_{2(s)} + \frac{7}{2}O_2 + H_2O \rightarrow Fe^{2+} + 2SO_4^{2-} + 2H^+ \quad (3)$$

The iron (II) product in the previous Equation (3) is oxidized further to iron (III) by the following Equation (4):

$$Fe^{2+} + \frac{1}{4}O_2 + H^+ \rightarrow Fe^{3+} + \frac{1}{2}H_2O \quad (4)$$

Finally, the hydrolysis of the Fe^{3+} produces iron(III) hydroxide and releases additional protons. The formation of the pale-yellow to reddish-orange iron(III)

hydroxide (yellow-boy) precipitate is a hallmark of AMD waters and is the result of Equation (5).

$$Fe^{3+} + 3H_2O \leftrightarrow Fe(OH)_{3(s)} + 3H^+ \quad (5)$$

Further, under the acidic conditions, the Fe^{3+} will exist in significant quantities as different species of iron(III) hydroxides that also influence further pyrite oxidation. In addition to the neutral species of iron(III) hydroxide, these additional species would include $Fe(OH)^{2+}$, $Fe(OH)_2^+$, $Fe(OH)_4^-$. The aforementioned positively charged species have been shown to also increase the abiotic pyrite oxidation rate [189].

In addition to the abiotic pyritic reactions, microbes are responsible for increasing the kinetics of these reactions. The rate-determining step, at the low pH values of pyrite dissolution, is the oxygenation of Fe^{2+} to Fe^{3+}. This is usually catalyzed by autotrophic bacteria such as *Ferrobacillus ferrooxidans*, *Ferrobacillus sulfooxidans*, and *Thiobacillus ferrooxidans* [191]. Such biotic reactions can accelerate the rate of conversion of Fe^{2+} to Fe^{3+} in Equation (4) via enzymatic catalysis by 6 to 8 orders of magnitude [191-193]. This regeneration of Fe^{3+}usually occurs as the result of indirect metabolic oxidation according to Equation (6) below:

$$4FeSO_4 + 2O_2 + 2H_2SO_4 \rightarrow 2Fe_2(SO_4)_3 + 2H_2O \quad (6)$$

In both the abiotic and biotic mediated AMD generation, Fe^{3+} is the key facilitator as can be seen in the previously presented equations. The effectiveness of Fe^{3+} breaking metal sulfide bonds is greater than that of protons. This is because Fe^{3+} is much more efficient at extracting electrons from the metal sulfide lattice than is O_2 [194]. Further,

the oxidative Fe^{3+} attack also applies to Equations (7)-(10) of other notable metal sulfide systems [193]:

$$PbS_{2(s)} + 8Fe^{3+} + 8H_2O \rightarrow 15Fe^{2+} + 2SO_4^{2-} + 16H^+ + Pb^{2+} \quad (7)$$

$$ZnS_{2(s)} + 8Fe^{3+} + 8H_2O \rightarrow 15Fe^{2+} + 2SO_4^{2-} + 16H^+ + Zn^{2+} \quad (8)$$

$$FeAsS_{(s)} + 13Fe^{3+} + 8H_2O \rightarrow 14Fe^{2+} + SO_4^{2-} + H_3AsO_{4(aq)} + 13H^+ \quad (9)$$

$$FeCuS_{(s)} + 16Fe^{3+} + 8H_2O \rightarrow 17Fe^{2+} + 2SO_4^{2-} + Cu^{2+} + 16H^+ \quad (10)$$

From the aforementioned reactions, it is clear that Fe^{3+} is pivotal in the creation and perpetuation of AMD along with the more ubiquitous water and oxygen. The idea of actively removing the iron from AMD has been attempted before with the use of hydrogen sulfide to precipitate the iron as an insoluble sulfide [195]. The expense and handling difficulties of hydrogen sulfide resulted in a cumbersome treatment method that was actually benefiting more from the additions of limestone used to adjust the pH.

Prevailing wisdom among many, regarding AMD, is perhaps best described by the title of an early paper on the subject, *Acid Mine Water + Limestone = Clean Stream* [196]. Today, most "best practices" seek only to minimize the exposure of pyritic rock to water and oxygen along with neutralization amendments like limestone. The ability of the proposed system is unique in that it will seek to remediate waters by sequestering the Fe^{3+} out of the environment via hybrid passive/active bioremediation. To better understand how such a biologically based system would effectively mitigate the Fe^{3+} ion

specifically, a discussion on the nutrient requirements of photosynthesizing algae is prudent.

In contrast to bacterial metabolism/catabolism, algae utilize the most common nuisance metals in ARD, iron and manganese, for biological processes associated with photosynthesis. Thus, algae have physiological systems that can readily remove these metals from the environment. It is important to note that algae's need for iron (specifically as Fe^{3+}) as a primary macronutrient, is only surpassed by its need for nitrogen and phosphorous. In terms of total physical composition, approximately 0.2 to 34µg·mg^{-1} dry weight of algae will be iron [197]. While iron is the most important of the metals required for critical photosynthetic functions, manganese is also an essential component of the water oxidizing center of photosynthesis [198]. The general mechanism for the assimilation of Fe^{3+} can be viewed in Figure 2.6.

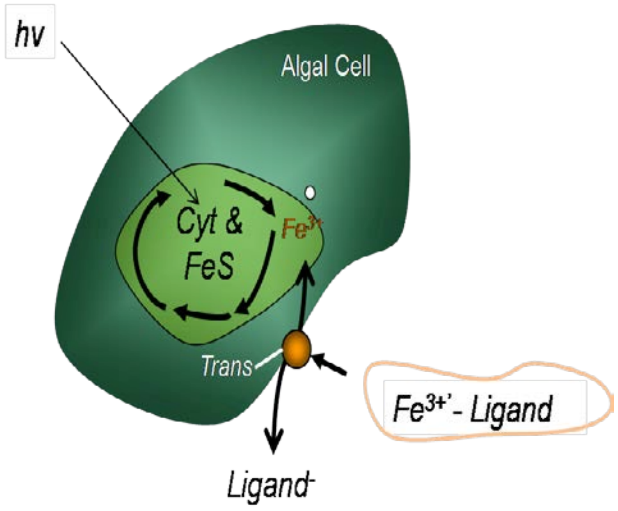

Figure 2.6. Microalgae uptake mechanism of Fe^{3+}

The diagram demonstrates that the inorganic species of Fe^{3+} chelate to a ligand which can either be produced by the algae, or by bacteria in the surrounding environment. The iron-ligand then interacts with the iron uptake sites called transferrin membrane-bound proteins, (*trans*) within the outer membranes of the algal cells. Once conveyed into the cells, the iron is generally used to assemble the large amounts of cytochromes and iron (II) sulfide (FeS) redox centers required for photosynthesis [155, 198].

Similar to conditions found in sea water, the Fe^{3+} in AMD can strongly react with water such that the iron in solution will be in both colloidal form and as metal-ligand complexes, such as siderophores or ferriooxamines that are produced by bacteria [199]. Algae have developed highly specialized systems for iron uptake where Fe^{3+} is exclusively selected for by plasma membrane bound transferrins [200]. As such, these bio-sorptive surfaces of algae not only efficiently collect Fe^{3+}, but take on a more important role of sequestering the iron within the biomass of the organism.

In addition to the ability of algae to mitigate Fe^{3+}, algae can also make direct improvements to the pH and the alkalinity of AMD waters without the expensive addition of limestone or other chemicals [201]. As an aquatic phototrophic organism, algae incorporate aqueous bicarbonates (HCO_3^-) by first transforming them into CO_2 through catalysis by carbonic anhydrase (CA). The resulting CO_2 is incorporated into the biomass via photosynthesis, and a carbonate (CO_3^{-2}) and water are released back to the environment as seen in Equation (11).

$$2HCO_3^- \xrightarrow{CA} CO_2\ (photosynthesis) + CO_3^{-2} + H_2O \qquad (11)$$

The result is an increase in pH through the formation of hydroxide ions (OH^-) upon carbonate's reintroduction to water, as well as more bicarbonate as seen in Equation 12.

$$CO_3^{-2} + H_2O \rightarrow HCO_3^- + OH^- \quad (12)$$

The major advantage to an algae-based bioremediation technology is that it is uniquely suited for AMD remediation based on the aforementioned merits of being able to selectively assimilate Fe^{3+} ions into the biomass while creating alkalinity.

2.4.4. Restoration of Soils. Algae can be used as a soil amendment to restore fertile cover for establishing flora. Unicellular calcareous algae produce unique “shields” of complex crystals of $CaCO_3$ via biomineralization in unique coccolith vesicles [202]. These would be useful for mixing with acidified soils. Algal biomass, both cyanobacteria and true eukaryotic, have been found to be excellent biofertilizers for crops such as sorghum [203]; however high costs in early analysis have hampered further development [204]. Based on research into the *terra preta* or “black earth” found in the Amazon rain forests of central South America, biochar from algae would likely make an excellent soil amendment as fine-grained charcoal has been used for millennia in agriculture as a soil conditioner [205]. Cost savings for mine remediation could be realized in the reduction of the total fertilizer required for reclamation projects as biochars from pyrolysis of algae biomass could help the soils hold onto phosphorous and agrochemicals as well as water. Because of its persistence in the soils due to being relatively inert, this could also represent a potential “low tech, low cost solution” for carbon sequestration that makes better use of carbon containing molecules then other methods [206].

2.4.5. Mining-Specific Issues with Employing Biotechnologies. The operational mining environment is a harsh landscape for most living organisms. Similarly, the aquatic environment within a mine can be very challenging for organisms to survive, let alone flourish. This particular section outlines some of the areas of most concern relating to the culture of microalgae.

2.4.5.1. Concerns with the toxicity of flotation reagents. Mineral processing operations can create potential issues with the culturing algae on mining effluent. A potential problem has been illustrated with studies of bacterial sensitivity to flotation reagents. At concentrations commonly found in mineral processing effluent, iron/mineral-oxidizing bacteria were found to be particularly sensitive to most of the flotation reagents [207]. While the intent of the aforementioned study was to examine the potential problems in using microorganisms to process gold-bearing and metal sulfide ores in bio-mining/bioleaching applications, it does reveals a potential vulnerability of growing algae on MIW.

At concentrations commonly found in mining effluent, bacteria were found to be particularly sensitive to most flotation reagents resulting in dramatically reduced populations due to cellular damage and death [145]. Other issues specific to bacterial growth for metal remediation on mining properties are the sensitivities of the bacteria to diesel fuel and other chemicals used in extraction and mineral processing. Specifically, some species of cyanobacteria exhibit decreasing *chlorophyll a* content when exposed to diesel fuel and gasoline [208].

Median tolerance limits for some reagents used in mining have been established for some of the most common chemicals used in mineral processing. Table 2.3 lists the

96-hour median tolerance limit (TLm96) or the median lethal concentration (LC50) for several reagents in relation to the inhibition of algal photosynthesis as well as other common aquatic bio-indictors [169].

However photosynthetic, eukaryotic algae can also degrade alkylphenols found in nonionic surfactants which is important for simultaneously treating these endocrine disrupting chemicals used in mineral processing [209].

Table 2.3. Table of hazardous chemicals used in mineral processing. The table has been reproduced from [169]. The TL_m96 values reported are equal to or less than 100 ppm by weight in water or the median aquatic lethal concentration is equal to or less than 100mg/L of material in water (LC_{50}) when administered for 96 hours to warm water fish such as bluegill or fathead minnow.

Reagent	Type	Fathead Minnow	Bluegill	Snail	Algal Photo-synthesis
Methyl isobutyl-carbinol	Frother	100-1000	-	-	-
Propylene glycol-methyl esters	Frother	>1000	>1000	100-1000	-
Long chain aliphatic alcohols	Frother	100-1000	50-100	100-100	100-200
Potassium amyl xanthate	Collector	1.8-18	100-200	1.0-10	100-200
Sodium isopropyl xanthate	Collector	0.18-1.8	0.01-0.1	10-100	10-100
Sodium ethyl xanthate	Collector	0.18-1.8	-	-	100-200
Minerec B (Dixanthogen)	Collector	-	1.0-10	100-200	
Isopropyl ethyl thionocarbamate	Promoter	10-100	10-50	10-100	100-200
Sodium Diethyl-dithiophosphate	Promoter	-	660-1000	>1000	-

2.4.5.2. Concerns with toxicity of metals. The mechanism of oxidative stress both increases reactive oxygen species (superoxide anion, O_2^-; hydrogen peroxide H_2O_2,

hydroxyl radical, •OH, and singlet oxygen O_2*) and reduces the antioxidant capacity within the cells of the algae [210]. Issues with types of dissolved metals can have a dramatic effect on stress in ecosystems exposed to mine drainage [211].

2.4.5.3. Concerns with acid. The acidity of many mine waters poses a significant problem for aquatic organisms. Most living cells maintain an internal biochemical state that is kept within a narrow range of pH neutrality. In the presence of increased concentrations of extracellular protons, the cell must invest heavily in actively pumping out H^+, possibly utilizing up to 50% of the ATP synthesized [36, 212]. Eukaryotic green microalgae that are acid adapted, such as *D. acidophila* demonstrate greatly reduced light harvesting complexes resulting in decreased total absorption of light [213]. Additionally, the biosorption capacity of biomass assemblages in activated sludge exhibited negligible uptake at low pH values (pH ≈ 1 to 2) [214].

2.4.5.4. Concerns with dissolved solids Another concern for cultivation of algae in MIW is the prevalence of dissolved solids. Algae can efficiently and effectively uptake most heavy metals and radioactive ions that may be entrained in these waters. Most metals found in MIW are dissolved and are found as part of the total dissolved solids (TDS). Metals become dissolved into the water as a result of the exposure of rock to oxygen and water. This exposure creates an environment where anions and cations are released resulting in increases in calcium, sulfate, magnesium and bicarbonate being dissolved in MIW [215, 216]. Further, underground operations or particularly deep pit operations can produce highly saline waters. The major concern with the dissolved solids is when the precipitate out as a result of forming insoluble oxides in responses to

exposure of MIW to higher pH environments. The accumulation of formerly dissolved solids have been found to be physical stressors for algae. [211].

2.5. LIGHT EMITTING DIODE DEVELOPMENT

One possible solution to fully exploit the biotechnological potential of algae is the employment of light-emitting diodes as grow lights [217-219]. Biological response to monochromatic light can alter carbon fixation activity in oil-producing algae [220]. Amino acid and protein production in algae has been found to be profoundly different when grown under blue light [154, 221]. Furthermore, the amount of light saturation (light intensity) can also have a dramatic effect on the photosynthetic apparatus of algae [222, 223]. The “light regime” in reference to PBRs is a common term that describes the irradiance of visible light on microalgae cells in experiments [11, 224-227]. Investigations of green algae showed that organisms grown under high intensity light developed smaller Chl antenna size that resulted in greater photosynthetic productivity and incident light efficiency [14, 228-232].

One of the major hurdles facing the research into the development of grow lights from LEDs was the absences of true-blue peak emission. The use of red LEDs had been comprehensively investigated by many research groups as the technology had been around since the 1960’s [217, 233-236]. The first major advancement in LED grow-light technology was the development of high-intensity red devices produced in high volumes as a result of research and development by Hewlett-Packard into aluminum-gallium-arsenide materials [237]. The next major advance in LEDs as a grow light technology was the development of a device with a peak wavelength in the visible blue light spectrum. The first true-blue LED (indium-gallium-nitride) was developed at the Nichia

Cooperation by Shuji Nakmura in 1999 [238]. In less than 20 years, the blue LED has revolutionized lighting as it provided the final piece of the red-green-blue additive color model (RGB) for creating efficient "white" light. As a result, few if any devices were available for consumers when the research project began and most blue emitting devices were not within the action spectrum of the photosystems for green plants. In fact, only a handful of very expensive residential LED replacement light bulbs came to market in 2008 and the U.S. Department of Energy had just rolled out the first L Prize competition for the further commercial development of solid-state lighting technologies when this project began [239]. The L Prize competition was not awarded until August of 2011 by Philips Lighting North America and since then LED devices have become more diverse, more efficient, and less expensive. The U.S. Department of Energy estimated that fewer than 400,000 LED lights were installed in the United States in 2009 which rapidly grew to over 78 million bulbs installed residentially in 2014 as a direct result of the 90% reduction in cost since 2008 [239]. The most recent update to the U.S. Department of Energy's Solid-State Lighting R& D Plan explains that LED lighting has considerable room for improvement in terms of technology as the DOE goal is a luminaire efficiency of over 200 $lm \cdot W^{-1}$ [240]. As a result, very little research utilizing LED blue grow lights for algae research had been documented prior to 2011 [241-247]. The blue LED device continues to be improved as blue phosphorescent organic materials have been created to improve the energy efficiency [248].

A major issue with efficiency of LEDs is the "trapped light" problem that has been observed since the birth of the technology in the 1960s. The active or light emitting region is actually formed, through epitaxial layering, within the semiconductor materials

as seen in Figure 2.7 that has been modified from [249]. The efficient liberation of photons from the active layer is confounded by the index of refraction of the surrounding layers. In materials with a high index of refraction, such as those found in most high-efficiency LEDs, the high-index of refraction of the semiconductor layers surrounding the active layer results in a very narrow escape cone for photons with the rest of the light trapped by internal reflection.

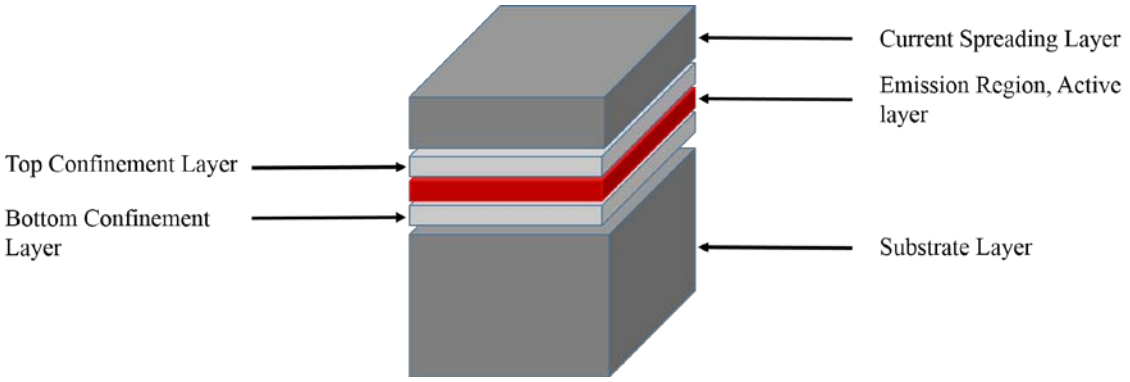

Figure 2.7. Typical layered structure of a high-brightness aluminum-gallium-indium-phosphorous (AlGaInP) LED.

Research into changing the refractive index of the materials has resulted in increases in light extraction, thus increasing the efficiency of the device. The study of the optical properties of the bioluminescent apparatus in fireflies (*Photuris Lampyridae*), has lead research scientists to developed novel supplementary over-layers for LEDs that improve light extraction by up to 55% [250].

More commonly, the physical shape of the device has been modified to improve the light extraction. Since LEDs are built up of different layers of materials as previously illustrated in Figure 2.7 using traditional semiconductor fabrication technologies, the most common geometric shape is the rectangular parallelepiped and results in large amounts of light trapped by internal reflection [249]. Ideal structures would be spheres or cones and the future is very promising with the advent of manufacturing technologies to cost effectively produce such 3-D structures [251].

3. MATERIALS AND METHODS

3.1 INTRODUCTION

The materials and methods developed for this project were extensive by virtue of the fact that the project involved the development of a completely new experimental laboratory within the Missouri University of Science & Technology's Rock Mechanics and Explosives Research Center. The development of the laboratory space and experimental infrastructure was funded in part by a grant from the Missouri University of Science & Technology's Energy Research and Development Center. Beginning with the selection of a model organism, the creation of the methodology and tools for professional quality experimental work in developing biotechnologies for mining applications was a considerable portion of the project described in this manuscript. What follows is an accounting of the exact method of development leading to the capstone experimental research project undertaken for partial fulfillment of the requirements for a PhD in mining engineering.

3.2. PHOTOTROPHIC MICROALGAE SELECTION

Multiple criteria were set for determining which organism would be employed in this work. The initial parameters were set by the physical and logistical constraints necessary to keep the overall cost of the proposed underground algal culture system competitive with more traditional and commercially proven OPS and PBR systems. Intuitively, the growth of non-photoautotrophic microorganisms or heterotrophic algae would have been better suited to the absolute darkness encountered in underground mines. However, underground mines are designed to optimize the *removal* of vast

amounts of commodities and not necessarily for bringing materials back into the mines. Heterotrophic bioreactors would require tremendous amounts of carbonaceous feedstock to be brought down into the mines. Compounding the high cost of procuring carbonaceous feedstock with the additional costs of transporting them into the mines would erase much, if not all, of the cost-benefit of utilizing the underground mining brownfields. Conversely, the transportation of electrical energy is easily accomplished with existing infrastructure into the underground spaces. Power transmission systems within underground mines are extensive and represent a considerable resource that is left abandoned in most mining operations when the mine is no longer in production. Taking advantage of the existing infrastructure through the utilization of artificial illumination of a strictly photoautotrophic organism was a key consideration in the selection of a model organism.

Similarly, the extensive ventilation of the underground mine spaces provides an equally well suited method of bringing in carbon, as CO_2, to strictly photoautotrophic organisms. Additionally, pneumatic systems for supplying gasses under pressure, such as pure CO_2 and/or ammonia into underground spaces are another omnipresent piece of infrastructure within underground mining operations. From an operational point of view, the use of photoautotrophic algae was determined to be the best way to fully leverage the existing infrastructure of underground mines as little to no development and additional equipment would be needed for bringing down into the mine spaces the two major resources required for industrial scale algae culture, light energy and CO_2. Further, infrastructure cost savings could be realized as algae could be concentrated in the underground and then transported to the surface via slurry pipelines similar to those used

in the dewatering of mine spaces. Similarly, the movement of nutrients could be accomplished as they are dissolved as a concentrate on the surface and pumped down into the underground mine spaces. As a result, almost all mechanical handling equipment, such as ore skips and LHDs (Load, Haul, and Dump machines), would not be needed, significantly offsetting capital and operational costs.

In order to maximize the cost savings found in the redevelopment of underground mining spaces, the project scope was distilled down to examining the growth of strictly photoautotrophic, eukaryotic, green algae on artificial lighting. If this most basic precept of the model could not be justified in terms of expense and environmental sustainability, the model would be easily invalidated.

3.3. SELECTION OF A HALOTOLERANT MICROALGAE

Further refinement of the scoping process for selecting a model organism was required after initial attempts to grow cultures of freshwater algae failed. The complete saturation of cultures by invasive mold and fungi into the freshwater algae cultures grown originally in the MS&T experimental mine illustrated a major unforeseen problem with the growth of algae in such spaces. While several ways of encapsulating the freshwater cultures were suggested, they were all ultimately dismissed because they eliminated any cost advantage over existing PBR systems. As a result, a switch to a marine/halotolerant species was made to mitigate the problems with contamination. An ancillary advantage with utilizing marine algae was the ability to utilize groundwater that occurs at depth in mines, and is often salty to briny. In the United States, a large portion of the ground water below 500ft (150 m) is considered saline where the dissolved salts range from 1000 to 10,000 parts per million [252]. Research from South Africa demonstrated a patented

process for “bio-desalination” of MIW in which HRAPs were used to effectively remove 80% of sulfates [111]. The switch to a marine/halotolerant algae species also fits well in keeping the model environmentally sustainable as the system would be able to utilize a water source that did not interfere with the needs of agriculture or municipalities. Finally, extremophillic organisms were determined to be a robust biotechnology due to the unique biology of the organisms [253].

A further consideration in the choice of the model algae species was to choose a species from a family with a long industrial pedigree. The genus of *Dunaliella* was an obvious choice in this respect. *D. salina* is one of only a handful of algae that have been successfully used in the commercial-industrial production of algal biomass. Starting in the 1970’s, *D. salina* has been cultivated in large outdoor ponds in Australia, Israel, China, and India for the specific purpose of collecting beta-carotene for the nutraceutical markets. Furthermore, the genus has been the subject of over 100 years of research [254]. The first formal description of the genus *Dunaliella* was made by E. C. Teodorescu in 1906 [23], and volumes have been written since as the genus has proven to be very easy to culture. The citations in the following list of characteristics has been limited to only those resources addressing the species *Dunaliella viridis*.

(a) Wide salinity tolerance (0.1 to 5M NaCl) [255-258]

(b) Tolerance to heavy metals [259]

(c) Resistant to large changes (≤ 3M) in salt concentration [260]

(d) Wall-less cells for easier disruption [261, 262]

(e) Resistance to variable nutrient concentration [262]

(f) Physiological plasticity to changing irradiance [263]

Comprehensive reviews of the state-of-the-art in research studies would include seminal works by Avon & Ben-Almotz, Borowitzka & Borowizka, Masiuk, and Oren that span over 100 years of the research on the many unique and commercial important species within the genus *Dunaliella* [22, 254, 264-268]. Further, some members of the genus have an exceptionally high oil content (*Dunaliella tertiolecta*) making them perfect candidates for further study on optimizing biofuel production [269-271]. Finally, several species within the genus have been discovered to have unique properties that may contribute to the success of future work in phytoremediation studies of mining properties. Many species within the *Dunaliella* genus are able to grow in relatively harsh conditions similar to those found on mining properties. The research effort is ongoing to discover and characterize more members of the genus. Thus far, examples from the *Dunaliella* genus include species that can flourish in extremely low pH, *Dunaliella acidophila (D. acidophila)* [272], and even a recently described species that can survive in the subaerial habitat of the Atacama Desert [273]. The choice of *Dunaliella parva (D. parva)* from the Culture Collection of Algae at the University of Texas at Austin (UTEX LB1983) was chosen to be the model species for this project based on a number of a factors. Since the production of biofuel as well as other chemical feedstocks are a high priority for the mining industry, an organism was needed that had the potential to produce suitable raw material for such applications. *D. parva* was identified in the literature as having a similar lipid chemical profile and content as *D. tertiolecta* [271], and as having shown that special phospholipids were used in retaining intercellular glycerol against strong osmotic pressures [274]. An additional advantage is that *D. parva* does not accumulate β-carotene like *D. salina* [275]. This advantage can manifest itself as cells expend energy

and cellular resources in creating useful precursors for biodiesel instead of β-carotene. Finally, *D. parva* was proven to be a strict phototroph in the research literature [276]. This attribute was particularly important to prevent confounding results as the main goal of the experimentation was to investigate providing absolutely all of the cellular energy via artificial illumination, and all of the cellular carbon from CO_2. Apart from these considerations, the *D. parva* strain in the lab that was purchased from UTEX had also proven to grow well in preliminary experiments in different media formulations. The biochemical machinery that provided the organism's halotolerant status also imbued it with the biochemistry and physiology to withstand infrequent culturing, and to tolerate wide temperature swings such as those encountered in the mining biotechnology laboratory. Furthermore, *D. parva* was not as well characterized in the research literature for growth under artificial lighting, especially under LEDs.

Micrographs of the *D. parva* under culture in the lab can be seen in Figure 3.1 that were taken with a digital microscope camera (Ken-A-Vision 1401KR Pupil Cam, Kansas City, MO, USA) attached to a American Optical microscope (Model #1034, American Optical Co., Buffalo, NY USA). The digital photograph was taken at 400x optical magnification. Shown in this digital photograph, taken at the beginning of the research project, are the two cell phenotypes types that were a constant source of consternation. The smaller, egg-shaped algae are the textbook flagellated organisms that comprise much of the morphology found in the genus of *Dunaliella*. However, the larger, more spherical cells in the picture were more difficult to classify. Early in the research project, the larger cells were thought to be undivided cells or zygotes of the algae. Later, the larger cells

were thought to be contaminant algae that may have come from an unfiltered field sample that was brought into the lab from Boothbay, ME.

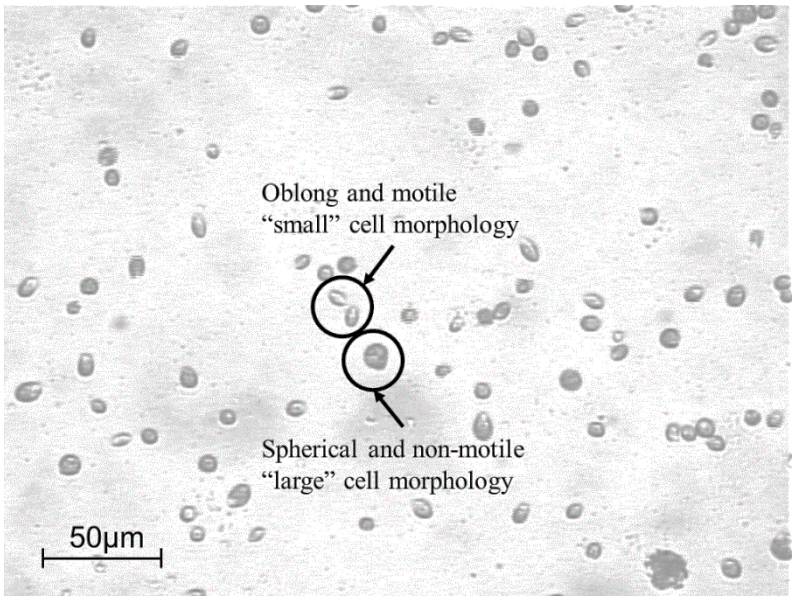

Figure 3.1. Digital photograph of UTEX LB1983 used in research project (from 2008).

Part of the reasoning behind the "contamination" theory came from observations that purified, stock samples showed no trace of the large cells. However, after transfer to bioreactors for experiments, the large cells would appear and grow at such a prolific rate that several experiments were halted as a result. For several years of the project, the larger algae would appear to overtake the experimental samples and many different methods were attempted to purify the samples. Occasionally, the larger cells would be seen in spot checks of stock cultures under light microscopes, but they were always very few. After endless cycles of attempts to purify the samples because of the presence of a

contaminant algae, experiments were finally performed to completion with the inclusion of the contaminate algae. Previously, the experiments were stopped as soon as a significant population of the contaminant algae were noted.

Investigations of different strains of *Dunaliella* had been analyzed in the literature according to their rDNA internal transcribed spacers (ITSs), and the UTEX LB1983 strain of *D. parva* was found to have more similarity to *Dunaliella. viridis (D. viridis)* in the analysis than with other conspecifics [277, 278]. Upon this discovery, that the strain of algae assumed to be *D. parva* was actually *D. viridis*, further review of the literature specific to *D. viridis* found that this particular member of the Dunaliella family has had a long history of being difficult to identify based on work translated from a seminal book on *Dunaliella* by Teodorescu [23]. The incompleteness and many inaccuracies in Teodorescu's 1906 original description of *D. viridis* contributed to a long standing confusion in the formal classification of the organism [22]. The result has been that names *D. viridis, D. parva*, and *D. euchlora* have been used without much scientific rigor and would explain why a mistake from a very respectable culture collection like UTEX could have been made. To help confirm the discovery, a sample of the algae was sent to be analyzed by Julie Sexton, the curator of the Culture Collection for Marine Phytoplankton (CCMP)[1]. Sexton reported that in the mixed sample of large and small algae cells, the larger cells had a decidedly un-*Dunaliella*-like appearance. However, when Sexton placed them into their incubators with fresh media and grow lights, only the smaller morphology were present after two weeks [279]. Evidence of dual morphology had been presented before where *Dunaliella salina* had exhibited two different

[1] In 2011, The CCMP was renamed the Provasoli-Guillard National Center for Marine Algae and Microbiota, NCMA

morphologies, “motile” and “vegetative,” [280] but not for *D. parva*. However, after the partial translation of the works by Masuik, a variation of *Dunialiella viridis* Teod., Var. *palmelloides*, was described as preferentially existing in the palmella stage whereby the algae lose their flagella, grow into a much larger coccoid form, and excrete a thick, extracellular layer of mucilage [22]. Formal DNA analysis of the algae would have been the logical next step, but such analysis was beyond the limited resources of the laboratory. However, publications in the literature about the misidentification of the UTEX LB1983 culture, and the corroborating observations from other scientists provide the support that the *D. parva* name was inaccurate. As a result, the model species of algae for the experiments in this project is correctly referred to as *D.viridis* and not *D. parva*.

3.4. MAINTENANCE OF CELL LINE PURITY

The maintenance of the purity of the algae cell line was a critical venture within the laboratory. Keeping pure samples of the model algae was a key consideration for the elimination of confounding experimental factors in the experimental protocols. The laboratory had only basic equipment for aseptic techniques and a number of procedures were employed as, initially, the apparent contamination of the model algae stocks seemed to be a constant problem. As a result, as stock cultures were refreshed every month, samples of the stocks were taken and isolated. The procedures for the following were adapted from both course training and text [198]. They included the following isolation techniques:

(a) Single-Cell Isolation by Micropipette

(b) Serial Dilution

Almost all isolations began by letting the media evaporate so that the salinity of the culture to be isolated increased to around 40‰ as the *D. viridis* proved to be halotolerant, and the salinity increase would serve as a first step to drive out contaminants. Preliminary work also showed that letting the algae culture go to a high salinity level eliminated most of the larger algae that were in the culture. Finally, isolation techniques were always applied to cultures growing in natural light and placed into full-formulations of stock maintenance media that had been autoclaved and cooled. As the preliminary work was done before the true identity of the algae was discovered, increasing the salinity probably only served to reinforce the morphogenesis of the algae into the smaller stage as the salinity increased.

3.4.1. Glassware and Equipment Cleaning Method. The preparation and cleaning of the glassware was a high priority given the perceived incidence of contamination in the stocks. New glassware was seasoned in accordance with procedures in Andersen's text [198]. Used glassware, such as test tubes and flasks containing algae grown for stock cultures or experiments, were first placed in a bleach (6 mL of commercial bleach per L) for 24 hr. Glassware was then rinsed with tap water, and then rinsed in a bath of sodium thiosulfate ($Na_2S_2O_3 \cdot 5H_2O$, Aquatic Ecosystems) that was created with 250 g per 1 L reverse osmosis water (RO,1 MΩ). Both used and new glassware were then hand scrubbed in a solution of Contrad 70 (Decon Lab, Inc. King of Prussia, PA, USA). Glassware and equipment were then rinsed three times with tap water, and then rinsed three times with RO,1 MΩ. The glassware was then steam autoclaved at 121°C & 2.0 atm for 30 min before being used.

3.4.2. Sterilization Procedures. As already noted, a steam-autoclave was utilized extensively for glassware sterilization. As is standard in method preparation, a steam autoclave reaching 121°C & 2.0 atm for 30 min was used to sterilize both liquid media and dry equipment. The preparations of media and associated chemicals were also sterilized by microfiltration methods. Vacuum filtration was accomplished with sterile, disposable 0.22μm, polyethersulfone (PES) filters (Corning®, 341174, 1000mL capacity). PES was chosen for its relatively high flow rates and protein retention characteristics that were important for removing biological material from both the rehydrated sea salts (synthetic seawater) and the natural seawater used in the lab. Fresh and synthetic saltwater used for sheath fluid in the flow cytometer were triple-filtered using the vacuum filters previously described. Stock vitamin mixtures were also vacuum sterilized directly into glass storage bottles with GL-45 screw caps. Finished culture media was steam sterilized as previously described within the respective test tubes and bioreactors that were inoculated.

3.5. GROWTH MEDIA DEVELOPMENT

Another aspect of the project was the development of a suitable working media for the experiments. The maintenance media in which algae are cultured in collections is formulated to primarily preserve the morphology of the organism. In these cases, “soil extract” and “enriched seawater” are not strictly quantifiable and are used to ensure that the algae do not undergo “test tube evolutions”. Furthermore, the nutrient additions are kept minimal as accelerated growth of the algae is not encouraged, but rather the slowest allowable population growth is preferred to prevent excessive re-culturing costs for these mostly non-profit organizations. As the purpose of the experiment in this project was to

analyze accelerating growth rates in algae, the standard culture media recipes needed to be tested and modified. The stock solution included with the UTEX LB1983 algae was Erdschreiber's Medium. Appendix contains the recipe provided by UTEX for the creation of their media. Initially, complete media was purchased from UTEX only for maintaining the stock cultures of algae. In order to develop a media for experimental purposes, the original media was deconstructed into its component parts. Two minor changes were made and they are noted in Appendix. Since the initial algae cultures in the lab were all from UTEX, they had independent recipes that were also evaluated for use with the *D. viridis*. These different recipes can also be found in Appendix along with the alterations made.

As part of the review of the methods, other media formulations were sought. Upon researcher request, the staff of the Bigelow Laboratory for Ocean Sciences at Boothbay, ME, suggested other media for the algae [281]. Evaluations of Prov50, f/2 and L1 were performed on *D. viridis* with a synthetic seawater base. The only results of the experiments that survived multiple computer failures encountered early on in the laboratory research that erased the experimental data files. The only surviving remnant of the data was recorded was as a graphic of data from experimental growth of *Dunaliella viridis* (at that time it was known as *D. parva*) and *Tetraselmis suecica* (UTEX LB 2286) within an internal Quarterly Research Summary prepared in October of 2008 in Figure Figure 3.2. The data presented show an increase in growth rates when synthetic seawater (as described in the Appendix) was substituted for natural sea water in the formulation of Prov 50. The trendlines found in Figure 3.2 reflect only the slope of the exponential

portion of the growth curves fit by eye and were not subject to the rigorous data analysis described in §3.14 of Material and Methods.

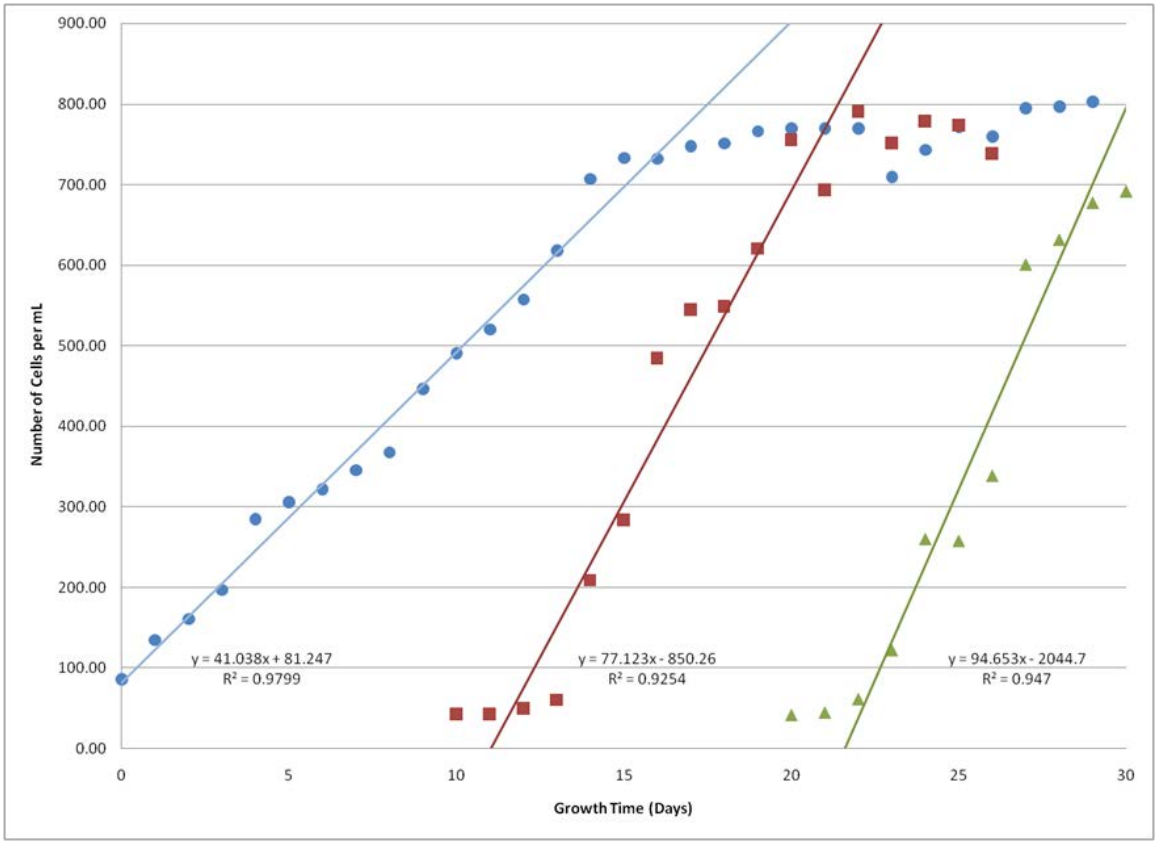

Figure 3.2. Comparison of *Dunaliella viridis* grown in Prov 50 media with natural seawater (blue circles) and synthetic seawater (green triangles). *Tetraselmis suecica* was grown in Prov50 and synthetic seawater is represented by red squares.

All recipes used and the modifications made in the experiments conducted can be found in the Appendix. The results present in Figure # demonstrate a notability better trend in the growth rate using the Prov50. From this point on in the experiments, *D. viridis* would

be cultured in a Prov 50 formulation for both stock cultures and experimental media. Major modifications to the formulation included:

(a) Using synthetic salt water in both experimental and stock media

(b) Doubling the concentration of nutrients for experimental media

(c) Leaving out the soil extract for experimental media

3.6. LIGHTING TECHNOLOGY EVALUATION

Detailed reviews of the literature revealed that there were far too many variables to adequately appraise the cost-benefit of subterranean algae culture utilizing photosynthetic algae without experimentation to determine ideal lighting conditions and the technology to support them. Conclusions based on the rudimentary cost-benefit analysis of existing illumination technologies did not provide definitive answers that could be confidently applied to specific systems of lighting and algae. The choice of the lighting device for this project was based on finding the lowest-cost photons of the required wavelength and energy that could be adequately scaled up to grow large cultures of algae. After surveying the state of the art in artificial lighting research, the light emitting diode (LED) was determined to be the most efficient device for generating the required light energy at the beginning of the experiments. Further, the future advances in LED efficiency have gained tremendous momentum as their refinement is driven by both extensive research and development, and economic factors that will continue to reduce the cost of producing the photons needed for supporting the model put forth in this project [251, 282] . Finally, additional operational cost savings was sought by deconstructing photosynthetically active radiation (PAR) into just the narrow wavelengths of visible light required for driving photosynthesis, and the application of

pulse-width modulation of the lighting. However, the literature results were again inconsistent in regards to definitive answers on how to specifically modify both the frequency of light and pulse-width to optimize growth. The complex interaction of biochemical factors in the photosynthetic process of the algae meant that experimentation would be necessary.

Specific evaluations of the different lighting technologies involved the exclusive use of a spectroradiometer to not only quantify the light quality (peak wavelength analysis), but also to measure of the spectral irradiance in units of watts per meter squared over the wavelength range in nanometers. The analytical instrumentation used for these evaluations included the following:

(a) A fiber optic coupled spectrometer with a range of 350-1150nm (GREEN-Wave-Vis, StellarNet, Inc., FL, USA)

(b) An integrating sphere (2 inch cube, IC2, StellarNet, Inc., Tampa, FL, USA)

(c) A cosine receptor (CR2 UV-VIS-NIR for 200-1700 nm with a 180° field of view, StellarNet, Inc., Tampa, FL, USA)

(d) A precision aperture was also employed in some cases (CR2-RA, 10% aperture, StellarNet, Inc., Tampa, FL, USA).

The precision aperture reduced the area of the cosine receptor by 90% to allow for measurement of the more powerful lights that were employed in the capstone experiments of the research project. Spectra Wiz software (32bit-version, StellarNet, Inc., FL USA) was used to capture spectrum data and analyze the files. Additionally, a NIST-calibration was performed on the equipment and a software file containing the

relevant software compensation for the spectrometer was included, (IRRAD-CAL file provided from StellarNet, Inc., FL, USA). The purpose of the software calibration was to allow the determination of the spectroradiometric properties of light sources. Cosine receptors provide a perfect cosine response to give accurate measurements of absolute intensity when multiple LED arrays are evaluated. Standard measurements were made using the procedures outlined by the company for evaluations of LEDs with their equipment [283].

The first step in determining the output of an LED was to set the proper voltage and current for the specific device. Power to the LEDs being evaluated was provided by an Agilent Technologies power supply (Model E3649A Dual Output, San Jose, CA, USA) that was also NIST calibrated (Z540 Certified, Certificate # CO15907-3, Newark Services, Aurora, CO, USA). The LEDs were allowed to warm up for 5 min, or until the digital mulitmeter (DMM) reading by the power supply showed a steady amperage for the device. This process allowed the semiconductor matrix to come into thermal equilibrium, and represented the "normal" average output of the device. In the case of the 5 mm through-hole devices, a heatsink was not necessary. Figure 3.3 illustrates the typical testing setup for a 5 mm through-hole device. However, a heatsink was required for the higher powered devices (Endor Star™ High-Power LED light Module, 3-Up, Deep-Red, 07007-PDRED-C & Endor Star™ High-Power LED light Module, 3-Up, Royal-Blue, 07007-PDR000-B, LEDdymanics, Inc., Randolph, VT USA) used in the capstone experiments of this project. A heatsink constructed of a single 1 mm (≈ 0.04 in) thick plate of copper that was cut into a square with sides approximately 10cm (3.9 in) long. A standoff of approximately 1 cm (≈ 0.4 in) was created with 14mm (≈ 0.5 in), #4

screws installed on the edges of the plate to allow air circulation underneath the device. A picture of an LED device used in the experiments is pictured in Figure 3.4.

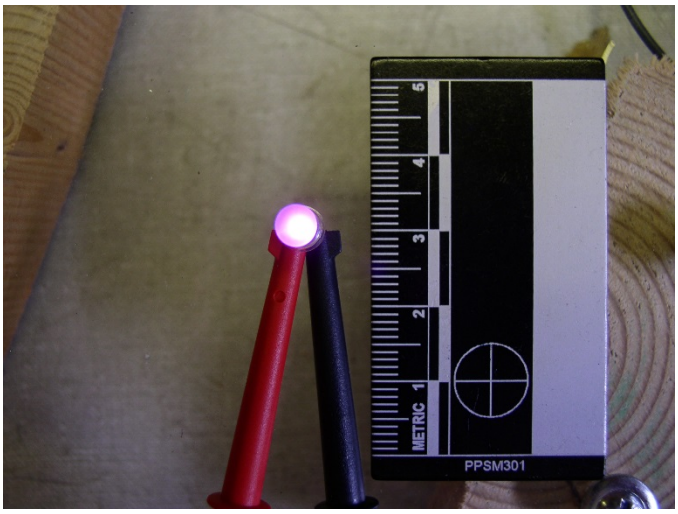

Figure 3.3. Experimental setup for taking spectroradiometric measurements with a 5 mm through-hole LED.

Passively, the copper heat sinks were able to maintain temperatures of between 50-54°C for the Royal-Blue devices, and between 67-72°C for the Deep-Red (ambient temperature between 20-23°C). The high-power devices, usually required 20 min to warm up until the DMM registered a stable amperage reading (0.841A for Royal-Blue and 0.855A for Deep-Red). Precision temperature measurements were made with a NIST traceable Type-K thermocouple (Fisher Scientific, 14-649-81, Pittsburgh, PA, USA).

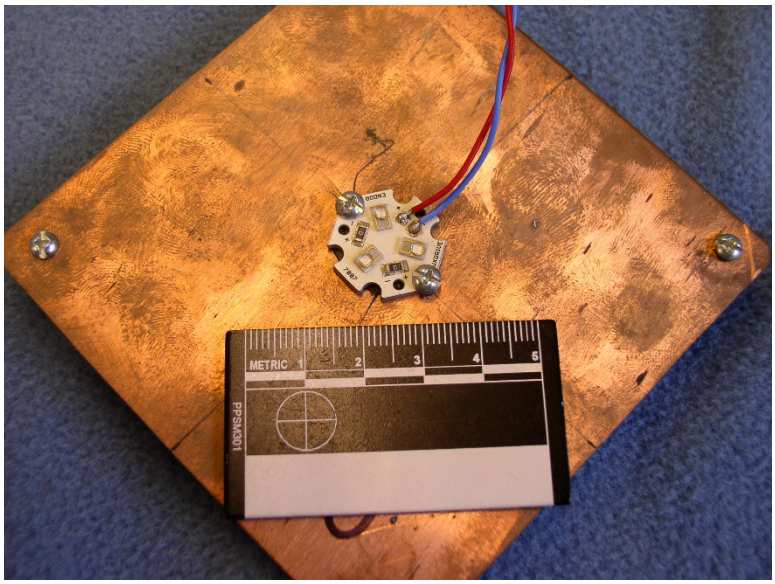

Figure 3.4. High-powered, 3-up LED (Endor Star™) mounted on copper heatsink.

Once LEDs were warmed up the analysis was conducted as follows:

(a) The integration sphere was placed over the light source and the integration time was adjusted in the SpectroWiz (Version 4.2) software to render the spectrum.

(b) Scope mode was chosen in the SpectaWiz to determine the optimal integration time for the scans of the LEDs. These initial measurements were done with counts as the abscissa and wavelength on the ordinate axis. The optimum integration time (in ms) was used to create a spectrum that utilizes between 90 and 95% of the abscissa scale.

(c) A calibration file was then loaded in order to use the spectrometer in spectroradiometer mode.

(d) A dark field spectrum, or dark scan, was then taken to "zero," a baseline measurement for the live spectrums. This was simply done by detaching the fiber optic cable from the cosine receptor or the integration sphere, and covering the end of the fiber optic port with a light proof cap. The unit of photon flux (area) density was recorded in μmol photons m^{-2} s^{-1}.

(e) Spectrums were saved and then exported to a spreadsheet program, "Microsoft Excel" (2007).

The peak emission wavelengths for experimental conditions were determined from the "Scope" mode of the SpectroWiz software using the integrating sphere previously described. The LEDs were powered by the 12 volt battery source previously described and regulated with a FlexBloc driver without any dimming or flashing added to the circuit. The results of the relative emissions from the red and blue LEDs used in the experiment are presented in Figure 3.5. The results showed a peak emission wavelength for the blue LED to be 449.5 nm and 660.0nm peak for the red Endor Star™ LEDs used in the experimental matrix for the capstone experiment.

In "Spectroradiometer" mode, the photosynthetic photon flux density PPFD was determined for each of the lighting conditions for each of the experimental illuminations within the experimental matrix. The PPFD was adjusted in the "Constant Illumination" experiments by using a precision 20 KOhm rotary potentiometer (20K-POT, LEDsupply, Randolph, Vermont, USA) to dim the LED. The LEDs needed to be dimmed because the illumination would be provided constantly whereas the flashing light would only be intermittent.

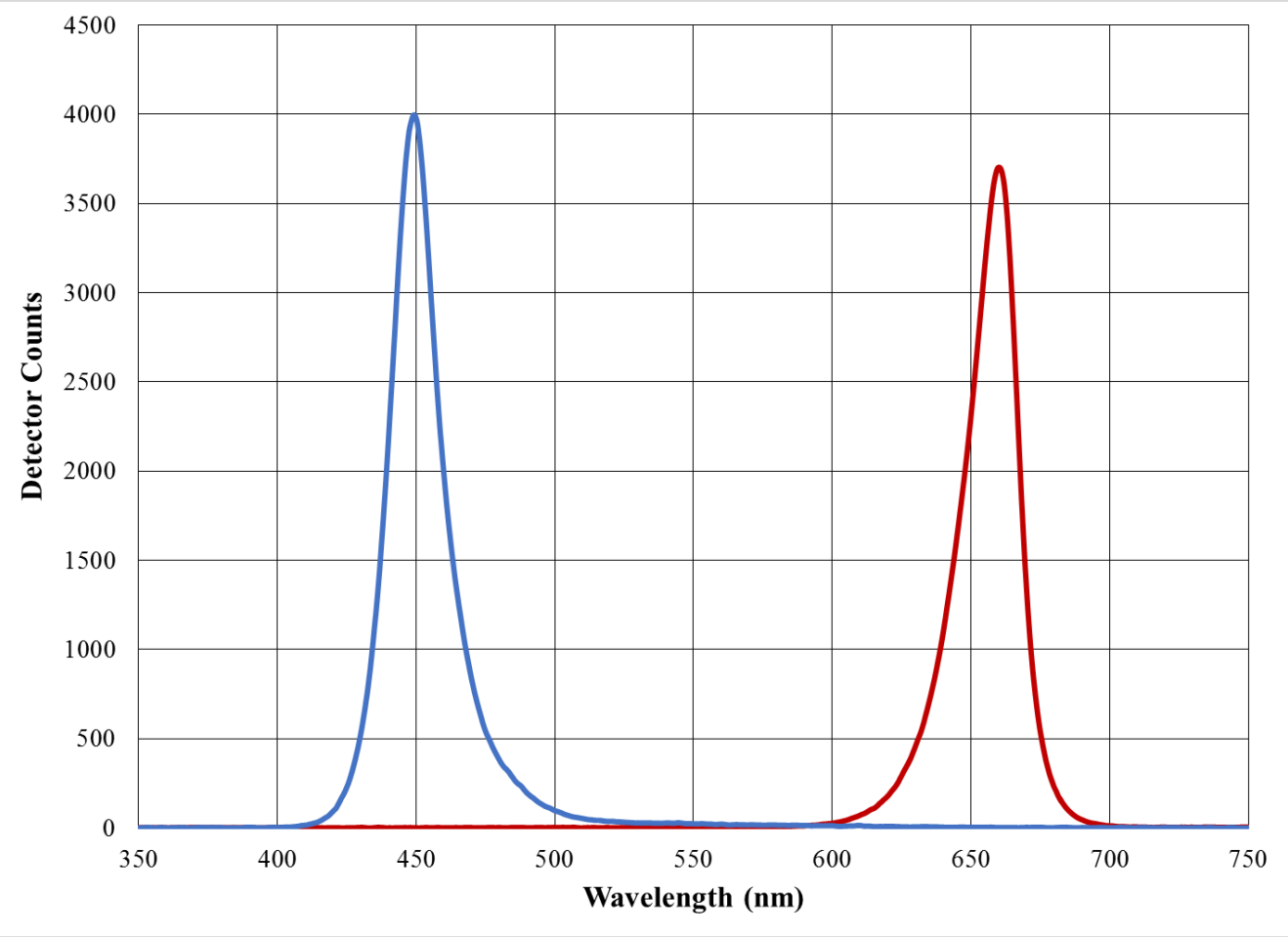

Figure 3.5. Plot of relative illumination intensity measured in "Detector Counts" versus the peak wavelengths of visible light emitted by blue (*left*, blue peak) and red (*right*, red peak) Endor Star™ 3-Up LEDs respectively.

To adjust the “Flashing illumination”, a potentiometer was also used in conjunction with a signal generator to adjust the PPFD for the red and blue light also. The PPFD for the flashing experiments were higher as they were only providing an equivalent illumination for a short duration (approximately 1% of the duty cycle). The resulting PPDF measured for the experiments are presented in Figure 3.5.

3.7. ENUMERATION METHODS

The primary source of data for the experiments relied on accurate accounting of the growth rates of the microalgae. Within the literature, such measurements of microalgae growth rates were done using many different procedures, leading to considerable disparate outcomes, which call into question the veracity of much of the data. While the first organisms seen by the human eye through a microscope were phytoplankton, visual counting of microalgae has been supplanted by a host of other, indirect methods striving to improve upon the tedium of counting and increasing the statistical reliability of enumeration of algae in experimental samples. An accounting of the different methods found in the literature is tabulated in Table 3.1. The table shows the many different methods, and their relative merits for use in studies of microalgae that rely on determination of growth rates.

3.7.1. Turbidimeter. Early in the project, a considerable amount of time and resources were put into the development of indirect methods of measuring the growth of algae in experiments. The first and most ambitious method was the development of a turbidimeter for estimations of growth rates within the PBRs constructed prior to the PhD project. Figure 3.7 illustrates the first attempt at creating a turbidimeter for indirect measurements of algae growth rates.

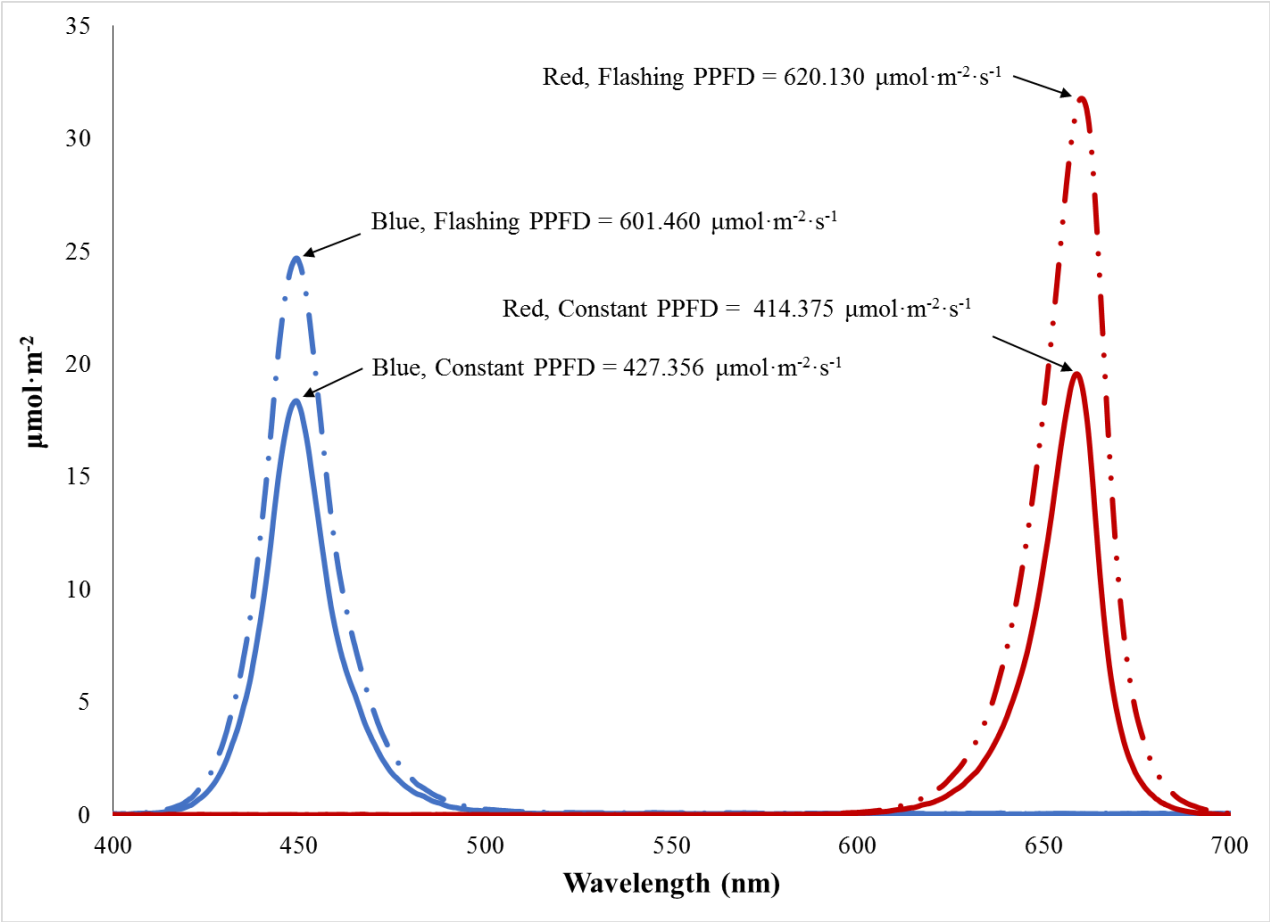

Figure 3.6. PPFD measured for each of the LED illumination regimes for the experiments described in the capstone experiment. Blue peaks (*left*) represent blue experiments and red peaks (*right*) represent red experiments. Solid lines represent constant illumination and dashed lines represent the flashing light illumination.

Table 3.1. Enumeration methods for microalgae.

Method	User Skill	Analysis Time	Statistical Significance	Sample Preparation	Capital Cost	Upkeep Cost	Notes	Ref.
Dry-weight Mass	Novice	Slow	Low	Minimal	Moderate	Low	Cannot determine any specific growth characteristics of the algae	[284]
Microscopy-Hemocytometer	Novice	Slow	Low	Minimal	Low	Low	Highly tedious and difficult for dilute, small, and rare cells	[242, 260]
Microscopy-Epifluorescence	Inter.	Slow	Low	Some	Moderate	Moderate	Great for small and rare cells. Can detect hard to visualize plankton	[285]
Microscopy-Image Analysis	Inter.	Slow	Medium	Minimal	Moderate to High	Moderate	No standard method in literature. Software interface can be cumbersome	[286]
Fluorimeter	Novice	Slow	Low	Minimal	Moderate	Moderate	Cannot detect cells that don't fluoresce without additional sample prep	[287]
Coulter Counter	Adv.	Rapid	High	Minimal	High	High	Counts all particles without being able to differentiate them on any other metric than size	[233, 241]
Flow Cytometry	Adv.	Rapid	High	Minimal to Extensive	Very High	High	Can differentiate cells on more than size metrics to detect different populations in a given sample. Addition of stains can make sample preparation complicated	[288-294]
Turbidity, LC	Inter.	Slow (calibration)/ Rapid (sample)	Low	Minimal	Moderate	Moderate	Only gives rough approximations of cell density based only on absorption of specific wavelengths of light	[295, 296]
Photometer, optical, O.D.	Adv.	Slow	Low	Extensive (absorbance to absorption)	Moderate	Low	Use a 560nm UV/vis Spectrophotometer correlated to dry weight	[243, 260, 297]

Turbidimeters, however, are a very poor substitute for accurately determining growth rates as the two factors, opacity and cell density, cannot be accurately correlated with much quantitative accuracy [285].

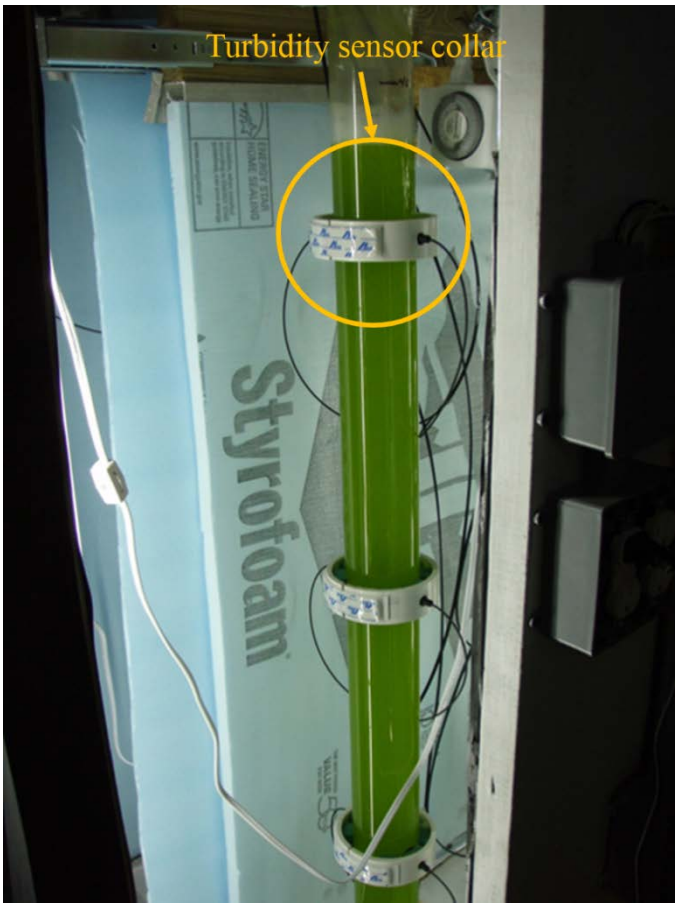

Figure 3.7. Initial, rudimentary turbidity sensor previously built for the project.

The disconnect between the attenuation of light and the relative number of cells comes from the fact that microalgae cells will modify the presence of photoactive pigment concentrations in response to different lighting conditions, nutrient levels, salinity, and

pH. As such, cells can become physically darker or lighter in terms of pigmentation resulting in a lack of correlation of numbers of cells with attenuation of light. Furthermore, cell detritus and dust can skew results since they cannot be discerned from algae in the global measure of turbidity [298]. Additionally, there are many factors in the growth medium that can also affect the absorption and/or the reflection of incident light. As such, the attenuation of the incident light used to measure the relative density of the algae cultures was determined to provide a misleading accounting of actual cell density. The data from these early experiments was discarded from this project.

3.7.2. Light Microscopes and Hemocytometers. The second method of cell counting used in the earlier stages of this project depended on the employment of a light microscope and a hemocytometer of 0.2 mm in depth with a Fuchs-Rosenthal pattern (Hausser Scientific, Co., Horsham, PA USA). Using techniques and training taken from an algae culture course at Bigelow Laboratory for Ocean Sciences at Boothbay, ME, cell counts were made visually and recorded on a click-counter. The count data was then further processed by dividing the cell count by the total volume of the hemocytometer to the proper degree of significance. Many issues were encountered with this counting method. The primary problems with the use of a hemocytometer were the user amount of time required and the user fatigue encountered. As explained in the research literature, the counting of enough individuals to provide a 95% confidence factor was required for the statistical significance to support conclusions on experimental treatments [299]. The minimum number of individuals that needed to be counted within a given volume was determined to be at least 100 individuals. In the early experiments, an exorbitant amount of time was needed to count the minimum number of individuals in each sample.

Furthermore, as the algae population reached exponential growth, the cultures would become much too dense, which required dilution of the samples. The dilution procedure was time consuming and cumbersome. The added handling of the samples also gave rise to more sources of error in the experimental determination of the cell counts, as each transfer incorporated the standard error in the glassware employed. The experimental throughput was very low as a result of the sample preparation and the amount of time needed to make accurate cell counts of the algae. As a result, a considerable effort was made to find a method to supplant pure visual counting methods to improve the quantity and quality of the experimental work.

3.7.3. Flow Cytometer. After a comprehensive review and consulting with experts in the field, enumerating algae by flow cytometry was determined to provide the necessary capabilities required for this project. While counting cells with a light microscope remained in use for monitoring stock cultures, a flow cytometer was employed for all determinations of cell density in experimental work. The major advantages of the machine were the ability to obtain count data, and to mitigate much of the user error associated with the techniques of light microscopy, while having the ability to count thousands of cells. Furthermore, the flow cytometer uses several concurrent parameters to enumerate cells based not only on size parameters, but also the auto fluorescence of the chlorophyll. The flow cytometer created a richer data set than could be obtained by any other method. In fact, the use of any other indirect method like turbidity or fluorimetry, would have missed one of the most significant findings of this project, the radical change in the morphology of *D. viridis* expressed under illumination by monochromatic lights.

In brief, the basic principles of flow cytometry allow for particle concentration to be estimated from illumination by laser light. The machine has several different methods to not only enumerate particles, but to provide a host of other information. The flow cytometer employed an air cooled, 15 mW Spectra-Physics 15 mW argon ion laser emitting at 488 nm. That laser beam would excite the chlorophyll (Chl) in photosystem II (PSII) to fluoresce in the deep red range (approximately 685 to 800 nm) and be detected by photomultiplier tubes mounted in the optics bench of the flow cytometer. Figure 3.8 shows a plot of the typical emission wavelengths from Chl-a and Chl-b when extracted with dimethyl ether with data provided from the software [17]. The flow cytometer used in the experimental work in this project could discriminate along five different parameters. The first parameter that would be resolved was called “Forward Scatter”. The forward scatter channel (FSC) would resolve the relative size (cross-sectional area) of the particles from the shadow cast by the cell as it moved in front of the laser beam. The second parameter the machine would record was called “Side Scatter”. The side scatter channel (SSC) also resolves the relative size of particles in a similar fashion as FSC. However, the scattering of light evaluated was orthogonal to the laser line. As a result, SSC information would also resolve the granularity and internal complexity of particles. The foremost utility of the FACScan resides in the machine’s ability to also discriminate fluorescent properties of particles when excited by the laser.

The three remaining parameters concern fluorescence. The optical bench of the FACScan was configured to split the emitted fluorescence into the following fluorescence channels (FL#), where photomultiplier tubes would absorb the following wavelengths of light:

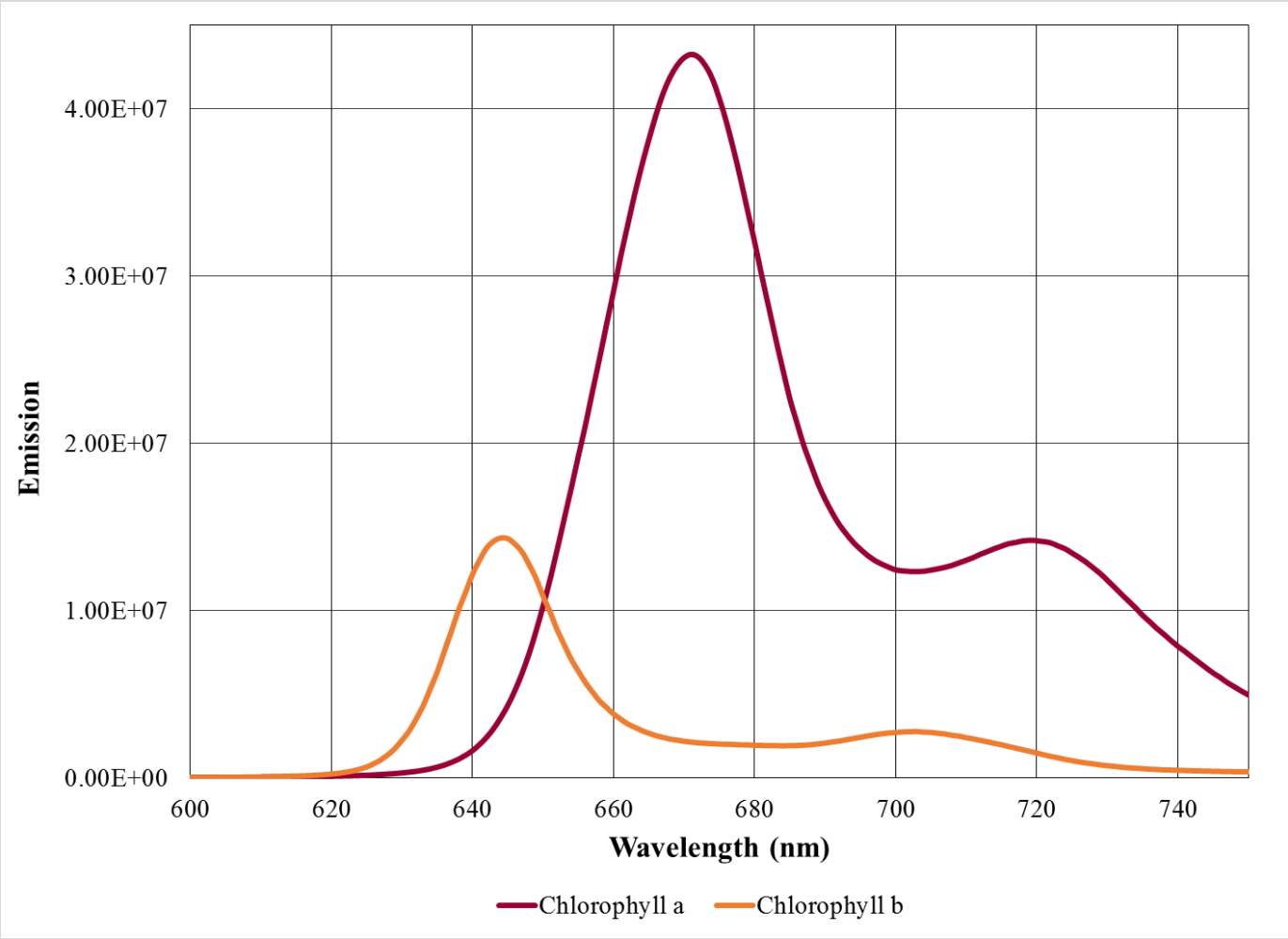

Figure 3.8. Emission spectrum information for Chl-a and Chl-b extracted in dimethyl ether.

(a) FL1 530 ± 15 nm -- green,

(b) FL2 585 ± 21 nm -- orange,

(c) FL3 >650 nm -- red

While the addition of specific binding dyes was not necessary for the work undertaken in this project, florescent staining is a major tool used in other fields of cellular and molecular biology, and has been applied to related work with *Dunaliella*, [294] specifically to *D. viridis* [300].

The ability to resolve the populations of distinct morphology was made possible by the employment of the flow cytometer and modified sampling procedures. The FACScan™ flow cytometer (Becton Dickenson, Mountain View, CA,USA) pictured in Figure 3.9 was employed to enumerate microalgal cells in experimental samples in the laboratory.

The FACScan flow cytometer uses a flow-through cuvette constructed of quartz that has excellent optical properties compared to other FC systems. The basic principle behind the operation of the FACScan is to hydro-dynamically focus the sample of cells such that the laminar flow created will usher the cells in the sample through the optical chamber in a single-file fashion ensconced within the central core of the sample fluid being drawn. Figure 3.10 is a basic diagram of the aforementioned process provided by N. Poulton [301]. Therefore, the key to the improving performance for the gravimetric technique used in this project was optimization of the fluidics system on the FACScan machine. The response of the fluidic system needs to be nearly instantaneous for the gravimetric technique used in this project. For that reason, several modifications were made to the machine. Optimization of this process involves careful regulation of the

back-pressure of the system that pushes the sample up into the machine. Machine modifications and upgrades were made under the direction of William Eads, Director of the Siteman Flow Cytometery Core Laboratory, Washington University School of Medicine, St. Louis, MO.

Figure 3.9. FACScan flow cytometer used for enumeration of microalgae cells grown in this study.

These major modifications to the FACScan included:

(a) Re-plumbing of the Fluidics System: The machine arrived to the laboratory with a completely stock configuration of the fluidics system. In brief, many fluidic lines in the sheath and waste paths were shortened and rerouted. In all, roughly 2 feet of tubing and 6 connections/terminations were eliminated. The result was a higher backpressure in the machine for better performance for the procedure used in this project.

Finally, the simplification and consolidation of the system greatly helped to make the machine easier to maintain.

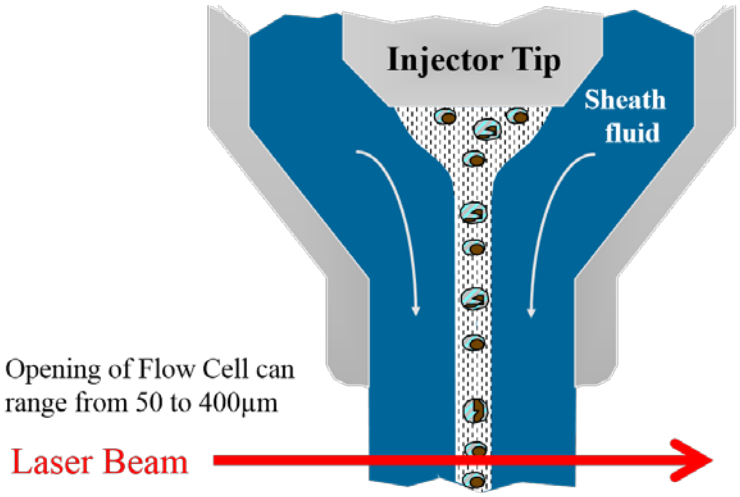

Figure 3.10. Diagram of the theory of operation for a standard flow cytometer.

(b) Elimination of the Sheath Filter: Because of the sporadic use of the machine and the high cost of consumables, the sheath filter assembly was removed and directly bypassed. This modification, again, shortened the fluidics path such that the machine response was optimized for the modified gravimetric method used in this project. The modification reduced the lag in the sheath supply and provided for a more instantaneous response when a sample was mounted to the sample injection port (SIP). Furthermore, the removal of the sheath filter reduced the amount of time needed to purge the synthetic salt water from the fluidics pathway when the machine fluidics path was rinsed as part of the shutdown procedures. Instead, 3L of sheath fluid (either salt or freshwater) was

vacuum filtered three-times using 0.22μm, PES filters (previously described) into sterilized plastic storage bottles for use during experiments.

(c) Modification of the SIP arm: A modified SIP arm was designed and machined to replace the standard equipment. The reason for the modification was that the standard arm would not allow for the modified technique used in this project for determining the microalgae's cell density in experiments. Figure 3.11 shows the specific parts that were designed and machined using waterjet technology for the modified SIP arm.

Figure 3.11. Modified SIP arm assembly designed for the research project.

The pieces were cut from 316 stainless steel plate that was 0.25 inches (6.35 mm) thick, fabricated with the waterjet machine. The rubber pad was also cut on the waterjet to

create a cushion for storage tubes mounted on the machine. Figure 3.12 is a picture of the installed SIP arm assembly in standard or storage configuration. Figure 3.13 is a picture of the SIP arm assembly in experimental configuration with the storage pad swung open to allow for the placement of the sample tube onto the SIP while in RUN mode.

Figure 3.12. Modified SIP arm installed on the FACScan in standard configuration.

Most other machines that employ the techniques used in this study cut the factory SIP support arm off to allow for the placement of the tube onto the SIP while the machine is in RUN mode. The modified SIP arm that was created as part of this project was used to

maintain the normal functionality of the machine for other investigators, in addition to providing support for the storage tube.

(d) Elimination of the Droplet Containment Tube: An ancillary piece of equipment was removed from the SIP assembly to help simplify the fluidics system. The tube was originally intended to eliminate drips of sheath fluid that would occur from the SIP assembly when placed in RUN mode. Figure 3.14 is a picture of the drip of sheath fluid from the droplet containment tube.

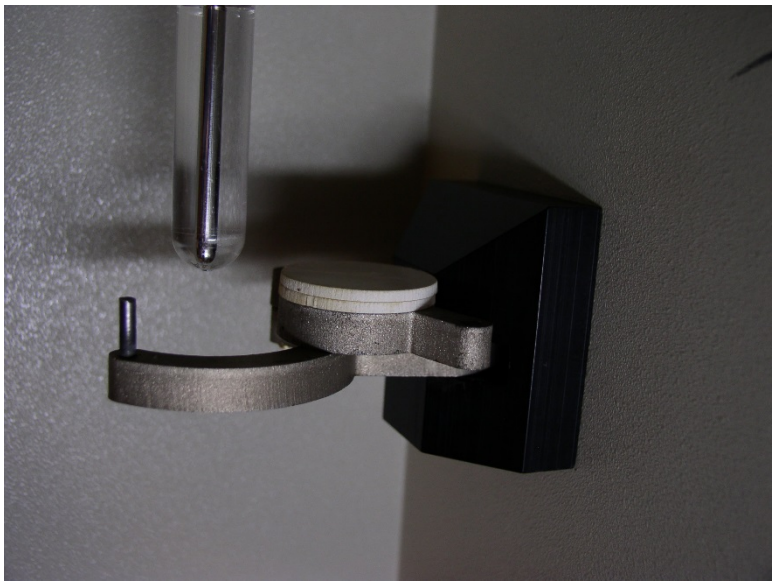

Figure 3.13. Modified SIP arm installed on FACScan in algae counting or "experimental" configuration.

Management of the extra drops of sheath fluid were a vital component of the gravimetric technique. The issue caused by allowing drops of liquid to mix with samples caused inaccuracies in the measurement of the actual volume of samples withdrawn into

the machine. The added drops from the sheath would create a smaller difference in the pre- and post- sample run mass, resulting in a higher cell density being calculated. The droplet containment tube was factory installed over the sample injection tube to vacuum up the occasional drips of sheath fluid that fell as the machine waited in the STANDBY position of the Fluid Control dial.

Figure 3.14. Picture of a drop of sheath fluid forming at the end of the SIP tube.

The elimination of the tube allowed for better gravimetric measurement of the actual sample mass that was pulled into the machine by being able to completely dry the SIP just before analyzing a sample on the machine and minimize error from additional

mass added to the sample tube. Along with the removal of the droplet containment tube, the droplet containment peristaltic pump (DCM) was disconnected and the fluidics bypassed as the DCM was no longer needed to manage the drops from the droplet containment tube.

(e) Preferential Calibration- Another modification of the generally accepted procedures of the FACScan operation was the preferential calibration of the machine to the FL3. When performing quality assurance and quality control (QA&QC) evaluations, Q&b validation particles were used (97-17890-00, Cyteck Development, Fremont, CA USA), and the machine was preferentially calibrated to optimize the machine sensitivity to detection of counts in the FL3 at the expense FL1 and FL2.

(f) Providing "Clean" Line Power: A final consideration in the setup and operation of the FACScan was to provide the appropriate "clean" line power to the machine. While often overlooked in the laboratory, the supply of pure sine wave power with additional voltage regulation is critically important in research that relies on sensitive electronic equipment. Furthermore, the analog nature of the FACScan machine meant that sags and surges in the power supply would directly impact the system's performance. Additionally, the protection of the power supply to the antiquated Apple Power Mac (Apple M8493 G4 733MHz "Quicksilver") that was used as the computer interface for the FACScan was also important to protect, as it also proved vulnerable to inconsistencies in the power supply to the lab. A Tripp Lite uninterruptable power supply (TRNF005, SmartOnline UPS 3000VA, Tripp Lite, Chicago, IL, USA) with battery back-up, voltage protection, and true pure-sine wave output was installed to protect the FACScan and the ancillary systems.

However, the age of the FACScan (built in 1989) and the rough condition of the used machine resulted in many major repairs to the system. These repairs were very costly in both time and resources. Major repairs were made to key systems that directly affected experimental results. Therefore, extensive QA&QC along with re-establishment of baseline data of the basic machine operations were carried out after each major repair. Major equipment replaced during the project included:

(a) Replacement of the cooling fans for the laser

(b) Replacement of the pressure transducer

(c) Replacement of the analog/digital interface

(d) Replacement of the flow proportioning valve assembly

(e) Replacement of the laser

(f) Replacement of two computer control systems and software

3.8. EXPERIMENTAL TEST STAND

The basic procedures of the experimental design involved testing the effects of different artificial lighting protocols on the growth response of the algae. As the experiments for this project were performed in a completely new start-up experimental laboratory, no existing experimental appliance for containing multiple experimental replicates with suitable infrastructure for maintaining consistent, light proof conditions for living organisms was available. As a result, much time and effort was devoted to the design and construction of a universal testing appliance for standardized testing of the required experimental replicates. A review of the literature for guidance revealed only a few instances of any mention of methods addressing light security in experiments. These included:

(a) aluminum foil covering the bioreactor [243]

(b) a dark box [242],

(c) “just in the dark”[233].

However, the mention of a light tight cabinet was also made in the literature [235, 302] and inspired the design of the test stand for this project.

The design and construction of a formal test stand was required in order to optimize the experimental infrastructure under which multiple replicates could be utilized in this project. The test stand provided a uniform experimental test bed to directly support the main experimental goal of the research of evaluating the response of algae growth rates to artificial illumination. Adequately isolating the individual experimental replicates while providing identical provisions for key utilities like electrical power and aeration were important to the veracity of the project. Key provisions of the formal test stand design were made to address the following:

(a) Provide centralized and standardized supplies of power and aeration

(b) Provide a light-tight environment for enabling individual replicates of experiments

(c) Streamline experimental procedures by providing a standard method for more effective and efficient experimentation while levering limited experimental resources

(d) Provide physical support for monitoring equipment and the experimental apparatus necessary for experiments.

The basic experimental apparatus consisted of a cabinet that was constructed out of 0.75 inch (19.0 mm) thick, furniture grade plywood. All of the carpentry was done by

the researcher using advanced cabinet making techniques to produce a robust and utilitarian testing bed to support the experimental efforts in the laboratory. Figure 3.15 shows the layout of the individual compartments and the router jig employed for creating the dado and rabbet joinery that was used to construct light tight joints in the experimental test stand.

Figure 3.15. Picture of the dado and rabbet joinery used to construct a light-tight experimental test cabinet.

The main cabinet features were ten individual compartments that were 8 in by 12 in by 48 in (20.3 cm by 30.5 cm by 122 cm) with individual supplies of filtered ambient air

controlled by acrylic flowmeters with a 0.04 to 0.50 liter per minute (LPM) range (FL-2010, Omega Engineering Co., Stanford CT, USA), and separate 110V GFI breakers for each compartment's electrical outlets. The flow meters were necessary as aeration of the culture was important for both the mass transfer of gases, and for keeping the algae agitated [284]. A flow rate for experiments was set between 0.40 and 0.50 LPM to maintain a sufficient amount of gas volume to culture volume as well as, adequately agitate the algae with the given aeration apparatus. A unique aspect of the design of the compartments was the use of a tambour door surfaced with a reflective silver film (NP5605STS-8, Stainless Interlocking Tambour, 5/8" wide x 5/16" thick, Tape-Ease, Denmark, WI, USA) that allowed the door to be rolled up to open up the top of the compartments such that cylindrical photobioreactors could span the entire height of the cabinet. All of the interiors of the compartments were surfaced with horticultural grade Mylar film. Another unique feature was a full-length access door on the front of the test cabinet so that aeration tubing could be accessed, as well as, wiring for power and lighting controls. Figure 3.16 is a picture of the finished experimental cabinet with the front access door closed. Figure 3.17 is a picture of the finished experimental cabinet with the front access door opened to reveal the electrical and air supply lines for each cabinet compartment.

Aeration to the experimental cabinet was provided by a diaphragm air pump producing 3.7 cubic feet per minute (CFM) (1.75 LPM) at one atmosphere of ambient pressure (Sweetwater® Linear II, SL94, Aquatic Ecosystems, Apopka, FL, USA). The air pump was plumbed into a pressure balancing loop of PVC conduit to more evenly distribute the air pressure to the individual flow meters.

Figure 3.16. Finished experimental cabinet with front access door closed.

Figure 3.17. Finished experimental cabinet with front access door opened.

A structure was designed and installed by the researcher to create a temporary dark room around the experimental cabinet to provide additional light security for experiments. The basic structure was built from 0.75 inch (19.0 mm) electrical conduit with special canopy fittings (C-1, C-2, C-3, & C-7, Pacific Superior Imports, Shade King Shade Canopies, Burleson, TX, USA) to create a framework which can be seen in Figure 3.18.

Figure 3.18. Picture of framework built around the experimental cabinet to support theater curtain.

From the conduit framing, black-out curtain purchased from a theater supply company (26oz. IFR Prestige Velour Remnant, eggplant, Rose Brand, Secaucus, NJ, USA) was applied in two layers to create a light-tight temporary darkroom around the experimental cabinet. The finished room is pictured in Figure 3.19.

Figure 3.19. Finished darkroom with black-out curtain applied.

A major factor adversely affecting the initial experiments was problems with the electrical supply in the laboratory. Strange results were being observed in the signal analysis of the pulsed light experiments. Oscilloscope plots of the pulsed signals would be exceptionally noisy, making auto detection of the frequency by the machine impossible. Extensive examination of the timing circuits and redesign of the LED drivers and controls did not improve the signals. A power outage in the laboratory caused an uninterruptable power supply to switch to battery-backup and the signal noise mostly disappeared. It became apparent that the source of the noise in the pulse-width signals was originating from electrical mains in the lab. To remedy the problem, experiments were switched over to running off of large, 12VDC, deep-cycle marine batteries (8052-161 D31M Blue Top, Optima Batteries, Milwaukee, WI, USA), with direct-current, buck-boost, power regulating LED drivers (A011 FlexBlock, LEDdymanics, Inc.,

Randolph, VT, USA). The new buck-boost drivers for the LEDs assured that a constant current was delivered to the LEDs as the batteries' voltage varied in response to discharge. This switch dramatically reduced the amount of noise in the circuit and made for more accurate measurement of the frequencies generated.

3.9. LED AND LED DRIVERS

The development of the LED portion of the project was also an evolutionary process leading up to the capstone project. Many of the LEDs available in the early years of the project were prohibitively expensive, did not produce the necessary peak wavelength, did not have good switching performance, and/or had energy outputs that were too low. LEDs were selected for this project based on their peak wavelength and their relation to the basic absorbance spectra data of Chl-a and Chl-b provided from "PhotochemCAD" (Version 2.1, The Lindsey Lab, North Carolina State University, Raleigh, NC, USA) and documented in the literature [17]. The analysis of the plots of pigment absorbance and other literature resources [175, 303-305] resulted in the following peak wavelength preferences:

(a) preferred "red" colors had wavelengths in the rage of 640 to 680 nm
(b) preferred "blue" colors had wavelengths in the rage from 420 nm to 460 nm

Many different devices were evaluated for creating light arrays. For the purpose of maximum utility and experimental flexibility, the standard 5 mm through-hole design was found to be the most flexible and least expensive option for creating grow light arrays. Figure 3.20 shows the typical 5 mm through-hole design as reproduced from the literature [249].

At the time the project began, the 5 mm through-hole design was the most widely available design, and had the greatest variety of color options available. The legs of the LEDs were spaced 0.098 in (2.5 mm) on center and fit into sockets from Mill-Max Mfg. Corp. (310-43-164-41-00100, 64 Position, through hole, Oyster Bay, NY, USA).

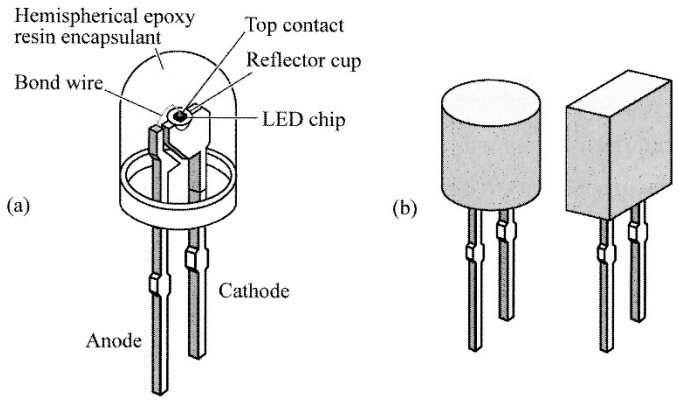

Figure 3.20. Typical anatomy of a 5 mm though-hole LED. Graphic reproduced from Schubert 2006 [249].

These single in-line sockets were then trimmed into pairs and soldered into commercially available printed circuit boards (PCBs) to allow for individual devices to be interchanged to create different color mixtures. The circuit boards were arranged in three parallel groups of three series sockets. Provisions in the PCB board could also incorporate carbon film resistors to better balance the current when LEDs of different manufacture and color were combined in the arrays. Single sockets cut from the buss were soldered directly to the PCB boards to also allow for the swapping out of resistors.

The result was a basic design that allowed LEDs to be interchanged within PCB boards to formulate different mixes of color. As illustrated in Figure 3.21, the boards were arranged with 9 sockets with provisions for resistors to provide proper current when different types of devices were on the same PCB.

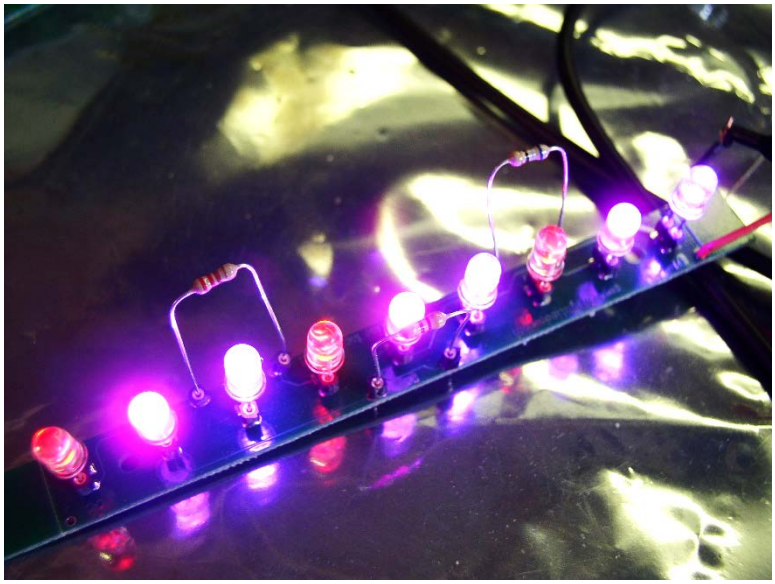

Figure 3.21. Photograph of first attempt to develop experimental grow-lights with 5mm through-hole LEDs.

The modular nature of the individual boards made it possible for different geometrical arrangements to be created. The first arrays using the nine-LED PCB boards consisted of hooking the boards into long strips to illuminate early tubular bioreactors used in the lab. This arrangement can be observed in operation in the lab in Figure 3.22. The bare circuit boards came in attached groups of 10 strips, with 9 LEDs in each, and could be used as a whole as pictured in Figure 3.23. Early boards were found to react

with salt from the algae samples and many experiments were impacted by faulty boards as a result.

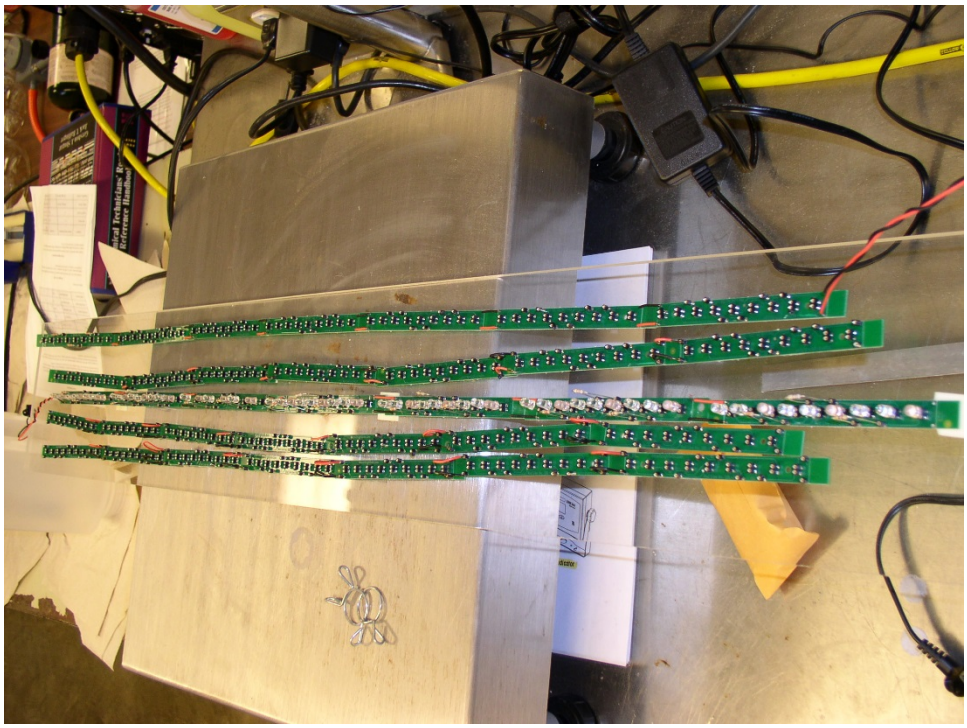

Figure 3.22. Photograph of light strips composed of the nine-LED PCB boards.

After issues arose with splashes of salt-water onto the arrays, the backs of the PCB boards were coated with liquid electrical tape. Coverage with insulating “liquid tape” alleviated some issues, but any splashes of culture media on the front of the LED arrays would short out the boards. A final attempt to alleviate issues with the nine-LED PCBs resulted in the most unique design. 5 mm LEDs mounted on the nine-LED PCB boards were arranged in a cage that conformed to the shape of the final bioreactor design. As

can be seen in the photographs in Figure 3.24, conducting wires were used for both power delivery and structural support to create a “cage” of light that resulted in more even coverage and an increase in the incident radiation level by conforming to the flask walls.

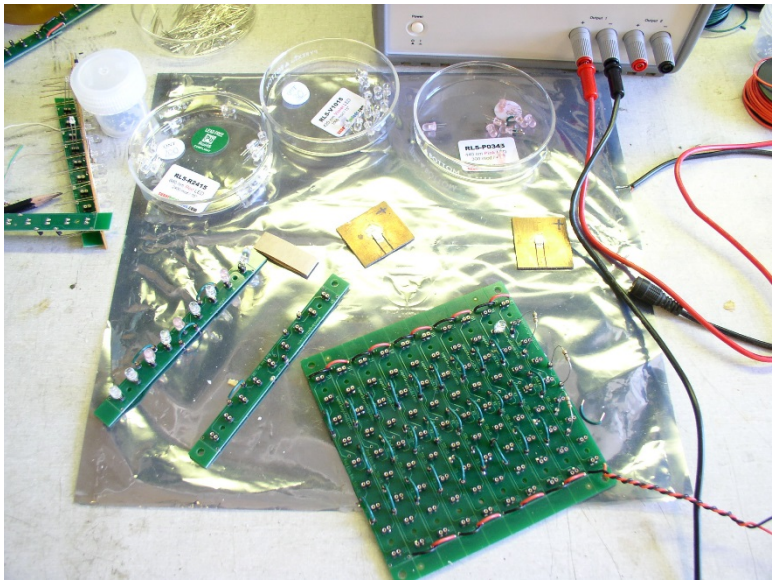

Figure 3.23. Photograph of nine-LED PCBs and a ninety-LED PCB array built by the researcher.

The conducting wires were then coated in the same liquid tape to insulate and protect the exposed wires. The design was an attempt to get the LEDs mounted closer to the microalgae in the bioreactor to increase the light energy incident on the microalgae. While an interesting design, it was discovered that circuitry would be needed to better balance the power for the different PCB boards in the array to provide a consistent current and therefore, a consistent illumination intensity from each LED component.

However, the main problem with the 5 mm component LEDs was the extremely low outputs of light energy. Huge arrays of the components were later built, but total emissions were still very low and only resulted in either, no growth or very slow growth rates in experiments.

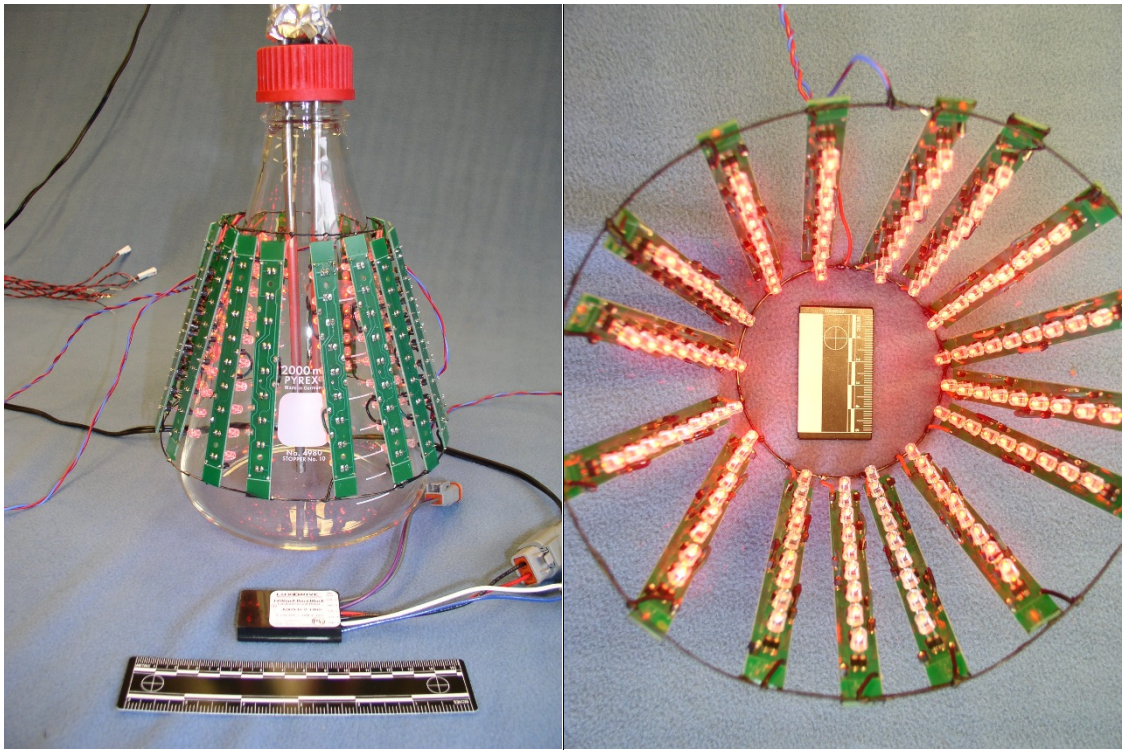

Figure 3.24. LED "cage" design built to accommodate a 2000mL Erlenmeyer flask used as a bioreactor.

Another lighting technology that was briefly investigated was electroluminescent wire (EL-wire). EL-wire works with an alternating current (AC) that is used to stimulate phosphors coated on a copper wire. The high voltage (120VAC) and high frequency (1.5-2.0 KHz) create a very efficient light emitting package that claims to be more

efficient than LEDs [306]. Further, the light emitted is continuous along the entire length of the device and radiates in 360° around the wire, making it perfect for the use of illuminating algae cultures from the inside of a bioreactor. The EL- wire is also very flexible and coated in a water resistant, clear polyvinylchloride (PVC) sleeve that made it an ideal candidate for the project. The EL-wire came packaged with a driver and 3m of wire. Purple wire was used in preliminary experiments (COM-10196, SparkFun, Niwot, CO, USA). Figure 3.25 is a photograph of this experimental setup. However, similar to the problems with the 5 mm through-hole LEDs, the EL-wire didn't have enough light energy output to inspire robust growth in preliminary experiments. As a result, this line of research was abandoned.

After the discovery of suitably high-powered LEDs in ranges that were not ideal, but close enough to those of the peak absorbance ranges in the Chl-a and Chl-b spectrums, the PCB arrays of 5 mm through-hole devices were abandoned completely. The specific devices purchased by the researcher and used in the capstone project were Endor Star™ High-Power LED light Module, 3-Up, Deep-Red, 07007-PDRED-C , and Endor Star™ High-Power LED light Module, 3-Up, Royal-Blue, 07007-PDR000-B (LEDdymanics, Inc, Randolph, VT, USA). The new LEDs also had provisions for the incorporation of different filters and lenses that could be directly attached to the factory LED mounts (Carclo CO-105xx series optics). While a few samples of the filters were evaluated in the lab, they were ultimately ruled out because of the attenuation in the light energy into the bioreactors. A photograph of the device mounted to a heat sink can be seen in the Figure 3.4 previously. Air lines were added to help cool the high-power LEDs by blowing ambient air over the heat sink. This was an important provision as the

enclosed space of the experimental test cabinet did not allow for adequate passive cooling of the devices.

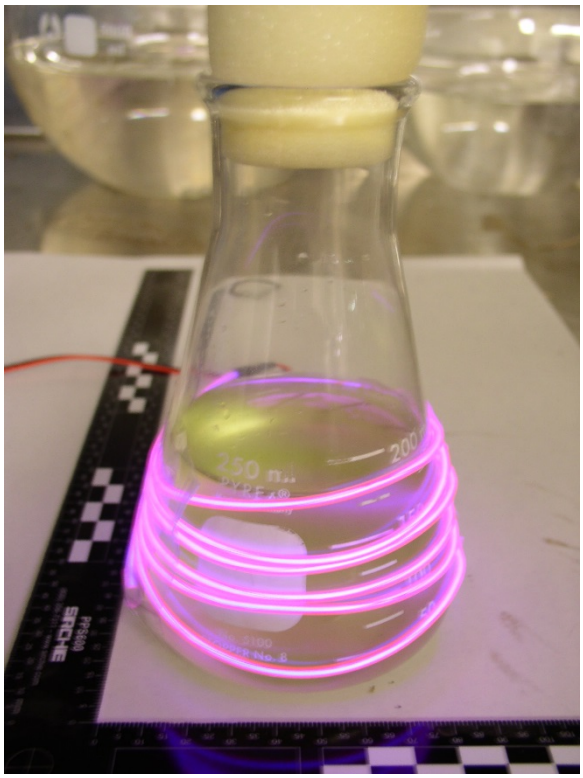

Figure 3.25. Picture of a preliminary experiment using EL-wire to grow microalgae.

Monitoring with a NIST-calibrated thermal couple showed that the temperature of the LEDs remained around 65°C and 75°C for the red and blue lights, respectively, which was under the manufacture recommended temperature of 100°C.

Furthermore, these new, high-powered LEDs were coupled with matched LED drivers that could be more easily incorporated with 12V DC battery powered supplies, as matching buck-boost supplies were available for their specific current requirements. The

specific LED drivers used were A011 FlexBlock made by LEDdymanics, Inc., (Randolph, VT, USA). Furthermore, these LED drivers could be easily integrated into the systems for producing light pulses without the need for specialized custom timing control circuitry. The availability of the FlexBlock drivers was a very important development in the research effort as LED drivers and pulse-width control were a continual source of problems in the preliminary work. The factory schematic from LEDdynamics for configuring the FlexBlock for pulse/strobe input is illustrated in Figure 3.26.

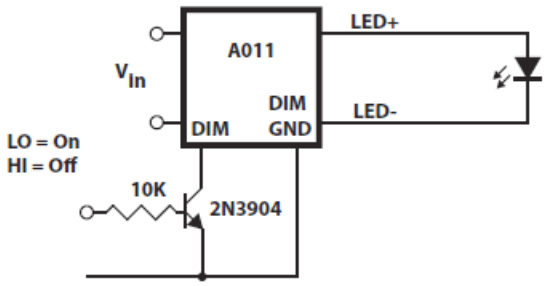

Figure 3.26. Electronic wiring diagram provided by manufacture for A011 FlexBlock as configured for pulsed illumination experiments with a small signal negative-positive-negative type transistor (2N3904).

A signal generator could trigger a relay to cause power to be modulated such that the LEDs would precisely pulse. A photograph of an example of the A011 FlexBloc device used is pictured in Figure 3.27. The FlexBloc LED drivers were further modified with the addition of Deutsch DT Series, 2-way, waterproof wire connectors (TE Connectivity

LTD, Schaffhausen, Switzerland) to connect to power, LEDs, and frequency modulation / dimming equipment.

Working closely with the electronic engineering staff of Missouri University of Science & Technology's Rock Mechanics and Explosives Research Center, a BK 3020 Precision Sweep/Function Generator (Dynoscan Corp., Chicago, IL, USA) was used along with a triggering relay to create pulses in the LEDs.

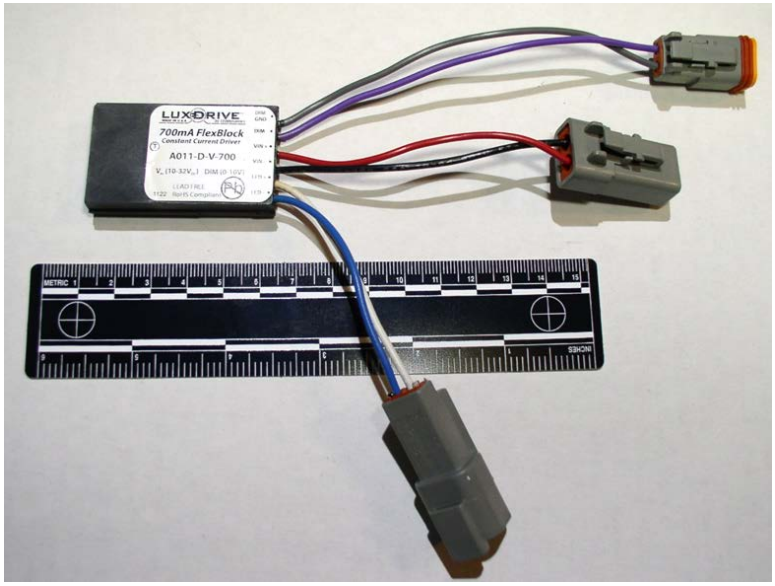

Figure 3.27. Photograph A011 FlexBlock modified for use within the experimental set-up for blue LEDs used in the capstone experiment

A Tektronix 2211 oscilloscope (50MHz, dual trace, Beaverton, OR,USA) was used to confirm the instrument settings and monitor the experimental set up throughout the capstone experiments. The specific signal characteristics can be seen in a photograph

of the oscilloscope output in Figure 3.28. The main issue with working with an antiquated frequency generator was the limitations on duty cycle and frequency stability.

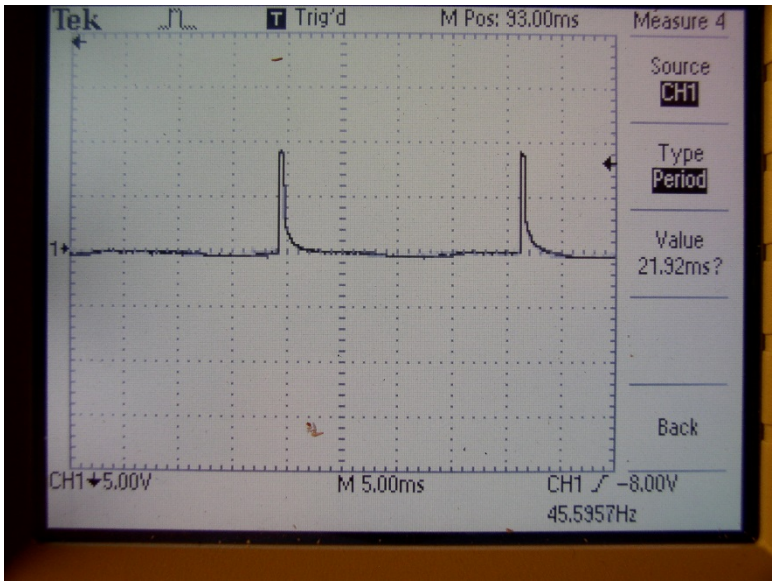

Figure 3.28. Photograph of oscilloscope measurements of the pulse-width modulation of LED light in experimental work.

The cycle period was roughly 1% of the duty cycle of the generator and the equipment was able to maintain a stable cycle of 21.92 ms which yielded a pulse of approximately 0.2 ms.

3.10. DEVELOPMENT OF EXPERIMENTAL BIOREACTORS

Another major consideration in the development of the material and methods for the research project included designing and building bioreactors. As with many other aspects of the experiment, the experimental bioreactors evolved until the capstone

research project was undertaken. Originally, the bioreactors were made of clear, extruded acrylic tubing with an internal diameter of 3 in (7.62 cm). The tubes were 1 m in length (39 in) and held 3 L (0.80 US gal) of volume. A photograph of an example of one of these bioreactors is found in the previous Figure 3.7. Endcaps had been machined to provide a base for fixtures and different ports with which to attach aeration lines and drain/fill valves. These endcaps were permanently epoxied into place, and were the main obstacle to completely sterilizing the tubes between experiments. Any small gap between the endcaps and the tubes provided a pocket from which algae were impossible to remove. The hard-to reach angles in the caps and the bleach-soaking method of sterilizing the tubes were thought to be inadequate and the source of persistent contamination problems. Furthermore, sterilization of the tubes proved to be cumbersome in transferring tubes from baths of bleach-water and sodium thiosulfate. Also, scrubbing the tubes scratched and reduced the clarity of the tubes. As a result, different photobioreactor designs were undertaken.

Glass tubing for laboratory plumbing was purchased from Schott A.G. Corp. North American distributer (Chesterfield, MO USA). The 3 in (7.62 cm) Schott Kimax® glass drain line (6501-3000, Jena, Germany), with bead-to-plain end couplings (6661-3000, Shott A.G. Corp., Jena, Germany) that were made of stainless steel and neoprene. These couplings would form a watertight seal between a standard glass bead and a straight run of pipe. A 5 foot (152.4 cm) length of 3 in (7.62 cm) O.D. rod of polyetherimide (PEI) was chosen for creating endcaps for the new bioreactors because the plastic is steam autoclavable (Natural, ULTEM 1000, ThyssenKrupp Materials North America, Southfield, MI, USA). These new glass pipe bioreactors were sized to fit

within the large autoclave in the Biology Department of Missouri University of Science & Technology. Only one prototype was able to be completed by the researcher before the design was abandoned. A photograph of the prototype can be seen in Figure 3.29 mounted in the experimental test stand.

Figure 3.29. Prototype of glass photobioreactors that replaced original extruded acrylic type. Note endcaps are constructed out of PVC and not PEI plastic in this model.

Unfortunately the glass beads on the tubing were machined incorrectly and were not watertight. Thus, the design was abandoned at great cost in both time and resources.

However, this design holds great promise for potential use in scaling up experiments, and should be reexamined at such time that expertise and resources become available.

Another design approach that was attempted to address contamination issues in the bioreactors was the design and construction of disposable, or single-use plastic bioreactors. Polyethylene bags were first proposed for culturing algae in the 1970's [307]. Samples of different types of plastic sheeting that were amenable to impulse sealing were obtained from Tufpak, Inc. (2.5 MIL PP94 CLR and 1.8 MIL PP94.5VR CLR, Ossipee, NH, USA). The polypropylene bag material was made into bags using an impulse sealer with a 39 inch (1 m) long sealing element (Kehtron model HI-1000MM, Wenzhou Hongzhan Packaging Machinery Co., LTD, China). Tests on different types of plastic sheeting produced satisfactory results in terms of light transmission, and the ability to be steam autoclaved. Light transmission losses due to the plastic were negligible when tested in the preferred red and blue wavelengths previously discussed. The plastics were able to be autoclaved without loss of structural integrity or leakage. However, cages were required to add mechanical support to the bags as the seams would split under the weight of the liquid culture contained within. A wider heating coil for the pressure sealer would have improved the bonding of the plastic sheeting, as the seal proved to be the most prone to leakage. However, the endcap designed initially for the glass pipe reactors were unable to be re-machined due to lack of resources. The disposable plastic bioreactor was abandoned as a result.

With perceived, persistent issues with contamination, the focus on the sterilization of the bioreactors via steam-autoclave was pursued. The final design was to incorporate a standard 2000 mL Erlenmeyer flask with an open GL-45 screw cap as seen in the

photograph in Figure 3.32. While use of a 2.8 L Fernbach flasks would have been ideal, the scientific literature specifically allowed for the use of 2 L Erlenmeyer flasks as a suitable replacement [280]. Specially designed three-port caps made from 316 stainless steel components were designed and built by the researcher. Each port consisted of three 6.35 mm (0.25 inch) O.D. tubes cut to different lengths as pictured in Figure 3.30.

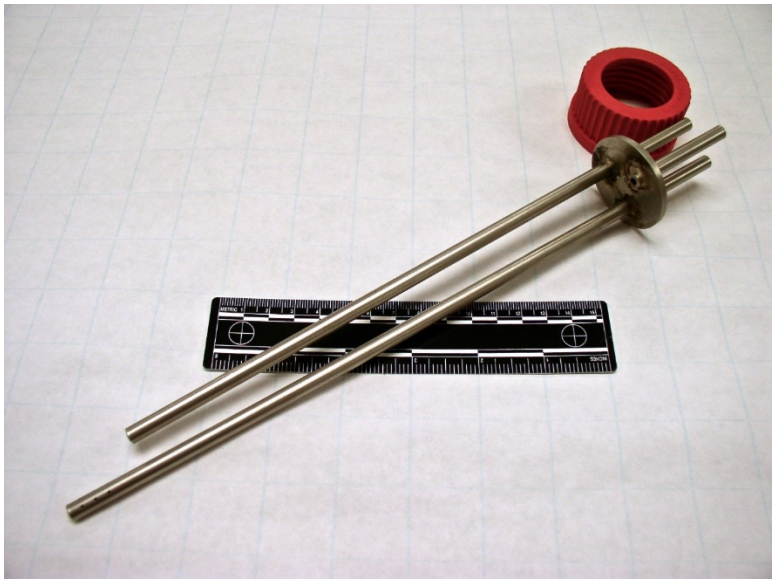

Figure 3.30. Stainless steel experimental port assembly for algae growth experiments reported in the capstone study.

The vent tube was the shortest of the assembly, measuring only 5 cm (1.97 in), and served as a "breather" for the assembly by allowing air to equalize inside the bioreactor when it was aerated, and when samples were withdrawn. A 1.5 in O.D., 0.22 μm nylon air filter was attached to the port via Tygon® tubing (E-3601, 0.25 in. I.D., 0.50 in O.D., Saint-Gobain Corp., Courbevoie, France). The second tube was cut in such a way as to

reach half-way into the volume of the 1 L liquid culture which was approximately 26 cm (10.2 in), depending on the exact height of 1 L of volume in the individual Erlenmeyer flask. Samples for cell enumeration were taken from this port with a steam-autoclaved , 25 cc syringe. The third port's tube that was submerged in the culture, was designed to reach almost completely to the bottom of the flask. In the last 1.5 cm (0.60 in) of the third tube, a series of 12 small ports measuring approximately 1 mm (0.039 in) were cut via water jet. These holes are orthogonal to one another to create a diffuser/aerator. The holes can be seen in Figure 3.31.

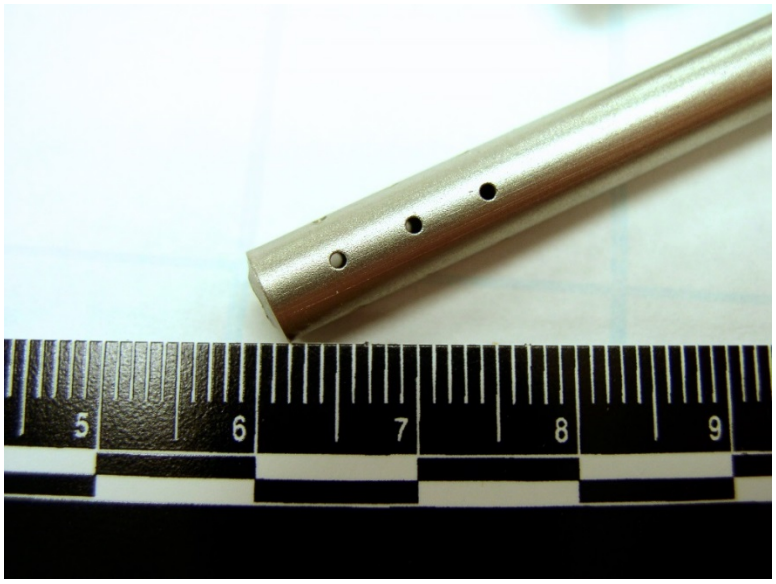

Figure 3.31. Photograph of small ports cut via waterjet into the aeration downtube.

The end of the tube aeration tube was plugged with a small piece of Viton gasket material (DuPont Performance Elastomers, L.L.C., Wilmington, DE, USA) , cut via waterjet, to

force the air out of the small ports to create currents enabling the agitating and mixing of the culture. The final working assembly can be seen in Figure 3.32 with syringe, air filter, and aeration line attached to the stainless steel manifold.

Figure 3.32. Final version of the bioreactor utilized in capstone experiments.

These units were completely autoclavable once loaded with growth medium in accordance with the procedure specified in §3.4.2.

3.11. DATA COLLECTION METHODS

Flow cytometers were developed for the express purpose of the identification and differentiation of cells used in health science research. The general practice is to use flow cytometers along with stains or fluorescent labels to probe cells for different activities such as intracellular antigens, apoptosis, and protein expression. The samples of cells analyzed by the FC are measured in terms of numbers of cells, cell volume, and cell morphological complexity, as well as those things that can be differentially labeled with fluorescent dyes. The overall cell density of the differentiated cells are only given relative, qualitative estimates based on the flow rate of the sample. In normal applications, enumeration of different cell types is only examined relative to the cell counts recorded and not in absolute quantity. In order to determine the absolute cell density, a modified method of gravimetrically determining the amount of the sample that was analyzed by the machine is required.

A modified technique that is outlined in the literature [285, 308], was taught by Poulton [301], and Sieracki [309] during a workshop held at the Bigelow laboratory for Ocean Sciences in East Boothbay, MA USA. The workshop included intensive training in aquatic cytometery in the J. J. MacIsaac Facility for Aquatic Cytometery that housed the first flow cytometer used in aquatic research. The technique taught by Poulton and Sieracki was employed in this study to determine the actual volume density of the algae samples withdrawn for analysis by the FACScan. The name-plate specifications for the sample pump rate on the machine were 60 $\mu L \cdot s^{-1}$ ± 7 $\mu L \cdot s^{-1}$ for the Hi-Flow setting, and 12 $\mu L \cdot s^{-1}$ ± 3 $\mu L \cdot s^{-1}$ for the Lo-Flow setting. The estimated uncertainty within the factory specified flow rates was too large to utilize in this project. Further, the relative age of the equipment, and the extensive modifications made on the machine listed on

pages 76-82 would also impact the rate at which the samples could be analyzed by the machine. An example of a typical QA&QC evaluation of the sample volume withdraw for Hi-and Lo-flow rates is presented in Figure 3.33 and Figure 3.34 respectively. The plots in both Figure 3.33 and Figure 3.34 illustrate the variability of the volume of samples withdrawn by the machine as determined from gravimetric analysis and corrected for temperature. Figure 3.33 and Figure 3.34 show a wide variation in the actual volume of the samples withdrawn during tests with samples of filtered RO water only. In each of the samples taken in Figure 3.33 and Figure 3.34 the run time was exactly the same (183 seconds) for each sample. However, when the actual sample volumes were statistically analyzed against the average nameplate value for each of the flow rates, a statistically significant difference was found ($p > 0.05$) using a t-test. Furthermore, the data was consistently skewed to give a higher volume then the average nameplate for each flow rate. This difference was attributed to modifications made to the machine.

The literature also recognizes the problem in consistent sample volume measurements determined solely from nameplate information on commercial flow cytometers [308]. As a result, the gravimetric method for determining sample volumes analyzed by the machine was utilized.

The basic experimental procedure began after the manufacturer's standard start-up procedures were complete. The instrument's initial settings were set as follows: FSC = E00, SSC gain =300, FL1 gain=400, FL2 gain =450, and FL3 gain=350. However, these were just starting points and were adjusted to optimize the particular conditions of each replicate sample for the best visualization of the counts.

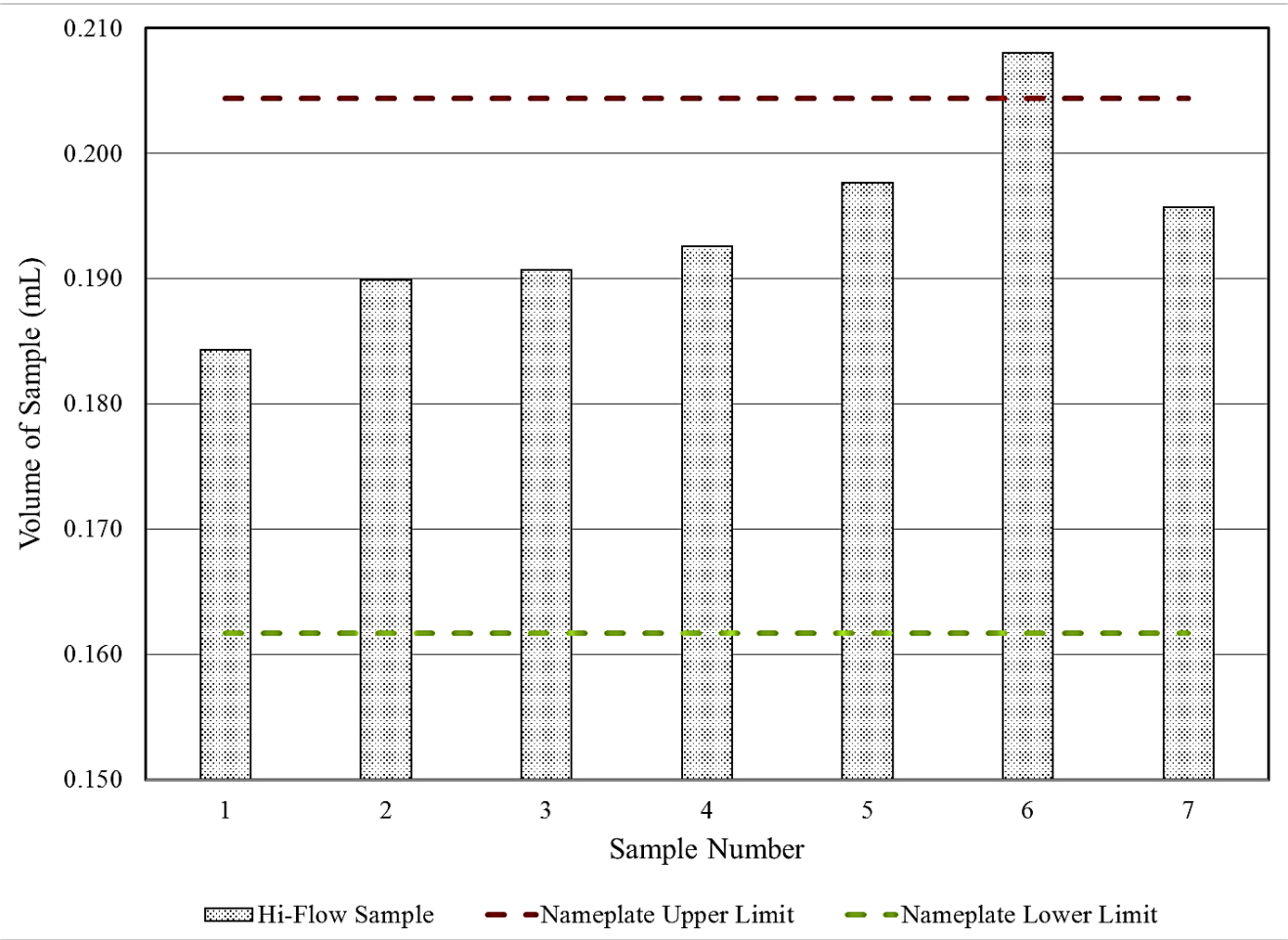

Figure 3.33. Hi flow rate samples (in mL), plotted along with the upper and lower limits as determined from the factory specifications.

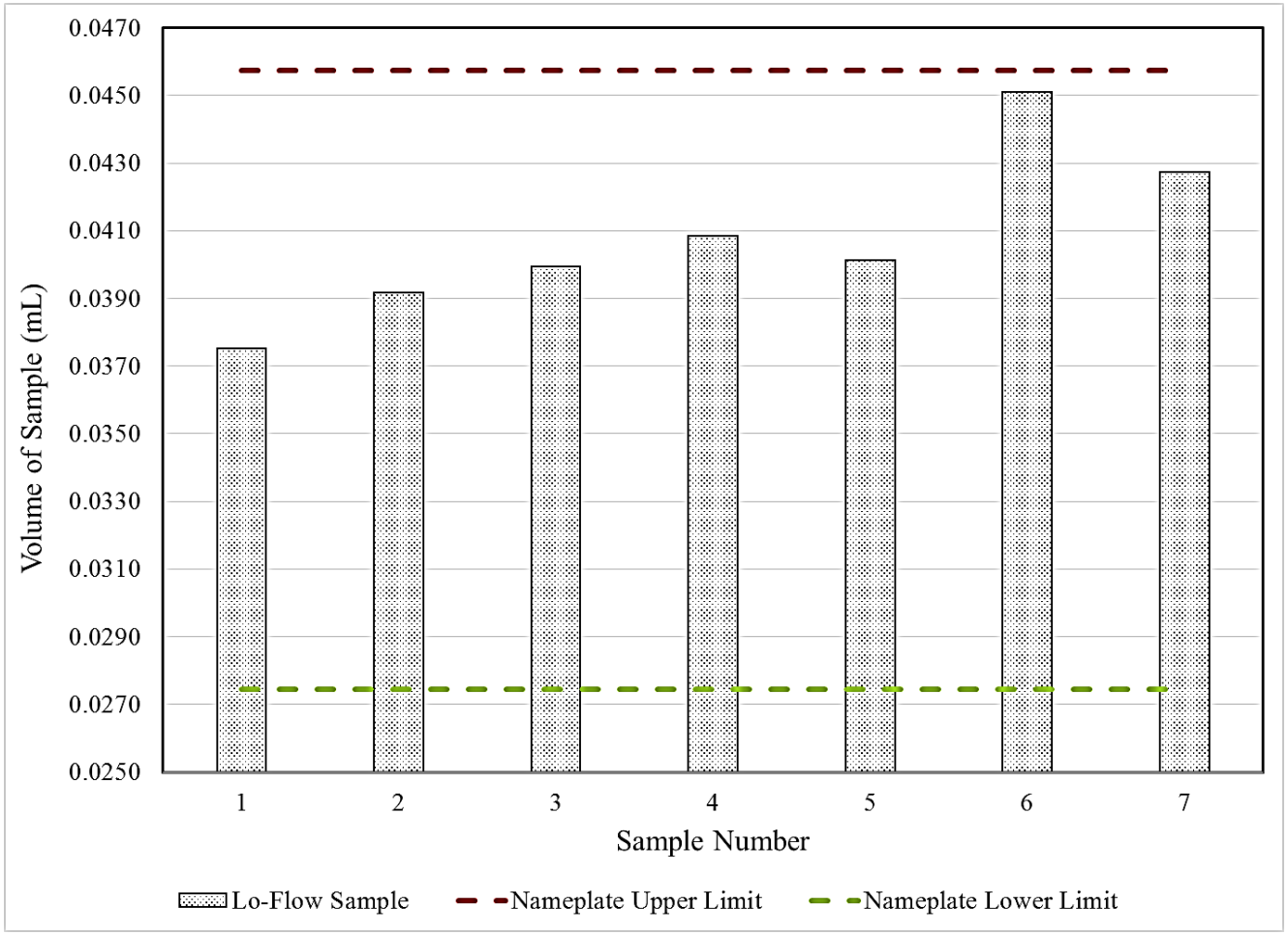

Figure 3.34. Lo flow rate samples (in mL) plotted along with the upper and lower limits as determined from the factory specifications.

For example, if samples were hard to detect, the FL3 gain may go to as high as 450, not 350. The basic procedure would be executed for each sample as follows (modified from [308]):

(a) Select the sample flow rate used for analysis (preference for Lo-flow).

(b) Place the machine in Ready mode.

(c) Fill the sample tube (Falcon 2063, Becton Dickenson, Mountain View, CA, USA) with a 2-3 mL sample.

(d) Weigh the sample on an analytical balance with a capacity of 110 g and a resolution of 0.1 mg (Ohaus Adventurer Pro Balance, AV114C, Pine Brook, NJ, USA).

(e) Quickly and smoothly seat the Falcon tube onto the SIP assembly, the instant after a droplet of the sheath fluid has fallen from the sample needle, and before the next one forms.

(f) Simultaneously start the software to initiate the sample analysis.

(g) Run the sample for between 3-5 min to yield a particle count between 1000 and 10,000 individuals.

(h) Remove the sample tube and simultaneous stop the sample analysis.

(i) Weigh the remaining volume of the sample.

(j) Syringe filter (25 mm diameter, 0.22 μm polyvinylidene fluoride filter, miyashop, Hong Kong, Hong Kong) the sample.

    (i) From the sample in the syringe, place a drop or two on to a hand-held salinity refractometer (Aquatic Eco-Systems, SR5-AQ, Apopka, FL, USA).

(ii) Deliver the balance of the syringe filtered sample into a 18x100mm test tube for pH determination.

The pH of the sample was determined by a S40 Mettler-Tolledo SevenMulti™ meter with ION module for ph/mV/ORP (Model# 51302807, Mettler-Tolledo, Switzerland) that was attached to an InLab Versatile Pro (Model # 51343031, Mettler-Tolledo, Switzerland) probe. The meter was calibrated using a three-point, segmented method with Mettler-Toledo Rainbow Pack Sachets (Product#: 51302080 Mettler-Tolledo, Switzerland). The display resolution was set for "three decimal" places, and the stability criterion was set to "normal". This calibration was performed once a week during experimental trials.

An amount of fluid equal to the volume of the amount of the sample withdrawn from the bioreactor would be returned to the bioreactor. The fluid would consist of either sterilized RO water, or sterilized synthetic sea water, based on salinity measurements. Salinity was strictly monitored as an indicator of the evaporation of media and to help to maintain the experimental volume of the bioreactor. In this way, the salinity was maintained within 2‰ in experiments.

Figure 3.35 demonstrates a data run for one sample taken during the capstone experiment (data file 0.063). Figure 3.35 illustrates the graphs used in discriminating the populations using bivariate dot plots and placing gates around areas of high dot density to determine cell counts. Specifically, dot plots were created in CellQuest (Version 3.3) software by selecting SSC (Y-axis) and FSC (X-axis) dot plots for the top graph in Figure 3.35. Similarly, the bottom graph in Figure 3.35 was created using FL3 (Y-axis) and SSC (X-axis), with all channels set to log scale.

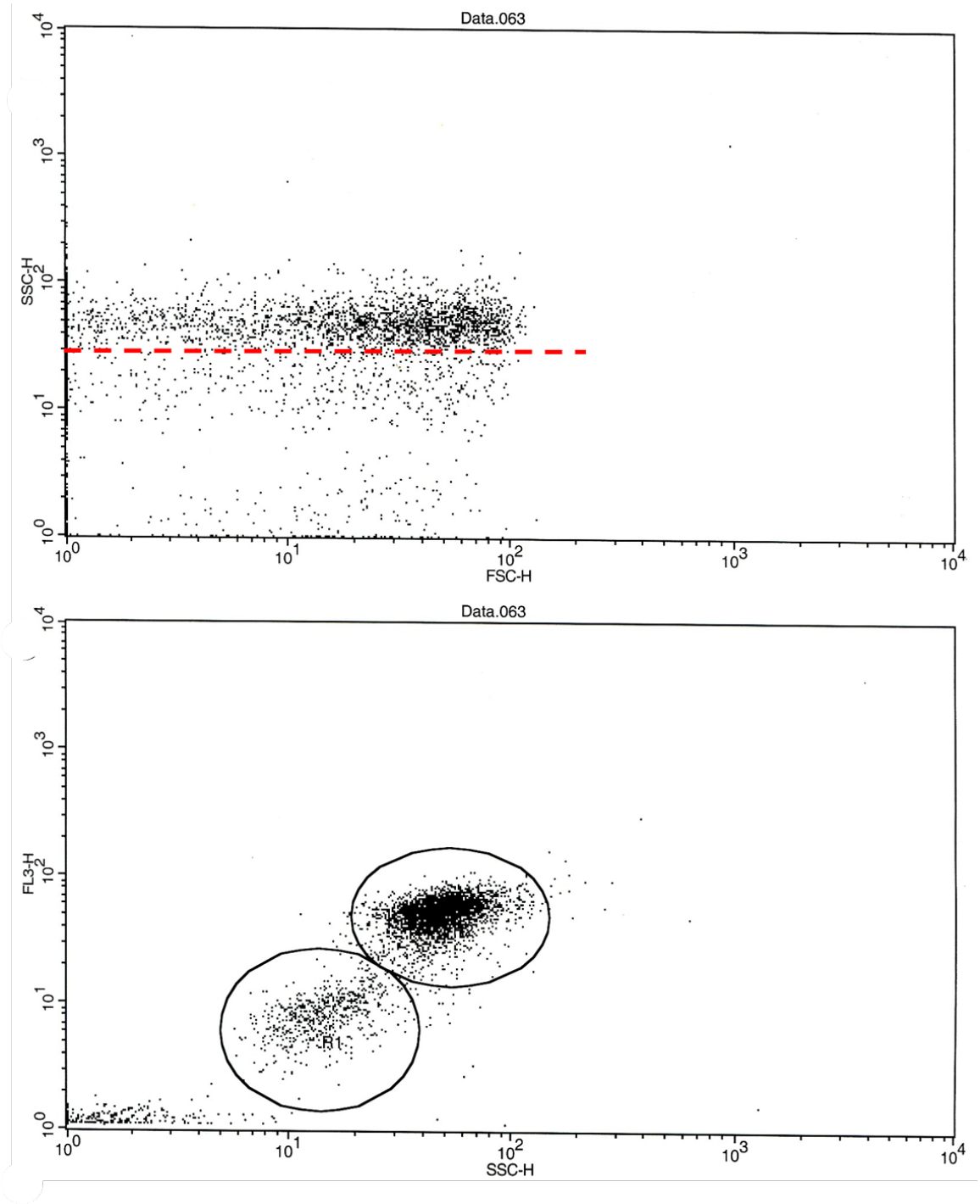

Figure 3.35. Example of sets of bivariate plots created in CellQuest software and monitored in real time during sample runs on FACScan. The red dashed line was added for improved clarity between two populations of cells.

Thus, the specific populations could be discriminated by observation of the bivariate log plots in real-time. Figure 3.35 shows distinct populations, both in size and red fluorescence in FL3 that clearly differentiate the different morphologies for *D. viridis* within the experimental sample. These counts were then recorded along with temperature, salinity, and pH data for the sample run. Counts were discarded or rerun under higher flow rates or longer times if they were found to be under 1000 individuals, as counts below 1000 were too low to be deemed statistically significant as explained previously.

The volume data for the cell densities used in the analysis were developed from the standard calculation of density of the water corrected for both temperature and salinity data, generated from the Equation (13) presented in the literature [310]. Specifically, the following equations were used to experimentally determine the density of water (ρ_{water}) in units of kg·m^{-3} for each sample, based on the sample temperature (T) in °C, and the salinity (S) in units of g·kg^{-1}:

$$\rho_{water} = \rho_T + aS + bS^{\frac{3}{2}} + cS^2 \tag{13}$$

The water density, as a function of only temperature, (ρ_T) was derived using the following equation:

$$\rho_T = 1000\left[1 - \frac{(T + 288.9414)}{(508929.2)(T + 68.12963)(T - 3.9863)^2}\right] \tag{14}$$

The coefficient *a* in the equation for ρ_{water} was calculated using the following equation:

$$a = (8.24493 \times 10^{-1}) - (T * 4.0899 \times 10^{-3}) + (T^2 * 7.6438 \times 10^{-5}) - (T^3 * 8.2467 \times 10^{-7}) + (T^4 * 5.3675 \times 10^{-9}) \quad (15)$$

The coefficient *b* in the equation for ρ_{water} was calculated using the following equation:

$$b = (-5.724 \times 10^{-3}) + (T * 1.0227 \times 10^{-4})(T^2 * 1.6546 \times 10^{-6}) \quad (16)$$

Finally, the coefficient c in the equation for ρ_{water} was calculated using the following value:

$$c = (48314 \times 10^{-4}) \quad (17)$$

The inverse of the ρ_{water} was then multiplied by the difference between the initial and final sample mass to derive the volume of the sample analyzed by the flow cytometer. Finally, the cell count taken from the dot plot of FL3 vs SSC was divided by the calculated volume to yield the cell density reported in $g \cdot mL^{-1}$.

3.12. PREPARATION FOR SAMPLE TREATMENT

To begin an experimental treatment, algae would first be drawn from stock cultures. These stock cultures would have been at least three weeks old, showing a green tint in the culture tube. Varying ambient conditions in the lab would impact the relative

maturation rate of the stock cultures as problems with consistent ambient temperature conditions were a persistent issue. As a result, the three week time period was only a guideline as cultures could take longer or shorter times to come to maturation. These stock cultures were grown in maintenance media that consisted of a full formulation of Prov50 as reported in the Appendix. Further, the media was made with natural seawater from Boothbay, ME that had a salinity of between 33‰ and 35‰. These stocks were also grown in natural sunlight, and would be supplemented with full-spectrum grow lights (T5 High Output fluorescent grow light, 6400 K@ 5000 lm, 4 ft, 54 W bulb, AFC Greenhouses, Buffalo Junction, VA USA) when daylight hours fell below 10 hrs, for a total of 12 hrs of illumination. Cell counts would be made in accordance with the light microscope methods previously discussed. A cell density of at least 10,000 cell·mL^{-1} was determined to be the critical cell density where the microalgae would reach the maximum density without mutual shading according to the research literature [233]. If at least 10,000 cell·mL^{-1} was observed, a 1 mL sample would be transferred into 15 mL of standard, full formulation Prov50, with a synthetic seawater base at a salinity of 33 ± 2‰ (Appendix). A primary and a backup test tube for each experimental replicate would be prepared. These cultures would be allowed to grow under natural sunlight, with supplemental artificial illumination as explained previously, until a green tint would be noticed in the tube, and critical cell density reached. The tubes would be sampled and counted again with light microscope methods as previously discussed, until the critical cell density was reached. A 1 mL sample would then be transferred into 15 mL of experimental growth media as previously described in the methods section. Again, a primary and a back-up test tube would be prepared for each experimental replicate.

These cultures would be allowed to grow again until a green tint was noted. The tubes would be sampled and counted with light microscope methods as previously discussed, until the critical cell density was reached. Experiments would begin with the transfer of 10 mL of culture into 1 L of experimental growth media that was sterilized in the bioreactor. An aeration supply line would be hooked up to the bioreactor and the flow meter adjusted to provide a flow rate of 0.30 to 0.40 LPM. A sterilized, 50 mL syringe would be connected to the sample port, and a 0.2 μm air filter would be connected to the vent port as seen in the Figure 3.32. As noted in the literature, the algae would need to be incubated in complete darkness in order to eliminate any energy for growth from intercellular substances taken up from the culture medium and synthesized under natural sunlight [242]. After three days, the experiment commenced with the taking of the first sample for analysis via flow cytometry as previously discussed.

3.13. STATISTICAL METHODS

A basic understanding of the expected population growth characteristics of microorganisms is required to provide background for the data treatment strategies unique to working with biostatistics. The determination of the rate of growth of a given sample is complicated by complex biological responses and adaptations. The first concept that needs to be addressed is the complex nature of the population growth of a model culture of microorganisms. Most all cultures of microorganisms, including unicellular algae, are suitably complex such that a linear graph of the population of organisms over time should yield a plot similar to the picture in Figure 3.36.

A mathematical representation of the visual model in Figure 3.36 is known as the Verhulst Population Growth Model that was first published by Pierre Verhulst in 1845,

the logistic model for population growth was described by the differential equation below [311, 312].

$$\frac{dN}{dt} = \frac{rN(N_A - N)}{N_A} \tag{18}$$

N represents the population as a count of individuals.

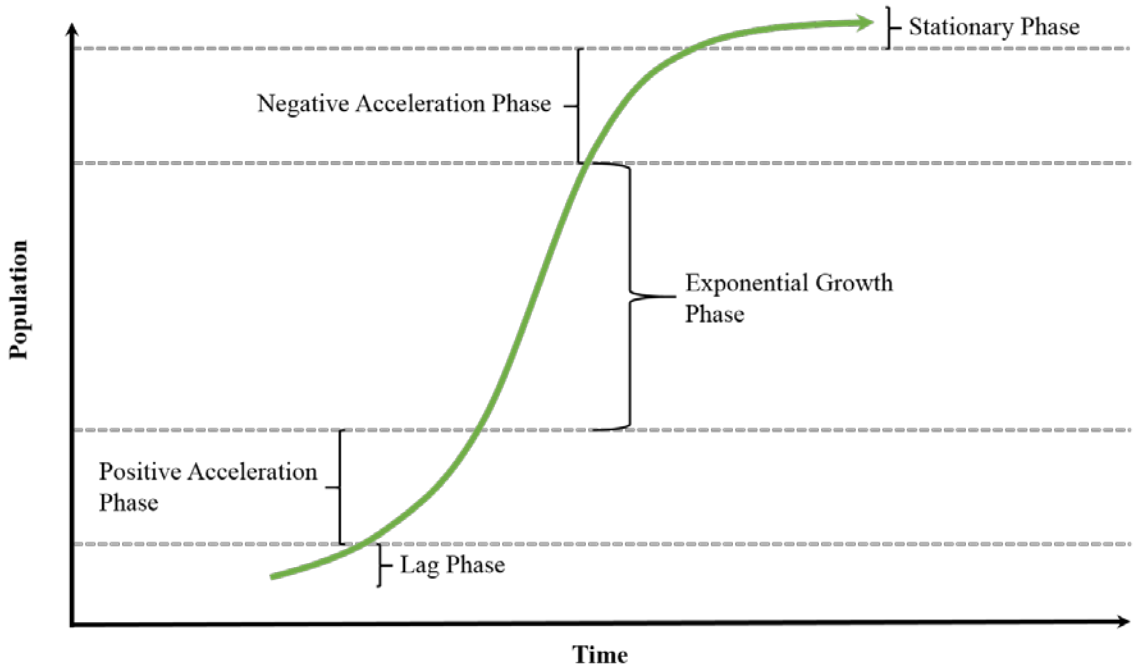

Figure 3.36. Standard growth curve with growth phases identified on the curve.

The *r* term is the Malthusian parameter which is a measure of the proportional rate of change in a population over time. This term is also called the *intrinsic rate of increase,*

or *instantaneous rate of increase* in other texts [313]. The value of N_A is the carrying capacity of the environment, otherwise known as the maximum sustainable population. Defining the ratio of the population as divided by the carrying capacity of the environment as equal to *x* ($x \equiv \frac{N}{N_A}$) yields the differential equation:

$$\frac{dx}{dt} = rx(1 - x) \tag{19}$$

The equation has the following solution when derived:

$$x(t) = \frac{1}{1 + \left(\frac{1}{x_0} - 1\right) e^{-rt}} \tag{20}$$

It should be noted that there are several published modifications to the basic logistical equation and research is ongoing in the field of biostatistics and ecological modeling that takes into account various different conditions and philosophical approaches to calculation of growth curves [314-316]. The limits on experimental determination of other relevant variables, like nutrient uptake over time or gravimetric analysis of the biomass produced, precluded the use of more sophisticated treatments of the growth curves in the experiments.

The biological significance of each section of the sigmoidal population growth curve can also be seen in Figure 3.36. An inoculum of algae transferred into fresh culture media is expected to progress though the basic stages: Lag Phase, Exponential Growth Phase, Stationary Phase, and Death Phase. Lag Phase is typically described as the period

when the algae are acclimating to the new environment. During this period, the algae are modifying biochemical systems within the cell to cope with the environmental factors of the new environment. Fresh media is replete with compounds that consist mainly of nitrogenous and phosphorous compounds (nutrients), trace metals, and at least one vitamin as described in the literature [280]. For example, an organism that moves from a depleted solution of media to a replete media will need time to adjust uptake mechanisms to cope with the higher concentrations of nutrients. Once the organisms become acclimated, the population growth will begin to accelerate. The acceleration in growth will continue until reaching an exponential rate. As the population of the algae starts to approach the carrying capacity of the environment, the rate of growth in the population will decelerate until reaching a steady-state where the rate of mortality is approximately equal to the addition of new organisms. Presuming that the culture media is not refreshed, the population will eventually start to decline as the rate of loss of individuals to mortality exceeds the additions of new organisms. In some very rapidly dividing populations, the rapid division of the population will result in an overshoot of the carrying capacity, and a steep decline will occur as members of the population die off at a faster rate than new organisms can be replenished. The resulting graph will not resemble a sigmoidal curve, but rather display a distinct peak in the linear plot of the population over time, that is interpreted as representing the rapid deceleration of growth as the population enters into the Death Phase. In either case, the upside or exponential growth region of plots of population density over time are of primary importance for the purpose of comparing experimental regimens, and for important estimates used in engineering larger culture systems. Conceptually, at the exponential point in the growth curve, the

population mortality is assumed to be zero, or otherwise insignificant to the overall growth rate. As a result, a key assumption in the analysis of the Exponential Growth Phase in a growth curve is that the rate of mortality (*m*) of the population is insignificant to the rate of additions to the population, which is defined as the specific growth rate (*k*). Using the following equation, the maximal rate at which the population would grow under ideal conditions can be determined as *r*, since it would be equal to the specific growth rate during exponential growth according to the following equation:

$$r = \mu - m \tag{21}$$

For the purposes of the study described here, the *r* value was further converted into a doubling time (T_2) with units of hours, using the first order reaction equation:

$$T_2 = \frac{0.6931}{r} \tag{22}$$

To determine the doublings per hour (*k*), the following calculation was also performed:

$$k = \frac{log_2 \frac{N_t}{N_o}}{\Delta t} \tag{23}$$

As noted in the literature, the continuous nature of exponential growth would mean that *r*, *k*, and T_2 have conceptual and numerical differences [313]. As an example presented in the literature, a culture with a value of *k* equal to one division per day would yield a

doubling time, T_2, of one day. However, the intrinsic growth rate, *r*, would be 0.69 per day as a result of the exponential nature of the data [313].

3.14. GROWTH CURVE ANALYSIS

The detailed analysis of the *r* values derived from the exponential portion of the population growth is the backbone for comparative assessment of the experiments performed. The exponential growth of the algae was of primary importance for this study as it would reveal the intrinsic growth rate data required to begin to evaluate the sustainability and economics of the proposed underground culture system. Likewise, basic engineering and design considerations require estimates of growth rates of the biomass for both production of biomass and environmental remediation. The first step in creating useful comparisons and eventual actionable data for mining engineering stakeholders was the creation of growth curve plots from the experimental data. The calculated cell density data from the three different replicates for each experimental treatment in the 2^2 factorial experimental design, were incorporated into the creation of linear plots representing the growth curve. Cell density and time course data were tabulated and plotted within spreadsheet software (Excel, Microsoft Corp). Cell density was consistently tabulated and plotted as the ordinate in units of cells·$mL^{-1}$and the time was organized as the abscissa in units of hr. Since the data contained two distinct populations of vastly different morphology, different x,y scatter plots were created for each experimental treatment which consisted of the following:

(a) A linear graph consisting of the mean cell density of the sum of the means for the large and small cell populations and bounded by plots of

the ±SE to yield a visual representation of a region around the mean representing a 95% confidence.

(b) A linear graph consisting of the mean cell densities of the small, large, and sum of the means for the large and small cell populations.

(c) A linear graph consisting of the mean cell density of the large morphology cell type population and bounded by plots of the ±SE to yield a visual representation of a region around the mean representing a 95% confidence.

(d) A linear graph consisting of the mean cell density of the small morphology cell type population and bounded by plots of the ±SE to yield a visual representation of a region around the mean representing a 95% confidence.

(f) Included with the growth curve plots type a, c, & d, was the average pH for the replicates that was measured over the same time period as the experiment.

To establish a confidence interval of 95% around the mean cell density values in the respective plots, a factor of 1.96 ± SE was calculated for each data point. The +SE and -SE data were then used to generate new data sets that were added to the plots of the mean value of the cell count data as independent plots. The dashed line plots above and below the solid line of the mean cell density for the respective plots creates an upper and lower boundary to the variability in the sampling of cell densities over the course of the experiment. The SE was used to give an indicator of how precise the estimate of the mean was for the cell densities plotted with in a 95% confidence interval. The main

consideration for using the SE was that the experiments were examining a relatively small number of samples that would produce a non-normal distribution. This method was recommended in the literature [317]. As a result, the application of SD was ruled out in favor of SE. The increase in sample size would lead to a decrease in the variability of sample means according to the central limit theorem. However, even with the triple redundant sampling of each replicate, the samples are still only a very small fraction of the entire volume of the reactor (on the order of 1%). The SEs were derived to assist in forming a more reliable estimate of how well the samples represented the entire population, so that reliable predictions about the performance of the experimental treatments could be made [317].

3.15. DERIVING THE INTRINSIC GROWTH RATE

Once the cell density and time course data were tabulated and graphs created, the data sets were evaluated to elucidate the exponential phase of the growth curves as part of the data analysis. The analysis was accomplished utilizing a modified method from Guillard (1973) to evaluate the growth curve data that was presented in the literature [313]. This straightforward method was selected to preserve the nuances of the actual experimental data that might be otherwise lost in extensive mathematical and theoretical treatments. Guillard's method stipulated that at least three consecutive data points would be required to derive the intrinsic growth rate for the Exponential Growth Phase. As explained in the literature, the technique utilizes "visual analysis" of the growth curve to identify the exponential portion of the growth curve, and then hand-fitting a linear trendline to three consecutive data points in the semi-log plot of cell density versus time.

Finally, the slope of the trendline would be determined and reported as the intrinsic growth rate.

The analysis performed in this project sought to improve upon Guillard's method by removing some of the more arbitrary aspects. The condition of the original procedure that *at least* three consecutive data points are chosen to represent the Exponential Growth Phase was preserved in the method used in this project. However, sets of three data points were fit to exponential curves and evaluated for the highest correlation of variance (R^2). Additionally, the data analysis included expanding the sets of data points to include adjacent data points, but only if their inclusion increased the value of R^2. Finally, the intrinsic growth rate was determined to be the exponential coefficient of the equation for the exponential trendline used to best fit the data. Descriptive statistics from the actual data points encompassed by the data set used to derive the *r*-value in the exponential curve fitting exercise, were also tabulated for analysis. The resulting data was distinguished from the entire data set by an inset box of either blue or red within the tabulation of the data for each treatment in the factorial experiment.

Thus, the size of the data set would be utilized as a factor in the analysis of the data. The more data points that would "fit" to an exponential curve, the better the "confidence" that the growth characteristics exhibited in the data set were exponential and were not an artifact of small sample size. The evaluation was carried out for data comprising the separate cell morphologies, large and small, as well as the total "sum of cell's" density data.

4. RESULTS

4.1 EXPERIMENTAL RESULTS

In the following sections, results will be presented for each part of the overall experiment. The figures and data tables introduced and described in the following sections describe the sum total results for each of the four treatments of the 2^2 factorial experiment. The results were further refined with examination of the population growth characteristics of the small and large cell morphology data obtained.

4.1.1. Constant Illumination Under Blue Light. Data from the experimental treatment of *D. viridis* with constant blue (450 nm) light was processed as described in the Material and Methods §3.14 and tabulated. Table 4.1 presents the data and derived results for the total combined cell counts of the large and small cell morphologies in the samples treated with constant illumination under blue (450 nm) light. Time versus mean cell density ($\bar{n}$) data from Table 4.1 were plotted on the primary abscissa and ordinate respectively, to create the solid black line plot in Figure 4.1. Dashed black line plots in Figure 4.1 denote the 95% confidence interval around the mean created from adding or subtracting the $\bar{n}$ to the product of 1.96 and the SE. Finally, the pH was plotted on the secondary ordinate as a solid orange line in Figure 4.1. Using the same aforementioned procedure, tables and plots were developed for only the large cell morphology and the small cell morphology.

Table 4.2 represents only data related to the large cell morphology in the treatment with constant blue (450 nm) light and was used to create the linear plot in Figure 4.2. The solid blue line plot in Figure 4.2 represents the mean cell density data for the large cell morphology. Dashed blue line plots in Figure 4.2 denote the 95%

confidence interval around the mean created from adding or subtracting the $\bar{n}$ to the product of 1.96 and the SE. Finally, the pH was plotted on the secondary ordinate as a solid orange line in Figure 4.2.

Table 4.3 represents only data related to the small cell morphology in the treatment with constant blue (450nm) light. Figure 4.3 was developed from the data presented in Table 4.3. The solid green line plot in Figure 4.3 represents the mean cell density data for the small cell morphology as presented in Table 4.3. Dashed green line plots in Figure 4.3 denote the 95% confidence interval around the mean created from adding or subtracting the $\bar{n}$ to the product of 1.96 and the SE. Finally, the pH was plotted on the secondary ordinate as a solid orange line in Figure 4.3.

Visual interpretation of the plotted data in Figure 4.1, Figure 4.2, and Figure 4.3 illustrates an extended lag time of nearly 60 hrs for the experiment before beginning the ascent to the maximum average cell density of just over 7000 cells·mL^{-1}. Figure 4.2 also shows that the large cell morphology of the algae dominated the growth of the population as a whole. The small morphology of the algae entered a fairly steady-state of growth over the same period, and throughout the decline in the large cell morphology population until the experiment was terminated.

The overall growth curve is not completely sigmoidal as the rapid decline in the population after 100 hrs does not demonstrate a traditional steady-state phase in Figure 4.1. The graph demonstrates a widening of the confidence interval as the data progresses into the later stages of the Exponential Growth Phase into the peak of the population growth, and only continuing for a short time in the Death Phase before narrowing.

Table 4.1. Combined cell morphology growth rate data for constantly illuminated cultures grown under blue (450 nm) light.

Time (hr)	0.0	15.1	49.5	60.4	72.4	84.2	96.1	108.2	120.6	132.7	144.1	156.3
$\bar{n}$ (cells·mL^{-1})	1018	1120	1018	646	1442	3659	4714	7087	3294	2365	1018	620
SE	81.9	39.3	81.9	59.0	117.0	271.9	222.7	371.5	354.6	63.2	81.9	30.7
$\bar{n}$ + (1.96 x SE)	1179	1197	1179	762	1671	4192	5151	7815	3989	2489	1179	680
$\bar{n}$ - (1.96 x SE)	858	1043	858	530	1212	3126	4278	6359	2599	2241	858	560
pH	7.662	7.719	7.855	7.798	8.430	8.380	8.750	8.982	9.076	9.095	9.191	9.235
N_2/N_1	1.10	0.909	0.634	2.232	2.538	1.288	1.503	0.465	0.718	0.431	0.609	
$\ln(N_2/N_1)$	0.0953	-0.0953	-0.455	0.803	0.931	0.253	0.408	-0.766	-0.331	-0.843	-0.496	
$\log_2(N_2/N_1)$	0.137	-0.137	-0.657	1.16	1.34	0.366	0.588	-1.11	-0.478	-1.22	-0.716	
$\Delta t=(t_2-t_1)$	15.1	34.4	10.9	12.1	11.8	11.9	12.1	12.4	12.1	11.4	12.1	
$\boldsymbol{r}$ (hr^{-1})	0.00633	-0.00277	-0.0418	0.0665	0.0790	0.0213	0.0336	-0.0620	-0.0273	-0.0740	-0.0409	
$\boldsymbol{k}$ (doublings per hr)	0.00913	-0.00399	-0.0603	0.0960	0.114	0.0308	0.0485	-0.0894	-0.0394	-0.107	-0.0590	
$\boldsymbol{T_2}$ (hr)	109.5	-250	-16.6	10.4	8.77	32.5	20.6	-11.2	-25.4	-9.37	-16.9	

Mean $\boldsymbol{r}$ from interval analysis	0.0556
Standard Deviation	0.0304
Standard Error	0.0175
Skewness	-1.41

Mean $\boldsymbol{k}$ from interval analysis	0.0802
Standard Deviation	0.0438
Standard Error	0.0253
Skewness	-1.41

Mean $\boldsymbol{T_2}$ from interval analysis	17.2
Standard Deviation	13.3
Standard Error	7.65
Skewness	1.70

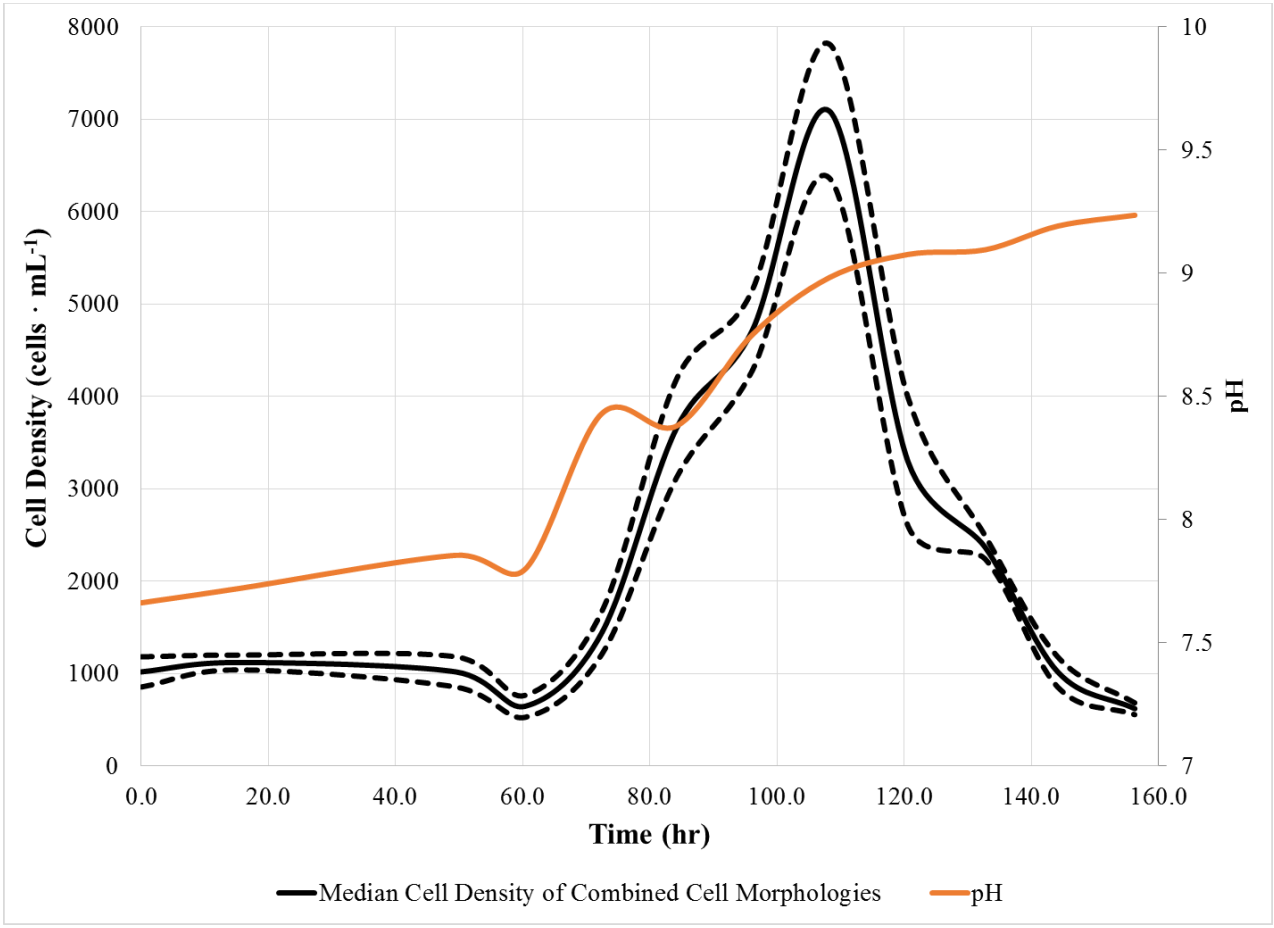

Figure 4.1. Plot time versus of the mean of the combined large and small cell morphologies' cell densities for constant illumination under blue (450 nm) light experiments. Included on the secondary ordinate is the pH taken over the same time period. Dashed lines represent the boundary of the 95% confidence interval around the mean cell densities.

Table 4.2. Large cell morphology growth rate data for constantly illuminated cultures grown under blue (450 nm) light.

Time (hr)	0.0	15.1	49.5	60.4	72.4	84.2	96.1	108.2	120.6	132.7	144.1	156.3
$\bar{n}$ (cells·mL^{-1})	287	706	211	348	967	3220	3972	6532	2788	1763	313	188
SE	46.4	41.8	19.5	34.1	91.1	235.1	218.8	424.8	316.1	51.4	29.1	19.2
$\bar{n}$ + (1.96 x SE)	378	788	249	415	1145	3681	4400	7365	3408	1864	370	225
$\bar{n}$ - (1.96 x SE)	196	624	173	281	788	2759	3543	5699	2169	1663	256	150
pH	7.662	7.719	7.855	7.798	8.430	8.380	8.750	8.982	9.076	9.095	9.191	9.235
N_2/N_1	2.46	0.30	1.65	2.78	3.33	1.23	1.64	0.43	0.63	0.18	0.60	
$\ln(N_2/N_1)$	0.899	-1.21	0.500	1.02	1.20	0.210	0.498	-0.851	-0.458	-1.73	-0.511	
$\log_2(N_2/N_1)$	1.30	-1.74	0.722	1.48	1.74	0.303	0.718	-1.23	-0.661	-2.49	-0.738	
$\Delta t=(t_2-t_1)$	15.1	34.4	10.9	12.1	11.8	11.9	12.1	12.4	12.1	11.4	12.1	
$\boldsymbol{r}$ (hr^{-1})	0.0597	-0.0351	0.0459	0.0847	0.102	0.0176	0.0410	-0.0688	-0.0377	-0.152	-0.0422	
$\boldsymbol{k}$ (doublings per hr)	0.0862	-0.0507	0.0662	0.122	0.147	0.0255	0.0592	-0.0993	-0.0544	-0.219	-0.0608	
$\boldsymbol{T_2}$ (hr)	11.6	-19.7	15.1	8.18	6.79	39.3	16.9	-10.1	-18.4	-4.57	-16.4	

Mean $\boldsymbol{r}$ from interval analysis	0.0776
Standard Deviation	0.0288
Standard Error	0.0166
Skewness	-1.05

Mean $\boldsymbol{k}$ from interval analysis	0.112
Standard Deviation	0.0415
Standard Error	0.0240
Skewness	-1.05

Mean $\boldsymbol{T_2}$ from interval analysis	10.0
Standard Deviation	4.45
Standard Error	2.57
Skewness	1.54

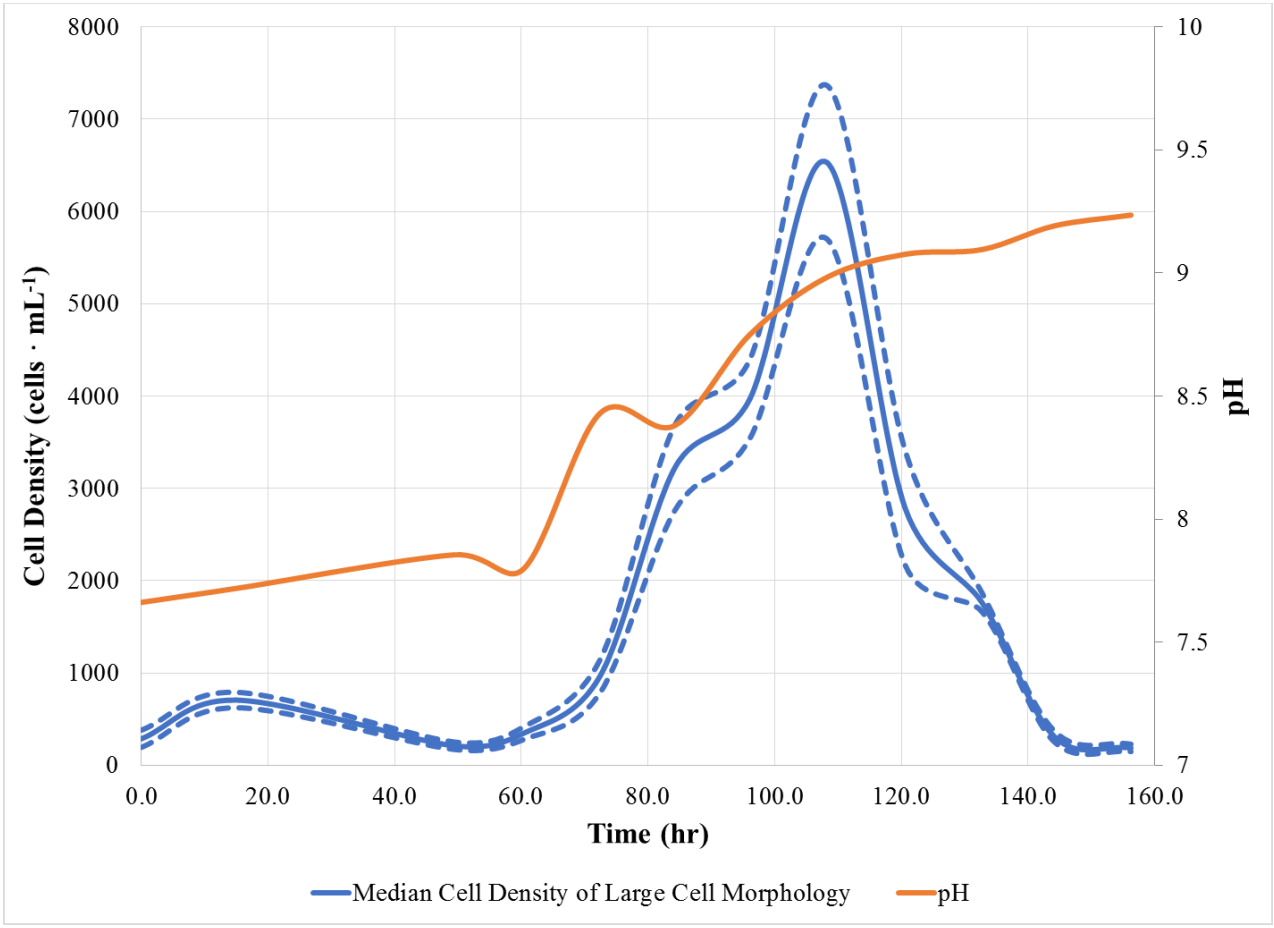

Figure 4.2. Plot of time versus only the large cell morphology's median cell densities for the constant illumination under blue (450 nm) light experiments. Included on the secondary ordinate is the pH taken over the same time period. Dashed lines represent the boundary of the 95% confidence interval around the mean cell densities.

Table 4.3. Small cell morphology growth rate data for constantly illuminated cultures grown under blue (450nm) light.

Time (hr)	0.0	15.1	49.5	60.4	72.4	84.2	96.1	108.2	120.6	132.7	144.1	156.3
$\bar{n}$ (cells·mL^{-1})	731	414	259	298	475	439	743	555	506	601	574	432
SE	83.4	9.3	31.5	26.6	26.6	68.5	56.6	55.4	47.5	20.0	32.2	16.9
$\bar{n}$ + (1.96 x SE)	894	432	321	350	527	573	854	664	599	640	637	465
$\bar{n}$ - (1.96 x SE)	567	396	197	246	423	305	632	447	413	562	510	399
pH	7.662	7.719	7.855	7.798	8.430	8.380	8.750	8.982	9.076	9.095	9.191	9.235
N_2/N_1	0.566	0.626	1.15	1.59	0.924	1.69	0.748	0.911	1.19	0.954	0.753	
$\ln(N_2/N_1)$	-0.569	-0.469	0.141	0.465	-0.0790	0.526	-0.291	-0.0929	0.173	-0.0470	-0.283	
$\log_2(N_2/N_1)$	-0.820	-0.676	0.203	0.671	-0.114	0.759	-0.420	-0.134	0.249	-0.0679	-0.409	
$\Delta t=(t_2-t_1)$	15.1	34.4	10.9	12.1	11.8	11.9	12.1	12.4	12.1	11.4	12.1	
$\boldsymbol{r}$ (hr^{-1})	-0.0378	-0.0136	0.0129	0.0385	-0.00671	0.0443	-0.0240	-0.0075	0.0142	-0.0041	-0.0234	
$\boldsymbol{k}$ (doublings per hr)	-0.0545	-0.0196	0.0186	0.0556	-0.0097	0.0639	-0.0346	-0.0108	0.0205	-0.0060	-0.0337	
$\boldsymbol{T_2}$ (hr)	-18.4	-50.9	53.7	18.0	-103	15.7	-28.9	-92.2	48.8	-168	-29.7	

Mean $\boldsymbol{r}$ from interval analysis	0.0130
Standard Deviation	0.0291
Standard Error	0.0168
Skewness	-0.19

Mean $\boldsymbol{k}$ from interval analysis	0.0188
Standard Deviation	0.0403
Standard Error	0.0233
Skewness	-1.65

Mean $\boldsymbol{T_2}$ from interval analysis	-23.2
Standard Deviation	69.4
Standard Error	40.1
Skewness	-1.73

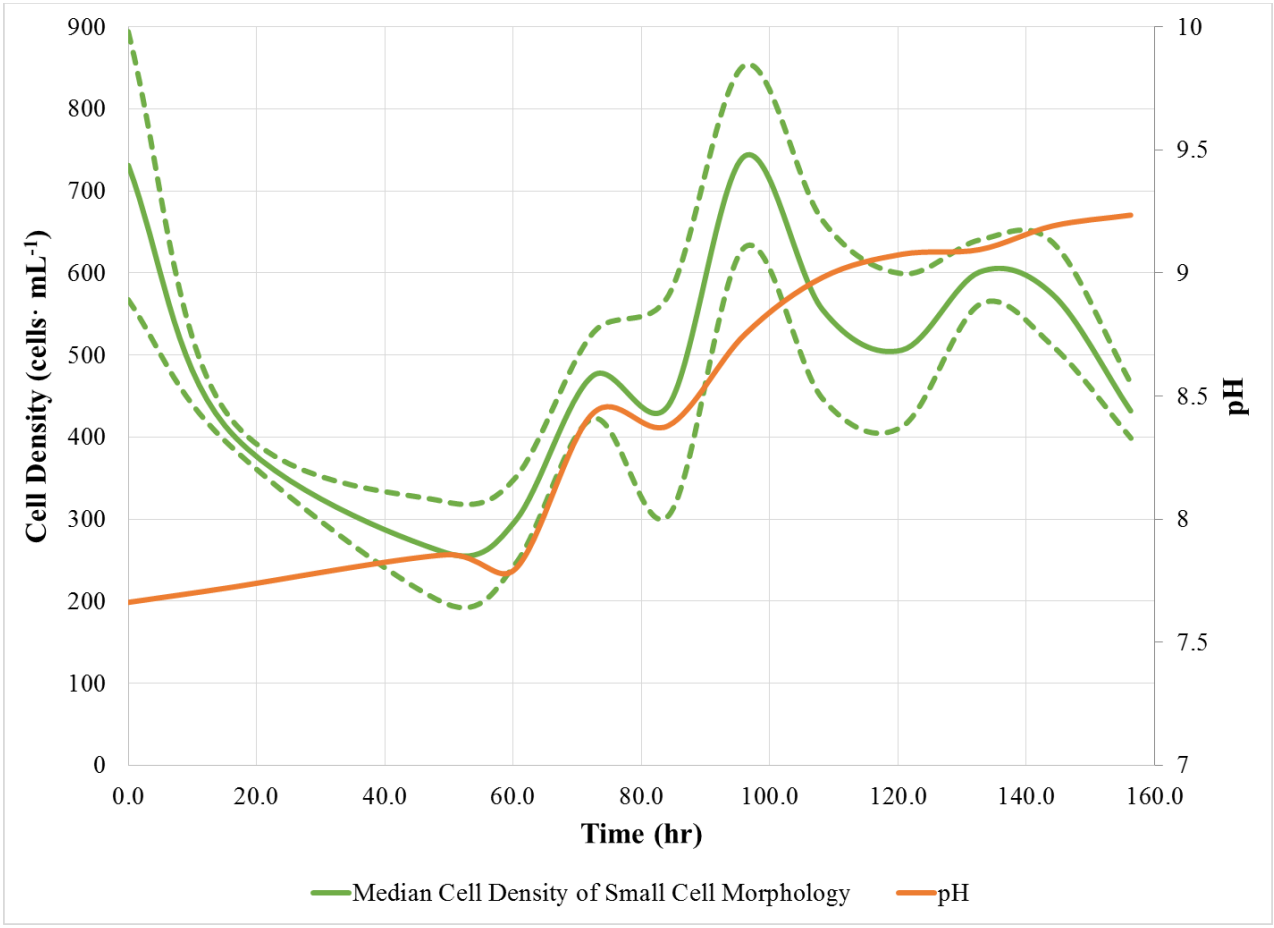

Figure 4.3. Plot of time versus only the small cell morphology's median cell densities for the constant illumination under blue (450 nm) light experiments. Included on the secondary ordinate is the pH taken over the same time period. Dashed lines represent the boundary of the 95% confidence interval around the mean cell densities.

The plot Figure 4.2 represents the same non-sigmoidal plot as exhibited in the Figure 4.1 because of the dominance of the larger cell morphology in growth phases of the experiment. Figure 4.2 exhibits the same widening of the confidence interval illustrated in Figure 4.1 as the population approaches the peak cell density, then peaks, and proceeds mid-way down the Death Phase. As the population density declines, the confidence interval contracts to an almost unperceivable level on the graph until the end of the experiment. The Figure 4.3 plot exhibits an immediate increase in the level of large morphology cells within the first experimental time interval. The increase is followed by a more gradual rise in the population density until around 60 hrs into the experiment, when the population reaches the beginning of the Acceleration of Growth phase. This subtle feature is lost on the Figure 4.1 graph, where the Lag Phase is almost flat as a rapid decrease in the population of the smaller cell morphology almost completely canceled out the increase in appearance of the larger cell morphology.

The graph of the small cell morphology in Figure 4.3 exhibited a more flat growth curve that did not fit as well into a classical model. The Lag Phase in Figure 4.3 actually demonstrated a distinct decrease in the population until around 60hrs when the small cell morphology population began to increase. However, the cell density of the small cell morphology only manages to recover to around the level of the initial concentration introduced into the bioreactor. Similar to the large cell morphology over the same time span, the small cell morphology had relative increases in the 95% confidence of the mean. Also notable are the comparative cell densities between the two morphologies. The cell densities of the small cell morphologies are around an order of magnitude less than that of the large cell morphologies throughout much of the experiment. Only in the

last few samples of the experiment do the cell densities of the small cell morphology reach those of the large cell morphology. However, that situation only occurs because the cell density of the large cell morphology has rapidly declined, and not because the small cell morphology has rapidly grown.

4.1.2. Flashing Illumination Under Blue Light. Data from the experimental treatment of *D. viridis* with blue (450 nm) light flashing at a frequency of 45.5 Hz was processed as described in the Material and Methods §3.14 and tabulated. Table 4.4 presents the data and derived results for the total combined cell counts of the large and small morphologies in the samples treated with flashing illumination under blue light. Time versus $\bar{n}$ data from Figure 4.4were plotted on the primary abscissa and ordinate respectively, to create the solid black line plot in the figure. Dashed black line plots in Figure 4.4 denote the 95% confidence interval around the mean created from adding or subtracting the $\bar{n}$ to the product of 1.96 and the SE. Finally, the pH was plotted on the secondary ordinate as a solid orange line in Figure 4.4. Using the same aforementioned procedure, tables and plots were developed for only the large cell morphology and the small cell morphology.

Table 4.5 represents only data related to the large cell morphology in the treatment with flashing blue (450nm) light and was used to create the linear plot in Figure 4.5. The solid blue line plot in Figure 4.5 represents the mean cell density data for the large cell morphology. Dashed blue line plots in Figure 4.5 denote the 95% confidence interval around the mean created from adding or subtracting the $\bar{n}$ to the product of 1.96 and the SE. Finally, the pH was plotted on the secondary ordinate as a solid orange line in Figure 4.5.

Table 4.6 represents only data related to the small cell morphology in the treatment with flashing blue (450nm) light. Figure 4.6 was developed from the data presented in Table 4.6. The solid green line plot in Figure 4.6 represents the mean cell density data for the small cell morphology as presented in Table 4.6. Dashed green line plots in Figure 4.6 denote the 95% confidence interval around the mean created from adding or subtracting the $\bar{n}$ to the product of 1.96 and the SE. Finally, the pH was plotted on the secondary ordinate as a solid orange line in Figure 4.6.

Visual interpretation of the plotted data in Figure 4.5 illustrates a lag time of nearly 40 hrs before the commencement of the Positive Acceleration Phase populations. The cell density peaks at over 12000 cells·mL^{-1} at two separate times within the plot. As was seen in Figure 4.5, the growth of the large cell morphology population dominates the plot of growth of the population as a whole in Figure 4.4. The small cell morphology population also demonstrated a positive growth phase at the same time as the larger cell type. The small cell morphology attained roughly one-half to one-third of the cell densities of the larger cell morphology throughout the experimental trial. The small cell morphology population peaked at around a mean cell density of 3700 cells·mL^{-1} , and the larger cell morphology peaked at just over 10000 cells·mL^{-1}. Figure 4.6 shows that the small cell morphology population reached a reasonable steady-state between hour 45 and hour 140 as the cell density fluctuated consistently between 3000 to 2000 cells·mL^{-1}. The plot of the mean cell densities of the large cell morphology clearly shows two distinct decreases in cell density, one around hour 75 and another around hour 100 that distort the graph away from a more classic growth curve in Figure 4.5.

Table 4.4. Combined cell morphology growth rate data for flashing (45.6 Hz) illuminated cultures grown under blue (450 nm) light.

Time (hr)	0.0	15.1	37.3	49.6	60.4	72.5	80.3	97.0	108.3	120.6	132.8	144.2	156.3
$\bar{n}$ (cells·mL^{-1})	814	1295	1719	3753	9267	8004	12451	10568	10904	12488	7801	4720	2113
SE	78.3	104.4	16.3	432.3	118.9	117.9	258.3	565.1	587.7	1374.7	265.7	436.4	77.8
$\bar{n}$ + (1.96 x SE)	968	1499	1750	4600	9500	8236	12957	11676	12056	15183	8322	5575	2265
$\bar{n}$ - (1.96 x SE)	661	1090	1687	2906	9034	7773	11944	9460	9752	9794	7280	3865	1960
pH	7.601	7.875	8.131	8.219	8.203	8.687	8.781	9.200	9.049	9.159	9.071	9.378	9.289
N_2/N_1	1.59	1.33	2.18	2.47	0.86	1.56	0.85	1.03	1.15	0.62	0.61	0.45	
$\ln(N_2/N_1)$	0.464	0.283	0.781	0.904	-0.147	0.442	-0.164	0.0313	0.136	-0.471	-0.502	-0.804	
$\log_2(N_2/N_1)$	0.669	0.409	1.13	1.30	-0.211	0.637	-0.237	0.0452	0.196	-0.679	-0.725	-1.16	
$\Delta t=(t_2-t_1)$	15.1	22.2	12.3	10.8	12.1	7.76	16.7	11.3	12.4	12.1	11.4	12.1	
r (hr^{-1})	0.0306	0.0128	0.0634	0.0840	-0.0121	0.0569	-0.00981	0.00277	0.0110	-0.0388	-0.0440	-0.0663	
k (doublings per hr)	0.0442	0.0184	0.0914	0.1212	-0.0175	0.0821	-0.0141	0.00400	0.0158	-0.0559	-0.0635	-0.0957	
$\boldsymbol{T_2}$ (hr)	22.6	54.3	10.9	8.3	-57.2	12.2	-70.7	250	63.1	-17.9	-15.7	-10.4	

Mean ***r*** from interval analysis	0.0451
Standard Deviation	0.0506
Standard Error	0.0292
Skewness	-1.41

Mean ***k*** from interval analysis	0.0650
Standard Deviation	0.0730
Standard Error	0.0421
Skewness	-1.41

Mean $\boldsymbol{T_2}$ from interval analysis	-12.7
Standard Deviation	38.6
Standard Error	22.3
Skewness	-1.72

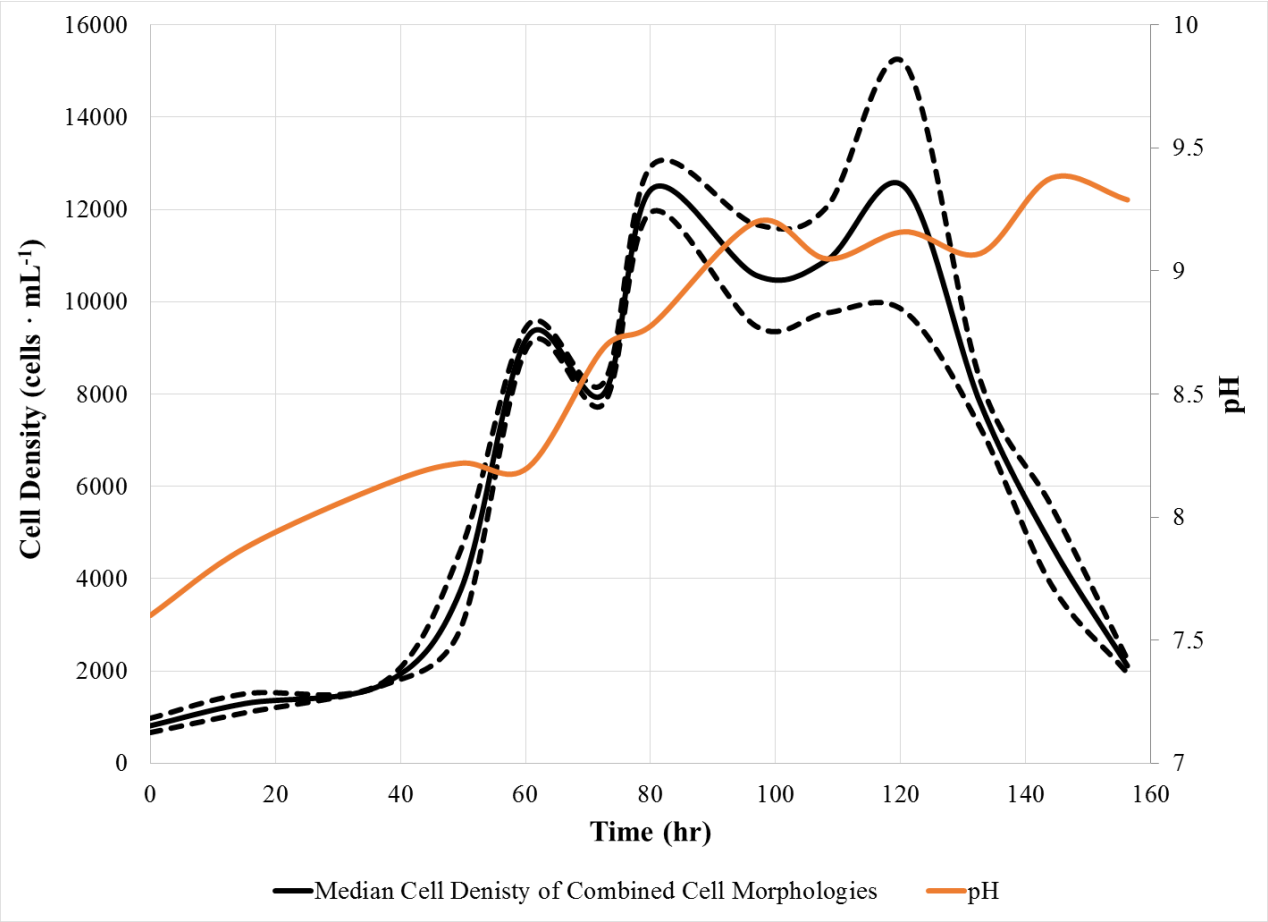

Figure 4.4. Plot time versus of the mean of the combined large and small cell morphologies' cell densities for flashing illumination (45.6 Hz) under blue (450 nm) light experiments. Included on the secondary ordinate is the pH taken over the same time period. Dashed lines represent the boundary of the 95% confidence interval around the mean cell densities.

Table 4.5. Large cell morphology growth rate data for flashing (45.6 Hz) illuminated cultures grown under blue (450 nm) light.

Time (hr)	0.0	15.1	37.3	49.6	60.4	72.5	80.3	97.0	108.3	120.6	132.8	144.2	156.3
$\bar{n}$ (cells·mL^{-1})	272	297	704	1310	6720	5240	9548	6843	7923	10187	5269	2341	159
SE	58.0	12.7	70.8	278.3	11.8	198.4	404.0	377.9	372.0	1258.2	223.4	365.1	35.6
$\bar{n}$ + (1.96 x SE)	386	322	843	1855	6743	5628	10339	7583	8652	12653	5707	3057	229
$\bar{n}$ - (1.96 x SE)	158	272	565	765	6697	4851	8756	6102	7194	7721	4831	1626	89
pH	7.601	7.875	8.131	8.219	8.203	8.687	8.781	9.200	9.049	9.159	9.071	9.378	9.289
N_2/N_1	1.09	2.37	1.86	5.13	0.78	1.82	0.72	1.16	1.29	0.52	0.44	0.07	
$\ln(N_2/N_1)$	0.0869	0.864	0.621	1.64	-0.249	0.600	-0.333	0.147	0.251	-0.659	-0.811	-2.69	
$\log_2(N_2/N_1)$	0.125	1.25	0.896	2.36	-0.359	0.866	-0.481	0.211	0.363	-0.951	-1.17	-3.88	
$\Delta t=(t_2-t_1)$	15.1	22.2	12.3	10.8	12.1	7.76	16.7	11.3	12.4	12.1	11.4	12.1	
$\boldsymbol{r}$ (hr^{-1})	0.00574	0.0390	0.0504	0.152	-0.0206	0.0773	-0.0199	0.0130	0.0203	-0.0543	-0.0711	-0.222	
$\boldsymbol{k}$ (doublings per hr)	0.00828	0.0562	0.0727	0.219	-0.0297	0.112	-0.0287	0.0187	0.0294	-0.0784	-0.103	-0.320	
$\boldsymbol{T_2}$ (hr)	121	17.8	13.8	4.6	-33.7	8.96	-34.8	53.4	34.1	-12.8	-9.75	-3.12	

Mean $\boldsymbol{r}$ from interval analysis	0.0804
Standard Deviation	0.0622
Standard Error	0.0359
Skewness	1.67

Mean $\boldsymbol{k}$ from interval analysis	0.116
Standard Deviation	0.0897
Standard Error	0.0518
Skewness	1.67

Mean $\boldsymbol{T_2}$ from interval analysis	12.0
Standard Deviation	6.78
Standard Error	3.92
Skewness	-1.07

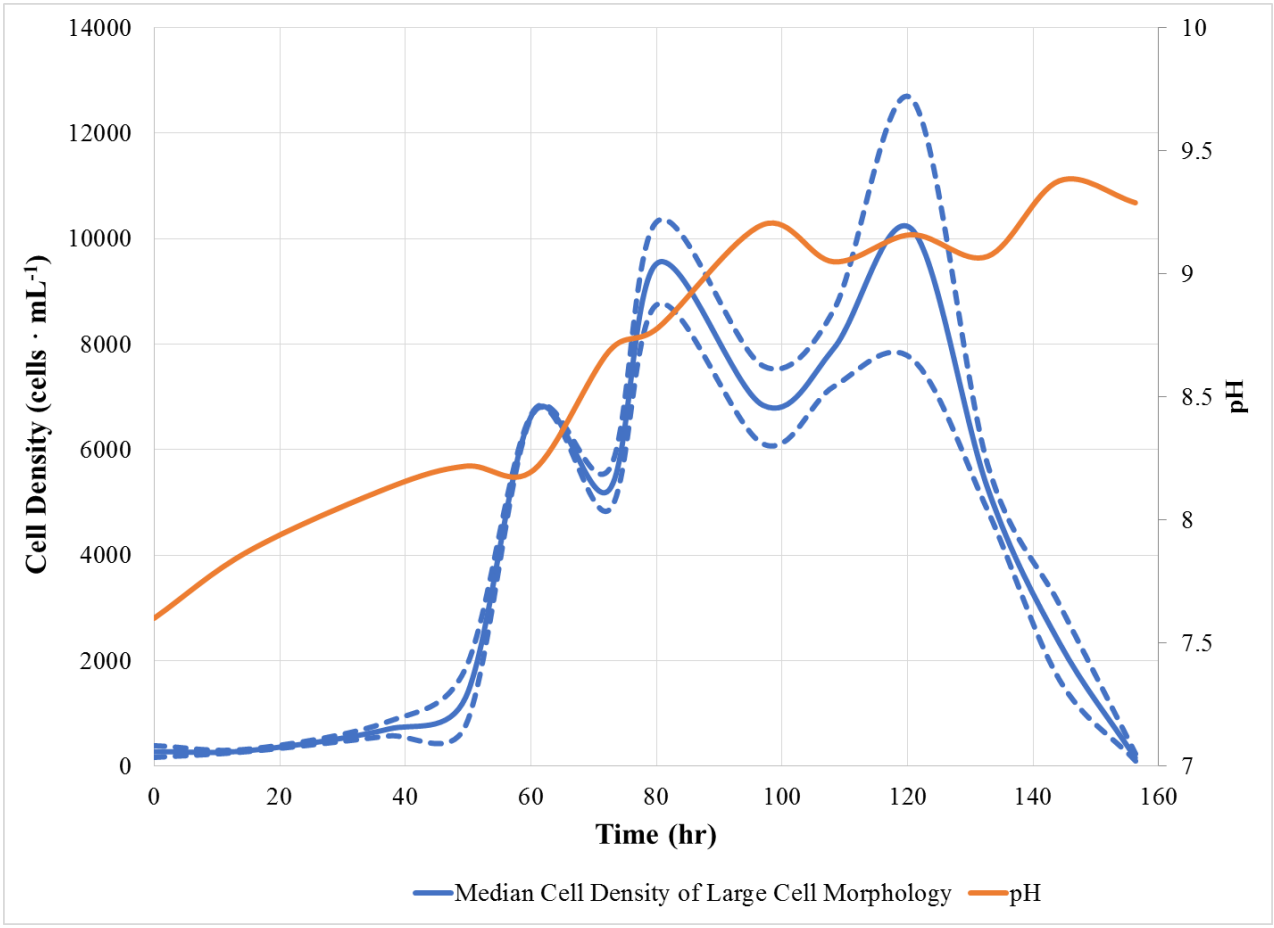

Figure 4.5. Plot of time versus only the large cell morphology's median cell densities for the flashing (45.6 Hz) illumination under blue (450 nm) light experiments. Included on the secondary ordinate is the pH taken over the same time period. Dashed lines represent the boundary of the 95% confidence interval around the mean cell densities.

Table 4.6. Small cell morphology growth rate data for flashing (45.6 Hz) illuminated cultures grown under blue (450 nm) light.

Time (hr)	0.0	15.1	37.3	49.6	60.4	72.5	80.3	97.0	108.3	120.6	132.8	144.2	156.3
$\bar{n}$ (cells·mL^{-1})	542	998	1015	2443	2547	2765	2903	3725	2982	2301	2532	2379	1954
SE	27.3	115.8	86.9	174.4	108.6	84.6	161.8	287.6	283.9	119.4	161.9	141.8	49.0
$\bar{n}$ + (1.96 x SE)	595	1225	1185	2785	2760	2931	3220	4289	3538	2535	2850	2657	2050
$\bar{n}$ - (1.96 x SE)	489	771	844	2101	2334	2599	2586	3162	2425	2067	2215	2101	1857
pH	7.601	7.875	8.131	8.219	8.203	8.687	8.781	9.2	9.049	9.159	9.071	9.378	9.289
N_2/N_1	1.84	1.02	2.41	1.04	1.09	1.05	1.28	0.800	0.772	1.10	0.939	0.821	
$\ln(N_2/N_1)$	0.610	0.0166	0.879	0.0417	0.0820	0.0487	0.249	-0.223	-0.259	0.0956	-0.0624	-0.197	
$\log_2(N_2/N_1)$	0.880	0.0239	1.268	0.0602	0.118	0.0703	0.360	-0.321	-0.374	0.138	-0.0901	-0.284	
$\Delta t=(t_2-t_1)$	15.1	22.2	12.3	10.8	12.1	7.8	16.7	11.3	12.4	12.1	11.4	12.1	
$\boldsymbol{r}$ (hr^{-1})	0.0403	0.000748	0.0713	0.00388	0.00678	0.00628	0.0149	-0.0197	-0.0210	0.00788	-0.00547	-0.0163	
$\boldsymbol{k}$ (doublings per hr)	0.0582	0.00108	0.103	0.00559	0.00978	0.00906	0.0215	-0.0284	-0.0302	0.0114	-0.00789	-0.0235	
$\boldsymbol{T_2}$ (hr)	17.2	926	9.72	179	102	110	46.5	-35.2	-33.1	88.0	-127	-42.6	

Mean $\boldsymbol{r}$ from interval analysis	0.00933
Standard Deviation	0.00485
Standard Error	0.0204
Skewness	1.71

Mean $\boldsymbol{k}$ from interval analysis	0.0135
Standard Deviation	0.00700
Standard Error	0.00404
Skewness	1.71

Mean $\boldsymbol{T_2}$ from interval analysis	86.4
Standard Deviation	34.8
Standard Error	20.1
Skewness	-1.63

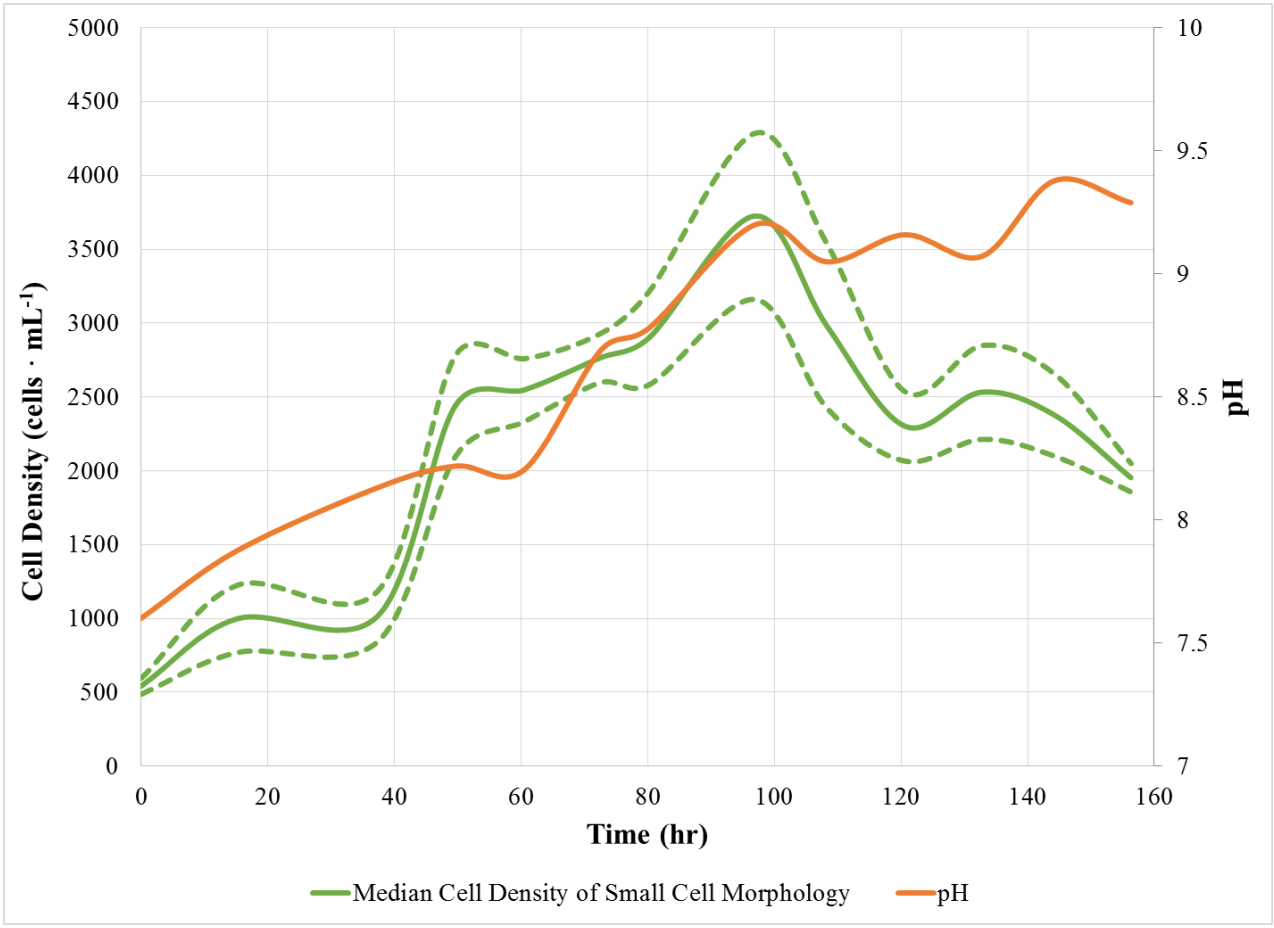

Figure 4.6. Plot of time versus only the small cell morphology's median cell densities for the flashing (45.6 Hz) illumination under blue (450 nm) light experiments. Included on the secondary ordinate is the pH taken over the same time period. Dashed lines represent the boundary of the 95% confidence interval around the mean cell densities.

As previously noted in Figure 4.4, the overall growth curve is not completely sigmoidal as declines in the overall cell density occur at hour 75 and hour 100. With the addition of the SE information, the graph demonstrates a widening of the confidence interval as the experiment matures. Early in the experiment, the 95% confidence interval is fairly consistent and demonstrates a very tight correlation with the mean data up until hour 80. As was also shown in Figure 4.4, the 95% confidence interval widens significantly in data points taken around the peak cell density for the experiment.

The Figure 4.5 plot represents the same non-sigmoidal plot as exhibited in the Figure 4.4. The overlay of SE information also shows the same widening of the confidence interval as the cells approach the peak cell density and throughout the peak. The decline in the cell density of the large cell morphology coincides with the decrease in the width of the 95% confidence interval. Another notable feature during the Lag Phase in the Figure 4.5 plot is an increase in the 95% confidence interval just as the cells are entering into the Positive Acceleration Phase and then decreases as the cells enter the Exponential Phase around hour 50 and lasts until the hour 80.

The graph of the small cell morphology in Figure 4.6 exhibited a mostly steady-state as the variation in the cell density only varied by about 1500 cells·mL^{-1} between hour 50 and hour 160. While a peak count of just over 3700 cells·mL^{-1} occurred at hour 95, the wide 95% confidence interval put the data reasonably within the range. The Lag Phase actually demonstrated a distinct decrease in the population until around hour 60 when the small cell morphology began to increase.

4.1.3. Constant Illumination Under Red Light. Data from the experimental treatment of *D. viridis* with constant red (660 nm) light was processed as described in the

Material and Methods §3.14 and tabulated. Table 4.7 presents the data and derived results for the total combined cell counts of the large and small morphologies in the samples treated with constant illumination under red light. Time versus mean cell density ($\bar{n}$) data from Table 4.7 were plotted on the primary abscissa and ordinate respectively, to create the solid black line plot in Figure 4.7. Dashed black line plots in Figure 4.1 denote the 95% confidence interval around the mean created from adding or subtracting the $\bar{n}$ to the product of 1.96 and the SE. Finally, the pH was plotted on the secondary ordinate as a solid orange line in Figure 4.7. Using the same aforementioned procedure, tables and plots were developed for only the large cell morphology and the small cell morphology.

Table 4.8 represents only data related to the large cell morphology in the treatment with constant red (660 nm) light and was used to create the linear plot in Figure 4.2. The solid red line plot in Figure 4.8 represents the mean cell density data for the large cell morphology. Dashed red line plots in Figure 4.8 denote the 95% confidence interval around the mean created from adding or subtracting the $\bar{n}$ to the product of 1.96 and the SE. Finally, the pH was plotted on the secondary ordinate as a solid orange line in Figure 4.8.

Table 4.9 represents only data related to the small cell morphology in the treatment with constant red (660 nm) light and was developed from the data presented in Table 4.9. The solid green line plot in Figure 4.3 represents the mean cell density data for the small cell morphology as presented in Table 4.9. Dashed green line plots in Figure 4.9 denote the 95% confidence interval around the mean created from adding or

Table 4.7. Combined cell morphology growth rate data for constantly illuminated cultures grown under red (660 nm) light.

Time (hr)	0.0	15.2	37.3	49.7	60.5	72.5	84.3	97.4	108.3	120.6	156.7	168.2	180.3
$\bar{n}$ (cells·mL^{-1})	1121	4338	15066	30340	36627	33024	21540	17900	29339	21810	26411	31769	37406
SE	99.1	306.7	678.4	1543.2	2098.7	4261.4	1061.1	898.1	532.1	693.8	502.8	1343.8	206.1
$\bar{n}$ + (1.96 x SE)	1315	4939	16396	33365	40740	41376	23620	19660	30382	23170	27396	34403	37810
$\bar{n}$ - (1.96 x SE)	927	3737	13737	27316	32513	24672	19460	16139	28296	20450	25425	29136	37002
pH	7.618	7.893	8.049	8.343	8.406	8.467	8.381	8.378	8.520	9.159	8.632	8.925	9.029
N_2/N_1	3.87	3.47	2.01	1.21	0.902	0.652	0.831	1.64	0.743	1.21	1.20	1.18	
$\ln(N_2/N_1)$	1.35	1.25	0.700	0.188	-0.104	-0.427	-0.185	0.494	-0.297	0.191	0.185	0.163	
$\log_2(N_2/N_1)$	1.95	1.80	1.01	0.272	-0.149	-0.616	-0.267	0.713	-0.428	0.276	0.267	0.236	
$\Delta t=(t_2-t_1)$	15.2	22.2	12.3	10.8	12.1	11.7	13.1	10.9	12.4	36.1	11.5	12.1	
r (hr^{-1})	0.0893	0.0561	0.0568	0.0175	-0.00857	-0.0365	-0.0141	0.0454	-0.0240	0.00530	0.0161	0.0135	
k (doublings per hr)	0.129	0.0810	0.0819	0.0252	-0.0124	-0.0526	-0.0204	0.0655	-0.0346	0.00764	0.0233	0.0194	
T_2 (hr)	7.76	12.4	12.2	39.7	-80.9	-19.0	-49.1	15.3	-28.9	130.8	43.0	51.4	

Mean r from interval analysis	0.0549
Standard Deviation	0.0294
Standard Error	0.0170
Skewness	-0.31

Mean k from interval analysis	0.0792
Standard Deviation	0.0424
Standard Error	0.0245
Skewness	-0.31

Mean T_2 from interval analysis	18.0
Standard Deviation	14.6
Standard Error	8.43
Sewness	1.87

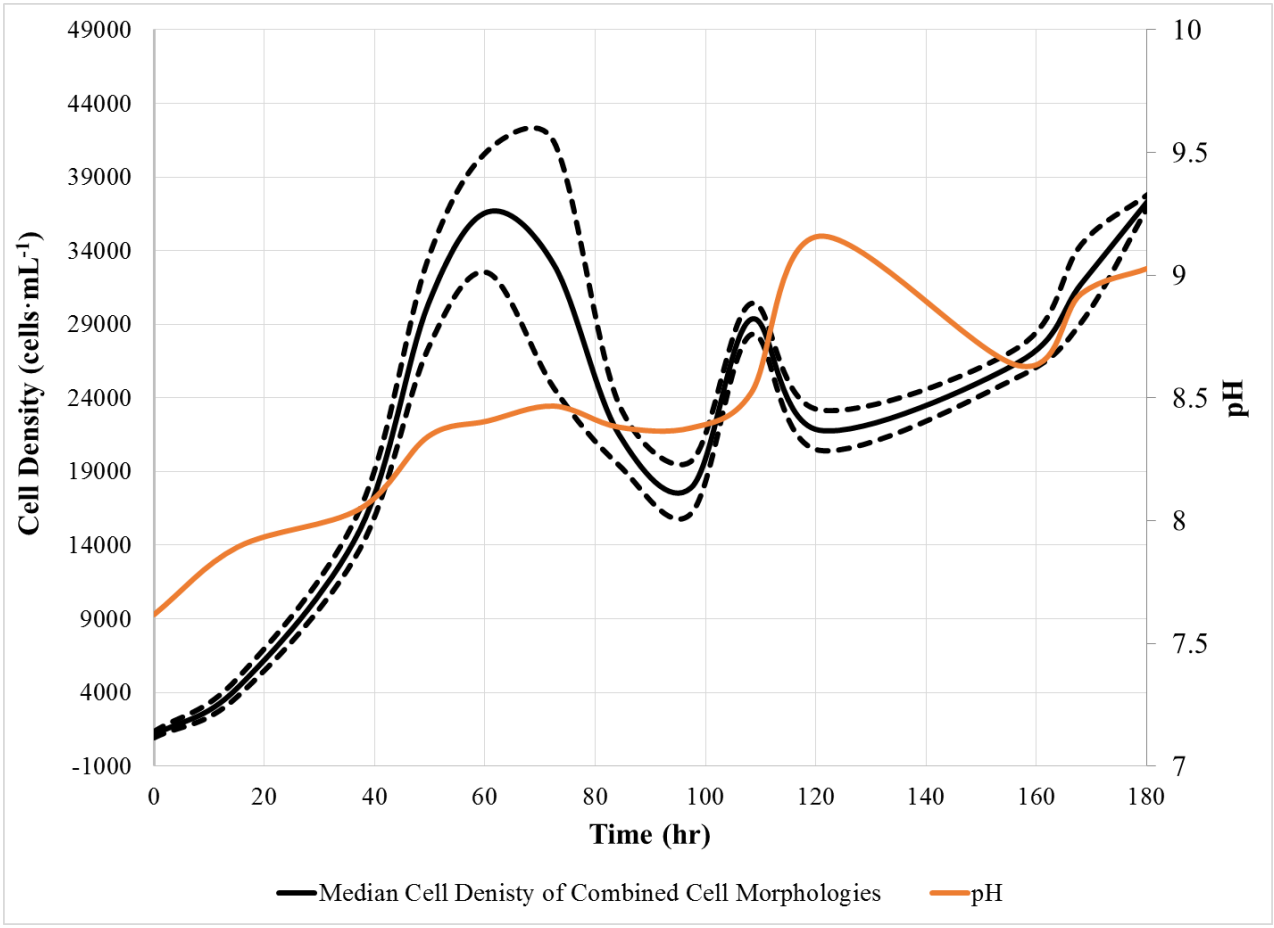

Figure 4.7. Plot time versus of the mean of the combined large and small cell morphologies' cell densities for constant illumination under red (660 nm) light experiments. Included on the secondary ordinate is the pH taken over the same time period. Dashed lines represent the boundary of the 95% confidence interval around the mean cell densities.

Table 4.8. Large cell morphology growth rate data for constantly illuminated cultures grown under red (660 nm) light.

Time (hr)	0.0	15.2	37.3	49.7	60.5	72.5	84.3	97.4	108.3	120.6	156.7	168.2	180.3
$\bar{n}$ (cells·mL^{-1})	336	2780	12374	24834	24920	22177	8289	4119	6933	2360	2260	1633	1426
SE	58.6	269.9	872.0	1686.8	1884.3	3665.0	817.2	559.7	422.4	49.4	71.0	237.4	92.2
$\bar{n}$ + (1.96 x SE)	451	3309	14083	28140	28613	29360	9890	5216	7761	2457	2399	2098	1607
$\bar{n}$ - (1.96 x SE)	222	2251	10665	21527	21227	14993	6687	3022	6105	2263	2121	1167	1246
pH	7.618	7.893	8.049	8.343	8.406	8.467	8.381	8.378	8.520	9.159	8.632	8.925	9.029
N_2/N_1	8.27	4.45	2.01	1.00	0.890	0.374	0.497	1.68	0.340	0.958	0.722	0.874	
$\ln(N_2/N_1)$	2.11	1.49	0.697	0.00347	-0.117	-0.984	-0.699	0.521	-1.08	-0.043	-0.325	-0.135	
$\log_2(N_2/N_1)$	3.05	2.15	1.00	0.00501	-0.168	-1.42	-1.01	0.751	-1.55	-0.063	-0.469	-0.195	
$\Delta t=(t_2-t_1)$	15.2	22.2	12.3	10.8	12.1	11.7	13.1	10.9	12.4	36.1	11.5	12.1	
$\boldsymbol{r}$ (hr^{-1})	0.139	0.0673	0.0565	0.000322	-0.00965	-0.0840	-0.0533	0.0479	-0.0872	-0.00120	-0.0284	-0.0111	
$\boldsymbol{k}$ (doublings per hr)	0.201	0.0971	0.0815	0.000464	-0.0139	-0.121	-0.0769	0.0690	-0.126	-0.00173	-0.0410	-0.0161	
$\boldsymbol{T_2}$ (hr)	4.97	10.3	12.3	2153	-71.8	-8.26	-13.0	14.5	-7.95	-576	-24.4	-62.2	

Mean $\boldsymbol{r}$ from interval analysis	0.0414
Standard Deviation	0.0360
Standard Error	0.0208
Skewness	-1.56

Mean $\boldsymbol{k}$ from interval analysis	0.0597
Standard Deviation	0.0519
Standard Error	0.0299
Skewness	-1.56

Mean $\boldsymbol{T_2}$ from interval analysis	725
Standard Deviation	1237
Standard Error	714
Skewness	1.73

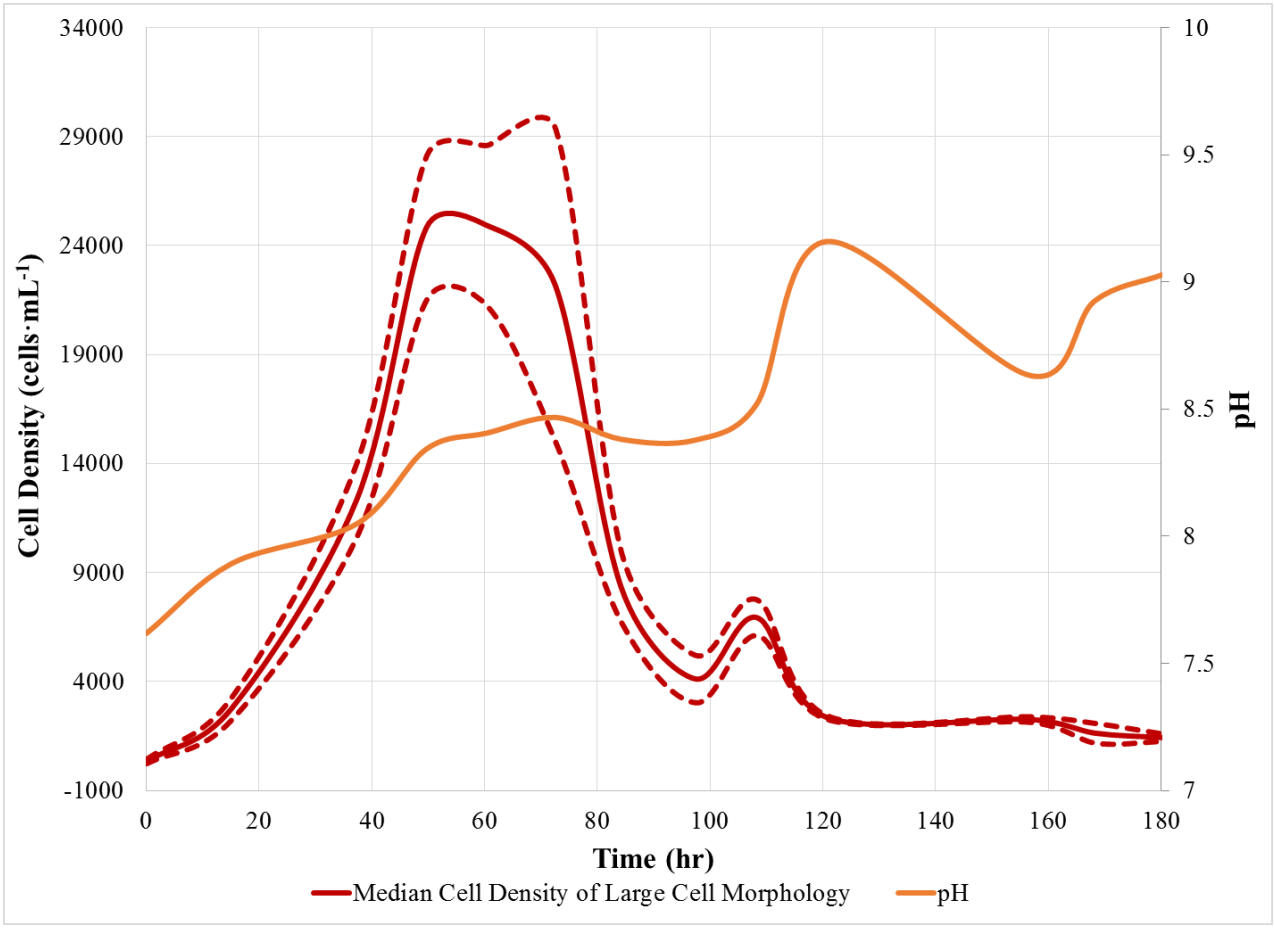

Figure 4.8. Plot of time versus only the large cell morphology's median cell densities for constant illumination under red (660 nm) light experiments. Included on the secondary ordinate is the pH taken over the same time period. Dashed lines represent the boundary of the 95% confidence interval around the mean cell densities.

Table 4.9. Small cell morphology growth rate data for constantly illuminated cultures grown under red (660nm) light.

Time (hr)	0	15.2	37.3	49.7	60.5	72.5	84.3	97.4	108.3	120.6	156.7	168.2	180.3
$\bar{n}$ (cells·mL^{-1})	785	1558	2692	5507	11707	10847	13251	13781	22406	19450	24151	30137	35979
SE	46.6	66.8	193.6	198.5	360.0	628.3	355.3	396.9	117.1	644.6	520.9	1231.4	160.0
$\bar{n}$ + (1.96 x SE)	876	1689	3072	5896	12413	12079	13948	14559	22635	20713	25172	32550	36293
$\bar{n}$ - (1.96 x SE)	693	1427	2313	5117	11001	9616	12555	13003	22176	18187	23130	27723	35666
pH	7.618	7.893	8.049	8.343	8.406	8.467	8.381	8.378	8.520	9.159	8.632	8.925	9.029
N_2/N_1	1.99	1.73	2.05	2.13	0.93	1.22	1.04	1.63	0.87	1.24	1.25	1.19	
$\ln(N_2/N_1)$	0.686	0.547	0.716	0.754	-0.076	0.200	0.039	0.486	-0.141	0.216	0.221	0.177	
$\log_2(N_2/N_1)$	0.989	0.789	1.03	1.09	-0.110	0.289	0.057	0.701	-0.204	0.312	0.319	0.256	
$\Delta t=(t_2-t_1)$	15.2	22.2	12.3	10.8	12.1	11.7	13.1	10.9	12.4	36.1	11.5	12.1	
$\boldsymbol{r}$ (hr^{-1})	0.0452	0.0247	0.0580	0.0700	-0.00631	0.0171	0.00298	0.0447	-0.0114	0.00599	0.0193	0.0146	
$\boldsymbol{k}$ (doublings per hr)	0.0653	0.0356	0.0837	0.101	-0.00911	0.0246	0.00431	0.0644	-0.0165	0.00865	0.0279	0.0211	
$\boldsymbol{T_2}$ (hr)	15.3	28.1	11.9	9.9	-109.8	40.6	232.2	15.5	-60.6	115.6	35.9	47.4	

Mean $\boldsymbol{r}$ from interval analysis	0.0495
Standard Deviation	0.0339
Standard Error	0.0112
Skewness	-0.56

Mean $\boldsymbol{k}$ from interval analysis	0.0714
Standard Deviation	0.0280
Standard Error	0.0161
Skewness	-0.56

Mean $\boldsymbol{T_2}$ from interval analysis	16.3
Standard Deviation	8.2
Standard Error	4.72
Skewness	1.58

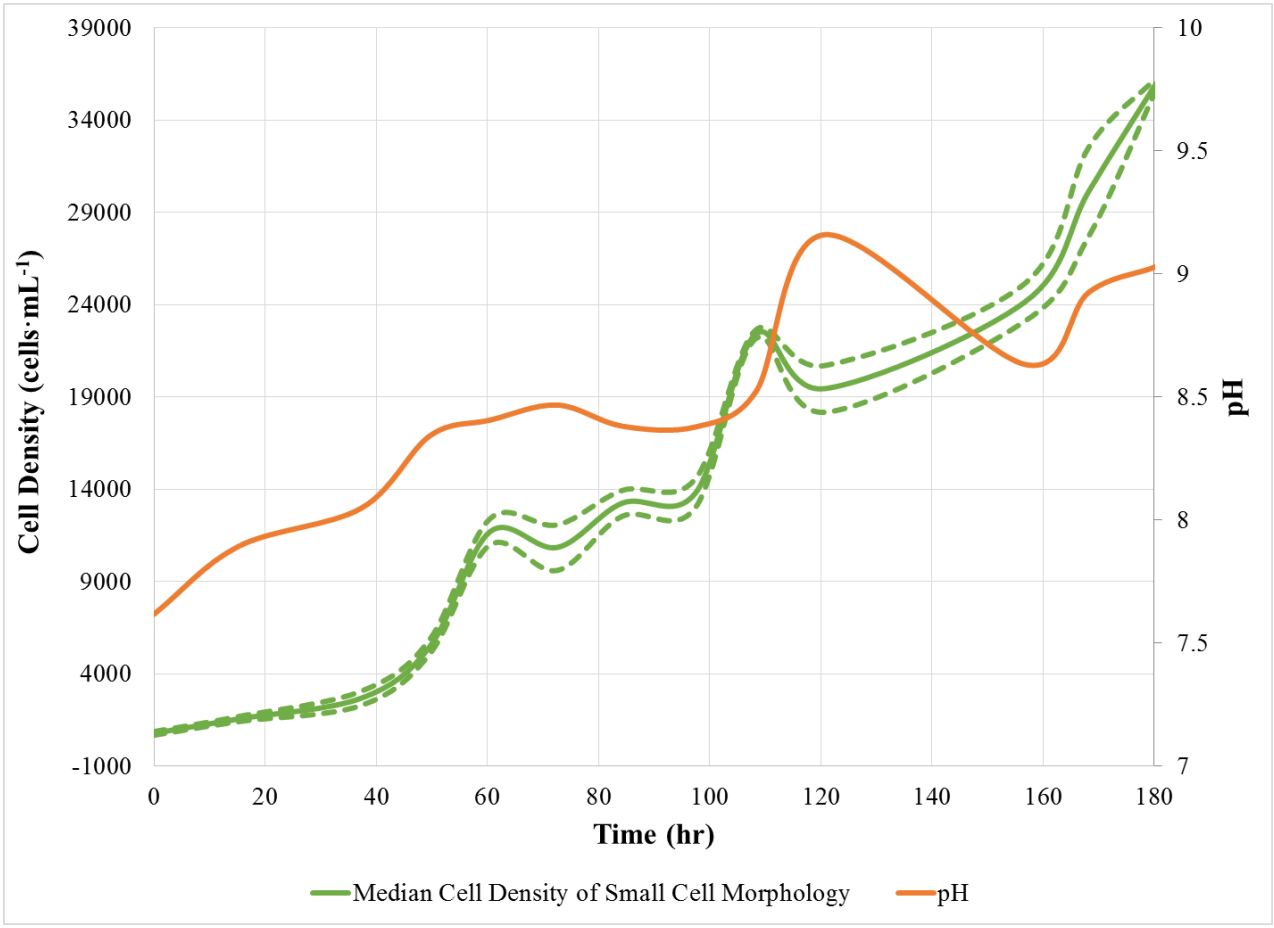

Figure 4.9. Plot of time versus only the small cell morphology's median cell densities for constant illumination under red (660 nm) light experiments. Included on the secondary ordinate is the pH taken over the same time period. Dashed lines represent the boundary of the 95% confidence interval around the mean cell densities.

subtracting the $\bar{n}$ to the product of 1.96 and the SE. Finally, the pH was plotted on the secondary ordinate as a solid orange line in Figure 4.6.

Visual interpretation of the plotted data in Figure 4.7 illustrates an immediate progression of the large cell morphology into the Acceleration Phase. The population density of the large cell morphology continues through a distinct exponential phase, roughly between hours 20 and 45, until reaching a mean peak density of just under 25000 cells·mL^{-1}. The small cell morphology takes on a more linear population growth profile throughout the duration of the experiment. With the exception of some intermediate peaks in the data, the small cell morphology continues to grow at a fairly linear rate and peaks with over 35000 cells·mL^{-1} when the experiment is terminated. Figure 4.7 also shows that the large cell morphology of the algae dominated the early portion of the growth of the population as a whole, and the small cell morphology of the algae dominated the cell counts from hour 80 until the termination of the experiment.

The overall growth curve presented in Figure 4.7 is not completely sigmoidal as the rapid decline in the sum of the large and small cell morphologies' mean cell densities decline significantly shortly after hour 60. However, the decline is halted around hour 95, and another small spike in the data is noted at about hour 110. The graph continues to steadily increase until the termination of the experiment. The plot in Figure 4.7 shows a fairly consistent and narrow 95% confidence interval all the way up to the major peak of the graph at just after hour 60. The peak of the graph in Figure 4.7 demonstrates a considerable widening of the confidence interval with a variation of between 4000-5000 cells·mL^{-1}. The 95% confidence intervals then narrows down again as the population

declines to hour 95. The samples taken afterwards show a fairly consistent 95% confidence in the mean until the termination of the experiment.

Figure 4.8 is the linear plot of the mean cell densities (cells·mL^{-1}) versus time (hr) of the following: Data for the large cell morphology is designated by the solid red line. A 95% confidence of the mean value is shown by the dashed red lines that represent the +SE (upper dashed line) and –SE (lower dashed line). The overlay of SE information also shows the same widening of the 95% confidence interval as was illustrated in Figure 4.7 at the peak cell density of around 25000 cells·mL^{-1}. A small stationary phase is inferred roughly between hour 50 and hour 70 in the experiment. A Death Phase then continues until hour 120 when the population again reaches a fairly steady-state of between 1400 and 2400 cells·mL^{-1}. The 95% confidence interval bounded by the dashed red lines is fairly constant up until the peak cell density. The plot is much wider at the beginning of the Death Phase interval, and then begins to close as the large cell morphology declines in population, until it is almost imperceptible at around hour 110.

Figure 4.9 is the linear plot of the mean cell densities (cells·mL^{-1}) versus time (hr) of the following: Data for the small cell morphology is designated by the solid green line. A 95% confidence of the mean value is shown by the dashed green lines that represent the +SE (upper dashed line) and –SE (lower dashed line). The graph of the small cell morphology exhibited a more linear growth curve that did not fit as well into a classical growth model. A discernable Lag Phase seems to occur until hour 40, and an Acceleration Phase seems to build until hour 60. The overall plot seems to demonstrate a more linear growth trend as a clear exponential phase, or any peak in cell densities is not readily apparent in the plot. The maximum density of the small cell type occurs at the

termination of the experiment when it surpasses 37000 cells·mL^{-1}. Unlike the plot of the large cell morphology over the same time span, the small cell morphology plot demonstrated only a very small and consistent 95% confidence of the mean. Also notable are the comparative cell densities between the two cell morphologies. The cell densities of the small cell morphology are around an order of magnitude less than that of the large cell morphology throughout much of the experiment. However, the steady growth of the small cell morphology eventually dominates the experiments as the large cell morphology retreats.

4.1.4. Flashing Illumination Under Red Light. Data from the experimental treatment of *D. viridis* with red (660 nm) light flashing at a frequency of 45.6 Hz was processed as described in the Material and Methods §3.14 and tabulated. Table 4.10 presents the data and derived results for the total combined cell counts of the large and small cell morphologies in the samples treated with flashing illumination under red (660 nm) light. Time versus $\bar{n}$ data from Figure 4.10 were plotted on the primary abscissa and ordinate respectively, to create the solid black line plot in the figure. Dashed black line plots in Figure 4.10 denote the 95% confidence interval around the mean created from adding or subtracting the $\bar{n}$ to the product of 1.96 and the SE. Finally, the pH was plotted on the secondary ordinate as a solid orange line in Figure 4.10. Using the same aforementioned procedure, tables and plots were developed for only the large cell morphology and the small cell morphology.

Figure 4.11 represents only data related to the large cell morphology in the treatment with flashing (45.6 Hz) red (660 nm) light and was used to create the linear plot in Figure 4.11. The solid red line plot in Figure 4.11 represents the mean cell density

data for the large cell morphology. Dashed red line plots in Figure 4.11 denote the 95% confidence interval around the mean created from adding or subtracting the $\bar{n}$ to the product of 1.96 and the SE. Finally, the pH was plotted on the secondary ordinate as a solid orange line in Figure 4.11.

Table 4.12 represents only data related to the small cell morphology in the treatment with flashing (45.6 Hz) red (660nm) light. Figure 4.12 was developed from the data presented in Table 4.12. The solid green line plot in Figure 4.12 represents the mean cell density data for the small cell morphology as presented in Table 4.12. Dashed green line plots in Figure 4.12 denote the 95% confidence interval around the mean created from adding or subtracting the $\bar{n}$ to the product of 1.96 and the SE. Finally, the pH was plotted on the secondary ordinate as a solid orange line in Figure 4.12.

Visual interpretation of the plotted data in Figure 4.10 shows that the plot takes on a classical sigmoidal S-curve with distinct phases. However, plots of the respective morphologies that underlie the plot of the sum of cell's cell densities show vastly different growth characteristics. A discernable Lag Phase of nearly 30hrs for the large cell morphology is shown in Figure 4.12. The influence of the large cell morphology on the sum of cell's cell densities continues until attaining a maximum cell density of just over 39000 cells·mL^{-1}. With the exception of a brief pause at hour 80, the large cell morphology continues a nearly exponential decline until hour 140 and a cell density of around 3000 cells·mL^{-1}, until the termination of the experiment. The small cell morphology shows a much steadier, more linear increase in cell density for the duration of the experiment and reaches a higher final cell density (47800 cells·mL^{-1}) than the large morphology.

Table 4.10. Combined cell morphology growth rate data for flashing (45.6 Hz) illuminated cultures grown under red (660 nm) light.

Time (hr)	0.00	15.2	37.3	49.7	60.5	72.6	84.3	97.4	108.2	120.6	132.8	144.2	156.4
$\bar{n}$ (cells·mL^{-1})	1354	3738	8767	37604	48277	41277	44599	38734	41155	31257	34276	43219	47809
SE	38.1	357.3	183.4	2180.9	5301.1	1437.8	3340.0	1925.5	4343.9	716.8	983.4	1188.0	643.9
$\bar{n}$ + (1.96 x SE)	1428	4438	9127	41879	58667	44095	51146	42508	49669	32662	36204	45547	49071
$\bar{n}$ - (1.96 x SE)	1279	3037	8407	33330	37887	38459	38053	34960	32640	29852	32349	40890	46547
pH	7.609	7.92	8.143	8.322	8.376	8.437	8.506	8.512	8.536	8.532	8.611	8.723	8.633
N_2/N_1	2.76	2.35	4.29	1.28	0.86	1.08	0.87	1.06	0.76	1.10	1.26	1.11	
$\ln(N_2/N_1)$	1.02	0.853	1.46	0.250	-0.157	0.0774	-0.141	0.0606	-0.275	0.0922	0.232	0.101	
$\log_2(N_2/N_1)$	1.47	1.23	2.10	0.360	-0.226	0.112	-0.203	0.0874	-0.397	0.133	0.334	0.146	
$\Delta t=(t_2-t_1)$	15.2	22.2	12.4	10.8	12.1	11.7	13.1	10.9	12.4	12.2	11.4	12.2	
r (hr^{-1})	0.0669	0.0385	0.118	0.0232	-0.0130	0.00662	-0.0107	0.00558	-0.0222	0.00758	0.0203	0.00830	
k (doublings per hr)	0.0966	0.0555	0.170	0.0335	-0.0187	0.00955	-0.0155	0.00805	-0.0321	0.0109	0.0294	0.0120	
$\boldsymbol{T_2}$ (hr)	10.4	18.0	5.89	29.9	-53.5	105	-64.6	124	-31.2	91.5	34.1	83.5	

Mean ***r*** from interval analysis	0.0744
Standard Deviation	0.0508
Standard Error	0.02930
Skewness	0.805

Mean ***k*** from interval analysis	0.107
Standard Deviation	0.0579
Standard Error	0.0335
Skewness	0.805

Mean $\boldsymbol{T_2}$ from interval analysis	17.9
Standard Deviation	12.0
Standard Error	6.92
Skewness	-0.0380

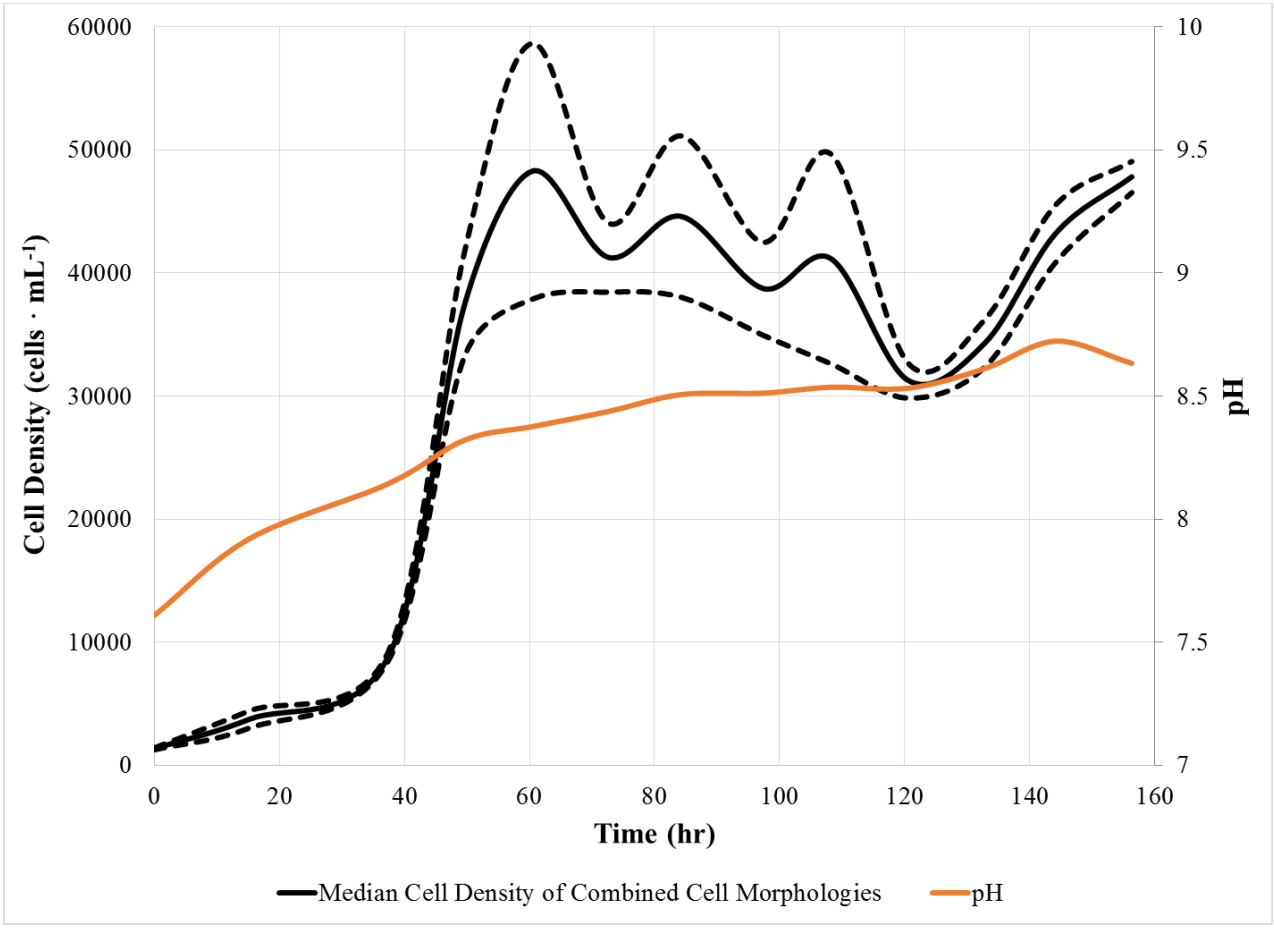

Figure 4.10. Plot time versus of the mean of the combined large and small cell morphologies' cell densities for flashing illumination (45.6 Hz) under red (660 nm) light experiments. Included on the secondary ordinate is the pH taken over the same time period. Dashed lines represent the boundary of the 95% confidence interval around the mean cell densities.

Table 4.11. Large cell morphology growth rate data for flashing (45.6 Hz) illuminated cultures grown under red (660 nm) light.

Time (hr)	0.0	15.2	37.3	49.7	60.5	72.6	84.3	97.4	108.2	120.6	132.8	144.2	156.4
$\bar{n}$ (cells·mL^{-1})	355	2314	6139	31944	39385	29679	28890	19068	10767	4961	2766	3316	2045
SE	54.5	274.3	230.0	1967.9	1114.0	1520.6	2971.4	2102.0	3885.7	325.4	363.1	152.4	143.2
$\bar{n}$ + (1.96 x SE)	462	2851	6589	35802	41568	32659	34714	23187	18383	5599	3477	3615	2325
$\bar{n}$ - (1.96 x SE)	248	1776	5688	28087	37202	26698	23066	14948	3151	4323	2054	3017	1764
pH	7.609	7.92	8.143	8.322	8.376	8.437	8.506	8.512	8.536	8.532	8.611	8.723	8.633
N_2/N_1	6.52	2.65	5.20	1.23	0.75	0.97	0.66	0.56	0.46	0.56	1.20	0.62	
$\ln(N_2/N_1)$	1.88	0.976	1.65	0.209	-0.283	-0.027	-0.416	-0.572	-0.775	-0.584	0.181	-0.484	
$\log_2(N_2/N_1)$	2.71	1.41	2.38	0.302	-0.408	-0.0388	-0.599	-0.825	-1.12	-0.843	0.262	-0.698	
$\Delta t=(t_2-t_1)$	15.2	22.2	12.4	10.8	12.1	11.7	13.1	10.9	12.4	12.2	11.4	12.2	
$\boldsymbol{r}$ (hr^{-1})	0.124	0.0440	0.133	0.0195	-0.0234	-0.00230	-0.0316	-0.0526	-0.0626	-0.0480	0.0159	-0.0397	
$\boldsymbol{k}$ (doublings per hr)	0.178	0.0635	0.192	0.0281	-0.0338	-0.00332	-0.0456	-0.0760	-0.0903	-0.0692	0.0230	-0.0573	
$\boldsymbol{T_2}$ (hr)	5.61	15.75	5.20	35.6	-29.6	-301	-21.9	-13.2	-11.1	-14.4	43.5	-17.4	

Mean $\boldsymbol{r}$ from interval analysis	0.0594
Standard Deviation	0.0676
Standard Error	0.0390
Skewness	0.05

Mean $\boldsymbol{k}$ from interval analysis	0.0857
Standard Deviation	0.0975
Standard Error	0.0563
Skewness	0.05

Mean $\boldsymbol{T_2}$ from interval analysis	6.51
Standard Deviation	23.7
Standard Error	13.66
Skewness	-0.682

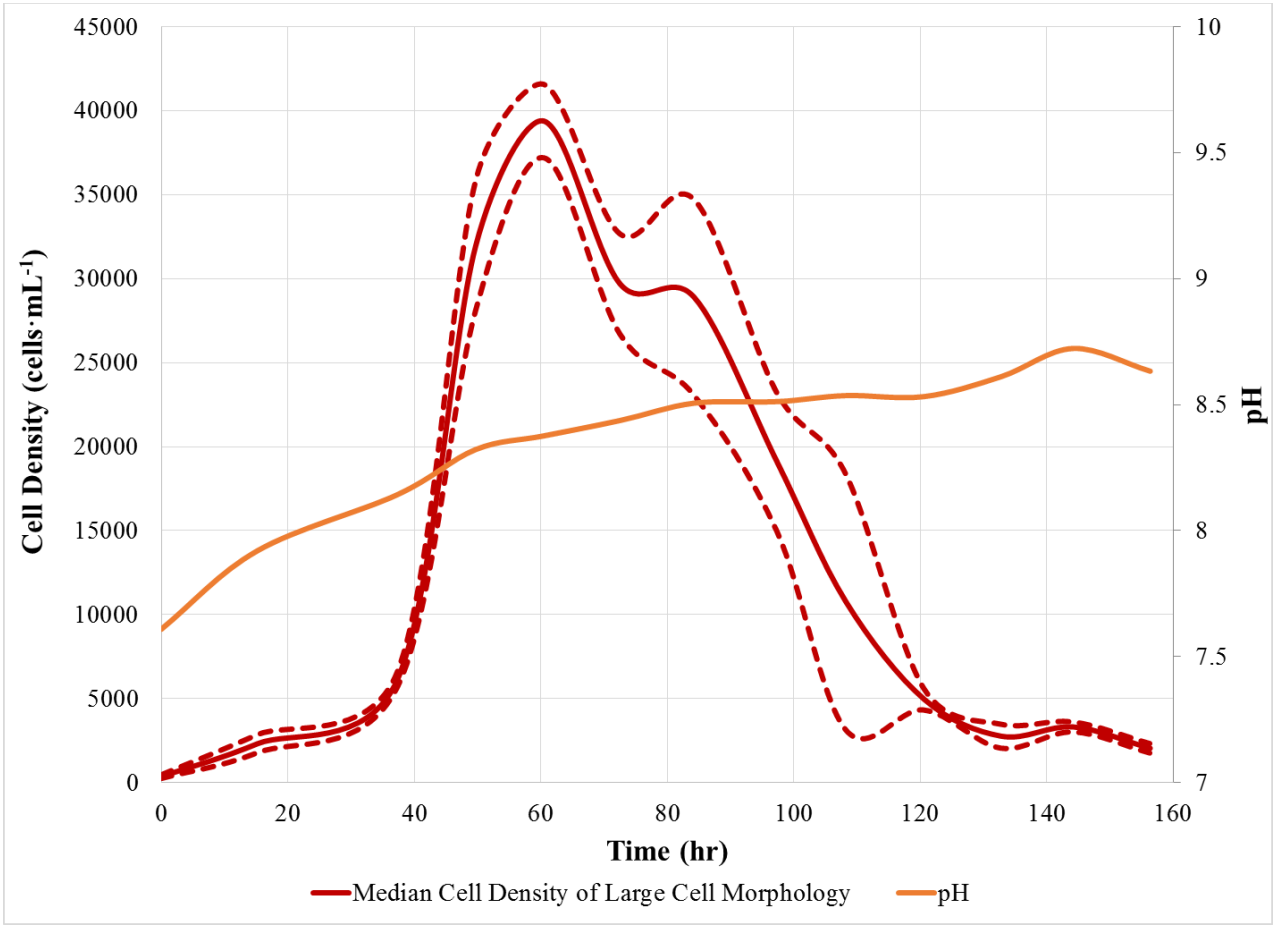

Figure 4.11. Plot of time versus only the large cell morphology's median cell densities for flashing (45.6 Hz) illumination under red (660 nm) light experiments. Included on the secondary ordinate is the pH taken over the same time period. Dashed lines represent the boundary of the 95% confidence interval around the mean cell densities.

Table 4.12. Small cell morphology growth rate data for flashing (45.6 Hz) illuminated cultures grown under red (660 nm) light.

Time (hr)	0.0	15.2	37.3	49.7	60.5	72.6	84.3	97.4	108.2	120.6	132.8	144.2	156.4
$\bar{n}$ (cells·mL^{-1})	999	1424	2628	5660	8892	11598	15709	19667	30388	26296	31511	39903	45764
SE	58.7	98.0	51.6	236.8	204.3	85.4	411.3	334.2	869.9	393.0	656.2	1036.4	685.2
$\bar{n}$ + (1.96 x SE)	1114	1616	2730	6124	9293	11766	16515	20322	32093	27067	32797	41934	47107.2
$\bar{n}$ - (1.96 x SE)	884	1232	2527	5196	8492	11431	14903	19012	28683	25526	30225	37872	44421.3
pH	7.609	7.92	8.143	8.322	8.376	8.437	8.506	8.512	8.536	8.532	8.611	8.723	8.633
N_2/N_1	1.43	1.85	2.15	1.57	1.30	1.35	1.25	1.55	0.87	1.20	1.27	1.15	
$\ln(N_2/N_1)$	0.355	0.613	0.767	0.452	0.266	0.303	0.225	0.435	-0.145	0.181	0.236	0.137	
$\log_2(N_2/N_1)$	0.511	0.884	1.107	0.652	0.383	0.438	0.324	0.628	-0.209	0.261	0.341	0.198	
$\Delta t=(t_2-t_1)$	15.2	22.2	12.4	10.8	12.1	11.7	13.1	10.9	12.4	12.2	11.4	12.2	
$\boldsymbol{r}$ (hr^{-1})	0.0234	0.0276	0.0620	0.0420	0.0220	0.0259	0.0171	0.0401	-0.0117	0.0149	0.0207	0.0113	
$\boldsymbol{k}$ (doublings per hr)	0.0337	0.0399	0.0895	0.0606	0.0317	0.0374	0.0247	0.0578	-0.0169	0.0214	0.0299	0.0163	
$\boldsymbol{T_2}$ (hr)	29.7	25.1	11.2	16.5	31.5	26.7	40.5	17.3	-59.3	46.6	33.4	61.5	

Mean $\boldsymbol{r}$ from interval analysis	0.0226
Standard Deviation	0.0195
Standard Error	0.0112
Skewness	-1.120

Mean $\boldsymbol{k}$ from interval analysis	0.0326
Standard Deviation	0.0281
Standard Error	0.0162
Skewness	-1.120

Mean $\boldsymbol{T_2}$ from interval analysis	12.2
Standard Deviation	36.2
Standard Error	20.89
Skewness	-2.108

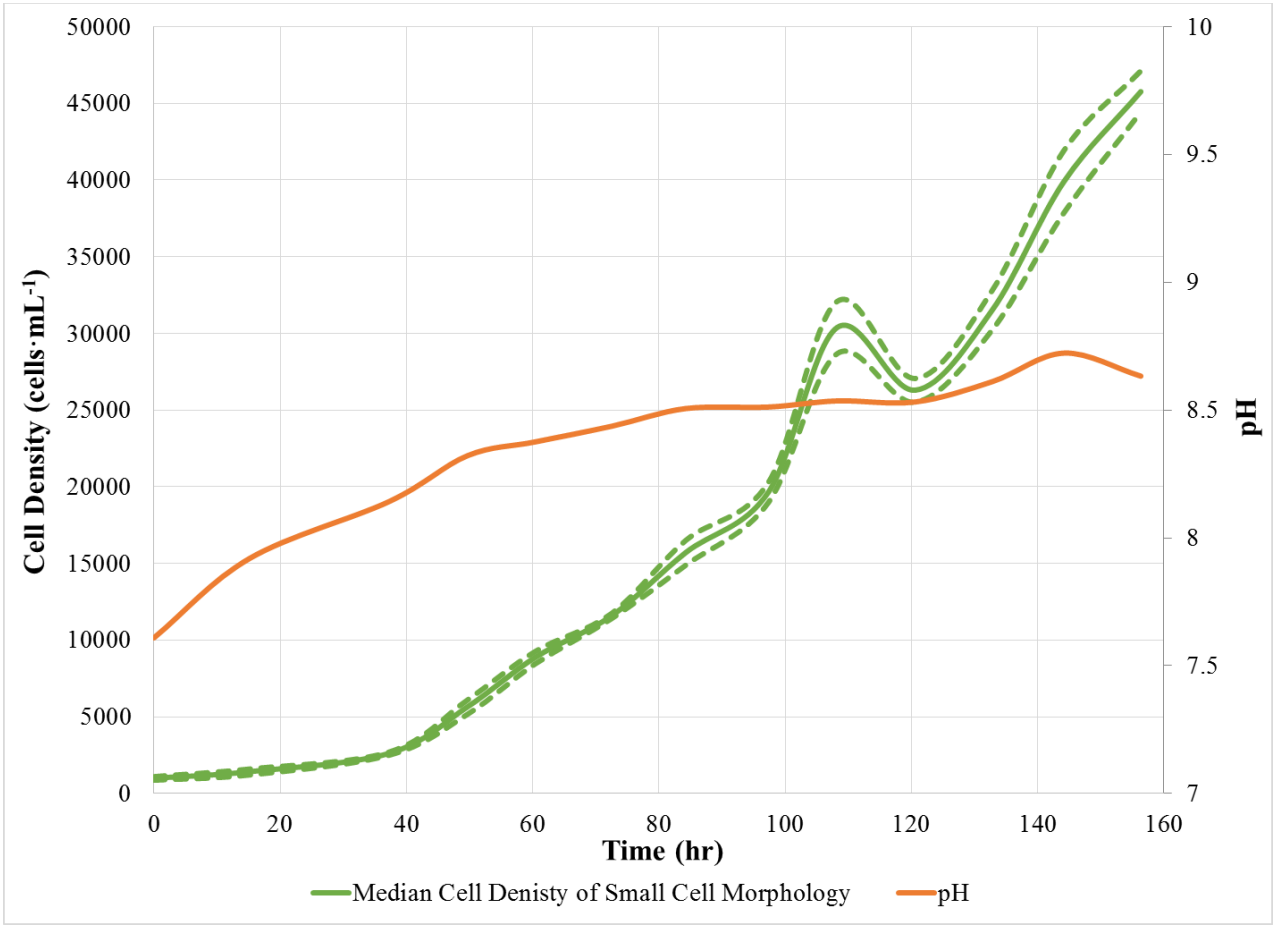

Figure 4.12. Plot of time versus only the small cell morphology's median cell densities for flashing (45.6 Hz) illumination under red (660 nm) light experiments. Included on the secondary ordinate is the pH taken over the same time period. Dashed lines represent the boundary of the 95% confidence interval around the mean cell densities.

The overall growth curve shape is a reasonable approximation of a classical sigmoidal growth curve in Figure 4.12. The many phases of the growth curve can be assigned to the graph. A Lag Phase had a duration of roughly 24 hours before beginning the Positive Acceleration Phase up to hour 40. From hour 40 to roughly hour 60, the population experienced exponential growth. The population then peaked with a cell density of around 48000 cells·mL^{-1}. The peak slightly overshot the steady-state which resulted in a fairly consistent cell density of between 45000 and 38000 cells·mL^{-1} from hour 70 to hour 105. The population then started to decline until regaining positive acceleration until the termination of the experiment. With the addition of the SE information, the graph demonstrates a significant widening of the confidence interval once it reaches the peak cell density then progresses into a steady-state. The 95% confidence interval then contracts significantly around hour 120 and is fairly consistent about the mean until the termination of the experiment.

Figure 4.11 is the linear plot of the mean the cell densities (cells·mL^{-1}) versus time (hr) of the following: Data for the large cell morphology is designated by the red line. A 95% confidence of the mean value is shown by the dashed red lines that represent the +SE (upper dashed line) and –SE (lower dashed line). The graph demonstrates a clear Lag Phase of about 24 hrs then completes the Positive Acceleration Phase by about hour 35. The population proceeds through the Exponential Growth Phase until reaching the peak cell density with a cell density of roughly 39000 cells·mL^{-1}. The overlay of SE information also shows a slight widening of the confidence interval as the cell densities approach the peak cell density. As the plot of cell densities decline, the confidence intervals widen further until about hour 70. The width of the 95% confidence interval

remains relatively constant until around hour 125 when the decline in the population stops. The 95% confidence interval contracts significantly at the same point as the population maintains a mean cell density of around 2000 and 3300 cells·mL^{-1},until the experiment is terminated.

Figure 4.12 is the linear plot of the mean cell densities (cells·mL^{-1}) versus time (hr) of the following: Data for the small cell morphology is designated by the solid green line. A 95% confidence of the mean value is shown by the dashed green lines that represent the +SE (upper dashed line) and –SE (lower dashed line). The graph of the small cell morphology exhibited a continual linear growth profile throughout the duration of the experiment. A barely perceivable Lag Phase could be parsed from the plot until around hour 40. From hour 40 until the end of the experiment, the growth of the small cell morphology maintained a very steady, nearly linear progression. One minor feature to the graph was a brief spike in the cell density counts around hour 110. The area bounded by the graphs of the positive and negative SE did not substantially change, or show extraordinary large spikes in the 95% confidence interval during the experiment. The 95% confidence interval did go from being nearly imperceptible, until around hour 110 when it began to gradually widen in rough proportion to the increase in the cell density until the experiment was concluded.

4.2. DERIVING THE INTRINSIC GROWTH RATE

Employing the modified method presented previously in 3.15, data was selected from each treatment as representative of the exponential phase of growth for each of the factorial experiments conducted in the capstone project. The selected data resulting from the analysis outlined in § 3.15 can be discerned in the Tables 4.1 – 4.12 as they have been

surrounded by a colored box that relates to the wavelength of light used in the experiment. Basic descriptive statistics for *r*, *k*, and t_2 where further carried out for the selected data points in each of the tables.

4.2.1. Intrinsic Growth Rate for Constant Illumination Under Blue Light. Determination of the intrinsic growth rate from the experiments conducted under constant illumination under blue (450 nm) light was conducted by graphing the cell time on the abscissa while using a logarithmic ordinate of the cell densities from the data points in Table 4.2 and Table 4.3 determined to best represent the exponential growth phase of the large cell morphology and the small cell morphology, respectively. The plot of the selected data found within the data set of the constant illumination under blue (450nm) light experiment, was fit to exponential trendlines for each of the cell morphologies. Figure 4.13 is a composite of the large and small cell morphologies' exponential growth phase plots, respectively. Additional exponential trendlines have been fit to each of the plots of the large and small cell morphologies to derive the growth rate from the exponential equation that is also included in Figure 4.13.

The data plotted for the large cell morphology (blue line) in Figure 4.13 was derived from a set of three consecutive points, from hour 60.3 to hour 84.2. The set of cell density data from that time period yielded the highest R^2 value of 0.9971, of any set of three data points tested against the curve. The resulting r value taken from the equation for the exponential trendline was 0.0933 hr^{-1}.

The data plotted for the small cell morphology (green line) in Figure 4.13 was found from a set of five consecutive points, from hour 49.5 to hour 96.1. The set of cell

density data from the time period yielded the highest R^2 value of 0.9019. The resulting r value taken from the derived equation for the exponential trendline was 0.0213 hr^{-1}.

The data that was calculated, but does not appear in Figure 4.13, was for the sum of the total cells. The exponential trendline was fit to a set of three consecutive points from hour 60.4 to hour 84.2. The set of cell density data from the time period yielded the highest R^2 value of 0.9975, and the resulting r value taken from the equation for the exponential trendline was 0.0728 hr^{-1}.

4.2.2. Intrinsic Growth Rate for Flashing Illumination Under Blue Light. Determination of the intrinsic growth rate from the experiments conducted under flashing (45.6 Hz) illumination under blue (450 nm) light was conducted by graphing the cell time on the abscissa while using a logarithmic ordinate of the cell densities from the data points in Table 4.5 and Table 4.6 determined to best represent the exponential growth phase of the large cell morphology and the small cell morphology, respectively. The plot of the selected data found within the data set of the flashing (45.6Hz) illumination under blue (450nm) light experiment, was fit to exponential trendlines for each of the cell morphologies. Figure 4.14 is a composite of the large and small cell morphologies exponential growth phase plots, respectively. Additional exponential trend lines have been fit to each of the plots of the large and small cell morphologies to derive the growth rate from the exponential equation that is also included in Figure 4.14.

The data plotted in Figure 4.14 for the large cell morphology (blue line) was found from a set of three consecutive data points from hour 15.1 to hour 49.6. The set of cell density data from that time period yielded the highest R^2 value of 0.9952 of any set of three data points tested against the curve.

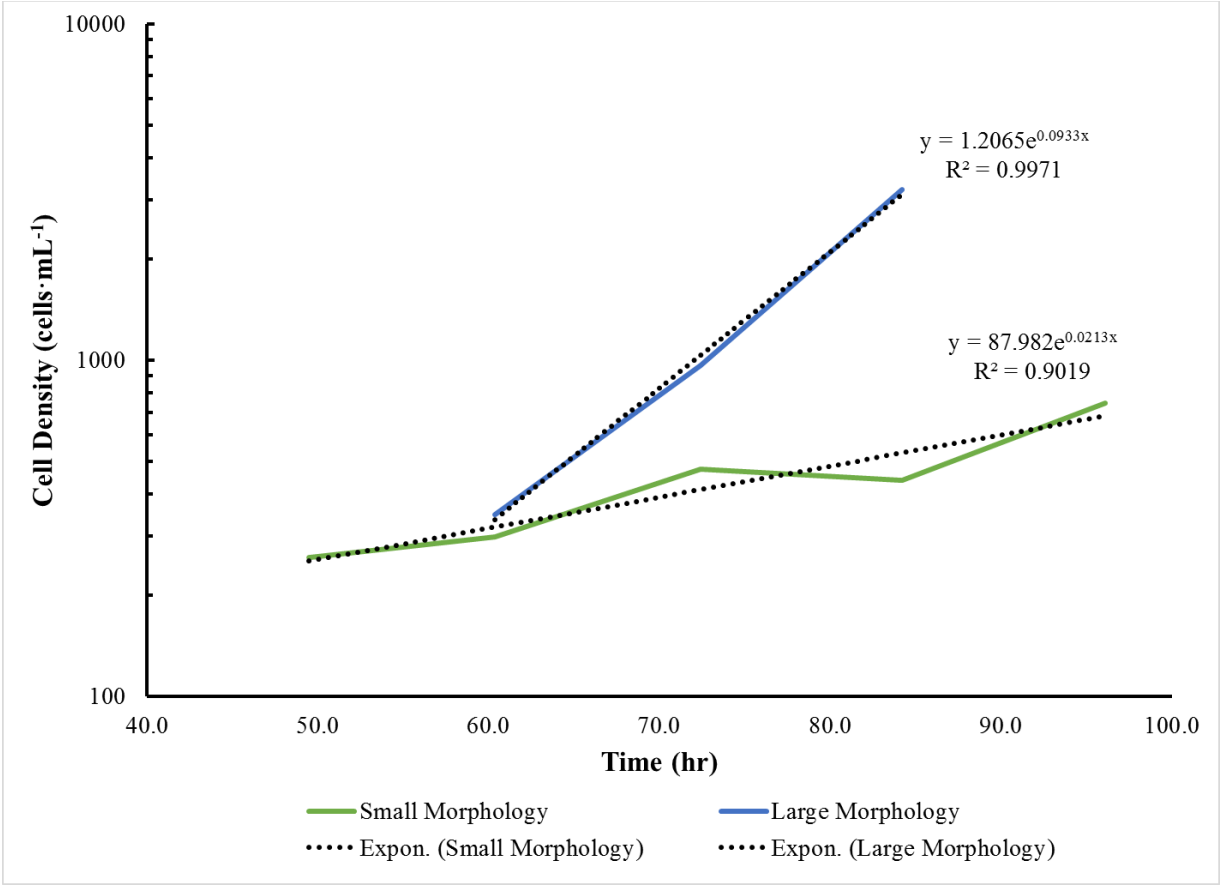

Figure 4.13. Plot of data points best representing exponential growth for the two cell morphologies in constant illumination under blue (450 nm) light experiments. The solid green line represents the small cell morphology's exponential growth phase and the solid blue line represents the large cell morphology's exponential growth phase. Dashed black lines represent the fitted exponential trendline for each exponential growth phase. Equations for the fitted trendlines have also been presented in the figure.

The resulting *r*-value taken from the equation for the exponential trendline was 0.0425 hr^{-1}.

The data plotted for the small cell morphology (green line) in Figure 4.14 was derived from a set of three consecutive data points from hour 60.4 to hour 80.3. The set of cell density data from the time period yielded the highest R^2 value of 0.9995. The resulting r value that was taken from the derived equation for the exponential trendline was 0.0066 hr^{-1}.

The data that was calculated, but does not appear in Figure 4.14, was for the sum of the total cells. The exponential trendline was fit to a set of three consecutive data points from hour 37.3 to hour 60.4. The set of cell density data from the time period yielded the highest R^2 value of 0.9936, and the resulting r value taken from the equation for the exponential trendline was 0.0726 hr^{-1}.

4.2.3. Intrinsic Growth Rate for Constant Illumination Under Red Light. Determination of the intrinsic growth rate from the experiments conducted under constant illumination under red (660 nm) light was conducted by graphing the cell time on the abscissa while using a logarithmic ordinate of the cell densities from the data points in Table 4.8 and Table 4.9 determined to best represent the exponential growth phase of the large cell morphology and the small cell morphology, respectively. The plot of the selected data found within the data set of the constant illumination under red (660 nm) light experiment, was fit to exponential trendlines for each of the cell morphologies. Figure 4.15 is a composite of the large and small cell morphologies exponential growth phase plots, respectively. Additional exponential trendlines have been fit to each of the

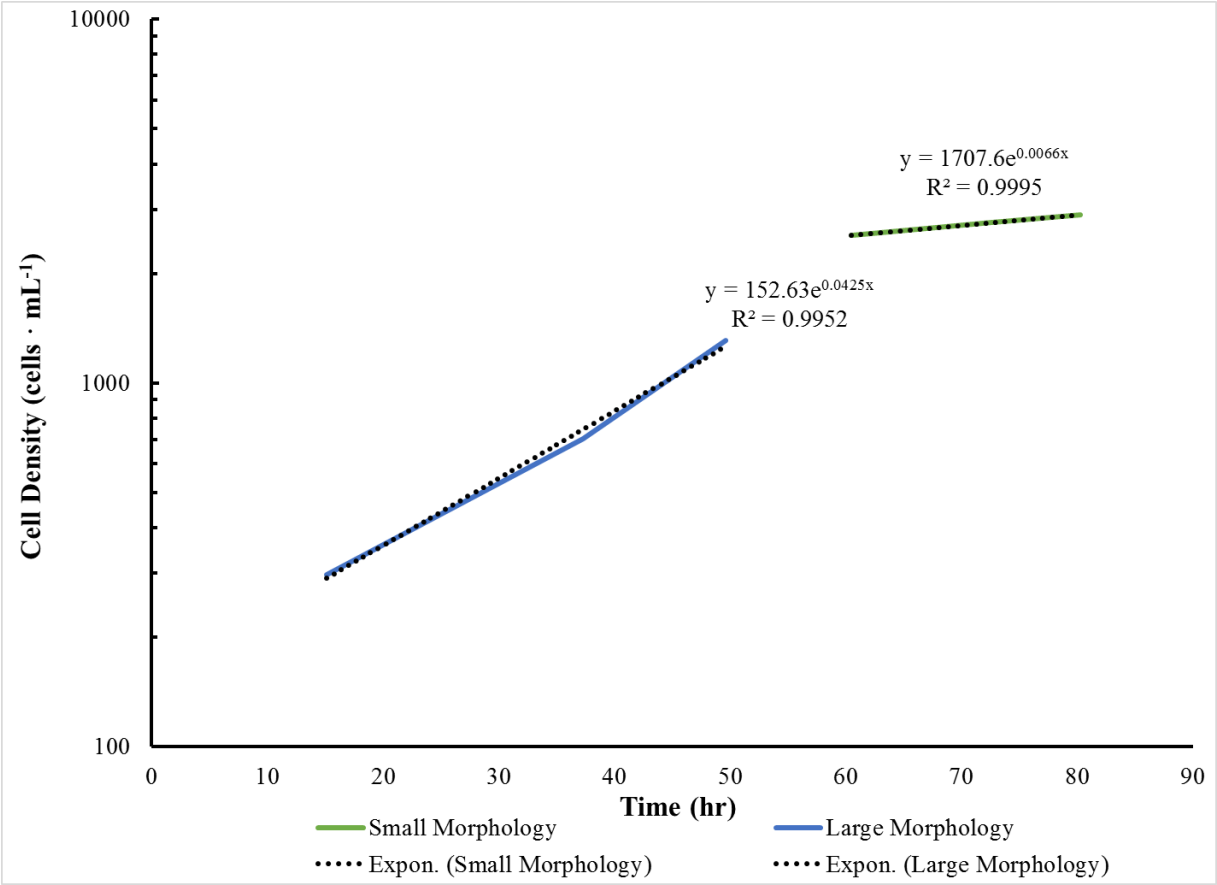

Figure 4.14. Plot of data points best representing exponential growth for the two cell morphologies in flashing (45.6 Hz) illumination under blue (450 nm) light experiments. The solid green line represents the small cell morphology's exponential growth phase and the solid blue line represents the large cell morphology's exponential growth phase. Dashed black lines represent the fitted exponential trendline for each exponential growth phase. Equations for the fitted trendlines have also been presented in the figure.

plots of the large and small cell morphologies to derive the growth rate from the exponential equation that is also included in Figure 4.15.

The data plotted in Figure 4.15 for the large cell morphology (red line) was derived from a set of three consecutive data points from hour 15.2 to hour 49.7. The set of cell density data from that time period yielded the highest R^2 value of 0.9981, of any set of three data points tested against the curve. The resulting *r* value taken from the equation for the exponential trendline was 0.0639 hr^{-1}.

The data plotted for the small cell morphology (green line) in Figure 4.15 was derived from a set of five consecutive data points from hour 0 to hour 49.7. The set of cell density data from the time period yielded the highest R^2 value of 0.9766. The resulting r value taken from the derived equation for the exponential trendline was 0.0367 hr^{-1}.

The data that was calculated, but does not appear in Figure 4.15, was for the sum of the total cells. The exponential trendline was fit to a set of three consecutive data points from hour 0 to hour 49.7. The set of cell density data from the time period yielded the highest R^2 value of 0.9878, and the resulting r value taken from the equation for the exponential trendline was 0.649 hr^{-1}.

4.2.4. Intrinsic Growth Rate for Flashing Illumination Under Red Light. Determination of the intrinsic growth rate from the experiments conducted under flashing (45.6 Hz) illumination under red (660 nm) light was conducted by graphing the cell time on the abscissa while using a logarithmic ordinate of the cell densities from the data points in Table 4.11 and Table 4.12 determined to best represent the exponential growth phase of the large cell morphology and the small cell morphology, respectively.

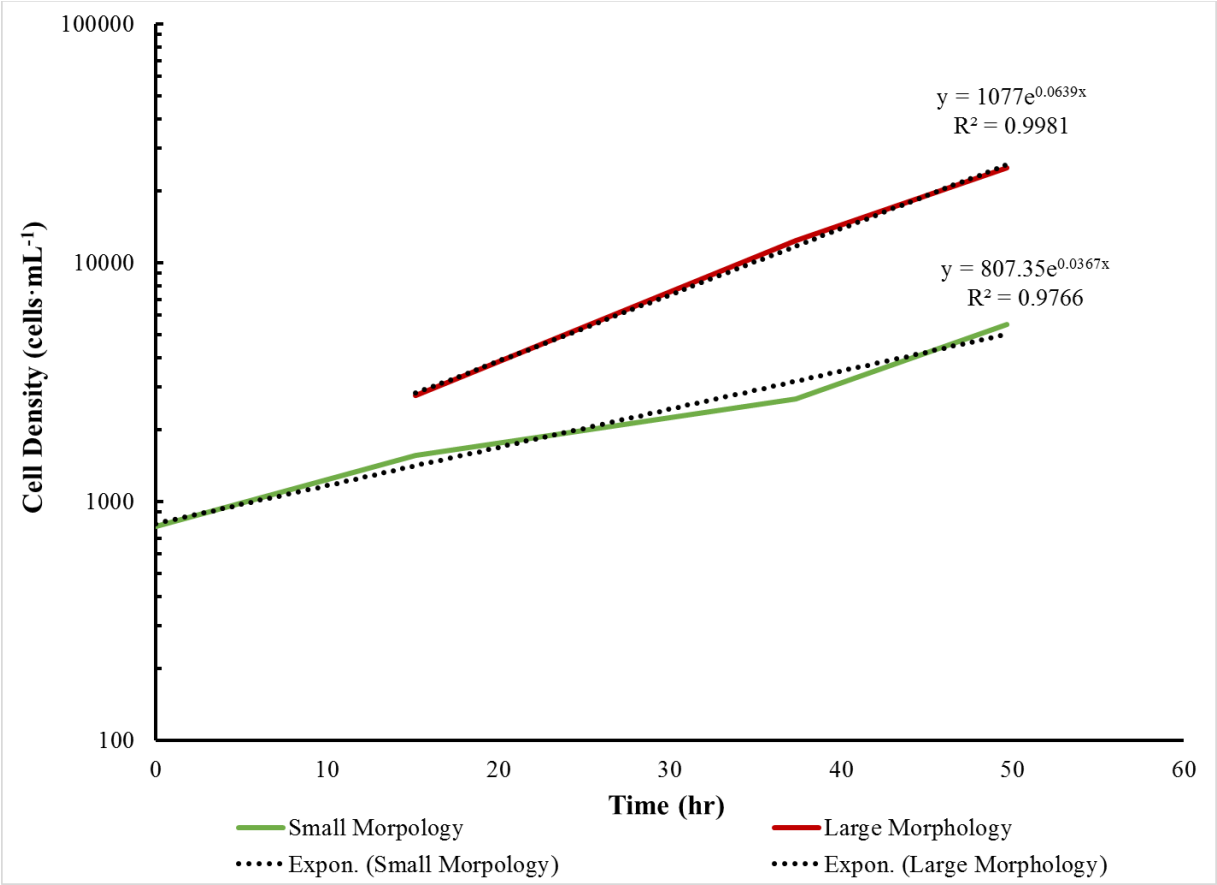

Figure 4.15. Plot of data points best representing exponential growth for the two cell morphologies in constant illumination under red (660 nm) light experiments. The solid green line represents the small cell morphology's exponential growth phase and the solid red line represents the large cell morphology's exponential growth phase. Dashed black lines represent the fitted exponential trendline for each exponential growth phase. Equations for the fitted trendlines have also been presented in the figure.

The plot of the selected data found within the data set of the flashing (45.6Hz) illumination under red (660nm) light experiment, was fit to exponential trendlines for each of the cell morphologies. Figure 4.16 is a composite of the large and small cell morphologies exponential growth phase plots, respectively. Additional exponential trendlines have been fit to each of the plots of the large and small cell morphology's to derive the growth rate from the exponential equation that is also included in Figure 4.16.

The data plotted in Figure 4.16 for the large cell morphology (red line) was derived from a set of three consecutive data points from hour 0 to hour 60.5. The set of cell density data from that time period yielded the highest R^2 value of 0.9633, of any set of three data points tested against the curve. The resulting r value taken from the equation for the exponential trendline was 0.0773 hr^{-1}.

The data plotted for the small cell morphology (green line) in Figure 4.16 was derived from a set of five consecutive data points from hour 49.5 to hour 108.2. The set of cell density data from the time period yielded the highest R^2 value of 0.9845. The resulting r value taken from the derived equation for the exponential trendline was 0.0266 hr^{-1}.

The data that was calculated, but does not appear in Figure 4.16, was for the sum of the total cells. The exponential trendline were fit to a set of three consecutive data points from hour 0 to hour 37.3. The set of cell density data from the time period yielded the highest R^2 value of 0.9752, and the resulting *r*-value taken from the equation for the exponential trend line was 0.0492 hr^{-1}.

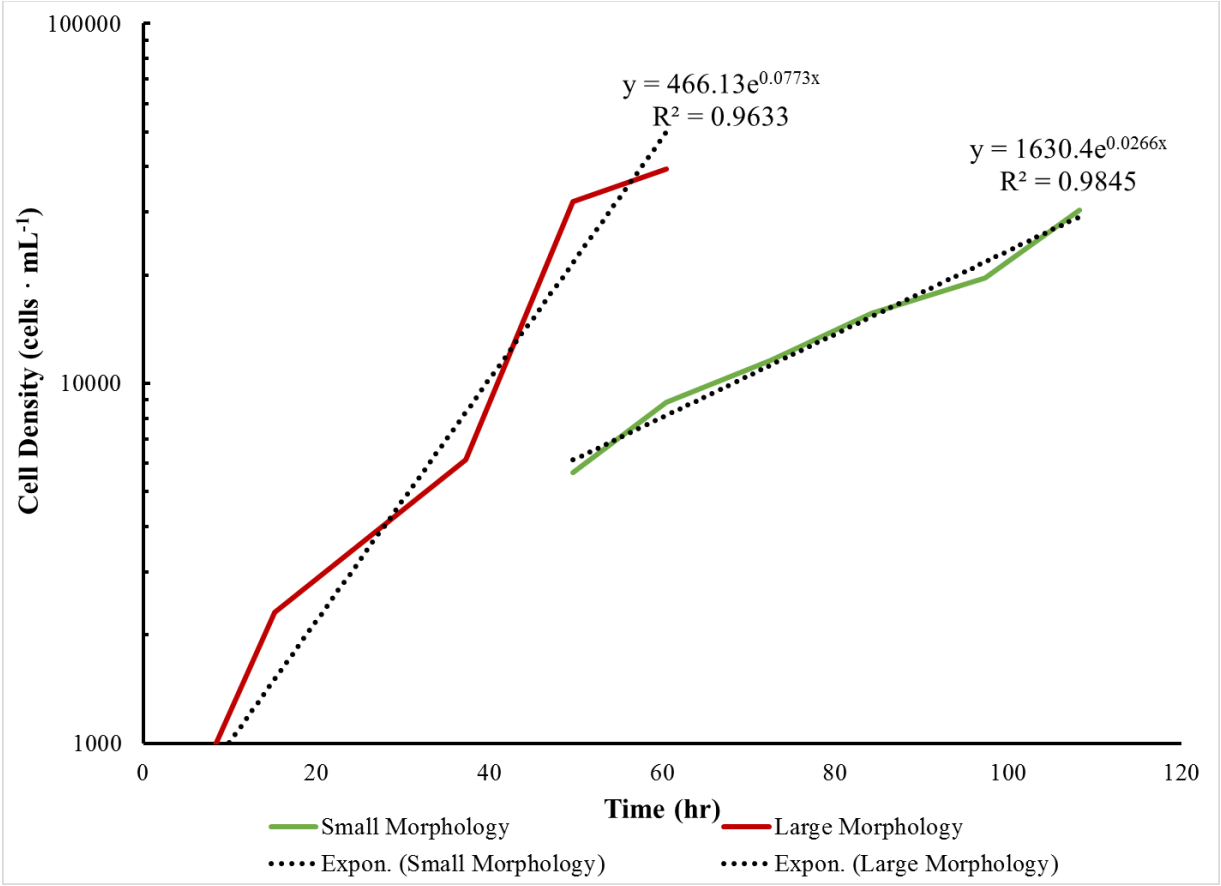

Figure 4.16. Plot of data points best representing exponential growth for the two cell morphologies in flashing (45.6 Hz) illumination under red (660 nm) light experiments. The solid green line represents the small cell morphology's exponential growth phase and the solid red line represents the large cell morphology's exponential growth phase. Dashed black lines represent the fitted exponential trendline for each exponential growth phase. Equations for the fitted trendlines have also been presented in the figure.

4.3. SUMMARY OF RESULTS

The results from the calculations and curve fitting exercises were organized into tables following the original experimental design previously presented in Table 1.2. The first summary table of data is presented in Table 4.13 where the data for the r values calculated from the sum total of the cell densities gives the overall results for the experiments. Table 4.14 presents the results for the large cell morphology in each of the four experiments. Table 4.15 presents the results for the r values for the small cell morphology in each of the experiments.

Table 4.13. Results summary for total cell density in experiments.

	Illumination Type	
Wavelength of Illumination	Constant Illumination	Flashing Illumination (45.6 Hz)
Blue peak emission wavelength (λ) ≈ 450nm	$r = 0.0727\ hr^{-1}$ $R^2 = 0.9975$	$r = 0.0726\ hr^{-1}$ $R^2 = 0.9937$
Red peak emission wavelength (λ) ≈ 660nm	$r = 0.0649\ hr^{-1}$ $R^2 = 0.9878$	$r = 0.0492\ hr^{-1}$ $R^2 = 0.9752$

Table 4.14. Results summary for the large cell morphology's cell densities in the respective experiments.

	Illumination Type	
Wavelength of Illumination	Constant Illumination	Flashing Illumination (45.6 Hz)
Blue peak emission wavelength (λ) ≈ 450nm	$r = 0.0933\ hr^{-1}$ $R^2 = 0.9971$	$r = 0.0425\ hr^{-1}$ $R^2 = 0.9952$
Red peak emission wavelength (λ) ≈ 660nm	$r = 0.0639\ hr^{-1}$ $R^2 = 0.9981$	$r = 0.0773\ hr^{-1}$ $R^2 = 0.9633$

Table 4.15. Results summary for the small cell morphology's cell densities in the respective experiments.

	Illumination Type	
Wavelength of Illumination	Constant Illumination	Flashing Illumination (45.6 Hz)
Blue peak emission wavelength (λ) ≈ 450nm	r = 0.0213 hr $^{-1}$ R^2= 0.9019	r = 0.0066 hr $^{-1}$ R^2= 0.9995
Red peak emission wavelength (λ) ≈ 660nm	r = 0.0367 hr $^{-1}$ R^2= 0.9766	r = 0.0266hr $^{-1}$ R^2= 0.9845

5. DISCUSSION

5.1 INTRODUCTION

The overall goal of this project was to launch a multidisciplinary study into the efficacy of combining algal biotechnology for the benefit of the mining industry, both economically and environmentally. Specifically, is it feasible to use abandoned/vacant/ unused mining properties to build a successful commercial-industrial culture of algae? As noted in the beginning of this paper, the issues to be solved are:

(a) Negative impacts due to variation in ambient light

(b) Negative impacts due to variation in ambient temperature

(c) Negative impacts due to a lack of biosecurity

(d) Competition for water resources with agriculture and municipalities

(e) Exorbitant infrastructure and manpower costs

These factors have limited the commercial-industrial culture of algae, except in niche markets. To make a final judgment on the efficacy of the proposed model each of these issues must be studied. The research for this dissertation was limited to a study of the use of artificial light to alleviate the first negative impact, the variation in ambient light. For the proposed model to work, artificial light must be able to replace ambient light. As part of the ongoing study, the bench work for this project concentrated on studying the effects of artificial illumination on the growth rate of the algae, *D. viridis.* Four properties of artificial illumination were studied and evaluated for their effect on the growth rate of algae, constant versus flashing light, and red versus blue wavelengths.

The first analytical discussion in this section will involve a close examination of the non-uniform data distribution. Second, reported growth rates and maximum cell

densities values for *D. viridis* are presented. Third, statistical differences in the growth rates for the different groups of treatments in the experiments will be analyzed. Fourth, an interpretation of observed growth behaviors is presented. A summary discussion will address a fundamental finding that will begin to move the research frontier in basic phycology as the experiments gave a glimpse of a truly novel discovery in the behavior of *D. viridis*.

5.2 NON-UNIFORM DATA DISTRIBUTION CONSIDERATIONS

Issues relating to the uniform distribution of the cells in the bioreactors may have played a role in the observed deviations of plots from a true S-shaped sigmoidal growth curve shown in Figure 3.36. Furthermore, some or all of the issues may have contributed to the observed fluctuation in the 95% confidence interval of the mean values of cell densities for the experiments. The main sources for irregularities and error in the recorded experimental data were identified as the sampling location within the bioreactor, the formation of biofilms, and the production of extracellular polysaccharides.

5.2.1 Sampling of Experimental Cultures. The method of sampling from the bioreactors should have favored the smaller, flagellated cell morphology. Therefore, the sampling should have been skewed to capture the motile, small cell morphology as they could stay in solution better under experimental conditions, than the large cell morphology. The bioreactors were designed to draw samples from the mid-depth of the volume. The experimental setup lacked sufficient agitation equipment, such as a shaker or magnetic stirring apparatus to prevent settling of the cells.

5.2.2 Exopolysaccharides and Extracellular Mucilage. While the presence of specific mucilage, or exopolysaccharides, was not able to be detected, it was anticipated,

based on the literature review, that there may have been some of these compounds present [253, 318, 319]. The wide standard error distribution in the cell densities of all of the experiments was noted specifically around the maximum cell densities. The research literature explained that the large cell morphology excretes a thick, extracellular layer of mucilage [22]. Direct microscopic analysis of samples confirmed the presence of such a layer in the large cell morphology in Figure 5.1.

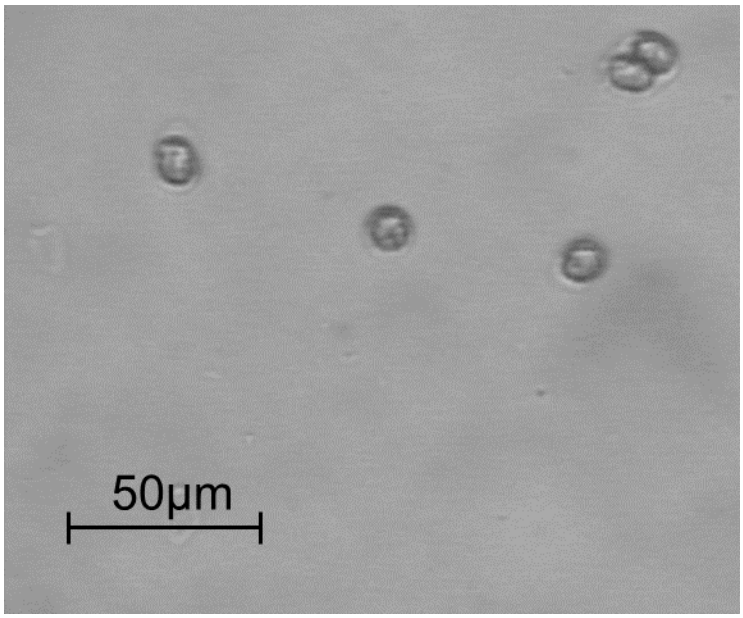

Figure 5.1. Micrograph of large cell morphology with faint outline of extra cellular mucilage surrounding cell (400x magnification).

Another observation presented in the literature noted that experimental samples that used vigorous aeration would exhibit “frothing” and *D. viridis* cells would clump together and fall out of solution [320]. The frothing was most likely the result of extracellular

compounds causing this effect. Such compounds secreted by the algae under study may have had the following effects on samples:

(a) The smaller, motile cell morphologies could have adhered to the mucilage of the larger cell morphology, which removed them from the solution. The result in the data would have been large standard errors in the cell counts of the smaller cell morphology, as the larger cell morphology would begin to peak. The standard errors would become smaller as the larger cell morphology would retreat.

(b) The larger cell morphologies would be more likely to stick to one another and settle out of solution. However, they would likely keep dividing in the biofilm in the bottom of the bioreactor. Thus, the growth rates and cell densities may have been greater than reported in the experimental work.

5.3. REPORTED LITERATURE VALUES FOR *D. VIRIDIS*

An upper bound for the r value in laboratory growth assays for *Dunaliella sp*. under ideal conditions was reported as 0.116 hr^{-1} (T_2 = 6 hours) [265]. Studies specific to *D. viridis* have a wide range of reported r values under ideal conditions in different experimental treatments. The information from ten different published research studies has been tabulated and is presented in Table 5.1. The table lists the following data (if available):

(a) Maximum Cell Density (10^6 cells·mL^{-1})

(b) Maximum Growth Rate (hr^{-1})

(c) Duration of the experiments

(d) Enumeration Methods

The oldest study reported in Table 5.1 provides information about *D. viridis* that was very similar to the results obtained in the bench work.

Table 5.1. Reported values for maximum cell density and growth rates.

Maximum Cell Density (10^6cells·mL^{-1})	**Maximum growth rate (hr^{-1})**	**Length of Experiment**	**Enumeration Method**	**Ref.**
2.75	n/a	96 hrs	n/a	[259]
4.04	0.179	17 days	Oxygen Evolution	[321]
n/a	0.0333	4 days	Coulter Counter	[322]
18	0.05	4 days	Coulter Counter	[263]
20	n/a	7 days	Coulter Counter	[323]
2.29	0.0071	7 days	Haemocytometer	[302]
6	n/a	20 days	Turbidity	[324]
8.56	0.030	n/a	Haemocytometer	[325]
5.5	0.035	200 hrs	Coulter Counter	[320]
0.036	n/a	16 days	Microscope	[326]

The maximum cell densities recorded in the Gibor paper [326] give values for maximum cell densities that range from 1200 to 36000 cells·mL^{-1}. These reported cell densities were consistent with the results obtained in the experimental work reported in this document. While the results reported in the literature were consistent with results of the bench work experiments, both were very different from the other nine studies. The other nine studies reported cell densities that were at least 1000x larger.

Other interesting conclusions from the references in Table 5.1 include the following:

(a) *D. viridis* growth rates depend on the photobioreactor design [324].

(b) *D.viridis* growth rates found in laboratory work were very low compared to those found in outdoor raceways [302].

5.4. STATISTICAL ANALYSIS OF GROWTH RATE DATA

The statistical analysis intended to accompany the original 2x2 factorial experimental design was a two-way analysis of variance (ANOVA) using the categories of wavelength of light (660nm "Red" or 450nm "Blue") and type of illumination (Constant or Flashing) to compare against the *r* values derived from the exponential trendline analysis previously described in Section 4. ANOVA analysis was found to be a standard method of analysis in the relevant research literature for experiments where growth rates were examined in relation to lighting regimes, as well as other treatments that examined nutrients, salinity, and cultivation time. [259, 300, 321, 325, 327, 328]. The discovery that the "contamination" in the experiments was most likely a different cell morphology of the same microorganism, given that the true identity of the algae was likely *D. viridis* and not *D. parva*, provided for an additional category for statistical analysis. As a result, a three-way ANOVA was conducted with SigmaPlot Software (Version 13.0, Systat Software, Inc., San Jose, CA, USA) with the addition of the category of cell size (Large or Small). A listing of the specific categories and data evaluated in the three-way ANOVA is in Table 5.2. The standard ANOVA analysis package within SigmaPlot software also provided important ancillary information to assure that proper assumptions were made about the data so that the statistical treatment was appropriate for the data. Tests of both normality and equal variance of the data were assessed prior to executing the three-way ANOVA. The test of normality was used to

determine if the samples originated from a random sample with a normal distribution [329].

Table 5.2. Data table for three-way ANOVA

Group #1	Group#2	Group #3	*r*-value
Small	Blue	Constant	0.0213
Small	Blue	Flashing	0.0066
Small	Red	Constant	0.0367
Small	Red	Flashing	0.0266
Large	Blue	Constant	0.0933
Large	Blue	Flashing	0.0425
Large	Red	Constant	0.0639
Large	Red	Flashing	0.0773

Similar testing of the data was performed in the research literature with the Kolmogorov-Smirnoff test [321]. The normality test performed in the analysis of the data for the project reported here employed the Shapiro-Wilk Test for Normality as provided in the SigmaPlot software. However, the output of the analysis did not include a *W* value as specified in the *NIST e-Handbook*, but rather a *P* value was presented in its place [329]. The interpretation of the P-value was similar to the W value, in that the value was reported as a decimal percentage, where a value approaching 1 represents the relative percentage (100%) that the random sample follows a normal distribution. The data for the three-way ANOVA conducted for the experiments passed the test for normal distribution with a P=0.968, and was then tested for equal variance employing the Brown-Forsythe Test.

The assessment of equal variance among biological samples is very important since biological systems tend not to be completely Gaussian. The literature only provided a few instances of specific statistical treatments in similar testing of green microalgae in experiments where growth rates were evaluated. Homoedasticidy was examined in the literature using the Cochran-Bartlett Test [321] and Levene's test [325]. The Cochran-Bartlett Test was not well suited for the small sample size in the work reported in the capstone experiments because of the sensitivity of the Cocharan-Bartlett Test to departures from normality. The Levene's test also suffers from a dependence on means which reduces the test's robustness when examining non-normal data [329] The Brown-Forsythe Test was determined to be a better test for the experimental data in the project as departures from strictly normal distributions were expected given the nature of working with living microorganisms.

Results from the three-way ANOVA are presented in Table 5.3. The three-way ANOVA concluded that only the cell size category proved a significant difference with better than a 95% confidence. To isolate which group significantly differed from the others, a multiple comparison procedure was performed with Holm-Šídák. The Tukey test was performed in similar published experiments comparing growth rates of microalgae to experimental treatments [259, 321]. However, the Holm-Šídák was determined to be more powerful and can stand alone from the ANOVA, rather than to only be used to follow-up ANOVA. The results of the Holm-Šídák can be seen in Table 5.4. The results determined that a significant difference related to cell morphology (Large or Small) was evident.

Table 5.3. Results of three-way ANOVA. Factors: DF= Degrees of Freedom; SS= Sum of Squares; MS= Mean of Squares; F= F-test factor; & P= test of the null hypothesis.

Factor	Cell Size	Light Color	Light Regime	Residual	Total
DF	1	1	1	4	7
SS	0.00432	0.00208	0.000484	0.00117	0.00617
MS	0.00432	0.00208	0.000484	0.000292	0.000882
F	14.778	0.713	1.656		
P	0.018	0.446	0.268		

Table 5.4. Results from Holm-Šídák analysis.

Comparison	Difference of Least Square Means	Standard Error	P	P< 0.050
Small vs. Large Cell Morphology	0.0464	0.00845	0.018	Yes
Blue vs. Red Light color	0.0102	0.00845	0.790	No
Constant vs. Flashing regime	0.0157	0.00845	0.0972	No

Additional examination of the data was performed utilizing Mann-Whitney Rank Sum Tests to evaluate the different groups with the growth rate data. The Mann-Whitney Rank Sum Test was employed over the Kolmogoorov-Smirnov Test used in the literature because the test is more sensitive to differences in distributions between the groups of data being tested. The Mann-Whitney test was applied to three different comparisons: Large cell morphology versus Small cell morphology, Blue versus Red light, and Flashing versus Constant illumination. The results of the data analysis are presented in Table 5.5. The outcome of the Mann-Whitney test determined that the mean of the

growth rates for the large cell morphology was statistically larger than the growth rates for the small cell morphology with a 95% confidence and significant power (greater than 0.800) for both one-tailed and two-tailed results. The comparisons of the Blue versus Red light and for the Flashing versus Constant illumination, demonstrated that the sample means did not show enough difference in the mean values of the growth rates to rule out the possibility that the difference seen is due to random sampling variability. However, the power calculated for both the one-tailed and two-tailed tests in each of the comparisons was less than 0.800, leading to the conclusion that the negative results may not be accurate.The only statistically significant difference in the experiments was the difference between the growth rates for the large and small cell morphologies. Additionally, the larger cell morphology had a statistically higher growth rate in all experiments. The other experiments did not provide any statistically significant differences between treatments with illumination or wavelength of light.

5.5. INTERPRETATION OF OBSERVED GROWTH BEHAVIOR

The maximum growth rates do not give a good indicator of the growth history of the algae population [330]. Therefore, the analysis of the growth rate data must be taken in the context of the experiment for adequate conclusions to be made about the experimental treatments. To accomplish the task, the numerical results were discussed in the context of the growth trends observed within the different experiments.

Table 5.5. The results of the Mann-Whitney Rank Sum analysis.

Group Name	**N**	**Mean**	**Standard Deviation**	**Standard Error of the Mean**
Blue	4	0.409	0.0379	0.0189
Red	4	0.511	0.0235	0.0118
Two-tailed P-value	0.663	One-Tailed P-value	0.332	
Power (α=0.050)	0.068	Power (α=0.050)	0.108	
Constant Illumination	4	0.0538	0.0317	0.0158
Flashing Illumination	4	0.0382	0.0299	0.0149
Two-tailed P-value	0.502	One-Tailed P-value	0.251	
Power (α=0.050)	0.068	Power(α=0.050)	0.108	
Small	4	0.0228	0.0125	0.00627
Large	4	0.0692	0.0215	0.0108
Two-tailed P-value	0.00972	One-Tailed P-value	0.00486	
Power (α=0.050)	0.872	Power (α=0.050)	0.948	

5.5.1. Constant Illumination Under Blue Light. The results of the experiments with constant illumination under blue (450 nm) light revealed interesting behaviors in the growth of the *D. viridis* under this experimental regime. A lack of a distinct exponential phase in the growth of the small cell morphology was evidenced by the R^2 value being the lowest of any experimental regime (0.9019). The experiment with constant illumination under blue light was the only experimental treatment with such a lack of a district exponential phase. Examination of the cell counts for the small cell morphology were very close to being statistically insignificant given the established thresholds for cell counts based on a 95% confidence interval that were established in Section 3. The initial sharp decline in the population was possibly indicative of metamorphosis of the small cells transforming into the large cell type. Such a conclusion is supported by an almost identical increase in the population of the large cell morphology in the same time period, resulting in a nearly flat line during the Lag Phase in the plot of the combined cells in Figure 4.1.

An example of the biofilm produced in the experiments with constant illumination under blue (450 nm) light is presented in the photograph of the bottom of a bioreactor taken through the neck of the Erlenmeyer flask in Figure 5.2. The more motile, small cell morphology should have been favored in the collection data as the large cells lacked flagella. However, just the opposite is seen in the data as the large cell morphology dominates in the experiment.

The sampling effect may also be responsible for another issue with the experimental work. The peak of the mean cell density for the large cell morphology was

just over 6500 cells mL^{-1}. This value was significantly less than most other experiments reported in the literature in Table 5.1.

Figure 5.2. Example of biofilm formed with constant illumination under blue (450 nm) light experiment.

The r value for the large cell morphology, 0.0933hr^{-1}, was near the high end of the range of growth rates reported in the literature. Another notable observation from the experiments with constant illumination under blue (450 nm) light was the two-tone appearance of the biofilm that accumulated at the bottom of the bioreactors. From interpretation of flow cytometry data, the darker pigmented biomass is believed to be the larger cell morphology. Along with size, the factors used in the bivariate plot analysis were correlated to the increase in fluorescence signal. The observed decade of difference in the logarithmic plots of the fluorescence signal in FL3 was interpreted as an increase in

pigments in the PSII system that resulted in a “brighter” response to excitation by the laser. Attempts to collect the biomass for further analysis and quantitatively confirm the observation were not possible do to the limitations of the laboratory.

5.5.2. Flashing Illumination Under Blue Light. The large cell morphology’s cell densities continued to exceed that of the small cell morphology’s cell densities for just over 100 hrs. The maximum growth rate of 0.0726 hr^{-1} derived for the large cell morphology was well within the range of growth rates reported in the literature. Further, the fitment of the exponential trendline was very good ($R^2 = 0.9952$), demonstrating that the large cell morphology did achieve a distinct Exponential Growth Phase.

An inverse relationship between the growth curve responses of the large and small cell morphologies to the flashing (45.6 Hz) illumination under blue (450 nm)light could be inferred from close examination of the growth rate plots. Just before a peak in the large cell morphology at hour 60, the small cell morphology showed a marked increase in cell density. Similarly, at hour 100, a spike in the small cell morphology preceded a large spike in the cell density of the large cell morphology at hour 120.

The small cell morphology exhibited exponential growth very late in the experiment ($R^2= 0.9937$). However, the r value was extremely low (0.0066hr^{-1}), but close to the lower bounds of what was reported in the literature.

Maximum cell densities were again much lower than many of the values published in the literature. The peak cell densities were $10.2x10^4$ cells·mL^{-1} and $3.72x10^4$ for cells·mL^{-1} for the large and small cell morphologies, respectively.

Sampling error likely occurred in the experiment as biofilm was also noted in the bioreactors for these experiments. A photograph from one of the replicates in Figure 5.3

illustrates the biofilm formed in the flashing (45.6 Hz) illumination under blue (450 nm) light experiments.

Figure 5.3. Example of biofilm formed in flashing (45.6 Hz) illumination under blue (450 nm) light experiments.

A notable feature of the biofilm was a distinct difference between pigmentation of the algae. The much darker green colonies of algae are seen in the margins of the field while the majority of the film is composed of the lighter color. The exact identity of the darker algae are suspected to be the remnants of the large cell morphology that were still actively dividing. This is alluded to by the fact that late in the experiment the population was dominated by the smaller cell morphology. Additionally, the majority of the larger cell morphology had peaked 100 hours prior to the termination of the experiment and the dead cells had lost their pigmentation.

5.5.3. Constant Illumination Under Red Light. The growth for the large cell morphology had a discernable exponential phase as noted from the fit of an exponential trendline ($R^2 = 0.9981$). The growth rate for the large cell morphology was 0.0639 hr^{-1} and was on the high end of the range of growth rates reported in the literature. The small cell morphology also had a reasonable approximation to an exponential growth phase with an R^2 value of 0.9766, and the inclusion of four data points in calculating the maximum r value of 0.0367 hr^{-1}. The growth rate for the small cell morphology was within the range reported in the literature.

Except for the initial time point, the large cell morphology dominated the early culture, quickly reaching peak cell density of just under $2.5x10^4$ cells·mL^{-1} by hour 50. The small cell morphology's cell densities accelerated at the point where the larger cell morphology's cell densities began to decline. The small cell morphology steadily increased in cell density, until attaining just under a maximum of $3.6x10^4$ cells·mL^{-1} by the end of the experiment at hour 180. While the analysis of the growth data identified a relatively long period of exponential growth in the culture of 50 hrs, the small cells may have only just begun to enter exponential growth towards the end of the experiment. Given that some experiments in the literature previously cited had durations from 20 to 144 days, the small cell morphology's growth curve may have just begun to accelerate at the end of the experiment. Absolute cell yields and peak densities must be observed with caution given the nature of the sampling error potentially favoring the small cell morphology. Figure 5.4 is a photograph of the biofilm accumulated on the bottom of the bioreactor for constant illumination under red (660 nm) light.

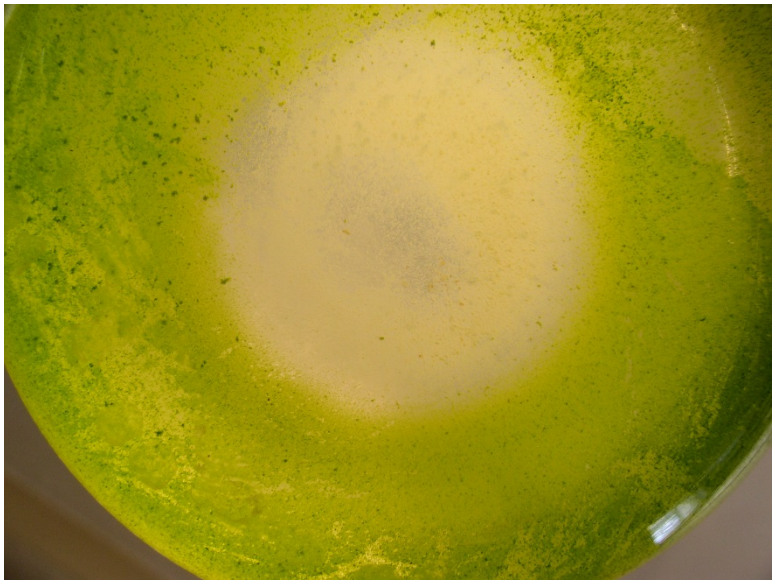

Figure 5.4. Example of biofilm formed in constant illumination under red (660 nm) light experiments.

The photograph in Figure 5.4 exhibits the same two-tone biofilm seen in previous experiments. However, the relative amount of darker pigmented cells are much less evident in the biofilm, and may reflect both the early peak in the experiments of the large cell morphology and the domination in the later time periods by the small, less pigmented cell morphology.

A distinct increase in the cell densities recorded around hour 108 showed a brief spike in the data. The suspected cause of the spike is possibly from replacement of experimental volume with filtered synthetic sea water. While evaporation of the experimental volume normally required additions with just RO water, the slight addition of too much RO water in a previous sampling event may have required that some salt was added back to the volume. Since the synthetic seawater is made from evaporated, natural

sea salts, some limiting nutrient(s) was likely re-introduced into the media causing a spike in the growth of both cell morphology types. Machine error was discounted because a spike in the pH just following the uptick in cell densities confirms that the spike was real and not a sampling error.

5.5.4. Flashing Illumination Under Red Light. The results of the experiments with flashing (45.6 Hz) illumination under red (660 nm) light showed further interesting behaviors by *D. viridis* in these experiments. The small cell morphology demonstrated the best fit to an exponential trendline of the two morphologies with an R^2 value of 0.9845 as compared to the large cell morphology's $R^2 = 0.9633$. Further, the small cell morphology growth rate value was derived from six data points, confirming that the small cells were most likely in exponential growth even with a slightly lower than ideal R^2 value. Similarly, the R^2 value for the large cell morphology was taken over five consecutive data points that improved the likelihood that the large cell morphology also experienced exponential growth. As a result, the derived r values have a good degree of confidence. The larger cell morphology demonstrated a higher r value than the smaller cell morphology with 0.0773 hr^{-1} to 0.0266 hr^{-1}, respectively. The large cell morphology compares well to established data in the literature and the small cell morphology is just out of the range.

Sampling errors were also anticipated in the data as a biofilm of algae was noted in the bioreactors. Figure 5.5 shows a photograph of a biofilm from one of the experimental replicates.

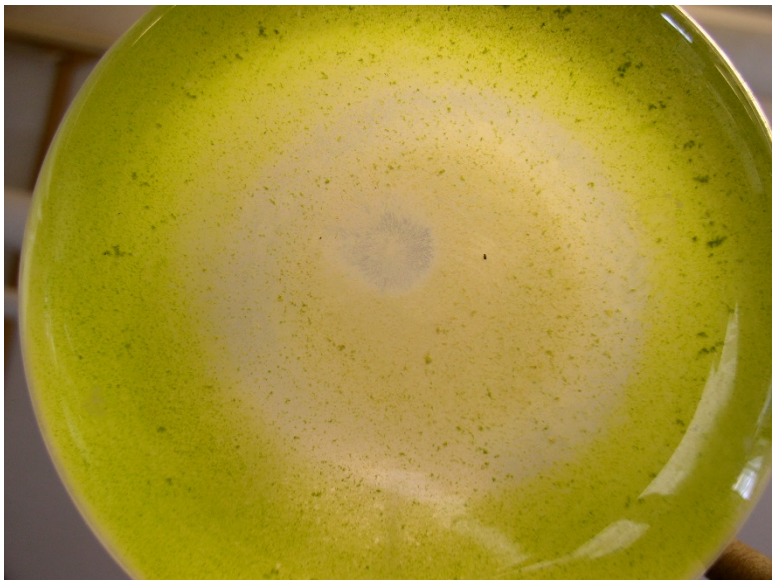

Figure 5.5. Example of biofilm formed in flashing (45.6 Hz) illumination under red (660 nm) light experiments.

Smaller flecks of the darker, large cell morphology can be seen in a field of much lighter green that is assumed to be a mixture of small cell morphology and photobleached, dead large cell morphology in Figure 5.5.

The growth curves of the two morphologies demonstrated very different behaviors in the flashing (45.6 Hz) illumination under red (660 nm) light experiment. The large cell morphology dominated early and peaked just before the smaller cell morphology's growth accelerated into the exponential phase. The Exponential Growth Phase was likely only in its early stages for the small cell morphology in the experiment. The literature reports that it took 10 days for *D. viridis* to reach the mid-exponential phase [331].

5.5.5. Light Color Comparisons. Red (660 nm) light experiments resulted in distinctive patterns of growth in the plots of the mean cell density of the large and small cell morphologies, respectively. The plots in Figure 5.6 and Figure 5.7 illustrate the early

peak in cell density in the large cell morphology for both red (660nm) light experiments. However, the small cell morphology continues a steady growth until it exceeds the maximum cell density of the large cell morphology just before the experiment is terminated. Experiments with the blue (450 nm) light also exhibited an early peak in the cell density of the large morphology. However, unlike the red (660 nm) light experiments, the small cell morphology plots remain flat and either do not fit an exponential trend or have insignificantly small growth rates.

Along with a distinctive pattern of growth between the light color experiments, a distinction could be made between maximum cell densities. Red (660 nm) light experiments had much greater maximum cell densities for both the large and small cell morphology when compared to the blue (450 nm) light experiments. Maximum cell densities from the red (660nm) light experiments were approximately 39,000 cells·mL $^{-1}$ and 46,000 cells·mL $^{-1}$ for the large and small cell morphologies, respectively. Maximum cell densities for the blue (450 nm) light experiments were approximately 10,000 cells·mL $^{-1}$ and 3,700 cells·mL $^{-1}$ for the large and small cell morphologies, respectively. Given that the cells were experiencing a very similar exposure to photons ($\approx 100 \mu mol \cdot m^{-2} \cdot s^{-1}$), the color of the light could have likely been responsible for the differences in maximum cell counts.

5.5.6. Discussion of Results for Illumination Comparisons. Differences in the maximum cell densities from the treatments exhibited some interesting results. The research literature reported that flashed (45.6 Hz) illumination increased photosynthetic efficiency, and therefore dramatically increased yields of algae in intensive cultures [219, 233, 332, 333]. In this project, experiments under red (660 nm) light, either constant or

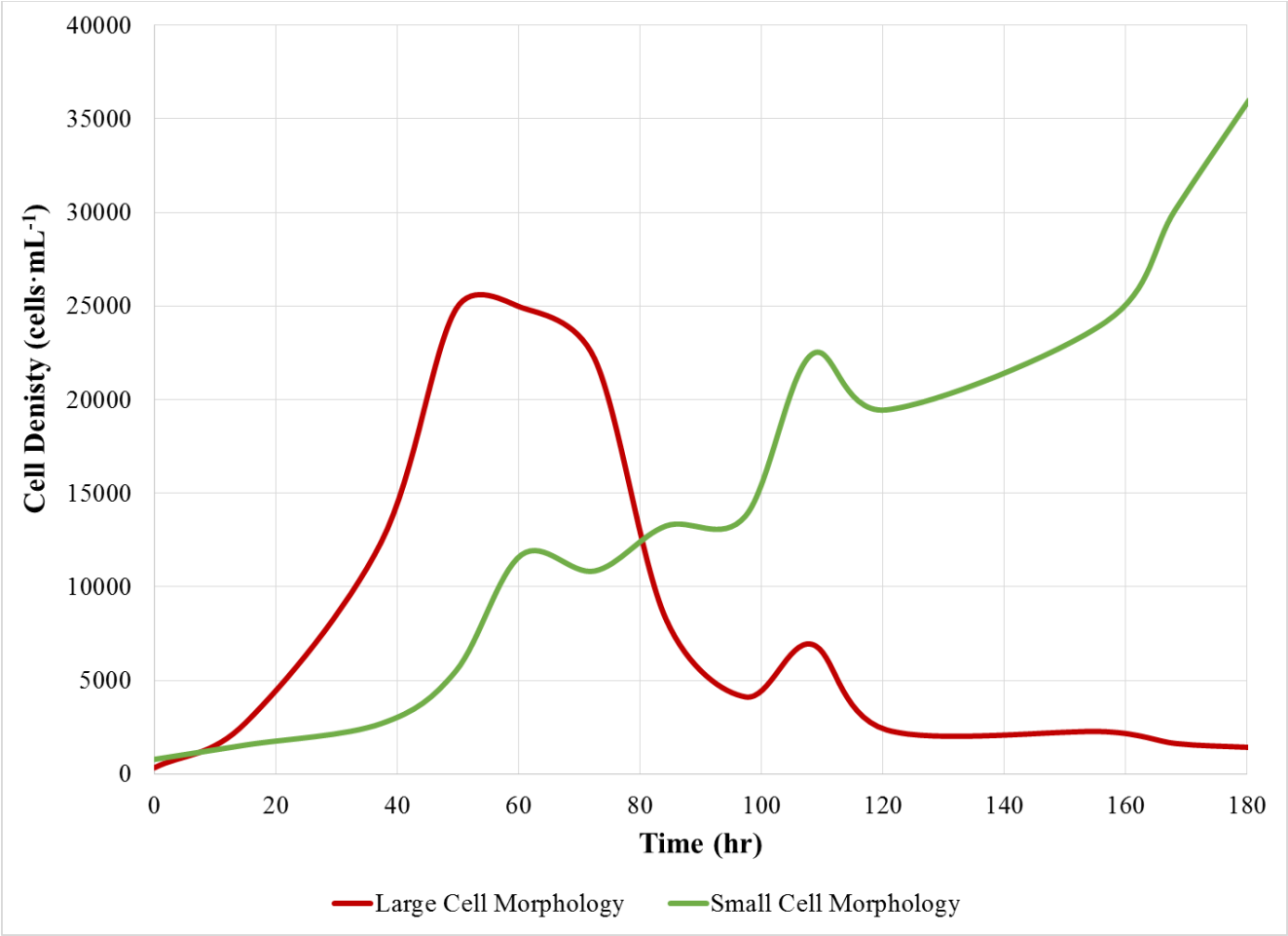

Figure 5.6. Plot of the median cell density over time for the large (solid red line) and small (solid green line) cell morphologies for experiments in constant illumination under red (660 nm) light.

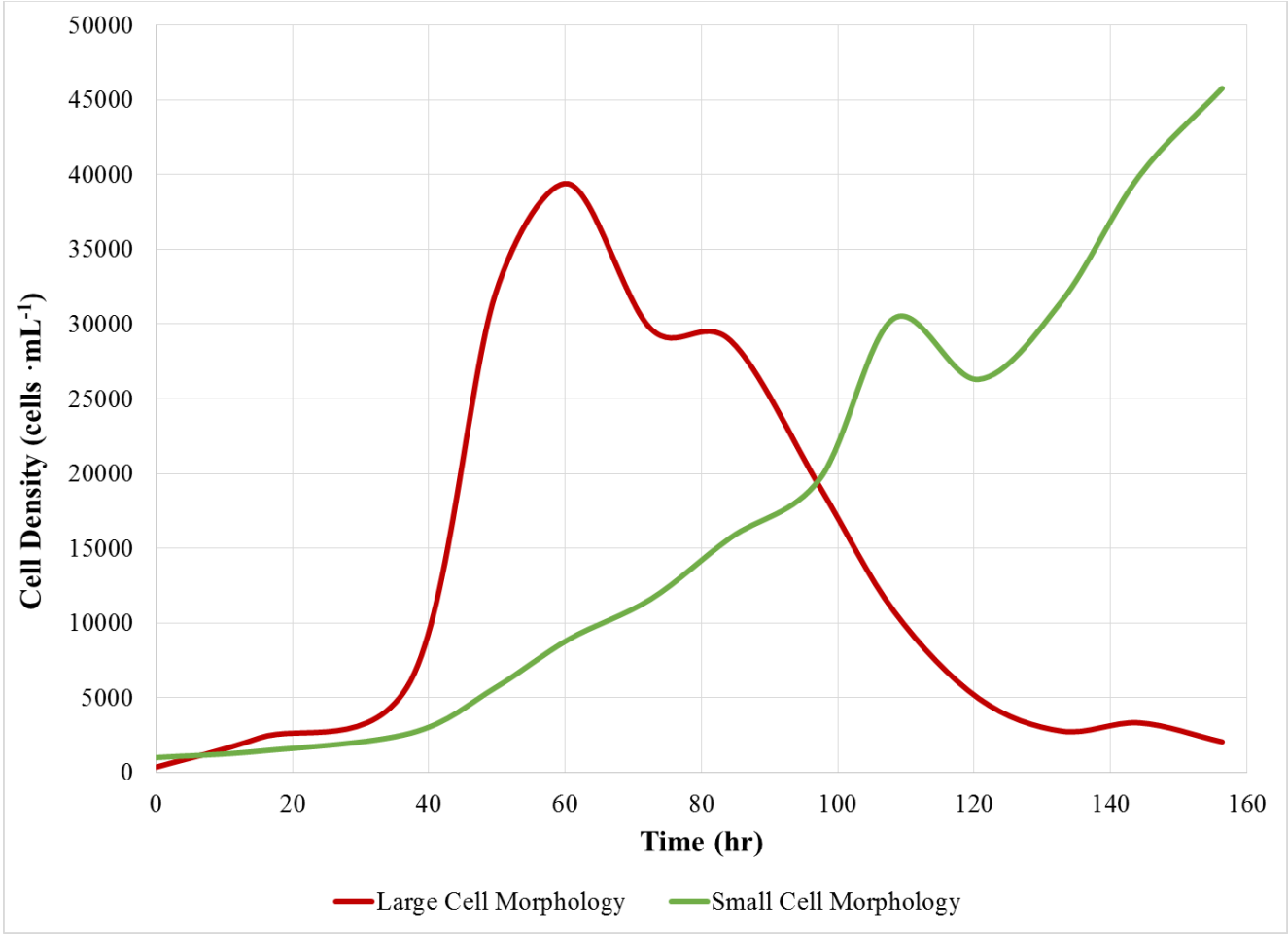

Figure 5.7. Plot of the median cell density over time for the large (solid red line) and small (solid green line) cell morphologies for experiments in flashing (45.6 Hz) illumination under red (660 nm) light.

flashing (45.6 Hz), exhibited very little difference between the growth rates for either of the cell morphologies. Experiments under blue (450 nm) light did demonstrate a significant difference between the constant illumination and the flashing (45.6 Hz) illumination for both the large and small cell morphology. However, the flashing (45.6 Hz) illumination under blue (450 nm) light demonstrated the opposite of what was expected where both cell morphologies had lower growth rates under flashing (45.6 Hz) light.

5.5. SUMMARY

The overall goal of this project was to launch a multidisciplinary study into the efficacy of combining algal biotechnology for the benefit of the mining industry, both economically and environmentally. In order for a commercial- industrial culture of algae to be viable for use in unused/abandoned/vacant mining properties, it is necessary to identify and isolate the factors of artificial illumination leading to the highest growth rate in algae, including constant versus flashing (45.6 Hz) light and blue (450 nm) versus red (660 nm) wavelength by experimental testing. This proposal is unique in that mining properties could be remediated and reclaimed while at the same time providing an environment for the commercial-industrial cultivation of algae with all its attendant benefits. Those benefits reviewed in the literature include: the replacement of fossil-diesel in base power production and in diesel powered equipment, as well as, remediation of mine influenced waters for acid remediation and heavy metals removal. It was not the purpose of this research to create new technologies, but to apply current technologies in a novel way. While this is a most ambitious project, the review of the literature identifies

the mining infrastructure and properties with the algal biotechnologies that can be integrated into this model.

The bench scale experiments investigated factors inherent in artificial illumination including constant versus flashing (45.6 Hz) illumination, and blue (450 nm) versus red (660 nm) wavelengths.

(a) The experimental results show that the halotolerant, strictly photoautotrophic, eukaryotic, green microalgae, *D. viridis* can be grown under only monochromatic wavelengths of light that relate to the maximum absorbance spectrum of chlorophyll.

(b) The experimental results show that morphological change related to some factor or combination of factors causes the rapid development and growth of the palmella morphology (large cells).

(c) The cell morphology, large or small, is statistically significant in the treatments of constant or flashing (45.6 Hz) illumination, and blue (450 nm) or red (660 nm) light. Further analysis shows that the growth rate for the larger cell morphology was consistently larger than that of the small cell morphology.

(d) Growth rates and maximum cell densities from the experimental results were successfully compared to published research studies.

(e) The experimental results do not suggest a statistically significant difference between constant or flashing (45.6 Hz) illumination. This was found to be contradictory to the published research literature.

However, specific experiments on *D. viridis* with flashing, or pulsed light regimes had not been attempted previously.

(f) The experimental results do not suggest a statistical difference between the blue (450 nm) and red (660 nm) wave lengths. The literature reports that the photosystems of green plants are more receptive to blue (450 nm) light and should have been able to incorporate the energy more efficiently. However, what was observed was a preference for the smaller cell morphology to exhibit exponential growth in experiments with red (660 nm) light.

(g) The experimental results showed that the use of flow cytometry was more efficient than microscopic counting of cells. However, cells might have been missed by that method, especially the large cell morphology that settled to the bottom of the bioreactor possibly taking with them the motile cells that may have been entangled with the extracellular mucilage of the larger cells.

(h) The experimental results were the first reported incident of the radical physical adaptation of *D. viridis* to different lighting regimes. The implication for the exploitation of this adaptation for the commercial-industrial culture of algae is potentially lower costs to harvest algae by selectively promoting the formation of the large cell morphology through the manipulation of artificial illumination. With larger cells, the effectiveness of separation technologies, like filtration or centrifugation, are more effective.

6. FUTURE WORK

6.1 RECOMMENDATIONS

A recognized path to continued prosperity in the mining sector is through innovations and applications of biotechnology to mining [128, 334-336]. In December of 2014, a large consortium comprised of the universities of Bath, Bristol, Cardiff, and Exeter; the Plymouth Marine Laboratory, the U.K. Coal Authority and a private waste management group have allied to investigate if algal biotechnologies can help remediate mine influenced waters while providing feedstock for biofuel [38]. The scientists and mining engineers of the GW4 Alliance are in the early stages of organizing an effort very similar to the project undertaken for the partial fulfillment of the requirements of the PhD in mining engineering and supports the scientific and academic merit of the endeavor. Similar to the faculty from the Camborne School of Mines in their project, the overall goal of this project was to launch a multidisciplinary study into the efficacy of combining algal biotechnology for the benefit of the mining industry, both economically and environmentally. Specific to this manuscript, was an investigation of using abandoned/vacant/unused mining infrastructure, to culture a commercially relevant, halotolerant, strictly photoautotrophic, eukaryotic, green microalgae for the express purpose of sustainably growing biomass at the commercial-industrial scale in underground mining brownfields.

The synergy of combining microalgae biotechnologies with the expertise of mining engineering has only just begun with the research project presented in this manuscript for the partial fulfillment of a PhD degree in mining engineering. A host of further experiments are necessary to refine and expand upon the preliminary data

obtained in this experimental research to continue to expand the research frontier, firmly establishing the groundwork for the potentially disruptive biotechnologies for the mining industry. The experimental research presented has only begun to address the first of the five major objectives required for the formal assessment of the relevant science and engineering for the multidisciplinary endeavor to establish key design, economic, and environmental elements for successful redevelopment and remediation of underground mines. As previously outlined in the beginning of this manuscript, the key issues to be investigated are:

(a) Negative impacts due to variation in ambient light

(b) Negative impacts due to variation in ambient temperature

(c) Negative impacts due to a lack of biosecurity

(d) Competition for water resources with agriculture and municipalities

(e) Exorbitant infrastructure and manpower costs

In the investigations already conducted to mitigate negative impacts of ambient lighting, novel results have been realized that have contributed to the basic science of phycology and have moved forward the realization of sustainable sources of liquid fuels and chemicals for the mining industry. It is fully anticipated that the continued research into the redevelopment of underground mining properties for commercial-industrial scale algae culture will continue to be a fertile area for scientific and engineering research.

Based on the results of both the review of the body of knowledge, and the experimental research, many more investigations are required to improve and extend upon the groundwork already established. In the careful selection of future work, the following guiding principles must be kept in the fore:

(i) The future work must continue to develop relevant engineering and design parameters based on experimental results and extended by relevant theoretical data.

(ii) The future work must also work to fully assess the formulated design parameters to conclude whether the proposed model improves upon existing OPC and PBR models in terms of economic and environmental impacts.

The following recommendations for future work will focus on the continued synthesis and application of algal biotechnologies for the mining industry:

Genomic Identification- Because of the historical problems in the proper identification of the *D. viridis*, formal genetic analysis of the algae used is required to conclusively determine the identity of the model algae used in this project. Based on immediate confusion in the literature with the exact identification of the UTEX LB1983 strain used in the experimental work, confirmation of the phenotypic identification with genomic information would be prudent [277].

Cell Physiology- Full characterization of the cell physiology, such as chlorophyll antenna size, need to be examined to begin to elucidate the exact morphological response to different illumination treatments on the cellular level. Observations in the literature record the onset of smaller, more photosynthetically efficient chlorophyll antenna size in *Dunaliella salina* and *Dunaliella tertiolecta* [229]. The reason for this investigation would be to compare experimental observations with the data in the literature that show.

that such a morphological change is possibly brought on by differences in the wavelength of light (i.e., color) and not just more intense light (2000 umol photon$\cdot m^{-2} \cdot s^{-1}$ of PAR).

Cell Biochemistry- The determination of the similarities and differences in the composition of the algal biomass under different lighting regimes and wavelengths is important to establish the possible downstream use and value of the biomass. Included in analysis would be an investigation in the identification and classification of extracellular excretions from the algae under different lighting regimes.

Mass Transfer- Important design and engineering information will be derived from further investigation of the total amounts and rate of transfer of nutrients and carbon into the algae under similar experiments with artificial lighting.

Energy Transfer- Economic and environmental sustainability of the proposed process depends directly on the efficiency in the transfer of electrical energy to chemical energy in the biomass.

Enhanced Enumeration- Employing modern flow cytometers with the ability to record images of the particles being analyzed would assist greatly in refining the identification and enumeration of the different cell morphologies. Further, the addition of cell sorting would also allow for exact selection of populations of different morphologies for further analysis to determine what factors cause the morphological changes discovered.

Continuous Culture- The establishment of continuous culture at the pilot scale within an underground mine.

Analysis of Biodiesel- Using analytical methods set forth by the National Renewable Energy Laboratory (Golden, CO USA) to evaluate the quality of the soy–derived for examination of the biodiesel derived specifically from *D. viridis* [337].

6.2. CONTRIBUTIONS OF THE PHD RESEARCH

As a discipline, mining engineers are much more accustomed to the tremendous scale of industrial commodities procurement and their management and have applied this perspective to evaluate algal culture systems. Thus far, the work with algal biotechnologies has yielded both basic scientific discoveries and has worked to advance the sustainability, both economically and environmentally, of the mining industry.

The mining department of the Missouri University of Science and Technology has taken a very progressive position on alleviating many of the major issues of cost and sustainability with the continued expansion of diesel power machinery within the mining industry. As a result, a substantive investment has already been made in the deployment of research laboratory space to investigate alternatives for liquid fuels while examining environmentally sustainable methods for producing the quality and quantity required. To this end, the research facility has been very active within a coalition of scientists and engineers for the purpose of establishing fundamental technologies and techniques for the utilization of existing subterranean mining infrastructure. However, as has been seen in similar projects in the U.K., considerably more resources need to be brought to bear to keep the research moving forward and the frontier of knowledge expanding.

APPENDIX

RECIPES FOR THE PREPARATION OF CULTURE MEDIA

Synthetic saltwater was prepared in 5 L batches. From previous exploratory experiments, ≈1.25 g of Instant-Ocean Sea Salt (Spectrum Brands, Blacksburg, Virginia, USA) to 1 L of culture water (≈ 2 MΩ reverse-osmosis water) would yield approximately1‰ when measured with a refractometer using equipment described in §3.11 of Material and Methods. The amount of salt added is a little larger than the theoretical amount of 1 g/L as a result of the Instant-Ocean Sea Salt containing non-dissolved solids that were bits of shell and sand due to it being a natural product. Typically, a 35‰ strength solution would be prepared as a slightly more concentrated stock solution because additions of nutrients, trace metals, and vitamins would slightly dilute the mix. The synthetic seawater would then be constantly stirred and boiled for at least 5min. The water was then vacuum filtered with 0.22 μm PES filter into a 2 L glass storage bottle with GL-45 threads to accept the bottle top vacuum filters previously described in §3.4.2 of the Materials and Methods. The filtered synthetic sea water would then be combined with other batches in a sterilized 5 gallon (20L) High Density Polypropylene carboy with spigot. Each 5 gallon (20L) batch of seawater would then be used as the base formulation of experimental growth media and as sheath fluid for the flow cytometer.

Natural Sea water was sourced from Culture Collection for Marine Phytoplankton. The water was taken directly from Booth Bay, ME and filtered and pasteurized by the personnel of the culture collection before being shipped in 3 gallon carboys to the lab. In preparation for use with stock cultures, the natural sea water was filtered with the same with 0.22 μm PES filter into a 2 L glass storage bottle with GL-45 threads to accept the bottle top vacuum filters previously described in §3.4.2 of the

Materials and Methods and then steam autoclaved at 121°C & 2.0 atm for 30 min before being incorporated into the media.

The original samples of *Dunaliella* from the UTEX Culture Collection were shipped in a half-strength Erdschreiber's Medium with a salinity of 15ppt. This media was used early on in the project for both maintaining stock cultures and for early experiments. A liter of Erdschreiber's Medium was purchased from the UTEX Culture Collection and primarily used to maintain cultures until sufficient skill had been developed for crafting the medium in the laboratory. Following the recipe was taken from the UTEX Culture Collection website (www.sbs.utexas.edu/utex/media.aspx) with a few minor alterations, every liter of full strength Erdschreiber's Medium was made using the materials and amounts listed in Table 1A.

Table 1A. Components of Erdschrieber's Medium from the UTEX Culture Collection.

Component		Amount	
1.	Steam autoclaved seawater (≈ 33 ± 2 ‰)	1	Liter
2.	P-IV Metal Solution	12	mL
3.	Soilwater: GR+ medium	50	mL
4.	0.7 <u>M</u> $NaNO_3$	3.33	mL
5.	0.02 <u>M</u> $NaHPO_4 \cdot 7H_2O$	3.33	mL
6.	Vitamin B_{12}	1	mL

Maintenance cultures were diluted to half-strength with steam autoclaved natural seawater. The first component of the recipe was altered from the original. The seawater component was originally collected from the Gulf of Mexico and was pasteurized by UTEX before being shipped to the laboratory. When the supply of original UTEX sourced seawater ran out, steam-autoclaved seawater from Boothbay, ME was substituted for the stock cultures. Synthetic seawater with a salinity of 30‰ was prepared by suitably diluting the 35‰ prepared stock solution previously described here.

The second component, the P-IV Metal Solution, was prepared as a stock solution in a 1000mL graduated cylinder that was rated "To Contain". Following the recipe for the P-IV Metal Solution posted on the UTEX Culture Collection website (www.sbs.utexas.edu/utex/media.aspx) the materials listed in Table 2A were added to the graduated cylinder.

Table 2A. P-IV Metal Solution for Erdschrieber's.

Component		Amount	
1.	dH_2O	900	mL
2.	$Na_2EDTA•2H_2O$	0.75	g
3.	$FeCl_3•6H_2O$	0.097	g
4.	$MnCl_2•4H_2O$	0.041	g
5.	$ZnCl_2$	0.005	g
6.	$CoCl_2•6H_2O$	0.002	g
7.	$NaMoO4•2H_2O$	0.004	g

The graduated cylinder was placed on a stirring hotplate set to 95°C and approximately 200 rpm to assist in the dissolving of the compounds. Once everything was dissolved, the total volume was brought up to 1000mL with dH_2O. The solution was transferred to a 2 L glass storage bottle and steam autoclaved as previously mentioned in §3.4.2 of the Material and Methods. Once cooled, the Trace Metal Solution was refrigerated.

The third component, the Soilwater, GR+ medium, was prepared as a stock solution. The method for creating the soil water was modified from that presented on the UTEX Culture Collection webpage. Potting Soil in the original UTEX recipe was replaced with soil taken from a strictly organic private garden located in Romney, IN. The soil consistency was a rich, black, loamy soil that had proven to be very fertile and without pesticide or herbicide residues. A concentrated soilwater was created with 50g of soil added to a graduated 500mL GL-45 glass media bottle. The media bottle was placed on a stirring hotplate set to 95°C and approximately 200 rpm while a volume of dH20 was added such that volume in the bottle was approximately 250mL. The solution was allowed to mix for an hour and was then filtered through 3 layers of unbleached coffee filters into second graduated 500mL GL-45 glass media bottle. The bottle was then steam autoclaved at 121°C & 2.0 atm for 30 min. The solution was then allowed to cool and refrigerated for 24 hours before the mixture was again filtered through 3 layers of unbleached coffee filters into a clean graduated 500mL GL-45 glass media bottle and autoclaved again. The process was repeated a third time before the mixture was vacuum filtered through a coarse cellulose filter paper (Whatman Grade 4) into a final 500mL GL-45 glass media bottle and steam autoclaved at 121°C & 2.0 atm for 30 min. No

further additions were made to the solution which was a modification as the original UTEX recipe added calcium carbonate to the mixture. The solution was then stored in the refrigerator, but was brought to room temperature before using.

The fourth component, 0.70M $NaNO_3$ (Sodium nitrate solution) was made in 1000mL batches using a "To Contain" graduated cylinder and adding 59.493g of chemical to 900mL of dH_2O and then the volume was brought up to 1000mL with dH_2O. This solution was then transferred to a 2 L glass storage bottle and bottle and steam autoclaved at 121°C & 2.0 atm for 30 min. Solution was then transferred to 250 mL, plastic low density polyethylene (LDPE) storage bottles and refrigerated.

The fifth component, 0.02 M Na_2HPO_4 (Sodium hydrogen phosphate solution) was made in 1000mL batches using a "To Contain" graduated cylinder and adding 5.3614g of $Na_2HPO_4 \cdot 7H_2O$ to 900mL of dH_2O and then the volume was brought up to 1000mL with dH_2O. This solution was then transferred to a 2 L glass storage bottle and bottle and steam autoclaved at 121°C & 2.0 atm for 30 min. Solution was then transferred to 250 mL, plastic low density polyethylene (LDPE) storage bottles and refrigerated.

The final component, Vitamin B_{12} stock solution was a two part process. The first process involved the preparation of 200mL of 50 mM HEPES buffer with a pH of 7.80by dissolving 2.4 grams of HEPES buffer in 190mL of dH_2O in a 1000 mL "To Contain" graduated cylinder that had been previously cleaned and steam autoclaved at 121°C & 2.0 atm for 30 min. The pH of the solution was monitored with pH meter adjusted with the addition of a small amount of potassium hydroxide (KOH) added to the solution while constantly stirred. Once the pH of the solution was adjusted to 7.8, 0.027

g of Vitamin B_{12} (cyanocobalamin) was added to the mixture while constantly stirring and 70°C heating. The final mixture was then filter sterilized with a bottle top filter into amber glass storage bottle (Kimble Chase RAY-SORB KIMAX media bottle, 14399250). The bottle top filter was the same type as previously described in §3.4.2 of the Materials and Methods.

Experimentation with other growth media was undertaken as the result of investigations conducted during a 7-day workshop at the Bigelow Laboratory for Ocean Science in Boothbay, ME (October 23-29, 2008). Three different growth mediums were applied and evaluated for use in the research project: f/2, L1, and Prov50. The first experimental media, f/2, is fully described in [198]. Since *Dunaliella* do not require silica, the $Na_2SiO_3 \bullet 9H_2O$ was excluded from the formulations used in the experiments. Table 3A is the modified recipe for f/2-Si that was used in the experiments.

Table 3A. Modified recipe for f/2-Si from the Bigelow Laboratory for Ocean Science.

Component		Amount	
1.	Steam autoclaved seawater (≈ 33 ± 2 ‰)	1	Liter
2.	Trace Metal Solution	1	mL
3.	0.88 M $NaNO_3$	2	mL
4.	0.019 M $NaHPO_4 \bullet 7H_2O$	2	mL
5.	Vitamin Stock Solution	1	mL

The first component of the recipe was altered from the original recipe in some cases. Steam-autoclaved seawater from Boothbay, ME was substituted with synthetic seawater of a similar salinity when the media was used for experiments. The natural seawater was retained for maintenance cultures. Furthermore, the maintenance cultures also had the amount of sodium nitrate and sodium hydrogen phosphate increased by 1 mL each in a 1 liter batch.

The second component, the Trace Metal Solution, was prepared as a stock solution in a 1000mL graduated cylinder that was rated "To Contain". Table 4A is the recipe used for the Trace Metal Solution from the literature [198].

Table 4A. Recipe for Trace Metals Solution for f/2-Si from the Bigelow Laboratory for Ocean Science.

Component		Amount	
1.	dH_2O	950	mL
2.	$Na_2EDTA•2H_2O$	4.36	g
3.	$FeCl_3•6H_2O$	3.15	g
4.	0.040 <u>M</u> $CuSO_4•5H_2O$	1	mL
5.	0.077 <u>M</u> $ZnSO_4•7H_2O$	1	mL
6.	0.040 <u>M</u> $CoCl_2•6H_2O$	1	mL
7.	0.026 <u>M</u> $NaMoO_4•2H_2O$	1	mL
8.	0.91 <u>M</u> $MnCl_2•4H_2O$	1	mL

Components 4-8 of the Trace Metal solution were prepared separately in 200mL, Class-A volumetric flasks and dH_2O to bring the solutions to the proper volume. Each of the components was steam autoclaved as previously mentioned in §3.4.2 of the Material and Methods once they were transferred to 500mL glass media storage bottles. The metals were then cooled and stored in a refrigerator. Components of the Trace Metal solution were brought up to room temperature before combining into the final stock solution of Trace Metals Solution.

A graduated cylinder was placed on a stirring hotplate set to 95°C and approximately 200 rpm to assist in the dissolving of the compounds. Once everything was dissolved, the total volume was brought up to 1000mL with dH_2O. The solution was transferred to a 2 L glass storage bottle and steam autoclaved as previously mentioned in §3.4.2 of the Material and Methods. Once cooled, the Trace Metal Solution was refrigerated.

The third component, 0.88 M $NaNO_3$ (Sodium nitrate solution) was made in 1000mL batches using a "To Contain" graduated cylinder and adding 75.00g of chemical to 900 mL of dH_2O and then the volume was brought up to 1000mL with dH_2O. This solution was then transferred to a 2 L glass storage bottle and bottle and steam autoclaved at 121°C & 2.0 atm for 30 min. Solution was then transferred to 250 mL, plastic low density polyethylene (LDPE) storage bottles and refrigerated.

The fourth component, 0.019M Na_2HPO_4 (Sodium hydrogen phosphate solution) was made in 1000mL batches using a "To Contain" graduated cylinder and adding 5.00g of $Na_2HPO_4 \cdot 7H_2O$ to 900 mL of dH_2O and then the volume was brought up to 1000mL with dH_2O. This solution was then transferred to a 2 L glass storage bottle and bottle and

steam autoclaved at 121°C & 2.0 atm for 30 min. Solution was then transferred to 250 mL, plastic low density polyethylene (LDPE) storage bottles and refrigerated.

The final component, Vitamin Stock Solution consisted of a three vitamins; thiamine (vitamin B_1), biotin (vitamin H) and cyanocobalamin (vitamin B_{12}) in the quantities presented in Table 5A.

Table 5A. Recipe for Vitamin Stock Solution for f/2-Si from the Bigelow Laboratory for Ocean Science.

Component		Amount	
1.	Thiamine	200	mg
2.	Biotin	10	mL
3.	Cyanocobalamin	1	mL

The first component of the Vitamin Stock Solution, the thiamine, was massed and added to a 1000mL class-A, volumetric flask. A biotin stock solution was created by adding 0.0200g into a 200mL, class-A volumetric flask and bringing the final volume up to 200mL. This solution was filter sterilized using the method previously described in §3.4.2 of the Materials and Methods before being deliverd to the 1000mL volumetric flask containing the thiamine. The cyanocobalamin solution used to make the Vitamin Stock Solution for the f/2 was taken “as is” from the solution prepared for the UTEX Erdschreiber’s Medium previously described. However, the concentration of the UTEX Vitamin B_{12} recipe was much less than the 1.0g per liter needed for the f/2. As a result,

7.4 mL of the UTEX Vitamin B_{12} stock solution was added to the 1000mL volumetric flask with the thiamine and biotin. The volume was then brought up to 1000mL and gently heated and stirred on a stirring hot plate set to 70° C and 135 rpm. Once all the components were completely dissolved, the mixture was vacuum filtered into a 2 L glass storage bottle and then autoclaved in accordance with the previously described methods in §3.4.2 of the Material and Methods. The solution was wrapped in tin-foil to keep light exposure to a minimum and placed into the freezer for storage.

The second experimental media, L1, is fully described in [198]. Since *Dunaliella* do not require silica, the $Na_2SiO_3 \bullet 9H_2O$ was excluded from the formulations used in the experiments. Table 6A is the modified recipe for L1-Si that was used in the experiments:

Table 6A. Recipe for L1-Si from Bigelow Laboratory for Ocean Science.

Component		Amount	
1.	Steam autoclaved seawater (≈ 33 ± 2 ‰)	1	Liter
2.	Trace Metal Solution	1	mL
3.	0.88 M $NaNO_3$	2	mL
4.	0.019 M $NaHPO_4 \bullet 7H_2O$	2	mL
5.	Vitamin Stock Solution	1	mL

The only difference between the L1 formula and the f/2 is that the Trace Metal Solution for the L1 media is more extensive than that for f/2 with the addition of selenous

acid, nickel (II) sulfate, sodium orthophosphate and sodium chromate. As a result, the Trace Metal Solution for the L1 media was purchased from Culture Collection of Marine Phytoplankton, Boothbay, ME. Table 7A is the recipe for the Trace Metal Solution as listed in [198].

Table 7A. Recipe for Trace Metals Solution for L1-Si from Bigelow Laboratory for Ocean Science.

Component		Amount	
1.	dH_2O	950	mL
2.	$Na_2EDTA•2H_2O$	4.36	g
3.	$FeCl_3•6H_2O$	3.15	g
4.	0.010 M $CuSO_4•5H_2O$	1	mL
5.	0.080 M $ZnSO_4•7H_2O$	1	mL
6.	0.050 M $CoCl_2•6H_2O$	1	mL
7.	0.082 M $NaMoO_4•2H_2O$	1	mL
8.	0.90 M $MnCl_2•4H_2O$	1	mL
9.	0.01 M H_2SeO_3	1	mL
10.	0.009 M $NiSO_4•6H_2O$	1	mL
11.	0.01 M Na_3VO_4	1	mL
12.	0.01 M K_2CrO_4	1	mL

The final experimental media, Prov50, is fully described in [198]. Table 8A is the recipe for Prov 50 that was used in the experiments.

Table 8A. Recipe for Prov 50 from Bigelow Laboratory for Ocean Science.

Component		Amount	
1.	Steam autoclaved seawater (≈ 33 ± 2 ‰)	1	Liter
2.	Trace Metal Solution	1	mL
3.	Alkaline Soil Extract Solution	1	mL
4.	0.88 M $NaNO_3$	2	mL
5.	0.019 M $NaHPO_4 \cdot 7H_2O$	2	mL
7.	0.50 M NH_4Cl	2	mL
6.	Vitamin Stock Solution	1	mL

The only difference between the Prov50 formula and the f/2 was the addition of ammonium chloride and an alkaline soil extract solution. A stock ammonium chloride solution was prepared by adding

The Alkaline Soil Extract Solution was different then the previously described Soilwater GR+ medium for the UTEX Erdschreiber's media. Following the directions from [198] was first prepared as concentrate that was later diluted 5:1 (by volume) for use in the Prov50 formulation. As with the Soilwater GR+ medium, the same soil taken from a strictly organic private garden located in Romney, IN was used. The soil consistency was a rich, black, loamy soil that had proven to be very fertile and without

pesticide or herbicide residues. A solution consisting of 100g of soil to 200g of dH_2O was added to a graduated 500mL GL-45 glass media bottle along with 0.40g of sodium hydroxide was also added to the mixture. The media bottle was placed on a stirring hotplate set to 95°C and approximately 200 rpm. The solution was allowed to mix for two hours and was then filtered through three layers of unbleached coffee filters into second graduated 500mL GL-45 glass media bottle. The mixture was then steam autoclaved at 121°C & 2.0 atm for 30 min. The solution was then allowed to cool and refrigerated for 24 hours before the mixture was again filtered through 3 layers of unbleached coffee filters into a clean graduated 500mL GL-45 glass media bottle and autoclaved again. The process was repeated a third time before the mixture was vacuum filtered through a coarse cellulose filter paper (Whatman Grade 4) into a final 500mL GL-45 glass media bottle and steam autoclaved at 121°C & 2.0 atm for 30 min. The solution was then stored in the refrigerator, but was brought to room temperature before using.

A working stock was created by diluting 40mL of the concentrated soil extract to 200mL in a class A volumetric flask. The working stock was transferred to a 250 mL glass media bottle and steam autoclaved at 121°C & 2.0 atm for 30 min. The solution was then stored in the refrigerator, but was brought to room temperature before using.

BIBLIOGRAPHY

1. Day, J.G., S.P. Slocombe, and M.S. Stanley, *Overcoming biological constraints to enable the exploitation of microalgae for biofuels.* Bioresource Technology, 2012. **109**(0): p. 245-251.

2. Jim, H., *Nanotechnology; Mining companies could achieve better fuel efficiency.* Mining Engineering, 2011. **63**(7): p. 70-71.

3. BCS, I., *Mining Industry Energy Bandwidth Study*, A.M.O.F.I.T. Program), Editor. 2007.

4. Sheehan, J., et al., *Look Back at the U.S. Department of Energy's Aquatic Species Program: Biodiesel from Algae; Close-Out Report*, in *Other Information: PBD: 1 Jul 1998*. 1998. p. Medium: ED; Size: 325 pages.

5. Craggs, R., D. Sutherland, and H. Campbell, *Hectare-scale demonstration of high rate algal ponds for enhanced wastewater treatment and biofuel production.* Journal of Applied Phycology, 2012. **24**(3): p. 329-337.

6. Pulz, O., *Photobioreactors: production systems for phototrophic microorganisms.* Applied Microbiology and Biotechnology, 2001. **57**(3): p. 287-293.

7. Park, J.B.K., R.J. Craggs, and A.N. Shilton, *Wastewater treatment high rate algal ponds for biofuel production.* Bioresource Technology, 2011. **102**(1): p. 35-42.

8. Pérez-López, P., et al., *Life cycle assessment of the production of the red antioxidant carotenoid astaxanthin by microalgae: from lab to pilot scale.* Journal of Cleaner Production, 2014. **64**(0): p. 332-344.

9. Cuaresma, M., et al., *Horizontal or vertical photobioreactors? How to improve microalgae photosynthetic efficiency.* Bioresource Technology, 2011. **102**(8): p. 5129-5137.

10. Carvalho, A.P., L.A. Meireles, and F.X. Malcata, *Microalgal reactors: a review of enclosed system designs and performances.* Biotechnol Prog, 2006. **22**(6): p. 1490-506.

11. Richmond, A., *Principles for attaining maximal microalgal productivity in photobioreactors: an overview.* Hydrobiologia, 2004. **512**(1-3): p. 33-37.

12. Quinn, J.C., C.W. Turner, and T.H. Bradley, *Scale-Up of flat plate photobioreactors considering diffuse and direct light characteristics.* Biotechnology and Bioengineering, 2012. **109**(2): p. 363-370.

13. Lundquist, T.J., et al., *A Realistic Technology and Engineering Assessment of Algae Biofuel Production*. 2010: Energy Biosciences Institute. p. 1-178.

14. Sforza, E., et al., *Adjusted light and dark cycles can optimize photosynthetic efficiency in algae growing in photobioreactors.* PLoS ONE 2012. **7**(6): p. e38975.

15. Degen, J., et al., *A novel airlift photobioreactor with baffles for improved light utilization through the flashing light effect.* Journal of biotechnology, 2001. **92**(2): p. 89-94.

16. Drews, G., *Contributions of Theodor Wilhelm Engelmann on phototaxis, chemotaxis, and photosynthesis.* Photosynthesis Research, 2005. **83**(1): p. 25-34.

17. Dixon, J.M., M. Taniguchi, and J.S. Lindsey, *PhotochemCAD 2: A Refined Program with Accompanying Spectral Databases for Photochemical Calculations¶.* Photochemistry and Photobiology, 2005. **81**(1): p. 212-213.

18. Ballottari, M., et al., *Evolution and functional properties of Photosystem II light harvesting complexes in eukaryotes.* Biochimica et Biophysica Acta (BBA) - Bioenergetics, 2012. **1817**(1): p. 143-157.

19. Jassby, A.D. and T. Platt, *Mathematical Formulation of the Relationship Between Photosynthesis and Light for Phytoplankton.* Limnology and Oceanography, 1976. **21**(4): p. 540-547.

20. Wilhelm, C., et al., *Minireview Photophysiology and primary production of phytoplankton in freshwater.* Physiologia Plantarum, 2004. **120**(3): p. 347-357.

21. Sarovar, M., et al., *Quantum entanglement in photosynthetic light-harvesting complexes.* Nat Phys, 2010. **6**(6): p. 462-467.

22. Masiuk, N.P., *Морфология, систематика, экология, географическое распространение рода Dunaliellia Teod. и перспективы его практического использования*. 1973, Kiev: Naukova dumka (Akademiia nauk Ukraïns'koï RSR).

23. Teodorescu, E.C., *Observations morphologiques et biologiques sur le genre Dunaliella.* Revue Générale de Botanique, ed. G.M. Bonnier. Vol. 18. 1906, Paris: Librairie générale de l'enseignement.

24. Chakalov, G., *Elsevier's dictionary of science and technology. Russian-English*. 1993, Amersterdam; New York: Elsevier.

25. Hogewoning, S.W., et al., *Blue light dose–responses of leaf photosynthesis, morphology, and chemical composition of Cucumis sativus grown under different combinations of red and blue light.* Journal of Experimental Botany, 2010. **61**(11): p. 3107-3117.

26. Saidak, T., *Biofuels Digest: Rio Tinto adds biodiesel at Aussie mining operations*. 2010, Newstex: Chatham.

27. Anonymous *Brazil's Vale To Invest $305 Million In Biodiesel Project*. 2009.

28. *Canada's Energem acquires jatropha biodiesel project in Mozambique.* Ethanol & Biodiesel News, 2007. **XIX**(32).

29. Schill, S.R. *Gaining Traction*. Biodisesel Magazine, 2008.

30. Gutzke, K. *Is biodiesel the answer*. Australasian Mining Review, 2013.

31. Anonymous, *Komatsu, Adaro, United Tractors Sign Biodiesel Fuel Agreement.* Clean Technology Insight, 2009.

32. Sapp, M., *Biofuels Digest: Indonesia pushes biodiesel for mining companies as mandate looms*. 2012, Newstex: Chatham.

33. Mclvor, A. *Mining and Energy*. Cleantech Magazine, 2010.

34. Volesky, B. and Z.R. Holan, *Biosorption of Heavy Metals.* Biotechnology Progress, 1995. **11**(3): p. 235-250.

35. Wang, J. and C. Chen, *Biosorbents for heavy metals removal and their future.* Biotechnology Advances, 2009. **27**(2): p. 195-226.

36. Bethmann, B. and G. Schönknecht, *pH regulation in an acidophilic green alga – a quantitative analysis.* New Phytologist, 2009. **183**(2): p. 327-339.

37. Doshi, H., et al., *Bioaccumulation of Heavy Metals by Green Algae.* Current Microbiology, 2008. **56**(3): p. 246-55.

38. Doward, J. *Groundbreaking biofuel project brings new life to Cornish mine*. The Guardian, 2014.

39. Bardi, U., *The Mineral Question: How Energy and Technology will determine the Future of Mining.* Frontiers in Energy Research, 2013. **1**.

40. Administration, U.S.E.I. *Petrolieum & Other Liquids*. Independent Statistics & Analysis, 2015.

41. Rudenno, V., *Indicative capital and operating ocsts*, in *Mining Valuation Handbook : Mining and Energy Valuation for Investors and Management.* 2012, John Wiley & Sons: Milton, QLD, AUS. p. 152-233.

42. Kecojevic, V., I. Vukotic, and D. Komljenovic, *Production, consumption and cost of energy for surface mining of bituminous coal.* Mining Engineering, 2014. **66**(1): p. 51-57.

43. Yépez-García, R.A. and J. Dana, *Directions in Development : Mitigating Vulnerability to High and Volatile Oil Prices : Power Sector Experience in Latin America and the Caribbean*. 2012, Herndon, VA, USA: World Bank Publications.

44. Deffeyes, K.S., E. Publishing, and I. ebrary, *Hubbert's peak: the impending world oil shortage*. Vol. [New].; STU - Studentition. 2009, Princeton, N.J: Princeton University Press.

45. Australian, G., *2015 Energy White Paper* D.o.I.a. Science, Editor. 2015, Commonwealth of Australia: Caberra, ACT. p. 84.

46. Science, A.G.D.o.I.a. *Mining*. 2015 [cited 2015 08/29/2015]; Available from: http://eex.gov.au/industry-sectors/mining/.

47. South Africa, R.o., *National Energy Act (34/2008): Published for public comments: Draft Regulations regarding Registration, Reporting on Energy Management and Submission of Energy Management Plans*, Energy, Editor. 2015, The Government Printing Works: Pretoria.

48. Sapp, M. *Biofuels Digest: Blue Horizon divests mines to focus on biodiesel*. Biofuels Digest, 2012.

49. *Eni Signs coorporation agreements with Sonagol*. 2011.

50. Limited, H.G.M.C., *Annual Inegrated Report*. 2014.

51. Gurgenci, H. and S.M. Aminossadati, *Investigating the Use of Methane as Diesel Fuel in Off-Road Haul Road Truck Operations.* Journal of Energy Resources Technology, 2009. **131**(3): p. 032202-9.

52. Mclvor, A. *Anglo Platinum: Promoting innovative fuel cell applications in South Africa, in mining - and beyond*. Cleantech Magazine, 2010. **Fuel Cell Special**.

53. Preiss, M.R. and S.P. Kowalski, *Algae and Biodiesel: Patenting energized as green goes commercial.* Journal of Commercial Biotechnology, 2010. **16**(4): p. 293-312.

54. Williams, P.J.l.B. and L.M.L. Laurens, *Microalgae as biodiesel & biomass feedstocks: Review & analysis of the biochemistry, energetics & economics*. Energy & Environmental Science, 2010. **3**(5): p. 554-590.

55. Fortescue Metals Groups LTD, D.E.M.P.L.a.L.C.P.L., *Analysis of Diesel Use for Mine Haul and Transport Operations*, E.a.T. Austrailian Government; Department of Resources, Editor. 2011.

56. Lasky, S.G., *How tonnage and grade relations help predict ore reserves.* Engineering and Mining Journal, 1950. **151**(4): p. 81-85.

57. *Preliminary Regulatory Economic Analysis and Preliminary Regulatory Flexibility Analysis Proposed Rule on 30 CFR Part 57 Diesel Particulat Matter Exposure of Underground Metal and Nonmetal Miners*, U.S.D.o. Labor, Editor. 2003.

58. *Fuel cell mine locomotive passes initial tests.* Fuel Cells Bulletin, 2002. **2002**(10): p. 5-6.

59. Harry, H., *Mining With Gas.* Mechanical Engineering, 2005. **127**(3): p. 12-12.

60. Miller, A.R., *Tunneling and mining applications of fuel cell vehicles.* Fuel Cells Bulletin, 2000. **3**(22): p. 5-9.

61. Anonymous, *Vale to invest in Biodiesel.* International Railway Journal, 2009. **49**(8): p. 7.

62. Bugarski, A.D., et al., *Aerosols Emitted in Underground Mine Air by Diesel Engine Fueled with Biodiesel.* Journal of the Air & Waste Management Association, 2010. **60**(2): p. 237-44.

63. Schultz, M.J., et al., *Using Biodiesel Fuels to Reduce DPM Concentrations; DPM Results Using Various Blends of Biodiesel Fuel Mixtures in a Stone Mine* M.S.a.H. Administration, Editor.

64. Hobbs, C.H., *Final Report: Tier 2 Testing o fBiodiesel Exhaust Emissions*. 2000.

65. Korotney, D., *A Comprehenisve Analsysis of Biodiesel Impacts on Exhausts Emission*. 2002, U.S. EPA National Vehicle and Fuel Emissions Laboratory.

66. *Summary Results from NBB/USEPA Tier 1 Health and Environment Effects Testing for Biodiesel Under the Requireemnts for USEPA Registration of Fuels and Fuel Additives (40 CFR Part 79, Sec 21 1 (b)(2) and 211 (3)) Final Report*. 1998, National Biodiesel Board: Jefferson City, MO USA.

67. Finch, G.L., et al., *EFFECTS OF SUBCHRONIC INHALATION EXPOSURE OF RATS TO EMISSIONS FROM A DIESEL ENGINE BURNING SOYBEAN OIL-DERIVED BIODIESEL FUEL.* Inhalation Toxicology, 2002. **14**(10): p. 1017-1048.

68. The University of California, D. and B. The University of California, *California Biodiesel Multimedia Evaluation Tier I Report*. 2009.

69. Attfield, M.D., et al., *The Diesel Exhaust in Miners Study: A Cohort Mortality Study With Emphasis on Lung Cancer.* Journal of the National Cancer Institute, 2012. **104**(11): p. 869-883.

70. Silverman, D.T., et al., *The Diesel Exhaust in Miners Study: A Nested Case–Control Study of Lung Cancer and Diesel Exhaust.* Journal of the National Cancer Institute, 2012. **104**(11): p. 855-868.

71. *IARC Monographs on the Evaluation of Carcinogenic Risks to Humans*. Vol. 100. 2012, Geneva, Switzerland: WHO Press.

72. Traviss, N., et al., *Biodiesel versus Diesel: A Pilot Study Comparing Exhaust Exposures for Employees at a Rural Municipal Facility.* Journal of the Air & Waste Management Association, 2010. **60**(9): p. 1026-33.

73. Bugarski, A.D., et al., *The Effectiveness of Slected Technologies Controling Diesel Emissions in an Underground- Isolated Zone Studey at Stillwater Mining Company's Nye Mine*, in *Final Report to Metal/Nometal Diesel Partnership*. 2004, National Institute of Occupational Safety and Health (NIOSH): Pittsburg, PA USA.

74. Tollinsky, N. *Biofuel goes underground*. Sudbury Mining Solutions Journal, 2011.

75. *Biodiesel Clears the Air in Underground Mines*, E.a.E.a.R. energy, Editor. 2009.

76. *Peabody Group Biodiesel Project*. 1999, The Peabody Group, Missouri Soybean Merchandising Council.

77. Fiscor, S., *More U.S. Underground Mines Turn to Biodiesel to Meet New MSHA Standard.* Engineering and Mining Journal, 2008. **209**(7): p. 102-105.

78. Odwyn Jones, I., *Health Challenges facing Underground Hard-rock Mining.* Australian Mining, 2015.

79. Agency, U.S.E.P., *National Emission Inventory (NEI) Air Pollutant Emissions Trend Data*. 2015.

80. Decker, H., et al., *Closing the Diesel Divide: Protecting Public Health From Diesel Air Pollution*. 2003, American Lung Association.

81. *Diesel Particulate Matter Exposure of Underground Coal Miners, Final Rule*, MSHA, Editor. 2001: Federal Register. p. 5706-5910.

82. *Diesel Particulate Matter Exposure of Underground Metal and Nonmetal Miners; Final Rule*, MSHA, Editor. 2001: Federal Register.

83. Williams, A., et al., *Biodiesel Effects on Diesel Particle Filter Performance; Milestone Report*, N.R.E. Laboratory, Editor. 2006: Golden, CO.

84. Boehman, A.L., J. Song, and M. ALam, *Impact of Biodiesel Blending on Diesel Soot and the Regeneration of Particulate Filters.* Energy Fuels 2005. **19**: p. 1857-1864.

85. Bugarski, A.D., S.J. Janisko, and E.G. Cauda, *Curtailment of Diesel Emissions*, in *Controlling Exposure to Diesel Emissions in Underground Mines*2012, Society for Mining Metallurgy and Exploration: Littleton, CO, USA. p. 148-269.

86. Weeks, B., et al., *Soybean Oil, No Longer Just for Cooking- ANSoy vs. ANFO.* The Journal of Explosives Engineering, 1997. **14**(3): p. 14-18.

87. Xia, W., J. Yang, and C. Liang, *Improving Oxidized Coal Flotation Using Biodiesel as a Collector.* International Journal of Coal Preparation & Utilization, 2013. **33**(4): p. 181-187.

88. Alonso, M.I., C. Castano, and A.B. Garcia, *Performance of Vegetable Oils as Flotation Collectors for the Recovery of Coal from Coal Fines Wastes.* Coal Preparation, 2000. **21**(4): p. 411-420.

89. Das, B. and P.S.R. Reddy, *The Utilization of Non-coking Coal by Flotation Using Non-conventional Reagents.* Energy Sources Part A: Recovery, Utilization & Environmental Effects, 2010. **32**(19): p. 1784-1793.

90. Energy Information, A., *Short-Term Energy Outlook;2015 ASI 3162-34*. 2015.

91. Congress, U.S., *Renewable Fuel Standard, as Amended by 2007 Energy Independence and Security Act (RSF2),* in *40*, U.S.E.P. Agency, Editor. 2012.

92. Roessler, M., *Allowable Biodiesel Blend Information Request- Liebherr Mining Equipment*, D.J. Vidt, Editor. 2015: Newport News, VA USA.

93. *Caterpillar showcases its 938K wheel Loader at the 2014 National Biodiesel Conference*. Consumer/Dealer/Product News, 2014.

94. *Every Advantage. Biodisel for Cummins Engines*. 2012, Cummins Inc.

95. Carter, R.A., *Can Biofuels Help Reduce Rising Mine Fleet Operating Costs?* Engineering and Mining Journal, 2006. **207**(2): p. 50-53.

96. Meenakshi, H.N., et al., *Corrosion Of Metals In Biodiesel From Pongamia Pinnata*. NACE International.

97. Sørensen, G., et al., *Microbial growth studies in biodiesel blends.* Bioresource Technology, 2011. **102**(8): p. 5259-5264.

98. Schleicher, T., et al., *Microbiological stability of biodiesel–diesel-mixtures.* Bioresource Technology, 2009. **100**(2): p. 724-730.

99. Chupka, G.M., et al., *Effects of Saturated Monoglyceride Polymorphism on Low-Temperature Performance of Biodiesel.* Energy & Fuels, 2011. **25**(1): p. 398-405.

100. Stansell, G., V. Gray, and S. Sym, *Microalgal fatty acid composition: implications for biodiesel quality.* Journal of Applied Phycology, 2012. **24**(4): p. 791-801.

101. Demirbas, A., *Progress and recent trends in biodiesel fuels.* Energy Conversion and Management, 2009. **50**(1): p. 14-34.

102. Pullen, J. and K. Saeed, *An overview of biodiesel oxidation stability.* Renewable and Sustainable Energy Reviews, 2012. **16**(8): p. 5924-5950.

103. Yaakob, Z., et al., *A review on the oxidation stability of biodiesel.* Renewable and Sustainable Energy Reviews, 2014. **35**: p. 136-153.

104. Validakis, V., *Biodiesel and its future in mining.* Australian Mining, 2012.

105. Spear, S.K., et al., *Renewable plant-based soybean oil methyl esters as alternatives to organic solvents.* Green Chemistry, 2007. **9**(9): p. 1008-1015.

106. Feinberg, D.A., *Fuel Options from Microalgae with Representative Chemical Compositions*. 1984, Midwest Research Institute: Golden.

107. Mauderly, J.L. and J.C. Chow, *Health Effects of Organic Aerosols.* Inhalation Toxicology, 2008. **20**(3): p. 257-288.

108. Swanson, K.J., M.C. Madden, and A.J. Ghio, *Biodiesel Exhaust: The Need for Health Effects Research.* Environmental Health Perspectives, 2007. **115**(4): p. 496-499.

109. Mauderly, J., et al., *Oxidative Stress, Inflammation, and Pulmonary Function Assessment in Rats Exposed to Laboratory-Generated Pollutant Mixtures.* Journal of Toxicology and Environmental Health, Part A, 2008. **71**(20): p. 1352-1362.

110. Elena, R.K., et al., *Mutagenicity of biodiesel or diesel exhaust particles and the effect of engine operating conditions.* journal of Environmental Engineering and Ecological Science, 2013. **2**(1).

111. Rose, P.D., et al., *An integrated algal sulphate reducing high rate ponding process for the treatment of acid mine drainage wastewaters.* Biodegradation, 1998. **9**(3-4): p. 247-257.

112. (INAP), I.N.f.A.P., *The Global Acid Rock Drainage Guide*. 2009.

113. *Best Available Pollution Control Technology*. 1992, The Environmental Applications Group LTD: Ontario. p. 64-66.

114. *Innovative Methods of Managing Environmental Releases at Mine Sites*. 1994, U.S. Environmental Protection Agency: Washington, D.C. p. 66-83.

115. Brierley, C.L., *Metal's Bioremediation*, in *New Remediation Technology in the Changing Environmental Arena*, B.J. Scheiner, et al., Editors. 1995, Society for Mining, Metallurgy, and Exploration, Inc.: Littleton, Colorado, USA. p. 205-209.

116. Gearheart, R., et al., *Free Water Surface Wetlands for Wastewater Treatment; A technology Assesment*, U.S.E.P. Agency and U.S.D.o.t. Interior, Editors. 1999: Phoenix, AZ USA.

117. Lottermoser, B.G., *Mine Wastes Characterization, Treatment, Environmental Impacts*. 2nd ed. 2007, Berlin; London: Springer.

118. Bruch, I., et al., *Improving the treatment efficiency of constructed wetlands with zeolite-containing filter sands.* Bioresource Technology, 2011. **102**(2): p. 937-941.

119. Mote, G., et al., *Constructed Wetlands: Classification, Functions and Treatement*, in *Constructed Wetlands*, J.K.a.S. Vigneswaran, Editor. 2009, Nova Science Publishers, Inc.: New York, NY, USA. p. 1-27.

120. Hijosa-Valsero, M., et al., *Statistical modelling of organic matter and emerging pollutants removal in constructed wetlands.* Bioresource Technology, 2011. **102**(8): p. 4981-4988.

121. Craggs, R.J., T. Lundquist, and J. Benemann, *Wastewater Treatment Pond Algal Production for Biofuel*, in *The Science of Algal Fuels*, R. Gordon and J. Seckbach, Editors. 2012, Springer Netherlands. p. 425-445.

122. Sivakumar, G., et al., *Integrated green algal technology for bioremediation and biofuel.* Bioresource Technology, 2012. **107**(0): p. 1-9.

123. Lohrey, C. and V. Kochergin, *Biodiesel production from microalgae: Co-location with sugar mills.* Bioresource Technology, 2012. **108**(0): p. 76-82.

124. Travieso, L., F. Benitez, and R. Dupeyrón, *Algae growth potential measurement in distillery wastes.* Bulletin of Environmental Contamination and Toxicology, 1999. **62**(4): p. 483-489.

125. Rawat, I., et al., *Dual role of microalgae: Phycoremediation of domestic wastewater and biomass production for sustainable biofuels production.* Applied Energy, 2011. **88**(10): p. 3411-3424.

126. Demirbas, M.F., *Biofuels from algae for sustainable development.* Applied Energy, 2011. **88**(10): p. 3473-3480.

127. Benoth, L., et al., *Biotechnologies for Remediation and Pollution Control in the Mining Industry*, in *Mineral Biotechnology - Microbial Aspects of Mineral Beneficiation, Metal Extraction, and Environmental Control*, S.K. Kawatra and K.A. Natarajan, Editors. 2001, Society for Mining, Metallurgy, and Exploration (SME). p. 207-218.

128. Gilbertson, B.P., *Creating value through innovation: biotechnology in mining.* Mineral Processing and Extractive Metallurgy, 2000. **109**(2): p. 61-67.

129. Allert, A.L., et al., *Effects of mining-derived metals on riffle-dwelling benthic fishes in Southeast Missouri, USA.* Ecotoxicology and Environmental Safety, 2009. **72**(6): p. 1642-1651.

130. Chang-Sheng, Q., et al., *Human Exposure Pathways of Heavy Metals in a Lead-Zinc Mining Area, Jiangsu Province, China.* PLoS ONE, 2012. **7**(11): p. 1-11.

131. Cooksey, C., *Health concerns of heavy metals and metalloids.* Science Progress, 2012. **95**(1): p. 73.

132. Rout, T.K., et al., *Heavy metals in dusts from commercial and residential areas of Jharia coal mining town.* Environmental Earth Sciences, 2015. **73**(1): p. 347-359.

133. Adamu, C.I., T.N. Nganje, and A. Edet, *Heavy metal contamination and health risk assessment associated with abandoned barite mines in Cross River State, southeastern Nigeria.* Environmental Nanotechnology, Monitoring & Management, 2015. **3**: p. 10-21.

134. Hendryx, M., K. O'Donnell, and K. Horn, *Lung cancer mortality is elevated in coal-mining areas of Appalachia.* Lung Cancer, 2008. **62**(1): p. 1-7.

135. Bhatnagar, A., et al., *Valorisation of marine Pelvetia canaliculata Ochrophyta for separation and recovery of nickel from water: Equilibrium and kinetics modeling on Na-loaded algae.* Chemical Engineering Journal, 2012. **200–202**(0): p. 365-372.

136. Travieso, L., R.O. Cañizares, and R. Borja, *Heavy metal removal by microalgae.* Bulletin of Environmental Contamination and Toxicology, 1999. **62**(2): p. 144-151.

137. Anonymous, *Engineered algea removes metal.* Chemical Engineering Progress, 1999. **95**(5): p. 15-15.

138. Environment, O.M., *Best available pollution control technology - industrial minerals sector*. 2nd ed. ed. 1993, Toronto, ON: Kilborn Inc. and Environmental Applications Group Ltd.

139. Volesky, B., *Detoxification of metal-bearing effluents: biosorption for the next century.* Hydrometallurgy, 2001. **59**(2–3): p. 203-216.

140. Vieira, R.H.S.F. and B. Volesky, *Biosoprtion: a solution to pollution?* International Microbiology, 2000. **3**(1): p. 17-24.

141. Romera, E., et al., *Biosorption with Algae: A Statistical Review.* Critical Reviews in Biotechnology, 2006. **26**(4): p. 223-235.

142. Darnall, D.W., et al., *Selective recovery of gold and other metal ions from an algal biomass.* Environmental Science & Technology, 1986. **20**(2): p. 206-208.

143. Khani, M., *Uranium biosorption by Padina sp. algae biomass: kinetics and thermodynamics.* Environmental Science and Pollution Research, 2011. **18**(9): p. 1593-1605.

144. Khani, M.H., et al., *Biosorption of uranium from aqueous solutions bynonliving biomass of marinealgae Cystoseira indica.* Electronic Journal of Biotechnology, 2006. **9**(2): p. 100-106.

145. Kilbane, J.J.I., *A biosystem for removal of metal ions from water*. 1990. Medium: ED; Size: Pages: (26 p).

146. Wu, Y., T. Li, and L. Yang, *Mechanisms of removing pollutants from aqueous solutions by microorganisms and their aggregates: A review.* Bioresource Technology, 2012. **107**(0): p. 10-18.

147. Anastopoulos, I. and G.Z. Kyzas, *Progress in batch biosorption of heavy metals onto algae.* Journal of Molecular Liquids, 2015. **209**(0): p. 77-86.

148. Mehta, S.K. and J.P. Gaur, *Use of Algae for Removing Heavy Metal Ions From Wastewater: Progress and Prospects.* Critical Reviews in Biotechnology, 2005. **25**(3): p. 113-152.

149. Davis, T.A., B. Volesky, and A. Mucci, *A review of the biochemistry of heavy metal biosorption by brown algae.* Water Research, 2003. **37**(18): p. 4311-4330.

150. Andrade, A.D., M.C.E. Rollemberg, and J.A. Nobrega, *Proton and metal binding capacity of the green freshwater alga Chaetophora elegans.* Process Biochemistry, 2005. **40**(5): p. 1931-1936.

151. Haug, A., *The Affinity of some Divalent Metals for Different Types of Alginates.* Acta Chemica Scandinavica, 1961. **15**(8): p. 1794-1795.

152. Gardea-Torresdey, J.L., et al., *Ability of immobilized cyanobacteria to remove metal ions from solution and demonstration of the presence of metallothionein genes in various strains.* Journal of Hazerdous Substance Research, 1998. **1**(2): p. 1-18.

153. Sakamoto, N., N. Kano, and H. Imaizumi, *Biosorption of uranium and rare Earth elements using biomass of algae.* Bioinorg Chem Appl, 2008: p. 706240.

154. Carvalho, A.P., C.M. Monteiro, and F.X. Malcata, *Simultaneous effect of irradiance and temperature on biochemical composition of the microalga Pavlova lutheri.* Journal of Applied Phycology, 2009. **21**(5): p. 543-552.

155. Kaplan, D., D. Christiaen, and S. Arad, *Chelating Properties of Extracellular Polysaccharides from Chlorella spp* Applied and Environmental Microbiology, 1987. **53**(12): p. 2953-2956.

156. Jaroslawiecka, A. and Z. Piotrowska-Seget, *Lead resistance in micro-organisms.* Microbiology, 2014. **160**(1): p. 12-25.

157. Freire-Nordi, C.S., A.A.H. Vieira, and O.R. Nascimento, *SELECTIVE PERMEABILITY OF THE EXTRACELLULAR ENVELOPE OF THE MICROALGA SPONDYLOSIUM PANDURIFORME (CHLOROPHYCEAE) AS REVEALED BY ELECTRON PARAMAGNETIC RESONANCE.* Journal of Phycology, 1998. **34**(4): p. 631-637.

158. Hernández-Carmona, G., et al., *Monthly variation in the chemical composition of Eisenia arborea J.E. Areschoug.* Journal of Applied Phycology, 2009. **21**(5): p. 607-616.

159. Park, J.B.K. and R.J. Craggs, *Wastewater treatment and algal production in high rate algal ponds with carbon dioxide addition.* Water Science & Technology, 2010. **61**(3): p. 633-639.

160. El Hafiane, F., A. Rami, and B. El Hamouri, *Mechanisms of nitrogen and phosphorus removal in a high rate algal pond.* Revue des Sciences de l'Eau, 2003. **16**(2): p. 157-172.

161. Mulbry, W., et al., *Treatment of dairy manure effluent using freshwater algae: Algal productivity and recovery of manure nutrients using pilot-scale algal turf scrubbers.* Bioresource Technology, 2008. **99**(17): p. 8137-8142.

162. Kangas, P. and W. Mulbry, *Nutrient removal from agricultural drainage water using algal turf scrubbers and solar power.* Bioresource Technology, 2014. **152**: p. 484-489.

163. Hauska, G., *[62] Measurement of phosphorylation associated with photosystem I*, in *Methods in Enzymology*, P. Anthony San, Editor. 1980, Academic Press. p. 648-658.

164. Crist, R.H., et al., *Interaction of Metals and Protons with Algae. 4. Ion Exchange vs Adsorption Models and a Reassessment of Scatchard Plots; Ion-Exchange Rates and Equilibria Compared with Calcium Alginate.* Environmental Science & Technology, 1994. **28**(11): p. 1859-1866.

165. Ashley, J. and S.R. Rushforth, *Growth of Soil Algae on Top Soil and Processed Oil Shale from the Utah Basin Utah USA.* Reclamation & Revegetation Research, 1984. **3**(1): p. 49-64.

166. Kothari, R., et al., *Experimental study for growth potential of unicellular alga Chlorella pyrenoidosa on dairy waste water: An integrated approach for treatment and biofuel production.* Bioresource Technology, 2012. **116**(0): p. 466-470.

167. Singh, A., S.K. Mehta, and J.P. Gaur, *Removal of heavy metals from aqueous solution by common freshwater filamentous algae.* World Journal of Microbiology and Biotechnology, 2007. **23**(8): p. 1115-1120.

168. Ting, Y.P., I.G. Prince, and F. Lawson, *Uptake of cadmium and zinc by the alga Chlorella vulgaris: II. Multi-ion situation.* Biotechnology and Bioengineering, 1991. **37**(5): p. 445-455.

169. Hadley, R.F. and D.T. Snow. *Water Resource Problems Related to Mining*. in *A symposium American Water Resources Association*. 1974. Denver, CO USA: American Water Resources Association.

170. Azov, Y., G. Shelef, and N. Narkis, *Effect of Hard Detergents on Algae in a High-Rate-Oxidation Pond.* Applied and Environmental Microbiology, 1982. **43**(2): p. 491-492.

171. Mohammady, N.-E., et al., *Temporal alterations of Nannochloropsis salina (Eustigmatophyceae) grown under aqueous diesel fuel stress.* Journal of Applied Phycology, 2005. **17**(2): p. 161-170.

172. Chmielewská, E. and J. Medved', *Bioaccumulation of Heavy Metals by Green Algae Cladophora glomerata in a Refinery Sewage Lagoon.* Croatica Chemica Acta, 2001. **74**(1): p. 135-145.

173. Gjessing, E.T., et al., *Bioavailability of aluminium in the presence of humic substances at low and moderate pH.* Science of The Total Environment, 1989. **81–82**(0): p. 683-690.

174. Selenska-Pobell, S., et al., *Selective accumulation of heavy metals by three indigenous Bacillus strains, B. cereus, B. megaterium and B. sphaericus, from drain waters of a uranium waste pile.* FEMS Microbiology Ecology, 1999. **29**(1): p. 59-67.

175. Fytianos, K., E. Evgenidou, and G. Zachariadis, *Use of macroalgae as biological indicators of heavy metal pollution in Thermaikos Gulf, Greece.* Bulletin of Environmental Contamination and Toxicology, 1999. **62**(5): p. 630-637.

176. Morin, K.A. and N.M. Hutt, *Mine-water leaching of nitrogen species from explosive residues*, in *GeoHalifax 2009, the 62nd Canadian Geotechnical Conference, and 10th Joint GCS/IAH-CNC Groundwater Conference*. 2009: Halifax, Nova Scotia, Canada. p. 1549-1553.

177. Revey, G.F., *Practical methods to control explosives losses and reduce ammonia and nitrate levels in mine water.* Mining Engineering, 1996. **48**: p. 61-64.

178. Forsyth, B., A. Cameron, and S. Miller, *Explosives and Water Quality*, in *Sudbury '95: Mining and the environment*, T.P. Hynes and M.C. Blanchette, Editors. 1995, CANMET Laurentian University: Sudbury, Canada. p. 795-803.

179. Houser, J.B., et al., *Wastewater Remediation Using Algae Grown on a Substrate for Biomass and Biofuel Production.* Journal of Environmental Protection, 2014. **5**(10): p. 897-906.

180. D'Aiuto, P.E., et al., *Algal turf scrubbers: Periphyton production and nutrient recovery on a South Florida citrus farm.* Ecological Engineering, 2015. **75**: p. 404-412.

181. Sutherland, D.L., et al., *Wastewater microalgal production, nutrient removal and physiological adaptation in response to changes in mixing frequency.* Water Research, 2014. **61**: p. 130-140.

182. Ray, N.E., D.E. Terlizzi, and P.C. Kangas, *Nitrogen and phosphorus removal by the Algal Turf Scrubber at an oyster aquaculture facility.* Ecological Engineering, 2015. **78**: p. 27-32.

183. Gehring, T., et al., *Modelling waste stabilisation ponds with an extended version of ASM3.* Water Science & Technology, 2010. **61**(3): p. 713-720.

184. Watanobe, M., et al., *Luxury phosphate uptake and variation of intracellular metal concentrations in Heterosigma akashiwo (raphidophyceae).* Journal of Phycology, 1989. **25**(3): p. 428-436.

185. Calloway, A. *Picatinny Arsenal engineers cook up new recipe for biofuel*. Picatinny Aresenal Public Affairs, 2015.

186. Vranesh, G. *Mine Drainage: The Common Enemy*. in *First International Mine Drainage Symposium*. 1979. Denver, CO USA: Freeman.

187. Williams, R.E., *Waste production and disposal in mining, milling, and metallurgical industries*. 1975, San Francisco: Miller Freeman Publications.

188. Jacobs, J.A., J.H. Lehr, and S.M. Testa, *Acid Mine Drainage, Rock Drainage, and Acid Sulfate Soils : Causes, Assessment, Prediction, Prevention, and Remediation*. 2014, Somerset, NJ, USA: John Wiley & Sons, Incorporated.

189. Evangelou, V.P., *Pyrite Oxidation and Its Control*. 1995, New York: CRC Press.

190. Strumm, W. and J.J. Morgan, *Aquatic Chemistry: Chemical equilibria and rates in natural waters*. 3rd ed. Environmental Science and Technology. 1996, New York: Wiley.

191. Williams, R.E., J. Baldwin, and D.R. Ralston. *Coping with Mine Drainage Regulations*. in *Proceedings of the First International Mine Drainage Symposium*. 1979. Denver, CO USA: San Francisco (Freeman).

192. Association, C.M., *Mine waste management: a resource for mining industry professionals, regulators, and consulting engineers*, ed. I.P.G. Hutchison and R.D. Ellison. 1992, Boca Raton: Lewis Publishers.

193. McLemore, V.T., *Basics of Metal Mining Influanced Water*. Management technologies for metal mining influenced water. Vol. 1. 2008, Littleton, CO USA: Society for Mining, Metallurgy, and Exploration.

194. Schippers, A. and W. Sand, *Bacterial Leaching of Metal Sulfides Proceeds by Two Indirect Mechanisms via Thiosulfate or via Polysulfides and Sulfur.* Applied and Environmental Microbiology, 1999. **65**(1): p. 319-321.

195. Zawadzki, E.A. and R.A. Glenn, *Sulfide Treatement of Acid Mine Drainage.* Bituminous Coal Res. Inc. Final Report L-290 to the Appalachian Regional Commission and the U.S. Department of the Interior, 1968(FWPCA): p. 94.

196. *Acid Mine Water + Limestone = Clean Stream.* Coal Age, 1969. **74**(2): p. 112-194.

197. Healey, F.P., *Inorganic Nutrient Uptake and Deficiency in Algae.* CRC Critical Reviews in Microbiology, 1973. **3**(1): p. 69-113.

198. Andersen, R.A. and M. Kawachi, *Traditional Microalgae Isolation Techniques*, in *Algal Culturing Techniques*, R.A. Andersen, Editor. 2005, Elsevier Academic Press: BurlingtonSan DiegoLondon. p. 83-101.

199. Soria-Dengg, S. and U. Horstmann, *Ferrioxamines B and E as iron sources for the marine diatom Phaeodactylum tricornutum.* Marine Ecology Progress Series, 1995. **127**: p. 269-277.

200. Fisher, M., A. Zamir, and U. Pick, *Iron Uptake by the Halotolerant Alga Dunaliella Is Mediated by a Plasma Membrane Transferrin.* Journal of Biological Chemistry, 1998. **273**(28): p. 17553-17558.

201. Azov, Y., *Effect of pH on Inorganic Carbon Uptake in Algal Cultures.* Applied and Environmental Microbiology, 1982. **43**(6): p. 1300-1306.

202. Bäuerlein, E., *Biomineralization of Unicellular Organisms: An Unusual Membrane Biochemistry for the Production of Inorganic Nano- and Microstructures.* Angewandte Chemie International Edition, 2003. **42**(6): p. 614-641.

203. Sistani, K.R. and R.W. Taylor, *Crop Recovery of Nitrogen-15 from Microalgae Grown in Simulated Inorganic-Wastewater Medium.* Journal of Environmental Science & Health Part A Environmental Science & Engineering, 1988. **23**(8): p. 745-756.

204. Wang, Q., et al., *Studies on mixed mass cultivation of Anabaena spp. (nitrogen-fixing blue-green algae, cyanobacteria) on a large scale.* Bioresource Technology, 1991. **38**(2–3): p. 221-228.

205. Lehmann, J. and S. Joseph, *Biochar for environmental management: science, technology and implementation*. 2015, London, New York: Taylor & Francis Group.

206. Lehmann, J. and M. Rondon, *Bio-Char Soil Management on Highly Weathered Soils in the Humid Tropics*, in *Biological Approaches to Sustainable Soil Systems*, N. Uphoff, et al., Editors. 2006, CRC Press: Boca Raton. p. 517-529.

207. Okibe, N. and D.B. Johnson, *Toxicity of flotation reagents to moderately thermophilic bioleaching microorganisms.* Biotechnology Letters, 2002. **24**(23): p. 2011-2016.

208. Kureyshevich, A.V. and V.P. Guseynova, *Influence of Oil Products on the Growth and Content of Pigments in the Cultures of Microcystis aeruginosa Kütz. emend. Elenk. and Desmodesmus armatus (Chod.) Hegew*. Hydrobiological Journal, 2008. **44**(4): p. 70-80.

209. Zhou, G.J., et al., *Cellular responses and bioremoval of nonylphenol and octylphenol in the freshwater green microalga Scenedesmus obliquus.* Ecotoxicology and Environmental Safety, 2013. **87**(0): p. 10-16.

210. Pinto, E., et al., *Review Heavy metal–induced oxidative stress in algae.* Journal of Phycology, 2003. **39**(6): p. 1008-1018.

211. Niyogi, D.K., W.M. Lewis, Jr., and D.M. McKnight, *Effects of stress from mine drainage on diversity, biomass, and function of primary producers in mountain streams.* Ecosystems, 2002. **5**(6): p. 554-567.

212. Messerli, M.A., et al., *Life at acidic pH imposes an increased energetic cost for a eukaryotic acidophile.* Journal of Experimental Biology, 2005. **208**(13): p. 2569-2579.

213. Langner, U.W.E., et al., *An energy balance from absorbed photons to new biomass for Chlamydomonas reinhardtii and Chlamydomonas acidophila under neutral and extremely acidic growth conditions.* Plant, Cell & Environment, 2009. **32**(3): p. 250-258.

214. Hammaini, A., et al., *Biosorption of heavy metals by activated sludge and their desoprtion characteristics.* Journal of Environmental Management, 2007. **84**: p. 419-426.

215. Younger, P.L., S.A. Banwart, and R.S. Hedin, *Mine Water Hydrology*, in *Mine Water*. 2002, Springer Netherlands. p. 127-270.

216. Geidel, G. and F.T. Caruccio, *Geochemical Factors Affecting Coal Mine Drainage Quality*, in *Reclamation of Drastically Disturbed Lands*, R.I. Barnhisel, R.G. Darmody, and W.L. Daniels, Editors. 2000. p. 105-129.

217. Lee, C.-G. and B.Ø. Palsson, *High-density algal photobioreactors using light-emitting diodes.* Biotechnology and Bioengineering, 1994. **44**(10): p. 1161-1167.

218. Richmond, A. and N. Zou, *Efficient utilisation of high photon irradiance for mass production of photoautotrophic micro-organisms.* Journal of Applied Phycology, 1999. **11**(1): p. 123-127.

219. Gordon, J.M. and J.E.W. Polle, *Ultrahigh bioproductivity from algae.* Applied Microbiology & Biotechnology, 2007. **76**(5): p. 969-975.

220. Baba, M., et al., *Wavelength specificity of growth, photosynthesis, and hydrocarbon production in the oil-producing green alga Botryococcus braunii.* Bioresource Technology, 2012. **109**(0): p. 266-270.

221. Oh, S.J., et al., *Effects of irradiance of various wavelengths from light-emitting diodes on the growth of the harmful dinoflagellate Heterocapsa circularisquama and the diatom Skeletonema costatum.* Fisheries Science, 2008. **74**(1): p. 137-145.

222. Bezerra, R.P., et al., *Effects of photobioreactor configuration, nitrogen source and light intensity on the fed-batch cultivation of Arthrospira (Spirulina) platensis. Bioenergetic aspects.* Biomass and Bioenergy, 2012. **37**(0): p. 309-317.

223. Bezerra, R.P., et al., *Effects of light intensity and dilution rate on the semicontinuous cultivation of Arthrospira (Spirulina) platensis. A kinetic Monod-type approach.* Bioresource Technology, 2011. **102**(3): p. 3215-3219.

224. Brindley, C., F.G. Acién Fernández, and J.M. Fernández-Sevilla, *Analysis of light regime in continuous light distributions in photobioreactors.* Bioresource Technology, 2011. **102**(3): p. 3138-3148.

225. Grobbelaar, J.U., *The influence of light/dark cycles in mixed algal cultures on their productivity.* Bioresource Technology, 1991. **38**(2-3): p. 189-194.

226. Nedbal, L., et al., *Microscopic green algae and cyanobacteria in high-frequency intermittent light.* Journal of Applied Phycology, 1996. **8**(4-5): p. 325-333.

227. Milligan, A.J. and E.M. Cosper, *Growth and photosynthesis of the 'brown tide' microalga Aureococcus anophagefferens in subsaturating constant and fluctuating irradiance.* Marine Ecology Progress Series, 1997. **153**: p. 67-75.

228. Melis, A., J. Neidhardt, and J. Benemann, *Dunaliella salina (Chlorophyta) with small chlorophyll antenna sizes exhibit higher photosynthetic productivities and photon use efficiencies than normally pigmented cells.* Journal of Applied Phycology, 1998. **10**(6): p. 515-525.

229. Melis, A., *Solar energy conversion efficiencies in photosynthesis: Minimizing the chlorophyll antennae to maximize efficiency.* Plant Science, 2009. **177**(4): p. 272-280.

230. Huner, N.A., G. Öquist, and A. Melis, *Photostasis in Plants, Green Algae and Cyanobacteria: The Role of Light Harvesting Antenna Complexes*, in *Light-Harvesting Antennas in Photosynthesis*, B. Green and W. Parson, Editors. 2003, Springer Netherlands. p. 401-421.

231. Mitra, M. and A. Melis, *Optical properties of microalgae for enhanced biofuels production.* Optics Express, 2008. **16**(26): p. 21807.

232. Nakajima, Y., M. Tsuzuki, and R. Ueda, *Improved productivity by reduction of the content of light-harvesting pigment in Chlamydomonas perigranulata.* Journal of Applied Phycology, 2001. **13**(2): p. 95-101.

233. Park, K.-H. and C.-G. Lee, *Effectiveness of Flashing Light for Increasing Photosynthetic Efficiency of Microalgal Cultures over a Critical Cell Density.* Biotechnology and Bioprocess Engineering, 2001. **6**(3): p. 189-193.

234. Tamburic, B., et al., *Design of a novel flat-plate photobioreactor system for green algal hydrogen production.* International Journal of Hydrogen Energy, 2011. **36**(11): p. 6578-6591.

235. Matthijs, H.C.P., et al., *Applications of Light-Emitting Dodes in Bioreactors: Flashing Light Effects and Energy Economy in Algal Culture (Chlorella pyrenoidosa).* Biotechnology & Bioengineering, 1996. **50**: p. 98-107.

236. Park, K.-H. and C.-G. Lee, *Optimization of algal photobioreactors using flashing lights.* Biotechnology and Bioprocess Engineering, 2000. **5**(3): p. 186-190.

237. Steranka, F.M., et al., *Red (AlGaAs) Light-emitting Diodes.* Hewlett-Packard, 1988. **39**(4): p. 84-88.

238. Zorpette, G., *Blue Chip*, in *Scientific American*. 2000. p. 30.

239. Energy, U.S.D.o., *Revolution Now: The Future Arrives for Five Clean Energy Technologies - 2015 Update.* 2015.

240. Energy, U.S.D.o., *Solid-State Ligting R&D Plan*, E.E.R. Energy, Editor. 2015.

241. Michel, K. and A. Eisentraeger, *Light-emitting diodes for the illumination of algae in ecotoxicity testing.* Environmental toxicology, 2004. **19**(6): p. 609-613.

242. Shikata, T., et al., *Effects of light quality on initiation and development of meroplanktonic diatom blooms in a eutrophic shallow sea.* Marine Biology, 2009. **156**(5): p. 875-889.

243. Wang, C.-Y., C.-C. Fu, and Y.-C. Liu, *Effects of using light-emitting diodes on the cultivation of Spirulina platensis.* Biochemical Engineering Journal, 2007. **37**(1): p. 21-25.

244. Červený, J., et al., *Photobioreactor for cultivation and real-time, in-situ measurement of O2 and CO2 exchange rates, growth dynamics, and of chlorophyll fluorescence emission of photoautotrophic microorganisms.* Engineering in Life Sciences, 2009. **9**(3): p. 247-253.

245. Chen, H.-B., et al., *Modeling on chlorophyll a and phycocyanin production by Spirulina platensis under various light-emitting diodes.* Biochemical Engineering Journal, 2010. **53**(1): p. 52-56.

246. Cuijuan, S., K. Hironao, and D. Delin, *Effects of blue light on gametophyte development of Laminaria japonica (Laminariales, Phaeophyta).* Chinese Journal of Oceanology and Limnology, 2005. **23**(3): p. 323-329.

247. Das, P., et al., *Enhanced algae growth in both phototrophic and mixotrophic culture under blue light.* Bioresource Technology, 2011. **102**(4): p. 3883-3887.

248. Zhang, Y., J. Lee, and S.R. Forrest, *Tenfold increase in the lifetime of blue phosphorescent organic light-emitting diodes.* Nat Commun, 2014. **5**.

249. Schubert, E.F., *Light-Emitting Diodes*. 2nd ed. 2006, New York: Cambridge Unversity Press.

250. Bay, A., et al., *Improved light extraction in the bioluminescent lantern of a Photuris firefly (Lampyridae).* Optics Express, 2013. **21**(1): p. 764-780.

251. Khanna, V.K., *Opportinities and Challenges of Solid-State Lighting*, in *Fundamentals of Solid-State Lighting : LEDs, OLEDs, and Their Applications in Illumination and Displays*2014, CRC Press: London, GBR. p. 491-504.

252. Reilly, T.E., et al., *Ground-Water Availability in the United States*, U.S.G. Survey, Editor. 2008, U.S. Geological Survey: Reston, VA USA. p. 27.

253. Begemann, M.B., et al., *Potential Enhancement of Biofuel Production Through Enzymatic Biomass Degradation Activity and Biodiesel Production by Halophilic Microorganisms*in *Halophiles and Hypersaline Environments*, A. Ventosa, A. Oren, and Y. Ma, Editors. 2011, Springer Berlin Heidelberg. p. 341-357.

254. Oren, A., *A hundred years of Dunaliella research: 1905-2005.* Saline Systems, 2005. **1**: p. 2.

255. Ben-Amotz, A. and M. Avron, *Glycerol and ß-carotene metabolism in the halotolerant alga Dunaliella: a model system for biosolar energy conversion.* Trends in Biochemical Sciences, 1981. **6**(0): p. 297-299.

256. Sun, X., et al., *Expression of the 26S proteasome subunit RPN10 is upregulated by salt stress in Dunaliella viridis.* Journal of Plant Physiology, 2010. **167**(12): p. 1003-1008.

257. Johnson, M.K., et al., *Effects of Salts on the Halophilic Alga Dunaliella viridis.* The Journal of Bacteriology, 1968. **95**(4): p. 1461.

258. Jiménez, C. and F.X. Niell, *Influence of high salinity and nitrogen limitation on package effect and C/N ratio in Dunaliella viridis.* Hydrobiologia, 2003. **492**(1): p. 201-206.

259. Marcano, L.B.C., et al., *Effect of cadmium on cellular viability in two species of microalgae (Scenedesmus sp. and Dunaliella viridis).* Biological trace element research, 2009. **130**(1): p. 86-93.

260. Ginzburg, M., et al., *The Adaptation of Dunaliella to Widely-Differing Salt Concentrations.* Journal of Experimental Botany, 1990. **41**(6): p. 685-692.

261. Aizawa, K. and S. Miyachi, *Photosynthesis: Biochemiocal and Physiological Adaptation*, in *Dunaliella: Physiology, Biochemistry, and Biotechnology*, M. Avron and A. Ben-Amotz, Editors. 1992, CRC Press: Boca Raton, FL. p. 45-47.

262. Jiménez, C., et al., *Phosphorylation of MAP kinase-like proteins mediate the response of the halotolerant alga Dunaliella viridis to hypertonic shock.* BBA - Molecular Cell Research, 2004. **1644**(1): p. 61-69.

263. Gordillo, F.J.L., et al., *Photosynthetic acclimation to photon irradiance and its relation to chlorophyll fluorescence and carbon assimilation in the halotolerant green alga Dunaliella viridis.* Photosynthesis Research, 2001. **68**(3): p. 225-235.

264. Borowitzka, M. and C. Siva, *The taxonomy of the genus Dunaliella (Chlorophyta, Dunaliellales) with emphasis on the marine and halophilic species.* Journal of Applied Phycology, 2007. **19**(5): p. 567-590.

265. Ben-Amotz, A., A. Shaish, and M. Avron, *The biotechnology of cultivating Dunaliella for production of β-carotene rich algae.* Bioresource Technology, 1991. **38**(2–3): p. 233-235.

266. Ben-Amotz, A. and M. Avron, *Accumulation of Metabolytes by Halotolerant Algae and Its Industrial Potential*, in *Annual Review of Microbiology*, L.N. Ornston, A. Balows, and P. Baumann, Editors. 1983, Annual Review Inc.: Palo Alto, California, USA. p. 95-119.

267. Oren, A., *Biotechnological Applications and Potientials of Halophilic Microorganisms*, in *Halophilic Microorganisms and their Environments*. 2002, Kluwer Academic Publishers: New York, New York, U.S.A. p. 357-388.

268. Borowitzka, L. and A. Brown, *The salt relations of marine and halophilic species of the unicellular green alga,Dunaliella.* Archives of Microbiology, 1974. **96**(1): p. 37-52.

269. Tang, H., et al., *Potential of microalgae oil from Dunaliella tertiolecta as a feedstock for biodiesel.* Applied Energy, 2011. **88**(10): p. 3324-3330.

270. Krohn, B.J., et al., *Production of algae-based biodiesel using the continuous catalytic Mcgyan® process.* Bioresource Technology, 2011. **102**(1): p. 94-100.

271. Evans, R.W., et al., *Lipid composition of halotolerant algae, Dunaliella parva lerche and Dunaliella tertiolecta.* Biochimica et Biophysica Acta (BBA) - Lipids and Lipid Metabolism, 1982. **712**(1): p. 186-195.

272. Hartmut, G. and U. Weis, *Dunaliella Acidophila- Life at pH 1.0*, in *Dunaliella: Physiology, Biochemistry, and Biotechnology*, M. Avron and A. Ben-Amotz, Editors. 1992, CRC Press: Boca Raton, FL p. 99-100, 102-103, 106-107, 109, 126-127, & 129-133.

273. Azúa-Bustos, A., et al., *A novel subaerial Dunaliella species growing on cave spiderwebs in the Atacama Desert.* Extremophiles, 2010. **14**(5): p. 443-452.

274. Hard, B.C. and D.J. Gilmour, *Comparison of lipid composition of Dunaliella parva 19/9 mutant and wild type cells.* British Phycological Journal, 1992. **27**(1): p. 91-92.

275. Jiménez, C., F.X. Niell, and J.A. Fernández, *The photosynthesis of Dunaliella parva Lerche as a function of temperature, light and salinity.* Hydrobiologia, 1990. **197**(1): p. 165-172.

276. Hard, B.C. and D.J. Gilmour, *The uptake of organic compounds by Dunaliella parva CCAP 19/9.* European Journal of Phycology, 1996. **31**(3): p. 217-224.

277. González, M.A., et al., *Phylogenetic Relationship Among Various Strains of Dunaliella (Chlorophyceae) Based on Nuclear its rDNA Sequences.* Journal of Phycology, 2001. **37**(4): p. 604-611.

278. Duc Tran, C.L., Trung Vo, Mariao Giordano, Sixto Portilla, Nguyen Doan, Dat Tran, Truc Mai and Le Bui, *Identification of Dunaliella Viridis Using its Markers.* International Journal of Applied Science and Technology, 2013. **3**(4): p. 118-126.

279. Sexton, J., *Need some ID help on a contaminate algae*, D.J. Vidt, Editor. 2012: email.

280. Guillard, R.R.L., *Culture of phytoplankton for feeding marine invertebrates*, in *Culture of Marine Invertebrate Animals*, W.L. Smith and M.H. Chanley, Editors. 1975, Plenum Press: New York. p. 26-60.

281. Guillard, R., *Media formulation for commercial growth*, D.J. Vidt, Editor. 2008: Boothbay, ME.

282. Energy, U.S.D.o., *Building Technologies Program Solid-State Lighting Technology Fact Sheet*, E.E.R. energy, Editor. 2013.

283. StellarNet. *Instruemnts for LED Analysis*. SpectroRadiometers 2011 November 2, 2011 [cited 2011 December 8, 2011]; Available from: https://youtu.be/YEnLKTrmlSk.

284. Pegallapati, A. and N. Nirmalakhandan, *Energetic evaluation of an internally illuminated photobioreactor for algal cultivation.* Biotechnology Letters, 2011. **33**(11): p. 2161-2167.

285. Sieracki, M.E., N. Poulton, and N. Crosbie, *Automated Isolation Techniques for Microalgae*, in *Algae Culturing Techniques*, R.A. Andersen, Editor. 2005, Elsevier: Burlington, MA Sandiego, CA. p. 101-116.

286. Hauer, T. and L. Jirka, *Image analysis - a simple method of algal culture growth assessment.* Journal of Applied Phycology, 2007. **19**(5): p. 599-601.

287. Reifarth, F., G. Christen, and G. Renger, *Fluorometric equipment for monitoring $P680^{+\bullet}$ reduction in PS II preparations and green leaves.* Photosynthesis Research, 1997. **51**(3): p. 231-242.

288. Button, D.K. and B.R. Robertson, *Kinetics of bacterial processes in natural aquatic systems based on biomass as determined by high-resolution flow cytometry.* Cytometry, 1989. **10**(5): p. 558-563.

289. Campbell, J.W., C.M. Yentsch, and T.L. Cucci, *Variance within homogeneous phytoplankton populations, III: Analysis of natural populations.* Cytometry, 1989. **10**(5): p. 605-611.

290. Campbell, J.W. and C.M. Yentsch, *Variance within homogeneous phytoplankton populations, I: Theoretical framework for interpreting histograms.* Cytometry, 1989. **10**(5): p. 587-595.

291. Czechowska, K. and J.R. van der Meer, *A flow cytometry based oligotrophic pollutant exposure test to detect bacterial growth inhibition and cell injury.* Environ Sci Technol, 2011. **45**(13): p. 5820-7.

292. Demers, S., K. Davis, and T.L. Cucci, *A flow cytometric approach to assessing the environmental and physiological status of phytoplankton.* Cytometry, 1989. **10**(5): p. 644-652.

293. Dubelaar, G.B.J., et al., *Optical plankton analyser: A flow cytometer for plankton analysis, II: Specifications.* Cytometry, 1989. **10**(5): p. 529-539.

294. Mendoza, H., et al. *Characterization of Dunaliella salina strains by flow cytometry: a new approach to select carotenoid hyperproducing strains*. Electronic Journal of Biotechnology, 2008. **11**, DOI: 10.2225/vol11-issue4-fulltext-2.

295. Forcato, D., R. Pécora, and S. Kivatinitz, *On-line biomass monitoring in bench-scale stirred bioreactors using parts of a liquid chromatography system.* Biotechnology Letters, 2002. **24**(23): p. 1999-2003.

296. Guillard, R.R. and J.H. Ryther, *Studies of marine planktonic diatoms. I. Cyclotella nana Hustedt, and Detonula confervacea (cleve) Gran.* Canadian Journal of Microbiology, 1962. **8**: p. 229-39.

297. Brindley, C., F.G. Acién, and J.M. Fernández-Sevilla, *The oxygen evolution methodology affects photosynthetic rate measurements of microalgae in well-defined light regimes.* Biotechnology and Bioengineering, 2010. **106**(2): p. 228-237.

298. Spiden, E.M., et al., *Quantitative evaluation of the ease of rupture of industrially promising microalgae by high pressure homogenization.* Bioresource Technology, 2013. **140**: p. 165-171.

299. Lund, J.W.G., C. Kipling, and E.D. Cren, *The inverted microscope method of estimating algal numbers and the statistical basis of estimations by counting.* Hydrobiologia, 1958. **11**(2): p. 143-170.

300. Jiménez, C., et al., *Cell division in the unicellular microalga Dunaliella viridis depends on phosphorylation of extracellular signal-regulated kinases (ERKs).* Journal of experimental botany, 2007. **58**(5): p. 1001-1011.

301. Poulton, N., *Counting Methods- Flow Cytometery Methods and Proceedures*, D.J. Vidt, Editor. 2008.

302. Moulton, T.P. and M.A. Burford, *The mass culture of Dunaliella viridis (Volvocales, Chlorophyta) for oxygenated carotenoids: laboratory and pilot plant studies.* Hydrobiologia, 1990. **204-205**(1): p. 401-408.

303. Ondrej, P., J.S. David, and A.B. Michael, *Chlorophyll a Fluorescence in Aquatic Sciences: Methods and Applications: Developments in Applied Phycology 4*. 2010, DE: Springer Verlag.

304. Cosgrove, J. and M.A. Borowitzka, *Chapter 1 Chlorophyll Fluorescence Terminology: An Introduction*, in *Chlorophyll a fluorescence in aquatic sciences : methods and applications*, D.J. Suggett, O. Prásil, and M.A. Borowitzka, Editors. 2011, Springer: Dordrecht.

305. Holzwarth, A.R., *Light absorption and harvesting*, in *Molecular to global photosynthesis*, M.D. Archer and J. Barber, Editors. 2004, Imperial College Press; Distributed by World Scientific Pub. Co.: London; River Edge, NJ. p. 43-80.

306. Dean, P.J., *Comparisons and contrasts between light emitting diodes and high field electroluminescent devices.* Journal of Luminescence, 1981. **23**(1): p. 17-53.

307. Baynes, S.M., L. Emerson, and A.P. Scott, *Production of Algae for use in the rearing of larval fish.* Fisheries Research Technical Report, 1979. **53**: p. 13-18.

308. Marie, D., N. Simon, and D. Vaulot, *Phytoplankton Cell Counting by Flow Cytometery*, in *Algal Culturing Techniques*, R.A. Andersen, Editor. 2005, Elsevier Academic Press: Burlington, MA. p. 253-268.

309. Sieracki, M.E., *Training in flow cytometery for the enumeration of microalgae*, D.J. Vidt, Editor. 2008: Boothbay, ME USA.

310. McCutcheon, S.C., J.L. Martin, and T.O.J. Barnwell, *Water Quality* in *Handbook of Hydrology*, D.R. Maidment, Editor. 1993, McGraw-Hill: New York. p. 3, 11.

311. Bacaër, N., *Verhulst and the logistic equation (1838)*, in *A Short History of Mathematical Population Dynamics*. 2011, Springer London. p. 35-39.

312. Peleg, M., M.G. Corradini, and M.D. Normand, *The logistic (Verhulst) model for sigmoid microbial growth curves revisited.* Food Research International, 2007. **40**(7): p. 808-818.

313. Wood, A.M., R.C. Everroad, and L.M. Wingard, *Measuring Growth Rates in Microalgal Cultures*, in *Algal Culturing Techniques*, R.A. Andersen, Editor. 2005, Elsevier Academic Press: Burlington, MA. p. 269-286.

314. Shirsat, N., et al., *Revisiting Verhulst and Monod models: analysis of batch and fed-batch cultures.* Cytotechnology, 2015. **67**(3): p. 515-530.

315. Tsoularis, A. and J. Wallace, *Analysis of logistic growth models.* Mathematical Biosciences, 2002. **179**(1): p. 21-55.

316. Sakanoue, S., *Extended logistic model for growth of single-species populations.* Ecological Modelling, 2007. **205**(1–2): p. 159-168.

317. McHugh, M.L., *Standardna pogreška: značenje i interpretacija. (Slovenian).* Standard error: meaning and interpretation. (English), 2008. **18**(1): p. 7-13.

318. Sakevich, A.I. and L.F. Osipov, *Relationship between Rates of Algal Biomass Gain and Concentration of Extracellular Organic Compounds.* Gidrobiologičeskij žurnal, 1983. **19**(5): p. 71-74.

319. Rohban, R., M.A. Amoozegar, and A. Ventosa, *Screening and isolation of halophilic bacteria producing extracellular hydrolyses from Howz Soltan Lake, Iran.* Journal of Industrial Microbiology & Biotechnology, 2009. **36**(3): p. 333-340.

320. VAN AUKEN, O.W. and I.B. McNULTY, *THE EFFECT OF ENVIRONMENTAL FACTORS ON THE GROWTH OF A HALOPHYLIC SPECIES OF ALGAE.* The Biological Bulletin, 1973. **145**(1): p. 210-222.

321. García, F., Y. Freile-Pelegrín, and D. Robledo, *Physiological characterization of Dunaliella sp. (Chlorophyta, Volvocales) from Yucatan, Mexico.* Bioresource Technology, 2007. **98**(7): p. 1359-1365.

322. Gordillo, F.J.L., et al., *Effects of light intensity, CO 2 and nitrogen supply on lipid class composition of Dunaliella viridis.* Journal of Applied Phycology, 1998. **10**(2): p. 135-144.

323. Gordillo, F.J.L., et al., *Influence of elevated CO2 and nitrogen supply on the carbon assimilation performance and cell composition of the unicellular alga Dunaliella viridis.* Physiologia Plantarum, 2003. **119**(4): p. 513.

324. Bozhkov, A.I. and N.G. Menzyanova, *Growth dynamics, lipid composition, and βετα-carotene content in cells of Dunaliella viridis Teod. under cultivation in different types of photobioreactors.* 1999. **1**(3): p. 31-39.

325. Ak, I., S. Cirik, and T. Goksan, *Effects of Light Intensity, Salinity and Temperature on Growth in Camalti Strain of Dunaliella viridis Teodoresco from Turkey.* Journal of Biological Sciences, 2008. **8**(8): p. 1356-1359.

326. GIBOR, A., *THE CULTURE OF BRINE ALGAE.* The Biological Bulletin, 1956. **111**(2): p. 223-229.

327. Jiménez, C. and F. Xavier Niell, *Influence of temperature and nitrogen concentration on photosynthesis of Dunaliella viridis Teodoresco.* Journal of Applied Phycology, 1990. **2**(4): p. 309-317.

328. Ruangsomboon, S., *Effect of light, nutrient, cultivation time and salinity on lipid production of newly isolated strain of the green microalga, Botryococcus braunii KMITL 2.* Bioresource Technology, 2012. **109**(0): p. 261-265.

329. NIST/SEMATECH, *Product and Process Comparisons*, in *e-Handbook of Statistical Methods*. 2012.

330. Furnas, M.J., *In situ growth rates of marine phytoplankton: approaches to measurement, community and species growth rates.* Journal of Plankton Research, 1990. **12**(6): p. 1117-1151.

331. Bozhkov, A.I., et al., *The Rate of Aging of the Dunaliella viridis Teodor. Culture Depends on the Algae Pre-Adaptation to Copper Sulfate Toxic Effect.* Advances in Aging Research, 2014. **3**(2): p. 187-198.

332. Sorokin, C. and R.T. Krauss, *The Effects of Light Intensity on the Growth Rates of Green Algae.* Plant Physiology, 1958. **33**(2): p. 109-113.

333. Kok, B. and W. Gott, *Activation Spectra of 700 mmu Absorption Change in Photosynthesis.* Plant Physiology, 1960. **35**(6): p. 802-8.

334. Brierley, J.A. and C.L. Brierley, *Present and future commercial applications of biohydrometallurgy.* Hydrometallurgy, 2001. **59**(2–3): p. 233-239.

335. Poulin, R. and R.W. Lawrence, *Economic and environmental niches of biohydrometallurgy.* Minerals Engineering, 1996. **9**(8): p. 799-810.

336. Rawlings, D.E., *Heavy metal mining using microbes.* Annual Review of Microbiology, 2002. **56**(1): p. 65.

337. Van Gerpen, J., et al., *Biodiesel Analytical Methods*. 2004, National Renewable Energy Laboratory: Golden, CO USA.

VITA

Daniel James Vidt was born in October of 1973 in Valparaiso, Indiana. Daniel attended Purdue University in West Lafayette, IN and earned a Bachelor of Science in Biology with a minor in Chemistry and a teaching license for grades 8-12 in Biology and Chemistry. During his tenure as a science instructor for McCutcheon High School in Lafayette, IN, he was a Golden Apple finalist for the Tippecanoe Chamber of Commerce, and co-coached an Indiana State Champion Academic Superbowl Team. Daniel left teaching in 2005 to enroll in the graduate program for Aquaculture at Purdue University in West Lafayette, IN where he assisted in the establishment of a laboratory for the development of novel proteomic methods for determining fin-fish malnutrition.

Daniel later transferred to the University of Missouri-Rolla, Rolla, MO having been awarded a Department of Education's Graduate Assistance in Areas of National Need (GAANN) in Energy Research Related to Sound Public Policy Fellowship for work in microbial fuel cells. He co-authored a book chapter on the subject in 2007 along with numerous poster presentations. Daniel graduated in 2008 with his Master of Science in Material Science and Engineering- Ceramic Engineering.

Daniel was then awarded a Missouri University of Science & Technology Chancellor's Fellowship for Ph.D. work in the Mining Department, developing algal based biotechnologies for mining. Daniel's research work with algae was reported in the New York Times on 11/02/2009. Daniel was later awarded the Henry DeWitt Smith Scholarship in 2010 by The American Institute of Mining, Metallurgical, and Petroleum Engineers (AIME) for his work. Daniel is also a co-author for a refereed book chapter on halophilic organism in 2011. In May 2016, he received his Ph.D. in Mining Engineering from the Missouri University of Technology, Rolla, Missouri, USA.